

**A THESIS SUBMITTED FOR THE DEGREE OF DOCTOR OF  
PHILOSOPHY**

by

**ZHAO XINHAI**

*B.Eng(Honors)*

Mathematical Modeling of Two-terminal Perovskite-Based Thin-film  
Tandem Solar Cells: Elucidating the Underlying Physics and Optimizing  
the Power Conversion Efficiency

Thesis Advisors:

- i. Associate Professor Birgersson, Karl Erik
- ii. Dr Xue Hansong

Examiners:

- i. Associate Professor Zhou Guangya
- ii. Dr Shen Lei

DEPARTMENT OF MECHANICAL ENGINEERING

NATIONAL UNIVERSITY OF SINGAPORE

2023



# Abstract

This PhD thesis focuses on the mathematical modeling of perovskite-based thin-film solar cells for effective clean energy harvesting. It includes detailed derivations of the optical system and electronics model for single-junction perovskite solar cells. We employ artificial neural networks to predict the performances of these solar cells with mean squared errors below  $10^{-3}$  when the predicted and actual outputs are normalized between -1 and 1. Additionally, comprehensive design guidelines are provided for two-terminal perovskite-based tandem solar cells, investigating current matching, light interference effects, and the S-shaped current-voltage characteristic. After sensitivity and loss analyses, parametric studies and optimizations predict optimized power conversion efficiencies of 30.5% and 28.0% for two-terminal perovskite-on-perovskite and perovskite-on-organic tandem solar cells, respectively. Lastly, a mixed-integer optimization approach for bifacial two-terminal perovskite-on-perovskite tandem solar cells is presented. We find the optimal and close-to-optimal cell architectures, including material combinations and layer thicknesses, that achieve the highest short-circuit current for devices operating under five different albedo conditions. This work aims to contribute valuable tools for understanding solar cell operation, optimizing device performance, and guiding future design enhancements. Future extensions of this work include further calibration and validation with experiment, multi-junction perovskite-based tandem solar cells, and digital twins applications.



## Declaration

I hereby declare that this thesis is my original work and it has been written by me in its entirety. I have duly acknowledged all the sources of information which have been used in the thesis.

This thesis has also not been submitted for any degree in any university previously.

Name: ZHAO Xinhai

赵昕海

Signature: \_\_\_\_\_

Date: 02/08/2023



# Acknowledgments

I would like to thank my supervisor, A/P Erik Birgersson, for his support and guidance. His enthusiasm, expertise in mathematical modeling, critical thinking for problem solving, inspiration and encouragement have accompanied me throughout my PhD journey. I have conquered several challenges under his supervision, and am very grateful for having this great opportunity to work with him.

I also thank my co-supervisor, Dr. Xue Hansong, for his guidance on modeling of perovskite solar cells. His knowledge in the field of photovoltaic provide essential support for my work. I appreciate his patience, supervision and encouragement during our regular discussions.

I want to thank my colleague, Tan Hu Quee, for accompany me throughout the journey. His presence allows me to view problems from different perspectives, and solve them with various approaches.

I gratefully acknowledge Solar Energy Research Institute of Singapore (SERIS) for providing me a conducive environment for solar cell research, and thank to my peers at SERIS for all their supports.

Finally, I would like to appreciate my parents for their understanding and supports of my oversea study. Their patience and love grant me motivation to overcome challenges in life.



# Contents

<b>Abstract</b>	<b>iii</b>
<b>Acknowledgments</b>	<b>i</b>
<b>List of Figures</b>	<b>xviii</b>
<b>List of Tables</b>	<b>xx</b>
<b>Nomenclature</b>	<b>xxvi</b>
<b>List of publications</b>	<b>xxvii</b>
<b>1 Introduction</b>	<b>1</b>
1.1 Background . . . . .	1
1.2 Perovskite solar cells . . . . .	2
1.2.1 The perovskite material . . . . .	2
1.2.2 Development . . . . .	3
1.2.3 Working principle . . . . .	5
1.3 Tandem solar cells . . . . .	5
1.3.1 2T perovskite-on-perovskite tandem solar cells . . . . .	7
1.3.2 2T perovskite-on-organic tandem solar cells . . . . .	8
1.4 Existing models for thin-film tandem solar cells . . . . .	8
1.4.1 2T perovskite-on-perovskite tandem solar cell models . . . . .	8
1.4.2 2T perovskite-on-organic tandem solar cell models . . . . .	9
1.5 Solar cells under bifacial operation . . . . .	10

---

1.6 Scope and objectives of the thesis . . . . .	11
<b>2 Optics</b>	<b>15</b>
2.1 Electromagnetism . . . . .	16
2.2 Coherent light propagation . . . . .	19
2.2.1 Absorbing boundary conditions . . . . .	19
2.2.2 Electric and magnetic fields in thin-film layers . . . . .	21
2.2.2.1 Single thin-film layer . . . . .	21
2.2.2.2 Double layer thin-film stack . . . . .	23
2.2.2.3 Thin-film stack with $N$ layers . . . . .	26
2.2.3 Absorptance, reflectance and transmittance . . . . .	28
2.2.4 Charge carrier generation . . . . .	31
2.2.5 Polarization and oblique incident light . . . . .	32
2.3 Incoherent light propagation . . . . .	33
2.3.1 Correction on incident light intensity . . . . .	34
2.3.2 The phase elimination method . . . . .	35
2.4 Verifications . . . . .	36
2.4.1 Thin-film layers . . . . .	36
2.4.2 Thin-film layers with glass substrate . . . . .	39
<b>3 Electronics</b>	<b>41</b>
3.1 Energy band level and charge carrier concentration . . . . .	42
3.2 Potential and electric field . . . . .	46
3.3 Charge carrier drift and diffusion . . . . .	47
3.4 Charge carrier recombination . . . . .	48
3.5 Summary . . . . .	50
3.5.1 Governing equation . . . . .	50
3.5.2 Boundary conditions . . . . .	51
3.5.3 Constitutive relations . . . . .	51

<b>4 Numerics</b>	<b>53</b>
4.1 Vectorized matrix calculation for optics . . . . .	53
4.2 Finite element method . . . . .	53
4.3 Monte Carlo simulation and sensitivity analysis . . . . .	54
4.4 Genetic algorithm . . . . .	56
<b>5 Neural network for perovskite solar cells</b>	<b>57</b>
5.1 Introduction . . . . .	57
5.2 Mathematical formulation . . . . .	58
5.3 Methodology . . . . .	62
5.3.1 Types of neural networks . . . . .	62
5.3.2 Data preparation . . . . .	63
5.3.3 Training of neural network . . . . .	64
5.3.4 Optimization of hyperparameters . . . . .	65
5.4 Results and discussions . . . . .	66
5.4.1 Visualization of data . . . . .	66
5.4.2 Neural network performance . . . . .	67
5.4.2.1 Baseline model: predicting all outputs . . . . .	68
5.4.2.2 Predicting device performance ( $V_{oc}$ , FF, $\eta$ ) . . . . .	72
5.4.2.3 Predicting recombination losses at MPP . . . . .	75
5.4.2.4 Predicting recombination losses at OC . . . . .	77
5.4.3 Calibration and validation . . . . .	78
5.5 Summary . . . . .	84
<b>6 2T perovskite-on-perovskite tandem solar cells</b>	<b>85</b>
6.1 Introduction . . . . .	86
6.2 Mathematical formulation . . . . .	87
6.2.1 Governing equations . . . . .	89
6.2.2 Boundary conditions . . . . .	90
6.2.3 Constitutive relations . . . . .	91

---

6.3	Verification and validation (optics) . . . . .	93
6.4	Calibration and validation (electronics) . . . . .	95
6.5	Results and discussions . . . . .	99
6.5.1	The interconnecting layer . . . . .	100
6.5.2	Light management . . . . .	103
6.5.3	Loss analysis . . . . .	105
6.5.4	Towards higher PCE . . . . .	109
6.5.5	Levelized cost of electricity . . . . .	112
6.5.6	Bifacial operation . . . . .	113
6.5.7	Sensitivity analysis . . . . .	114
6.5.7.1	Correlation from normal distribution . . . . .	116
6.5.7.2	Correlation from Latin hypercube and random sampling	120
6.6	Summary . . . . .	125
<b>7</b>	<b>2T perovskite-on-organic tandem solar cells</b>	<b>127</b>
7.1	Introduction . . . . .	127
7.2	Mathematical formulation . . . . .	129
7.2.1	Governing equations . . . . .	130
7.2.2	Boundary conditions . . . . .	131
7.2.3	Constitutive relations . . . . .	132
7.3	Calibration and validation . . . . .	135
7.4	Sensitivity analysis . . . . .	140
7.5	Loss analysis . . . . .	143
7.6	Interconnecting layer . . . . .	144
7.7	Towards a more efficient device . . . . .	147
7.8	Summary . . . . .	150
<b>8</b>	<b>Mixed-integer optimization on bifacial tandem solar cells</b>	<b>153</b>
8.1	Introduction . . . . .	153
8.2	Mathematical formulation . . . . .	155

8.3 Validation . . . . .	163
8.4 Results and discussions . . . . .	164
8.4.1 Mixed-integer optimization . . . . .	164
8.4.1.1 Monofacial devices . . . . .	169
8.4.1.2 Low albedos . . . . .	169
8.4.1.3 High albedos . . . . .	170
8.4.1.4 Transmittance . . . . .	171
8.4.1.5 Further guidelines for materials and thicknesses . . . . .	171
8.4.2 External quantum efficiency . . . . .	173
8.4.3 Sensitivity analysis . . . . .	174
8.4.4 Device performance . . . . .	176
8.4.5 Cost consideration . . . . .	177
8.5 Summary . . . . .	177
<b>9 Conclusion</b>	<b>179</b>
<b>10 Outlook</b>	<b>183</b>
<b>Bibliography</b>	<b>187</b>



# List of Figures

1.1	ABX <sub>3</sub> crystal structure for perovskite material where A and B are cations, and X is an anion. . . . .	3
1.2	PCE developments for four types of single-junction solar cells from year 2010 to 2023 [12], with the Shockley-Queisser limit indicated [13]. . . .	4
1.3	General device structures with the incoming and transmitted light spec- trum for (a) a 4T tandem solar cell and (b) a 2T tandem solar cell. . . .	6
2.1	(a) Horizontally polarized ( $z$ -direction) electric field and (b) correspond- ing vertically polarized ( $y$ -direction) magnetic field for an electromag- netic wave (TEM mode) propagating in the $x$ -direction with velocity $v$ . .	17
2.2	Schematic of a single thin-film layer bounded by glass, with wave prop- agating in the $x$ - direction and the electric field perturbing in the $z$ - direction. . . . .	21
2.3	Schematic of a double layer thin-film stack bounded by air. . . . .	23
2.4	Schematic of a $N$ layer thin-film stack bounded by air. . . . .	26
2.5	Schematic of a $N$ layer thin-film stack bounded by glass and air. . . . .	34
2.6	(a) Real and (b) imaginary parts of the optical electric field obtained from semi-analytical solution (lines) and solving the system of equations nu- merically (squares) at 400 nm (blue), 600 nm (red), and 800 nm (green) wavelengths for an one layer thin-film. . . . .	37

---

2.7 (a) Real and (b) imaginary parts of the optical electric field obtained from semi-analytical solution (lines) and solving the system of equations numerically (squares) at 400 nm (blue), 600 nm (red), and 800 nm (green) wavelengths for a five-layer thin-film stack. The vertical dashed lines indicate the interfaces between thin-film layers. . . . .	37
2.8 Real and imaginary parts of the optical electric field in (a-b) top perovskite layer and (c-d) bottom perovskite layer of a ten-layer thin-film stack in a 2T perovskite-on-perovskite tandem solar cell obtained from semi-analytical solution (lines) and solving the system of equations numerically (squares) at 400 nm (blue), 600 nm (red), and 800 nm (green) wavelengths. . . . .	38
2.9 EQE calculated from semi-analytical matrix formulation with phase elimination method (red line), solving the system of equations numerically together with phase elimination method (circle), and general transfer matrix method with an incoherency correction term (plus sign). . . . .	39
3.1 Schematic of a typical p-i-n structured planar perovskite solar cell. Here, $l$ is the layer thickness, the roman numerals indicate the interfaces between layers, and {G,F,H,P,E,B} are superscripts that denote the corresponding layers. . . . .	42
3.2 Energy band diagram for a p-i-n structured planar perovskite solar cell. .	43
5.1 Input and output parameters of the full optoelectronic model for a planar perovskite solar cell. . . . .	60
5.2 Neural network architectures for a planar perovskite solar cell with three hidden layers–HL1, HL2, and HL3, and with the outputs being (a) the device performances, (b) recombination losses at MPP, and (c) recombination losses at OC. Here, not all the nodes in the inputs and hidden layers are shown for the sake of simplicity. . . . .	61

5.3 Distributions of the inputs (a-b) and outputs (c) parameters. Here, all inputs and outputs are normalized between -1 and 1. The horizontal red line inside of each box denotes the sample median, the top and bottom edge of each box represents the upper and lower quartiles, and the red plus signs are the outliers with values more than 1.5 times of the interquartile range away from the box. . . . .	66
5.4 Actual values from full optoelectronic model and results from baseline neural network prediction for the (a) open-circuit voltage, (b) fill factor, and (c) power conversion efficiency. The blue plus signs and red circles represent the training data and testing data, respectively. . . . .	69
5.5 Actual values from full optoelectronic model and results from baseline neural network prediction for the (a) radiative recombination loss, (b) SRH recombination loss, (c) auger recombination loss, (d) surface recombination loss at interface IV, and (e) surface recombination loss at interface V at the MPP. The blue plus signs and red circles represent the training data and testing data, respectively. . . . .	70
5.6 Actual values from full optoelectronic model and results from baseline neural network prediction for the (a) radiative recombination loss, (b) SRH recombination loss, (c) auger recombination loss, (d) surface recombination loss at interface IV, and (e) surface recombination loss at interface V at the OC. The blue plus signs and red circles represent the training data and testing data, respectively. . . . .	71
5.7 Actual values from full optoelectronic model and results from neural network prediction for the (a) open-circuit voltage, (b) fill factor, (c) power conversion efficiency. The blue plus signs and red circles represent the training dataset and testing dataset B, respectively. . . . .	74

5.8 Actual values from full optoelectronic model and results from neural network prediction for the (a) radiative recombination loss, (b) SRH recombination loss, (c) Auger recombination loss, (d) interfacial recombination loss at IV, (e) interfacial recombination loss at V at MPP. The blue plus signs and red circles represent the training dataset and testing dataset B, respectively. . . . .	76
5.9 Actual values from full optoelectronic model and results from neural network prediction for the (a) radiative recombination loss, (b) SRH recombination loss, (c) Auger recombination loss, (d) interfacial recombination loss at IV, (e) interfacial recombination loss at V at OC. The blue plus signs and red circles represent the training dataset and testing dataset B, respectively. . . . .	78
5.10 Simulated (lines) and experimental (symbols) $i - V$ curves for Cells A (red), B (blue) and C (green). . . . .	83
6.1 Schematic diagram for the 2T perovskite-on-perovskite tandem solar cell considered. The interfaces are denoted by the roman numerals. $l$ is the layer thickness. The superscripts G, F, H, P, E, T, and B denotes the glass, front contact, hole-transporting, perovskite, electron-transporting, interconnecting/tunneling layer, and the back contact layers, respectively. The subscripts $t$ and $b$ denote the top and bottom subcells, respectively. . . . .	87
6.2 (a) Refractive index and (b) extinction coefficient for glass (green line with upper triangle), ITO (green line with circle), PTAA (blue line with upper triangle), top cell perovskite (blue line with square), C60 (blue line with lower triangle), $\text{SnO}_2$ (green line with square), PEDOTPSS (red line with upper triangle), bottom cell perovskite (red line with square), BCP (green line with diamond) and Cu (green line with lower triangle). Here, C60 in the bottom cell shares the same optical properties with the top cell C60. . . . .	94

6.3 (a) Generation profiles from the phase elimination method (symbols) and from the semi-analytical solution (lines) for top subcell (blue) and bottom subcell (red); (b) EQE from the semi-analytical solution (lines) and from experiment (symbols) for top subcell (blue) and bottom subcell (red). . . . .	95
6.4 Predicted (lines) and experimental measured (circles for calibration and squares for validation) current-voltage curves for top perovskite cell (blue), bottom perovskite cell (red), and 2T perovskite-on-perovskite tandem solar cell (green). . . . .	99
6.5 (a) Current limiting behavior of a 2T perovskite-on-perovskite tandem solar cell achieved by ICL in the model, with the red dotted lines showing how current is limited for the calibrated parameters (red diamond); (b) Current-voltage curves when trap-assisted recombination coefficient is varied from $\tau^T = 10^{-12}$ s to $\tau^T = 10^{-5}$ s. . . . .	100
6.6 Simulated $i - V$ curves of the tandem devices with (a) the charge carrier mobility in the interconnecting layer changed from $10^{-6}$ to $10^{-1}$ m <sup>2</sup> /V/s and (b) density of states in the interconnecting layer being $10^{18}$ (red), $10^{19}$ (green), and $10^{20}$ (blue) 1/m <sup>3</sup> . Here, there is no obvious perturbations of $i - V$ curves with changes in charge carrier mobility in (a). . . . .	102
6.7 Simulated $i - V$ curves of the 2T perovskite-on-perovskite tandem solar cells with SnO <sub>2</sub> (blue) and IZO (red). . . . .	103
6.8 PCE, represented by the symbol $\eta$ , of the 2T perovskite-on-perovskite tandem solar cell at different top and bottom perovskite thicknesses with (a) 70 nm and (b) 30 nm front contact, showing the first (blue square) and second (blue circle) local highest PCE points for the parameter ranges considered here. . . . .	104

6.9 Loss due to radiative, auger and SRH recombinations in the perovskite layers and interface recombinations between perovskite layers and their adjacent carrier transporting layers at (a) MPP (in top subcell: magenta square; in bottom subcell: blue square); and (b) $V_{oc}$ (in top subcell: green square; in bottom subcell: red square). The percentage loss is calculated as each individual recombination loss divided by the total recombination loss for the parameters considered here. . . . .	105
6.10 $V_{oc}$ and PCE of the 2T perovskite-on-perovskite tandem solar cell when the effective surface recombination velocities at (a) interface IV; (b) interface IX; and trap-assisted recombination lifetime in (c) top perovskite; (d) bottom perovskite are varied. . . . .	107
6.11 Pathway to improve the PCE of the 2T perovskite-on-perovskite tandem solar cell, (a) showing the change in $V_{oc}$ , FF and PCE when intrinsic transport properties are adjusted based on Table 2 and (b) the corresponding current-voltage curves from experiment (Exp), calibration (Cal), model prediction with adjusted parameters (Adj) in Table 6.2, together with model prediction from bifacial operation (Bif). . . . .	111
6.12 Fishbone diagram for the parameters involved in the 2T perovskite-on-perovskite tandem solar cell modeling, with the twenty eight chosen stochastic parameters for Monte Carlo simulation in blue, top four determined most sensitive parameters in red, and next four influential parameters in yellow. . . . .	115
6.13 Sensitivity rankings of the stochastic parameters involved in the 2T perovskite-on-perovskite tandem solar cell from a normally distributed input for (a) $V_{oc}$ ; (b) $i_{sc}$ ; (c) FF; and (d) PCE. . . . .	116

---

6.14 Input and output parametric space including the top four parameters for the case of normal distribution, with dataset for the highest PCE (magenta line); PCE larger than 25% (red line); PCE within 23% to 25% (green line); PCE smaller than 23% (cyan line); the lowest PCE (blue line); and the calibration case (dotted line) shown. . . . .	117
6.15 Correlation matrix for the relations among the top four most sensitive parameters and the PCE, in the case of normal distribution. . . . .	119
6.16 Sensitivity rankings of the stochastic parameters involved in the 2T perovskite-on-perovskite tandem solar cell from a Latin hypercube sampled input for (a) $V_{oc}$ ; (b) $i_{sc}$ ; (c) FF; and (d) PCE. . . . .	120
6.17 Input and output parametric space including the top four parameters for the case of Latin hypercube sampling, with dataset for the highest PCE (magenta line); PCE larger than 25% (red line); PCE within 22% to 25% (green line); PCE smaller than 22% (cyan line); the lowest PCE (blue line); and the calibration case (dotted line) shown. . . . .	121
6.18 Correlation matrix for the relations among the top four most sensitive parameters and the PCE, in the case of Latin hypercube sampling. . . .	122
6.19 Sensitivity rankings of the stochastic parameters involved in the 2T perovskite-on-perovskite tandem solar cell from a random sampling input for (a) $V_{oc}$ ; (b) $i_{sc}$ ; (c) FF; and (d) PCE. . . . .	123
6.20 Input and output parametric space including the top four parameters for the case of random sampling, with dataset for the highest PCE (magenta line); PCE larger than 25% (red line); PCE within 22% to 25% (green line); PCE smaller than 22% (cyan line); the lowest PCE (blue line); and the calibration case (dotted line) shown. . . . .	124
6.21 Correlation matrix for the relations among the top four most sensitive parameters and the PCE, in the case of random sampling. . . . .	125
7.1 Schematic diagram of a 2T perovskite-on-organic tandem solar cell. . .	129

7.2 (a) Simulated and experimental $i - V$ curves for cells calibrated; (b) experimental $i - V$ curves for 2T perovskite-on-organic tandem solar cells with different interconnecting layer thicknesses. . . . .	138
7.3 Sensitivity rankings of the stochastic parameters involved in the 2T perovskite-on-organic tandem solar cell for (a) open-circuit voltage ( $V_{oc}$ ), (b) short-circuit current density ( $i_{sc}$ ), (c) fill factor, and (d) PCE ( $\eta$ ). . . . .	140
7.4 Percentage contributions to the total recombination loss due to different loss channels at (a) MPP and (b) open-circuit voltage. . . . .	143
7.5 Simulated $i - V$ curves of the 2T perovskite-on-organic tandem solar cells with IZO (blue) and SnO <sub>2</sub> (red). . . . .	146
7.6 Relationship between the charge carrier mobility, interfacial recombination velocities, layer thicknesses, and the output PCEs from the parametric sweep study. . . . .	147
8.1 Schematic of a 2T perovskite-on-perovskite tandem solar cell. Here, the Roman numerals denote the interfaces, $l$ is the layer thickness; and G, F, H, P, E, I, and B denote the glass, front-contact, hole-transporting, perovskite, electron-transporting, interconnecting, and back-contact layers, respectively. The subscripts $t$ and $b$ denote the top and bottom subcells, respectively. . . . .	155
8.2 Inputs, constraints, and outputs considered in the mixed integer optimization for 2T perovskite-on-perovskite tandem solar cells. Here, $I_0$ is the solar irradiance of the front incident light, $R_a$ is the spectral albedo, $n$ is the refractive index, and $\kappa$ is the extinction coefficient. . . . .	158
8.3 (a) Energy band diagrams for the materials for the 2T perovskite-on-perovskite tandem solar cells; (b) front incident light based on the ASTM G173-03 global tilt solar spectrum; and (c) albedo values for roof shingle (red), green grass (green), white sand (cyan), snow (blue), and 0.2 albedo (orange). . . . .	160

8.4 Refractive indices (n) and extinction coefficients ( $\chi$ ) for the materials in the optimization: (a-b) FTO (blue), ITO (red), IZO (green), AZO (magenta) and Soda-lime glass (orange); (c-d) spiro-OMeTAD (blue), $\text{NiO}_x$ (red), PEDOT-PSS (green) and PTAA (magenta); (e-f) $\text{CsFAPb}(\text{I}_{1-x}\text{Br}_x)_3$ with bandgaps of 1.62 eV (blue), 1.67 eV (red), 1.70 eV (green), 1.73 eV (orange), 1.75 eV (cyan), and 1.80 eV (magenta); (g-h) $\text{MAPb}(\text{I}_{1-x}\text{Br}_x)_3$ with bandgaps of 1.68 eV (blue), 1.85 eV (red), and 2.03 eV (green); (i-j) $\text{MAPbI}_3$ (blue), $\text{FAPbI}_3$ (red), $\text{MAPbBr}_3$ (green), and $\text{MAPbCl}_3$ (orange); (k-l) $(\text{FASnI}_3)_{1-x}(\text{MAPbI}_3)_x$ with bandgaps of 1.07 eV (blue), 1.13 eV (red), 1.25 eV (green), and 1.30 eV (orange), together with $\text{FASnI}_3$ (cyan); (m-n) $\text{SnO}_2$ (blue), PCBM (red) and C60 (green); (o-p) Au (blue), Ag (red for back contact, orange for interconnecting layer), and Cu (green). . . . .	162
8.5 (a) Optimized top perovskite materials and their best short-circuit current densities in the optimized 2T perovskite-on-perovskite tandem solar cells under different albedo conditions: monofacial (MF, 0 albedo), 0.2 albedo (0.2), roof shingle (RS), green grass (GG), white sand (WS) and snow (S). Here, the bottom perovskite material is $(\text{FASnI}_3)_{1-x}(\text{MAPbI}_3)_x$ for all cases, with a bandgap of 1.07 eV except the one marked by * in RS, where the bandgap is 1.13 eV. (b) Optimal perovskite bandgaps and layer thicknesses for the top and bottom subcells with the corresponding photogenerated current densities and short-circuit current density in the 2T perovskite-on-perovskite tandem solar cells. Here, $I_{total}$ is the total irradiance, $E_{g,t}$ and $E_{g,b}$ are the top and bottom perovskite bandgaps respectively, $T$ is the average transmittance from the top subcell entering the bottom subcell, and $i_{ph,t}$ and $i_{ph,b}$ are the top and bottom photogenerated current densities, respectively; and (c) optimal thicknesses of the remaining layers. . . . .	165

---

8.6 Relative frequencies of the materials that have been identified as the best choice in (a) the front-contact, (b) top hole-transporting, (c) top electron-transporting, (d) interconnecting, (e) bottom hole-transporting, (f) bottom electron-transporting and (g) back-contact layers of the twenty-four optimized 2T perovskite-on-perovskite tandem solar cells. . . . .	172
8.7 External quantum efficiencies (EQEs) of the top subcells (red) and bottom subcells (blue) for the optimized 2T perovskite-on-perovskite tandem solar cells: (a) monofacial, (b) 0.2 albedo, (c) roof shingle, (d) green grass, (e) white sand and (f) snow. . . . .	173
8.8 Probability distribution functions for the short-circuit current densities from the sensitivity analysis for 2T perovskite-on-perovskite tandem solar cells under different albedo conditions: (a) monofacial, (b) 0.2 albedo, (c) roof shingle, (d) green grass, (e) white sand and (f) snow. The statistics of the short-circuit current densities under various operation spectral albedos are highlighted in (g); and the short-circuit current densities from mixed-integer optimizations are indicated by blue vertical lines in (a)-(f). . . . .	175

# List of Tables

5.1	Input and output parameters collected from the full optoelectronics model for training of neural network. . . . .	63
5.2	Optimized hyperparameters and neural network performances for predicting all thirteen device performances ( $V_{oc}$ , FF, $\eta$ , and recombination losses at MPP and OC). The mean squared errors are calculated based on the normalized data. . . . .	68
5.3	Optimized hyperparameters and neural network performances for predicting the device performance ( $V_{oc}$ , FF, $\eta$ ). . . . .	73
5.4	Optimized hyperparamters and neural network performances for predicting the recombination losses at MPP. . . . .	75
5.5	Optimized hyperparamters and neural network performances for predicting the recombination losses at OC. . . . .	77
5.6	Parameters for the calibration of the first neural network model for Cell A [5]. Here, SEM stands for scanning electron microscopy. . . . .	79
5.7	Parameters for the calibration of the first neural network model for Cell B [5]. . . . .	80
5.8	Parameters for the calibration of the first neural network model for Cell C [27]. . . . .	81
6.1	Parameters for the top subcell (TC), bottom subcell (BC) and the interconnecting layer (ICL). The references are stated in the last three columns. Some of the parameters are fitted (Fit) based on calibration. .	97

6.2	Parameters from calibrated model (Cal) and from adjusted parameter set (Adj) in the top subcell (TC) and bottom subcell (BC) for achieving a 30.5% PCE 2T perovskite-on-perovskite tandem solar cell. . . . .	111
6.3	<i>i – V</i> characteristics, FF and PCE of the 2T perovskite-on-perovskite tandem solar cell from experiment (Exp), model calibration (Cal), model prediction with adjusted parameter values (Adj) and the bifacial operation (Bif). . . . .	112
7.1	Mathematical model parameters for the stand-alone single junction perovskite top cell and the 2T perovskite-on-organic tandem solar cell with Ag as interconnecting layer. The layer thicknesses are estimated from scanning electron microscopy diagram (SEM). . . . .	136
7.2	Optical data for the materials considered. . . . .	137
7.3	Mathematical model parameters that are different from Table 7.1 for the champion tandem solar cell with IZO as interconnecting layer (cell 3), and the second batch of tandem solar cell with 2, 4, 6, and 20 nm IZO as interconnecting layer (cell 4 to 7). . . . .	138
8.1	Sources of optical data (refractive index, $n$ , and extinction coefficient, $\kappa$ ), energy levels, and work functions for the materials considered for the mixed-integer optimization. . . . .	161
8.2	Experimental [145] and simulated short-circuit current densities for monofacial (MF) and bifacial 2T perovskite-on-perovskite tandem solar cells with various top perovskite bandgaps and under two different albedos. .	164
8.4	Material combinations and layer thicknesses in monofacial (MF) and bifacial 2T perovskite-on-perovskite tandem solar cells for optimal short-circuit current. . . . .	168

# Nomenclature

## Mathematical Symbols

$A_q$	auger recombination coefficient for species $q$	$\text{m}^6 \text{s}^{-1}$
$B_{rad}$	radiative recombination coefficient	$\text{m}^3 \text{s}^{-1}$
$c_e^0$	electron concentration at X	$\text{m}^{-3}$
$C_G$	Incoherency correction	
$c_h^0$	hole concentration at III	$\text{m}^{-3}$
$c_i$	intrinsic carrier concentration	$\text{m}^{-3}$
$c_q$	concentration of species $q$	$\text{m}^{-3}$
$c_{q,trap}$	trap density for species $q$	$\text{m}^{-3}$
$D$	carrier diffusion coefficient	$\text{m}^2 \text{s}^{-1}$
$d$	scaled down glass thickness	m
$\Delta E_{trap}$	energy difference between the valence band and trap energy level eV	
$E_0$	magnitude of incident optical electric field	$\text{V m}^{-1}$
$E_R$	magnitude of incident optical electric field	$\text{V m}^{-1}$
$E_{0,b}$	magnitude of incident optical electric field from the rear side	$\text{V m}^{-1}$
$E_g$	energy band gap	eV

$E_T$	magnitude of transmitted optical electric field	$\text{V m}^{-1}$
$E_z$	optical electric field magnitude	$\text{V m}^{-1}$
$I_0$	incident spectral irradiance	$\text{W m}^{-2}$
$G$	generation rate	$\text{m}^{-3} \text{s}^{-1}$
$i_p$	photogenerated current density	$\text{A m}^{-2}$
$i_{tot}$	total current density	$\text{A m}^{-2}$
$j_{aug}$	auger recombination carrier flux	$\text{m}^{-2} \text{s}^{-1}$
$j_q$	flux for species $q$	$\text{m}^{-2} \text{s}^{-1}$
$j_{rad}$	radiative recombination carrier flux	$\text{m}^{-2} \text{s}^{-1}$
$j_{rec}$	Total recombination carrier flux	$\text{m}^{-2} \text{s}^{-1}$
$j_s^{\text{IV}}$	surface recombination flux at IV	$\text{m}^{-2} \text{s}^{-1}$
$j_s^{\text{V}}$	surface recombination flux at V	$\text{m}^{-2} \text{s}^{-1}$
$j_s^{\text{VIII}}$	surface recombination flux at VIII	$\text{m}^{-2} \text{s}^{-1}$
$j_s^{\text{IX}}$	surface recombination flux at IX	$\text{m}^{-2} \text{s}^{-1}$
$j_{srh}$	SRH recombination carrier flux	$\text{m}^{-2} \text{s}^{-1}$
$k$	wave number	$\text{m}^{-1}$
$k_0$	wave number in air	$\text{m}^{-1}$
$k_{en}$	organic layer recombination reduction factor	
$l$	layer thickness	$\text{m}$
$m^*$	effective mass	$\text{kg}$
$n$	refractive index	

$N_a$	ionized acceptor impurity concentration	$\text{m}^{-3}$
$N_c$	conduction band density of state	$\text{m}^{-3}$
$N_d$	ionized donor impurity concentration	$\text{m}^{-3}$
$N_v$	valence band density of state	$\text{m}^{-3}$
$P$	exciton dissociation probability in the charge transfer state	
$p$	device power density	$\text{W m}^{-2}$
$\Pi$	jump in carrier concentration	
$p_{in}$	normalized one sun power density	$\text{W m}^{-2}$
$Q$	time averaged energy dissipation rate	$\text{J m}^{-3} \text{s}^{-1}$
$R$	net recombination rate in a layer	$\text{m}^{-3} \text{s}^{-1}$
$r$	complex Fresnel reflection coefficient	
$R_{aug}$	auger recombination rate	$\text{m}^{-3} \text{s}^{-1}$
$R_{Lan}$	Langavin recombination rate	$\text{m}^{-3} \text{s}^{-1}$
$R_{rad}$	radiative recombination rate	$\text{m}^{-3} \text{s}^{-1}$
$R_{srh}$	Shockley-Read-Hall recombination rate	$\text{m}^{-3} \text{s}^{-1}$
$S_j$	source term for charge carrier transport	$\text{m}^{-3} \text{s}^{-1}$
$S_\psi$	source term for electrical potential	$\text{m}^{-2}$
$T$	temperature	K
$t$	complex Fresnel transmission coefficient	
$V_a$	applied voltage	V
$V_b$	built-in voltage	V

$v_e$  effective surface recombination velocity between P and E  $\text{m}^4 \text{s}^{-1}$

$v_h$  effective surface recombination velocity between H and P  $\text{m}^4 \text{s}^{-1}$

$W$  work function eV

## Constants

$a_1$  constant in the field effect function

$a_2$  constant in the field effect function

$a_3$  constant in the field effect function

$\beta$  constant in the field effect function

$c$  light speed in vacuum  $\text{m s}^{-1}$

$e$  elementary charge C

$\epsilon_0$  permittivity in free space  $\text{F m}^{-1}$

$h$  Planck's constant  $\text{J s}$

i imaginary unit

$k_B$  Boltzmann constant  $\text{m}^2 \text{kg s}^{-2} \text{K}^{-1}$

$m_0$  electron rest mass kg

## Greek Symbols

$\alpha$  absorbing coefficient  $\text{m}^{-1}$

$\chi_e$  electron affinity eV

$\chi_h$  ionization potential eV

$\varepsilon$  material permittivity  $\text{F m}^{-1}$

$\Gamma$  interconnecting layer field effect function

$\kappa$	extinction coefficient	
$\lambda$	wavelength of light in air	$\text{m}^{-1}$
$\lambda_l$	absorbing range lower bound	$\text{m}^{-1}$
$\lambda_u$	absorbing range upper bound	$\text{m}^{-1}$
$\mu$	carrier mobility	$\text{m}^2 \text{V}^{-1} \text{s}^{-1}$
$R_a$	effective spectrally responsive albedo	
$\tau$	Shockley-Read-Hall recombination carrier lifetime	s
$\tau^{\text{ICL}}$	Trap-assisted recombination coefficient in interconnecting layer	s

### Roman Numerals

I	interface between air and G
II	interface between G and F
III	interface between F and top cell H
IV	interface between top cell H and P
IX	interface between bottom cell P and E
V	interface between top cell P and E
VI	interface between top cell E and interconnecting layer
VII	interface between interconnecting layer and bottom cell H
VIII	interface between bottom cell H and P
X	interface between bottom cell E and C
XI	interface between C and B
XII	interface between B and air

**Superscripts**

B	back contact
C	capping layer
E	electron-transporting layer
F	front contact
G	glass
H	hole-transporting layer
ICL	interconnecting layer
O	organic layer
P	perovskite layer

**Subscripts**

+	property below interface
-	property above interface
<i>b</i>	bottom cell
<i>e</i>	electron
<i>h</i>	hole
<i>t</i>	top cell

# List of publications

- **Paper 1.** X. Zhao, H. Q. Tan, E. Birgersson, H. Xue, “Elucidating the underlying physics in a two-terminal all-perovskite tandem solar cell: A guideline towards 30% power conversion efficiency”. *Solar Energy*, **231**, pp. 716–731 (2022).
- **Paper 2.** X. Zhao, H. Q. Tan, E. Birgersson, W. Chen, Y. Hou, H. Xue, “Modeling and sensitivity analysis of a two-terminal perovskite on organic tandem solar cell”. *Cell Reports Physical Science*, **3.9**, p. 101038 (2022).
- **Paper 3.** X. Zhao, H. Q. Tan, E. Birgersson, H. Xue, “A mixed-integer optimization for bifacial two-terminal perovskite-on-perovskite tandem solar cells”. *Solar Energy*, **262**, p. 111905 (2023).
- **Paper 4.** X. Zhao, H. Q. Tan, E. Birgersson, H. Xue, “Coupled optical-artificial neural network model for p-i-n planar perovskite solar cells—towards a digital twins application”. *Manuscript in Preparation*.



# Chapter 1

## Introduction

In this chapter, we provide an overview of single-junction perovskite solar cells and perovskite-based thin-film two-terminal (2T) tandem solar cells. We introduce perovskite materials, advancements in perovskite solar cells, and perovskite-based tandem solar cells, including those operating under bifacial conditions. We then summarize the scope of this thesis, which seeks to establish comprehensive design guidelines for high-performance 2T perovskite-based tandem devices.

### 1.1 Background

Efficient energy harvesting is increasingly critical in addressing the global energy challenge. Renewable energy sources, which have a minimal impact on greenhouse gas emissions and global warming, have garnered significant attention in research [1]. Solar power, in particular, stands out due to its cost-effectiveness and minimal greenhouse gas emissions.

Various photovoltaic devices have been developed to harness solar energy, including mono/poly crystalline and amorphous silicon solar cells, III-V or gallium arsenide (GaAs) solar cells, dye-sensitized solar cells, organic solar cells, and perovskite solar cells. Combining these cell types into tandem configurations has emerged as a promising approach to achieving higher power conversion efficiency (PCE). Monolithic tandem configurations, in particular, broaden the light spectrum absorption and improved the

open-circuit voltage, leading to improved overall performance.

Perovskite materials, with tunable band gaps, are commonly utilized in tandem applications. To further enhance the development of perovskite-based thin-film solar cells, there are critical areas for improvement, including PCE, device stability, and the feasibility of large-scale production. Two potential pathways for enhancing PCE involve perovskite-based tandem solar cells and devices operating under bifacial conditions. This thesis focuses on mathematically modeling perovskite-based thin-film solar cells, with the goal of capturing their fundamental physics and providing comprehensive guidelines to achieve higher PCE.

## 1.2 Perovskite solar cells

### 1.2.1 The perovskite material

Perovskite-structured compounds are frequently employed as absorbers in photovoltaics. Perovskite typically exhibits an ABX<sub>3</sub> crystal structure [2, 3, 4], as depicted in Figure 1.1. In this structure, A represents a large cation, such as Cs<sup>+</sup>, Rb<sup>+</sup>, methylammonium (MA<sup>+</sup>), or formamidinium (FA<sup>+</sup>). Cation B is typically Pb<sup>2+</sup>, but other cations, like Sn<sup>2+</sup>, can be used to create lead-free perovskites. X is commonly a halogen anion, such as I<sup>-</sup> or Br<sup>-</sup>. Well-known perovskite materials have chemical compositions like methylammonium lead iodide (MAPbI<sub>3</sub>) and formamidinium lead iodide (FAPbI<sub>3</sub>). Perovskite can also possess a mixed and more complex composition, as observed in Cs<sub>0.2</sub>FA<sub>0.8</sub>PbI<sub>1.8</sub>Br<sub>1.2</sub> [5]. This characteristic allows perovskite to have a tunable band gap [6], making it an excellent light absorber across the entire visible solar emission spectrum.

Perovskite materials typically showcase high optical absorption coefficients [3, 7, 8], low exciton binding energy [9, 10], excellent carrier mobility, and substantial diffusion lengths [7, 11]. These exceptional optical and charge carrier transport characteristics position perovskite as a promising material for high-efficiency solar cells.

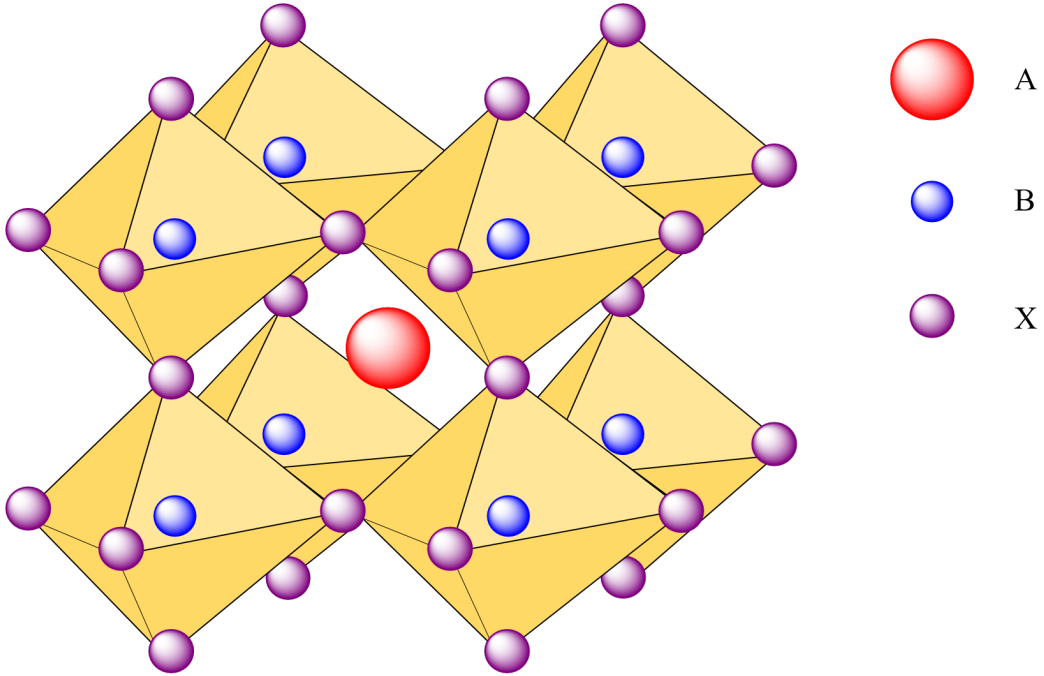


Figure 1.1:  $ABX_3$  crystal structure for perovskite material where  $A$  and  $B$  are cations, and  $X$  is an anion.

### 1.2.2 Development

Among common solar cells, single-junction perovskite solar cells have seen a substantial increase in their PCE in recent years, reaching 26.0% in 2023 [12]. Figure 1.2 illustrates the PCE improvements in perovskite solar cells, as well as in silicon heterojunction solar cells, organic solar cells, and copper indium gallium selenide (CiGS) solar cells. Perovskite solar cells have achieved a remarkable 10% increase in PCE over the past decade, surpassing CiGS solar cells. Notably, perovskite solar cells continue to exhibit a consistently upward trend in performance, whereas the PCE improvements for other technologies like Si heterojunction, CiGS, and organic solar cells have remained relatively stagnant over the years. These factors position perovskite solar cells as promising candidates to reach a 30% PCE in the future.

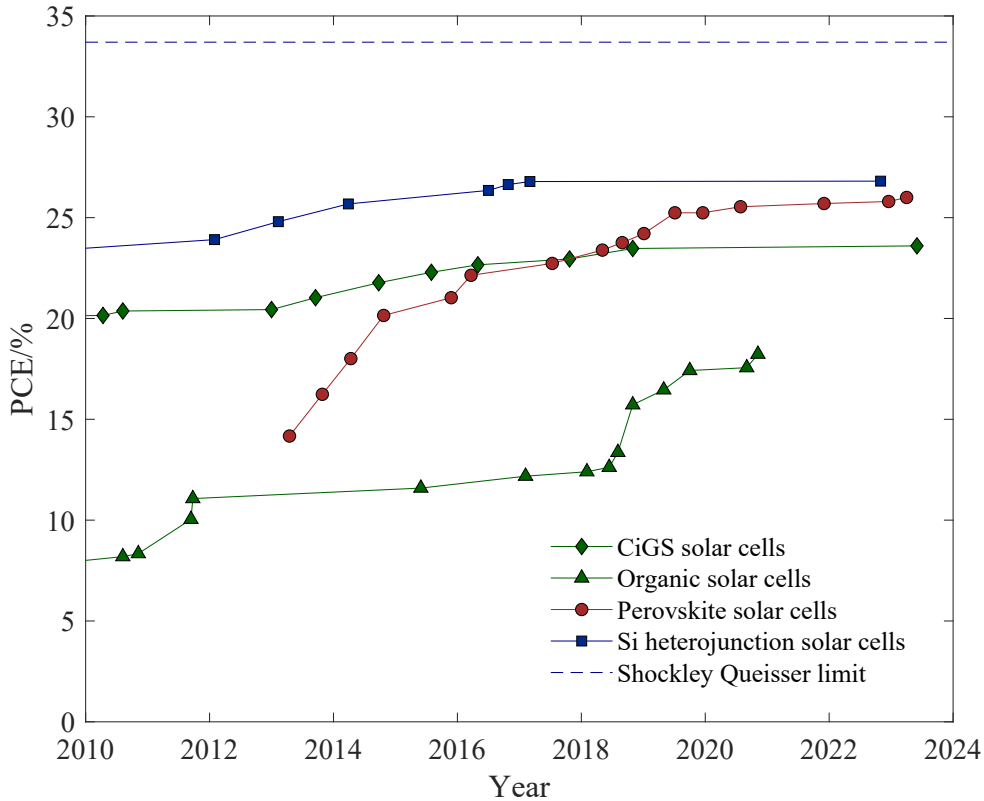


Figure 1.2: PCE developments for four types of single-junction solar cells from year 2010 to 2023 [12], with the Shockley-Queisser limit indicated [13].

The design of perovskite solar cells has progressed from a nanodot/mesoporous configuration to a planar p-i-n heterojunction structure [2]. Current perovskite solar cells fall into two main categories: n-i-p or p-i-n structures, depending on layer arrangements, and can have different types of perovskite layers, either mesoscopic or planar [4, 14]. These devices convert solar energy into electricity through a sequence of photoexcitation, charge separation, transportation, and recombination. Modeling perovskite solar cells can help us better understand these optoelectronic behaviors [15, 16, 17].

Multiple cell architectures have been investigated to enhance light absorption and minimize surface recombination. Various deposition and fabrication techniques have been explored to optimize charge carrier transport in perovskite solar cells and boost their PCE. Despite these efforts, the current PCE still falls short of the Shockley-Queisser (SQ) limit [13]. In this regard, a novel method to further enhance the PCE—tandem application—will be discussed later.

### 1.2.3 Working principle

A typical planar perovskite solar cell comprises five essential layers: the perovskite active layer, hole- and electron-transport layers, and front- and back-contact layers. When a photon with sufficient energy surpasses the perovskite's band gap, it excites electrons from the valence band to the conduction band, creating electron-hole pairs. To facilitate the separation of these pairs and transport holes and electrons to their respective contacts, a hole-transporting layer with a higher valence band energy level (after aligning the Fermi level) and an electron-transporting layer with a lower conduction band energy level are employed. By connecting the solar cell to a battery to complete the circuit, light energy is converted into electricity, which can then be stored.

To establish an effective optical architecture and ensure seamless charge carrier transport in the device, it is crucial to carefully select materials for the various layers, ensuring proper alignment of band energy levels. Commonly used materials for the hole-transporting layer include spiro – OMeTAD [18, 19, 20], PEDOT : PSS [21], NiO<sub>x</sub> [22], PTAA [18], and many more. For the electron-transporting layer, materials like SnO<sub>2</sub> [23], PCBM [24], and C60 [25] are frequently employed. Transparent oxides are generally chosen for the front-contact layer, while metals are typically used for the back-contact layer. Ideally, these electrodes should facilitate Ohmic contacts and maintain precise energy level alignments.

## 1.3 Tandem solar cells

A tandem solar cell consists of a minimum of two distinct subcells that can be electrically connected in series or mechanically stacked. For effective light spectrum capture, these subcells must be arranged in descending order of band gap, starting from the side facing the incoming light source. Perovskite materials, with their adjustable band gap [6], are commonly used as the high band gap subcell, playing a pivotal role in tandem solar cells.

Tandem solar cells are generally categorized as either four-terminal (4T) or 2T tandem cells. Taking perovskite-on-perovskite tandem solar cells as an example, in 4T

tandems, two separate perovskite solar cells are fabricated, and they are electrically isolated. In contrast, 2T tandems consist of two perovskite subcells connected in series with an interconnecting layer between them. Figure 1.3(a) and (b) illustrate the typical device structures for 4T and 2T tandem solar cells, along with their incoming and transmitted spectra. Compared to 4T devices, 2T tandem cells experience fewer optical losses due to a reduced number of layers, making them a more accessible and cost-effective option to manufacture.

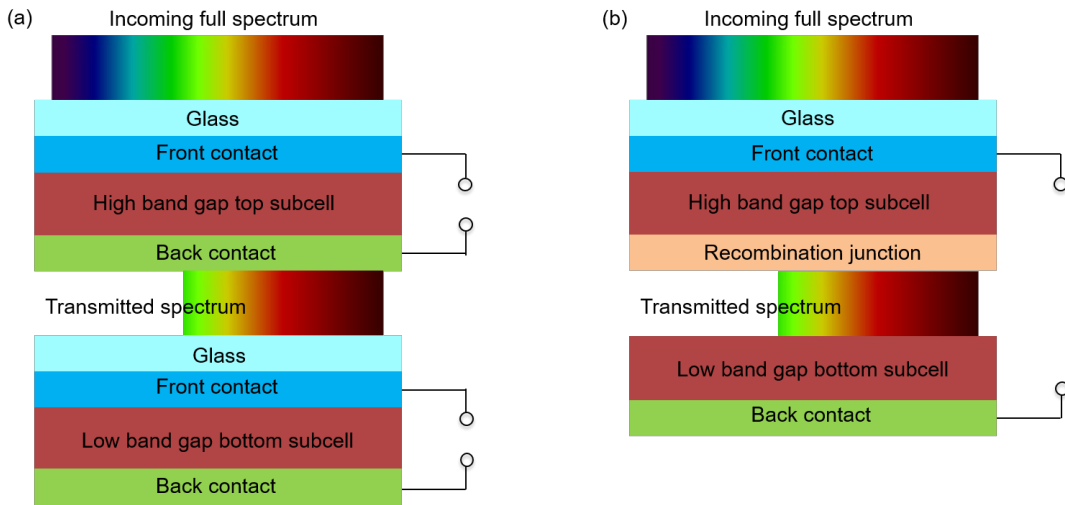


Figure 1.3: General device structures with the incoming and transmitted light spectrum for (a) a 4T tandem solar cell and (b) a 2T tandem solar cell.

A crucial aspect of 2T tandem solar cells is the interconnecting layer, which serves as a conduit for transmitting charge carriers between the subcells. This layer must enable an adequate flow of charge carriers; otherwise, it can limit the current generated by the device since the subcells are electrically connected in series. To understand and model the behavior of this layer, various approaches are employed, including charge-carrier tunneling and charge-carrier recombination. Both methods assess the net current flow achievable when the subcells are interconnected. Common materials used for the interconnecting layer include thin-film transparent oxides and metals with a thickness of less than 20 nm [26, 27].

2T perovskite-based thin-film tandem solar cells have gained significant attention as cost-effective photovoltaic devices, thanks to recent advancements in PCEs [28]. These tandem cells come in various configurations, including perovskite-on-silicon, perovskite-

on-perovskite, perovskite-on-copper indium gallium selenide, and perovskite-on-organic tandem solar cells, achieving record PCEs of 33.7% [12], 28.0% [29], 24.2% [30], and 24.0% [31], respectively. This thesis primarily focuses on modeling thin-film devices, specifically perovskite-on-perovskite and perovskite-on-organic tandem solar cells.

### 1.3.1 2T perovskite-on-perovskite tandem solar cells

A perovskite-on-perovskite tandem solar cell is a type of multi-junction tandem solar cell based on perovskite materials. It employs cost-effective perovskite materials as the light absorbers in both subcells, with the top cell being semi-transparent and having a high band gap, while the bottom cell features a low band gap. Ensuring current matching, where the photogenerated current densities from the top and bottom subcells are equal, is crucial for efficient 2T tandem solar cells since the subcells are electrically connected in series. As a result, band gap engineering and optical design for 2T perovskite-on-perovskite tandem solar cells are essential to avoid significant losses caused by current mismatch.

2T perovskite-on-perovskite tandem solar cells have shown rapid development in recent years, achieving a certified PCE of 24.2% for a 1 cm<sup>2</sup> small area cell in 2019 [32]. Lin et al. then employed a low band gap, lead-reduced, Pb/Sn alloyed metal halide perovskite as the bottom cell absorber, with the oxidation of SnO<sub>2</sub> suppressed, resulting in a higher PCE of 24.5% [5]. With these state-of-the-art devices, 2T perovskite-on-perovskite tandem solar cells have made significant progress, reaching a PCE of 28.0% in 2023 [29], surpassing the 26.0% PCE record for single-junction perovskite solar cells. Nevertheless, while the PCE of 2T perovskite-on-perovskite tandem solar cells has exceeded that of single-junction perovskite solar cells, it still lags behind the 42% theoretical limit for a 2T tandem solar cell [33] and the SQ limit. Consequently, there is room for further PCE improvement, and exploring the intrinsic properties of tandem devices through modeling is essential to pave the way for highly efficient, cost-effective perovskite-on-perovskite tandem solar cells.

### 1.3.2 2T perovskite-on-organic tandem solar cells

The 2T perovskite-on-organic tandem solar cell is another promising thin-film tandem device. In recent years, its PCE has risen from 18% to 24% [27, 31, 34, 35, 36, 37, 38, 39]. While it currently lags behind 2T perovskite-on-perovskite tandem solar cells in terms of PCE, it remains a promising option due to several advantages, including broad band-gap tunability [40, 41] and fewer challenges in solution processing [37]. Additionally, its flexibility opens up opportunities for various flexible tandem solar cell applications.

## 1.4 Existing models for thin-film tandem solar cells

### 1.4.1 2T perovskite-on-perovskite tandem solar cell models

To understand the underlying physics, several optoelectronic models have been used to analyze 2T perovskite-on-perovskite tandem solar cells. In a study by Singh and Gagliardi, a drift-diffusion analysis delved into the influence of recombination, layer thicknesses, carrier mobility, and work function on the PCE of these tandem cells [42]. Their findings emphasize the potential for up to a 4% PCE increase through work function adjustments. Subsequently, Singh *et al.* proposed a model for lead-free perovskite-on-perovskite tandem solar cells, identifying the optimal electron-transporting layer material, as well as the optimized work functions and absorber layer thicknesses [43]. However, their models do not incorporate the recombination junction, a crucial element of 2T tandem devices, and they employ filtered spectra as the light sources for the bottom cells, resulting in incomplete coupling of the optical systems between the top and bottom cells.

Soldnera *et al.* employ an analytical model that combines the general transfer matrix method with a p-i-n semiconductor equivalent-circuit model [44]. They propose that factors such as photocurrent, surface recombination, carrier diffusion length, built-in voltage, and series resistance play a crucial role in enhancing the PCE of a 2T perovskite-on-perovskite tandem solar cell. While their analytical model demands fewer computational resources in comparison to numerical models, it lacks experimental validation and does

not account for all the various recombination mechanisms both within the device and at the recombination junction.

Hossain *et al.* present a model for a 2T perovskite-on-perovskite tandem solar cell, utilizing a three-dimensional finite-difference time domain simulation for optics and a finite element method for carrier drift-diffusion. Their work demonstrates how optimizing the optical system within the cell, in conjunction with enhancing charge carrier transport, can push the PCE closer to its theoretical limit. However, their computational-heavy three-dimensional numerical approach does not account for the glass layer, which reduces optical losses through reflection. Additionally, in their model, the recombination junction is simplified as a combination of a hole-transporting layer and an electron-transporting layer, so the impact of a recombination junction composed of an interconnecting layer on the performance of a 2T perovskite-on-perovskite tandem solar cell is not explicitly explored.

In summary, while existing studies have offered valuable insights into modeling this type of tandem solar cell, they fall short in addressing crucial aspects of the cell. Specifically, on the optical side, they do not account for either the glass layer or the light interference effects between the top and bottom cells. On the electronic side, the recombination junction is either neglected or oversimplified. As a result, there remains a need for a more comprehensive 2T perovskite-on-perovskite tandem solar cell model.

#### **1.4.2 2T perovskite-on-organic tandem solar cell models**

There is a limited number of models for 2T perovskite-on-organic tandem solar cells. Xie *et al.* and Chen *et al.* have employed semi-empirical models to predict optimal band-gaps, short-circuit current densities, and practical PCE limits, providing guidelines for current matching [34, 35, 36]. Wang *et al.* utilized a modified diode model to investigate the electrical system of these tandem cells and explore the influence of various hole-transporting materials on charge carrier extraction [38]. Nonetheless, none of these current models can comprehensively address the coupled optics and charge carrier transport in the entire tandem solar cell.

## 1.5 Solar cells under bifacial operation

Bifacial operation is one way to further improve the performance of tandem solar cells by absorbing both front and rear incident light, thereby increasing short-circuit current densities. When designing 2T bifacial tandem solar cells, an essential parameter to consider is the spectral albedo, which represents the ratio between the power of back-incident light and that of front-incident light. With the inclusion of back-incident light, it becomes crucial to prioritize light management and optimize the optical architecture to achieve current matching. This means that, under different operating albedos, tandem devices should be designed with varying band gaps to minimize optical losses.

Researchers have primarily focused on optimizing bifacial 2T perovskite-on-perovskite tandem devices through band gap engineering. For instance, M. Soldera *et al.* [44] identified an optimal short-circuit current density of approximately  $185 \text{ A/m}^2$  for ideal monofacial 2T perovskite-on-perovskite tandem solar cells, assuming no parasitic absorption in transparent contact layers. They explored various transparent oxides for the conductive layer, as well as different materials like  $\text{NiO}_x$ , PEDOT:PSS,  $\text{SnO}_2$ , and PCBM for the hole- and electron-transporting layers, keeping the perovskite materials constant. Additionally, Chantana *et al.* [45] optimized the band gaps of the subcells in ideal 2T tandem solar cells under bifacial operation using the SQ limit, revealing a trade-off between the optimal band gaps of the two subcells, both converging to approximately 1.5 eV under high albedo values. MT. Hörantner and HJ. Snaith [46] enhanced 2T tandem solar cell performance by improving current matching across various solar spectra. Currently, there is no comprehensive study that simultaneously considers material choice, layer thickness, and spectral albedos for the optimal design of a 2T perovskite-on-perovskite tandem solar cell, which will be discussed further in Chapter 8.

## 1.6 Scope and objectives of the thesis

The main goals of this thesis are to advance the field of perovskite-based thin-film solar cells by developing robust mathematical models. These models will serve as valuable tools for understanding the key principles that govern their operation, optimizing device performance, and providing guidance for future design improvements.

Chapter 2 focuses on the mathematical aspects of optics, starting with an exploration of light as the energy source for solar cells and progressing into electronics. The chapter includes detailed derivations to explain how to calculate the optical electric field in multilayer thin films, and how to determine parameters like reflectance, transmittance, and absorptance for photovoltaic applications. The objective of this chapter is to establish a comprehensive mathematical framework for optics that can be applied to various solar cell configurations, including planar perovskite solar cells, as well as monofacial and bifacial 2T perovskite-on-organic and perovskite-on-perovskite tandem solar cells.

Chapter 3 delves into the electronic aspects of the model. It discusses the generation of electron-hole pairs upon photoexcitation, with their generation rate calculated using the optics model from Chapter 2. The electronic model is built upon the band energy levels of the front- and back-contact layers, hole- and electron-transporting layers, and the perovskite layer, incorporating the drift-diffusion model. The combination of Chapters 2 and 3 results in a comprehensive optoelectronic model suitable for planar perovskite solar cells, and it can be readily extended to monofacial and bifacial 2T perovskite-on-perovskite and perovskite-on-organic tandem solar cells.

Chapter 4 offers insights into various numerical techniques, including vectorized matrix operations for computing the optical electric field in Matlab, the finite element method in Comsol for solving equations related to the optical electric field, electrical potential, and charge-carrier drift and diffusion. Additionally, it covers Monte Carlo simulation and sensitivity analysis.

Chapter 5 introduces artificial neural networks designed for p-i-n structured single-junction perovskite solar cells. We employ data from the optoelectronic model in Chapters 2 and 3 to train, validate, and test the neural networks. We optimize the hyperpa-

rameters using Bayesian optimization and assess the network's performance based on mean square error. The primary purpose of these neural networks is to offer a faster and computationally less intensive alternative to the full electronic model. The goal is to streamline device characterization, establish digital twins that bridge simulation and experiment, and provide recommendations for parameter tuning in the future.

Chapter 6 introduces an optoelectronic model tailored for 2T perovskite-on-perovskite tandem solar cells. This model accounts for coherent and incoherent light propagation, optical interference effects, charge carrier conservation (encompassing various recombination mechanisms), and trap-assisted recombination flux at the recombination junction. Following model calibration and validation, we propose strategies for enhancing the efficiency of tandem devices and delve into the underlying physics, including light interference effects and charge carrier transport at the interconnecting layer. This model offers versatility and can be adapted and calibrated for various 2T perovskite-on-perovskite tandem solar cells, offering valuable insights for device development.

Chapter 7 is dedicated to adapting the earlier 2T perovskite-on-perovskite tandem solar cell model for 2T perovskite-on-organic tandem solar cells. This effort places a significant focus on the material resistivity of the interconnecting layer, losses within both the top perovskite subcell and the bottom organic subcell, and strategies for optimizing PCE. The primary objective is to provide comprehensive guidelines for enhancing the performance of 2T perovskite-on-organic tandem solar cells, and gain a deeper understanding of the interconnecting layer's role and propose how to best optimize it in this specific device.

Chapter 8 introduces a mixed-integer optimization approach for optimizing the optics of 2T perovskite-on-perovskite tandem solar cells. Our goal is to identify the most suitable material combinations, layer thicknesses, and optimal short-circuit current densities for both monofacial and bifacial 2T perovskite-on-perovskite tandem solar cells. This mixed-integer method takes into account frequently used materials and aims to tackle the challenges associated with achieving current matching in bifacial tandem devices during the design and fabrication process.

Finally, in Chapters 9 and 10, we discuss potential improvements for the aforementioned works, focusing on making the models more efficient, generalized, and extendable to cover various device architectures.



# Chapter 2

## Optics

Electromagnetism or optics plays a significant role in the field of photovoltaic system. In a solar cell, the active layer converts light energy into electricity by exciting electrons from the valence band to the conduction band through photon absorption. This chapter focuses on applying optics to thin-film solar cells to facilitate the modeling and simulation of photogenerated current density. We begin by introducing the principles of electromagnetism, including Maxwell's equations and the general solutions derived from Helmholtz equation, and how to apply these concepts to thin-film solar cells. Additionally, we address the correction for incoherence due to the thick glass layer. The optical principles discussed in this chapter are validated through numerical solutions, forming a crucial component of the mathematical formulations used for perovskite-based single-junction and tandem solar cells in Chapters 5 to 8.

## 2.1 Electromagnetism

The Maxwell's equations in the time domain are

$$\nabla \times E(x,t) + \frac{\partial B(x,t)}{\partial t} = 0, \quad (2.1)$$

$$\nabla \times H(x,t) - \frac{\partial D(x,t)}{\partial t} = J(x,t), \quad (2.2)$$

$$\nabla \cdot D(x,t) = \rho, \quad (2.3)$$

$$\nabla \cdot B(x,t) = 0, \quad (2.4)$$

with the constitutive relations

$$D(x,t) = \epsilon E(x,t), \quad (2.5)$$

$$B(x,t) = \mu H(x,t), \quad (2.6)$$

for linear isotropic materials where there are no polarization and magnetization densities in the medium. Here,  $E$  is the electric field,  $x$  is the position vector,  $B$  is the magnetic induction,  $H$  is the magnetic field,  $D$  is the electric displacement,  $J$  is the current density,  $\rho$  is the total electric charge density,  $\epsilon$  is the permittivity, and  $\mu$  is the permeability.

The above Maxwell's equations can be transformed into the frequency domain and simplified into the following Helmholtz equations, which describe the behavior of uniform monochromatic light—specifically, transverse electric-magnetic (TEM) sinusoidal plane waves propagating in the  $x$ - direction, where the electric field components are in the  $z$ - direction, and the magnetic field components are in the  $y$ - direction (see Figure 2.1):

$$\frac{d^2 E_z(x)}{dx^2} + k^2 E_z(x) = 0, \quad (2.7)$$

$$\frac{d^2 H_y(x)}{dx^2} + k^2 H_y(x) = 0. \quad (2.8)$$

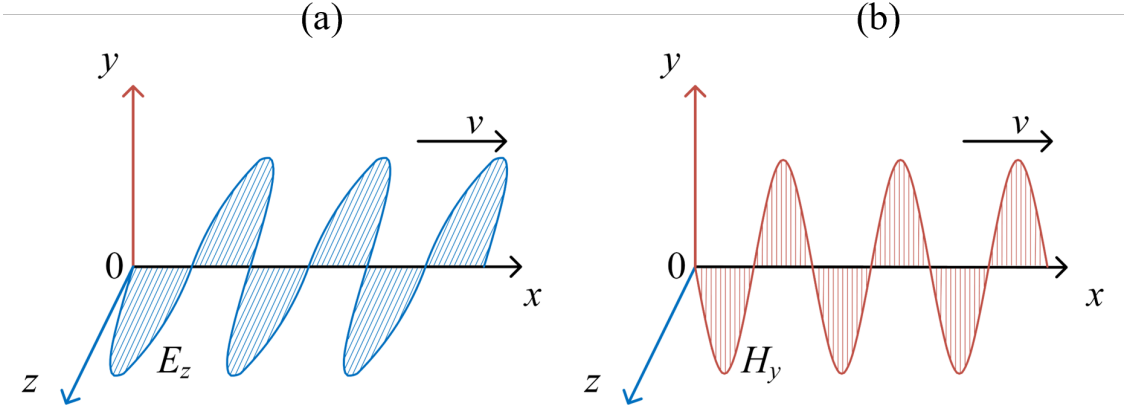


Figure 2.1: (a) Horizontally polarized ( $z$ -direction) electric field and (b) corresponding vertically polarized ( $y$ -direction) magnetic field for an electromagnetic wave (TEM mode) propagating in the  $x$ -direction with velocity  $v$ .

Here,  $E_z$  is the electric field magnitude,  $H_y$  is the magnetic field magnitude, and  $k$  is the wave number of the medium defined as

$$k = k_0(n - i\kappa), \quad (2.9)$$

$$k_0 = \frac{2\pi}{\lambda}, \quad (2.10)$$

where  $k_0$  is the wave number in air,  $n$  is the refractive index,  $\kappa$  is the extinction coefficient, and  $\lambda$  is the wavelength in air.

In addition, for isotropic dielectric materials where the relative permeability is 1,  $H_y$  is related to  $E_z$  by

$$H_y(x) = -\frac{1}{i\omega\mu_0} \frac{dE_z(x)}{dx}, \quad (2.11)$$

where  $\omega$  is the angular frequency,  $\mu_0$  is the permeability in air. We can therefore focus on the Helmholtz equation for electric field and the general solution for Eq. 2.7 is

$$E_z(x) = C_1 e^{-ikx} + C_2 e^{ikx}. \quad (2.12)$$

Here,  $C_1$  and  $C_2$  are two integration constants determined by the boundary conditions. We adopt the convention that  $C_1 e^{-ikx}$  represents a forward-propagating wave component,

while  $C_2 e^{ikx}$  represents a backward-propagating wave component. The integration constants,  $C_1$  and  $C_2$ , are consequently referred to as the reference magnitudes of forward- and backward-propagating waves, respectively. To enhance clarity in subsequent discussions, we will substitute  $C_1$  and  $C_2$  by  $A$  and  $B$ , respectively, and append numerical subscripts to indicate the layer numbers for more straightforward notations.

From the time-averaged Poynting vector, the intensity or irradiance,  $I$ , is

$$I(x) = \langle S \rangle = \frac{1}{2} \operatorname{Re} (E_z(x) H_y^*(x)). \quad (2.13)$$

More details about explanations and derivations of the above equations in electromagnetism could be found from the works of Griffiths and Inglefield [47].

Additionally, we take note that the photon energy,  $E_{ph}$ , is related to the frequency and wavelength of light as follows:

$$E_{ph} = hf = \frac{hc}{\lambda}, \quad (2.14)$$

where  $h$  is the Planck constant,  $f$  is the frequency,  $c$  is the speed of light. We know that when the photon energy is higher than the band gap,  $E_g$ , of a semiconductor material, photo-excitation takes place and the electrons move from the valence band to the conduction band; i.e:

$$\frac{hc}{\lambda} > E_g, \quad (2.15)$$

and hence

$$\lambda_u = \frac{hc}{E_g}, \quad (2.16)$$

where  $\lambda_u$  is the upper bound for the wavelength of incident light which a semiconductor material can absorb.

## 2.2 Coherent light propagation

Sunlight, originating from black-body radiation, is considered as an incoherent light source. Its coherent length varies with temperature and ranges from a minimum of 600 nm to around 10  $\mu\text{m}$  [48, 49]. In the context of photovoltaic applications, such as perovskite solar cells, the layers, excluding the substrate, typically have thicknesses ranging from tens to a few hundred nanometers, which are in general smaller than the coherent length of the light source. Consequently, we can treat these layers as thin-film layers and apply coherent light propagation, where the waves exhibit a consistent relationship with each other, resulting in well-defined wave interferences. In addition, we have assumed monochromatic plane wave on the surface of incidence (AM15G spectrum), and the coherent propagation of light refers to both temporal and spatial coherence.

The thin-film stack of the perovskite solar cell is always fabricated on a substrate, often an optical glass with a typical thickness exceeding 1 mm. This thickness significantly surpasses the coherent length of the light source, leading us to regard the light propagation in the thick glass layer as spatially incoherent. More in-depth discussions on the optical considerations related to the treatment of the glass substrate will be provided in the next section.

### 2.2.1 Absorbing boundary conditions

We consider a stack of thin-film layers that is linear, isotropic and homogeneous, bounded by air and with no surface roughnesses, we can capture the wave propagation with the Helmholtz equation:

$$\frac{d^2E_z}{dx^2} + k^2E_z = 0, \quad (2.17)$$

Typical boundary conditions for the electric field between two materials can be found by requiring continuity of the electric field and its derivative in the wave-propagation

direction across the interface; i.e.:

$$E_z|_- = E_z|_+, \quad (2.18)$$

$$\frac{dE_z}{dx}|_- = \frac{dE_z}{dx}|_+, \quad (2.19)$$

where the subscripts – and + indicate the properties just before and after the interface, respectively, with respect to the positive  $x$ -direction. Substituting the found general solution in Eq. 2.12 into Eq. 2.18 and 2.19 gives

$$E_z|_- = E_0 + E_R, x = 0; \quad (2.20)$$

$$E_z|_+ = E_T + E_{0,b}, x = l_{tf}, \quad (2.21)$$

and

$$\frac{dE_z}{dx}|_- = ik_0(-E_0 + E_R), x = 0; \quad (2.22)$$

$$\frac{dE_z}{dx}|_+ = ik_0(-E_T + E_{0,b}), x = l_{tf}; \quad (2.23)$$

where  $l_{tf}$  is the total thickness of the thin film stack. Here, we have replaced the integration constants in the general solution with  $E_0$ ,  $E_R$ ,  $E_T$ , and  $E_{0,b}$ , which can be found in Figure 2.2 to 2.4.  $E_0$ ,  $E_R$ ,  $E_T$ , and  $E_{0,b}$  are the magnitudes of the electric field that incidents on the thin-film layer from the front side, reflects from the thin-film layer from the front side, transmits through the thin-film layer to air, and incidents from the rear side. From Eq. 2.20 and 2.22,  $E_R$  can be eliminated, allowing us to write

$$\frac{dE_z}{dx} = -2ik_0E_0 + ik_0E_z, x = 0. \quad (2.24)$$

Similarly, from Eq. 2.21 and 2.23, we find a boundary condition without  $E_T$ :

$$\frac{dE_z}{dx} = 2ik_0E_{0,b} - ik_0E_z, x = l_{tf}. \quad (2.25)$$

The Helmholtz equation can be solved with the two absorbing boundary conditions in Eq. 2.24 and 2.25 numerically. The settings in Comsol are summarized in Chapter 4: Numerics.

## 2.2.2 Electric and magnetic fields in thin-film layers

In this subsection, we present a semi-analytical solution for the optical electric field. This approach offers a notable advantage over numerical solutions to the Helmholtz equation, as it minimizes computational costs and eliminates the need for a finite element solver.

### 2.2.2.1 Single thin-film layer

We start from a single thin-film layer, as illustrated in Figure 2.2, and generalize our solutions to any number of thin-film layers.

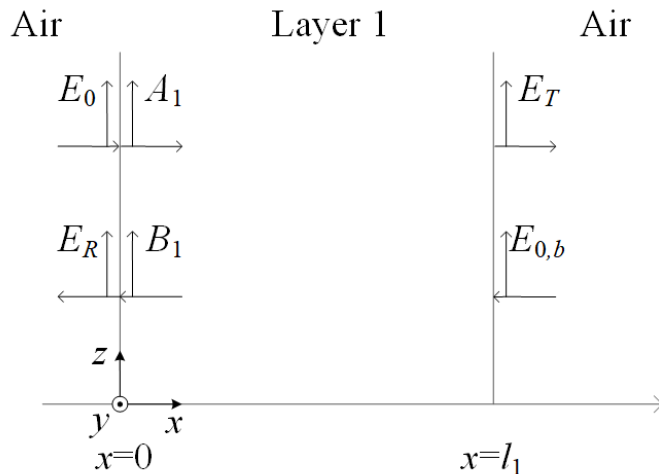


Figure 2.2: Schematic of a single thin-film layer bounded by glass, with wave propagating in the  $x$ - direction and the electric field perturbing in the  $z$ - direction.

$E_z$  can be solved with a system of equations from the boundary conditions. The electric field across the thin-film layer could be expressed as

$$E_z = \begin{cases} E_0 + E_R & x = 0 \\ A_1 e^{-ik_1 x} + B_1 e^{ik_1 x} & 0 \leq x \leq l_1 \\ E_T + E_{0,b} & x = l_1 \end{cases} \quad (2.26)$$

For isotropic dielectric materials, the relative permeability is 1, and hence the corresponding magnetic field, given by Eq. 2.11, becomes

$$H_y = \begin{cases} \frac{k_0}{\omega\mu_0}(E_0 - E_R) & x = 0 \\ \frac{k_1}{\omega\mu_0}(A_1 e^{-ik_1 x} - B_1 e^{ik_1 x}) & 0 \leq x \leq l_1 \\ \frac{k_0}{\omega\mu_0}(E_T - E_{0,b}) & x = l_1 \end{cases}. \quad (2.27)$$

From continuity of fields, we obtain the following system of equations from the two boundaries at  $x = 0$  and  $x = l_1$ :

$$E_0 + E_R = A_1 + B_1, \quad (2.28)$$

$$k_0(E_0 - E_R) = k_1(A_1 - B_1), \quad (2.29)$$

$$A_1 e^{-ik_1 l_1} + B_1 e^{ik_1 l_1} = E_T + E_{0,b}, \quad (2.30)$$

$$k_1(A_1 e^{-ik_1 l_1} - B_1 e^{ik_1 l_1}) = k_0(E_T - E_{0,b}), \quad (2.31)$$

Here,  $E_0$  and  $E_{0,b}$  are the known incident electric field magnitudes, and hence we have four equations and four unknowns:  $E_R$ ,  $A_1$ ,  $B_1$  and  $E_T$ .

Substitute  $E_R$  from Eq. 2.28 to Eq. 2.29 allows us to write

$$(k_0 + k_1)A_1 + (k_0 - k_1)B_1 = 2k_0E_0. \quad (2.32)$$

Similarly, substitute  $E_T$  from Eq. 2.30 to Eq. 2.31 gives

$$(k_0 - k_1)A_1 e^{-ik_1 l_1} + (k_0 + k_1)B_1 e^{ik_1 l_1} = 2k_0E_{0,b}. \quad (2.33)$$

The system of equations (Eq. 2.32 and 2.33) can be written in a matrix form as

$$\bar{\mathbf{A}}\bar{\mathbf{x}} = \bar{\mathbf{B}}, \quad (2.34)$$

where the matrices  $\bar{\mathbf{A}}$ ,  $\bar{\mathbf{x}}$  and  $\bar{\mathbf{B}}$  are

$$\bar{\mathbf{A}} = \begin{bmatrix} k_0 + k_1 & k_0 - k_1 \\ (k_0 - k_1) e^{-ik_1 l_1} & (k_0 + k_1) e^{ik_1 l_1} \end{bmatrix}, \quad (2.35)$$

$$\bar{\mathbf{x}} = \begin{bmatrix} A_1 \\ B_1 \end{bmatrix}, \quad (2.36)$$

$$\bar{\mathbf{B}} = \begin{bmatrix} 2k_0 E_0 \\ 2k_0 E_{0,b} \end{bmatrix}. \quad (2.37)$$

The unknowns  $A_1$  and  $B_1$  can be found by solving

$$\bar{\mathbf{x}} = \bar{\mathbf{A}} \setminus \bar{\mathbf{B}}. \quad (2.38)$$

We are then able to calculate  $E_R$  and  $E_T$  from Eq. 2.28 and 2.30.

### 2.2.2.2 Double layer thin-film stack

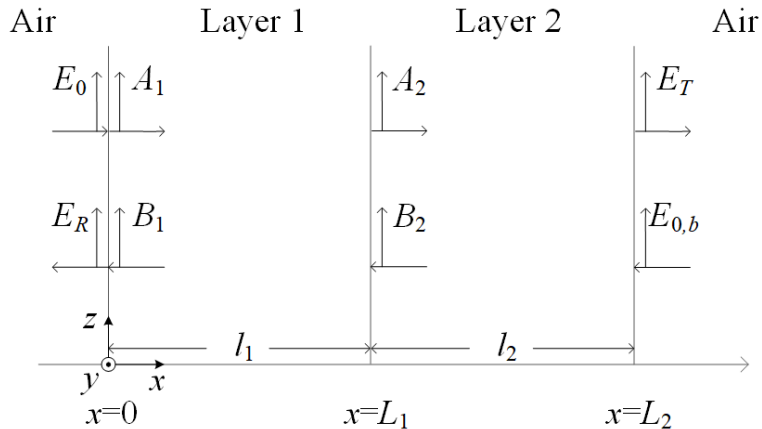


Figure 2.3: Schematic of a double layer thin-film stack bounded by air.

We now consider a stack of two thin-film layers with different optical properties bounded by air, as shown in Figure 2.3. The electric and magnetic fields across the thin-film layers

could be expressed as

$$E_z = \begin{cases} E_0 + E_R & x = 0 \\ A_1 e^{-ik_1 x} + B_1 e^{ik_1 x} & 0 \leq x \leq L_1 \\ A_2 e^{-ik_2(x-L_1)} + B_2 e^{ik_2(x-L_1)} & L_1 \leq x \leq L_2 \\ E_T + E_{0,b} & x = L_2 \end{cases}, \quad (2.39)$$

$$H_y = \begin{cases} \frac{k_0}{\omega\mu_0}(E_0 - E_R) & x = 0 \\ \frac{k_1}{\omega\mu_0}(A_1 e^{-ik_1 x} - B_1 e^{ik_1 x}) & 0 \leq x \leq L_1 \\ \frac{k_2}{\omega\mu_0}(A_2 e^{-ik_2(x-L_1)} - B_2 e^{ik_2(x-L_1)}) & L_1 \leq x \leq L_2 \\ \frac{k_0}{\omega\mu_0}(E_T - E_{0,b}) & x = L_2 \end{cases}, \quad (2.40)$$

where  $L_1 = l_1$ ,  $L_2 = l_1 + l_2$ ,  $k_1$  and  $k_2$  are the thickness and wave number of the second thin-film layer, respectively.

The system of equations becomes

$$E_0 + E_R = A_1 + B_1, \quad (2.41)$$

$$k_0(E_0 - E_R) = k_1(A_1 - B_1), \quad (2.42)$$

$$A_1 e^{-ik_1 l_1} + B_1 e^{ik_1 l_1} = A_2 + B_2, \quad (2.43)$$

$$k_1 \left( A_1 e^{-ik_1 l_1} - B_1 e^{ik_1 l_1} \right) = k_2 (A_2 - B_2), \quad (2.44)$$

$$A_2 e^{-ik_2 l_2} + B_2 e^{ik_2 l_2} = E_T + E_{0,b}, \quad (2.45)$$

$$k_2 \left( A_2 e^{-ik_2 l_2} - B_2 e^{ik_2 l_2} \right) = k_0 (E_T - E_{0,b}), \quad (2.46)$$

which can be rewritten as

$$(k_0 + k_1)A_1 + (k_0 - k_1)B_1 = 2k_0E_0, \quad (2.47)$$

$$A_1e^{-ik_1l_1} + B_1e^{ik_1l_1} - A_2 - B_2 = 0, \quad (2.48)$$

$$\frac{k_1}{k_2}A_1e^{-ik_1l_1} - \frac{k_1}{k_2}B_1e^{ik_1l_1} - A_2 + B_2 = 0, \quad (2.49)$$

$$(k_0 - k_2)A_2e^{-ik_2l_2} + (k_0 + k_2)B_2e^{ik_2l_2} = 2k_0E_{0,b}, \quad (2.50)$$

with

$$E_R = A_1 + B_1 - E_0, \quad (2.51)$$

$$E_T = A_2e^{-ik_2l_2} + B_2e^{ik_2l_2} - E_{0,b}. \quad (2.52)$$

Again, Eq. 2.47 to 2.50 can be written in a matrix form as

$$\bar{\mathbf{A}}\bar{\mathbf{x}} = \bar{\mathbf{B}}, \quad (2.53)$$

where the matrices  $\bar{\mathbf{A}}$ ,  $\bar{\mathbf{x}}$  and  $\bar{\mathbf{B}}$  are

$$\bar{\mathbf{A}} = \begin{bmatrix} k_0 + k_1 & k_0 - k_1 & 0 & 0 \\ e^{-ik_1l_1} & e^{ik_1l_1} & -1 & -1 \\ \frac{k_1}{k_2}e^{-ik_1l_1} & -\frac{k_1}{k_2}e^{ik_1l_1} & -1 & 1 \\ 0 & 0 & (k_0 - k_2)e^{-ik_2l_2} & (k_0 + k_2)e^{ik_2l_2} \end{bmatrix}, \quad (2.54)$$

$$\bar{\mathbf{x}} = \begin{bmatrix} A_1 \\ B_1 \\ A_2 \\ B_2 \end{bmatrix}, \bar{\mathbf{B}} = \begin{bmatrix} 2k_0E_0 \\ 0 \\ 0 \\ 2k_0E_{0,b} \end{bmatrix}. \quad (2.55)$$

We have obtained a  $4 \times 4$  squared matrix  $\bar{\mathbf{A}}$  with four unknowns that can be solved through matrix operation.

### 2.2.2.3 Thin-film stack with $N$ layers

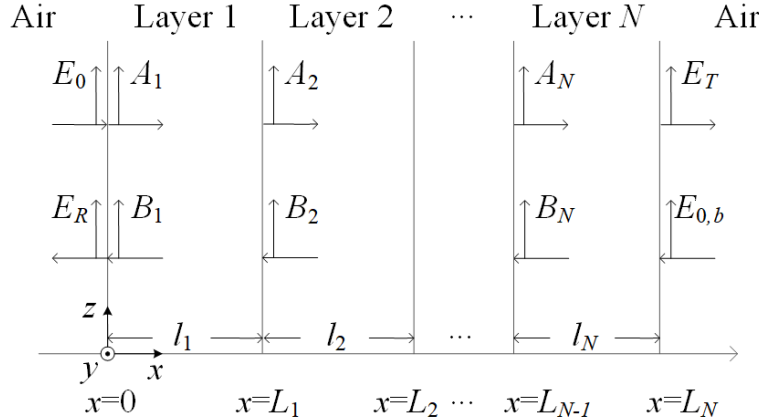


Figure 2.4: Schematic of a  $N$  layer thin-film stack bounded by air.

Next, we look at a thin-film stack with  $N$  layers shown in Figure 2.4. The electric and magnetic fields are

$$E_z = \begin{cases} E_0 + E_R & x = L_0 \\ A_n e^{-ik_n(x-L_{n-1})} + B_n e^{ik_n(x-L_{n-1})} & L_{n-1} \leq x \leq L_n, 1 \leq n \leq N, \\ E_T + E_{0,b} & x = L_N \end{cases} \quad (2.56)$$

$$H_y = \begin{cases} \frac{k_0}{\omega\mu_0}(E_0 - E_R) & x = L_0 \\ \frac{k_n}{\omega\mu_0}(A_n e^{-ik_n(x-L_{n-1})} - B_n e^{ik_n(x-L_{n-1})}) & L_{n-1} \leq x \leq L_n, 1 \leq n \leq N, \\ \frac{k_0}{\omega\mu_0}(E_T - E_{0,b}) & x = L_N \end{cases} \quad (2.57)$$

where

$$L_0 = 0, \quad (2.58)$$

$$L_n = \sum_1^n l_i, \quad (2.59)$$

and  $n$  is an integer. The system of equations are

$$(k_0 + k_1)A_1 + (k_0 - k_1)B_1 = 2k_0E_0, \quad (2.60)$$

$$A_n e^{-ik_nl_n} + B_n e^{ik_nl_n} - A_{n+1} - B_{n+1} = 0, 1 \leq n \leq N-1 \quad (2.61)$$

$$\frac{k_n}{k_{n+1}} A_n e^{-ik_nl_n} - \frac{k_n}{k_{n+1}} B_n e^{ik_nl_n} - A_{n+1} + B_{n+1} = 0, 1 \leq n \leq N-1 \quad (2.62)$$

$$(k_0 - k_N)A_N e^{-ik_Nl_N} + (k_0 + k_N)B_N e^{ik_Nl_N} = 2k_0E_{0,b}, \quad (2.63)$$

which allows us to write out the  $2N \times 2N$  square matrix  $\bar{\mathbf{A}}$ ,  $2N \times 1$  matrix  $\bar{\mathbf{x}}$  and  $2N \times 1$  matrix  $\bar{\mathbf{B}}$  as

$$\bar{\mathbf{A}} = \begin{bmatrix} k_0 + k_1 & k_0 - k_1 & 0 & 0 & \cdots & \cdots & 0 & 0 \\ \bar{\mathbf{S}}_1 & \bar{\mathbf{S}} & 0 & 0 & \cdots & & 0 & 0 \\ & & 0 & 0 & \cdots & & 0 & 0 \\ 0 & 0 & \bar{\mathbf{S}}_2 & \bar{\mathbf{S}} & \ddots & & \vdots & \vdots \\ 0 & 0 & \ddots & \ddots & \ddots & & 0 & 0 \\ \vdots & \vdots & & & & & 0 & 0 \\ 0 & 0 & \cdots & 0 & 0 & \bar{\mathbf{S}}_{N-1} & \bar{\mathbf{S}} \\ 0 & 0 & \cdots & 0 & 0 & & \\ 0 & 0 & \cdots & 0 & 0 & (k_0 - k_N)e^{-ik_Nl_N} & (k_0 + k_N)e^{ik_Nl_N} \end{bmatrix}, \quad (2.64)$$

$$\bar{\mathbf{x}} = \begin{bmatrix} A_1 \\ B_1 \\ \vdots \\ A_N \\ B_N \end{bmatrix}, \bar{\mathbf{B}} = \begin{bmatrix} 2k_0E_0 \\ 0 \\ \vdots \\ 0 \\ 2k_0E_{0,b} \end{bmatrix}, \quad (2.65)$$

$$\bar{\mathbf{S}}_n = \begin{bmatrix} e^{-ik_nl_n} & e^{ik_nl_n} \\ \frac{k_n}{k_{n+1}} e^{-ik_nl_n} & -\frac{k_n}{k_{n+1}} e^{ik_nl_n} \end{bmatrix}, \bar{\mathbf{S}} = \begin{bmatrix} -1 & -1 \\ -1 & 1 \end{bmatrix}. \quad (2.66)$$

We are able to find the  $2N + 2$  unknowns by solving

$$\bar{\mathbf{x}} = \bar{\mathbf{A}} \setminus \bar{\mathbf{B}}, \quad (2.67)$$

together with

$$E_R = A_1 + B_1 - E_0, \quad (2.68)$$

$$E_T = A_N e^{-ik_N l_N} + B_N e^{ik_N l_N} - E_{0,b}. \quad (2.69)$$

A general solution has been found, which could be applied to a thin-film stack with any number of layers.

### 2.2.3 Absorptance, reflectance and transmittance

In the context of solar cells, we are interested in the following quantities from optics: the power absorbed, as well as the power loss due to reflection and transmission.

Once the electric field magnitude are known in a thin-film layer, the magnetic field magnitude can be calculated through Eq. 2.11 as

$$H_y = -\frac{1}{i\omega\mu_0}(-ikAe^{-ikx} + ikBe^{ikx}), \quad (2.70)$$

$$= c\epsilon_0(n - i\kappa)(Ae^{-ikx} - Be^{ikx}), \quad (2.71)$$

where the following relations have been used during simplifications:

$$\omega = \frac{2\pi c}{\lambda}, \quad (2.72)$$

$$c = \frac{1}{\sqrt{\epsilon_0\mu_0}}, \quad (2.73)$$

$$k = \frac{2\pi}{\lambda}\tilde{n}, \quad (2.74)$$

$$\tilde{n} = n - i\kappa = \sqrt{\frac{\epsilon\mu}{\epsilon_0\mu_0}}, \quad (2.75)$$

and  $\tilde{n}$  is the complex refractive index.

Recalling the definition of irradiance,

$$I(x) = \frac{1}{2} \operatorname{Re} (E_z H_y^*) , \quad (2.76)$$

we find, after some algebra, that

$$I(x) = \frac{1}{2} c \epsilon_0 [nA^2 e^{-\alpha x} - nB^2 e^{\alpha x} - 2\kappa A B \sin(2nk_0 x)] , \quad (2.77)$$

where  $\alpha$  is the absorption coefficient in the form

$$\alpha = \frac{4\pi\kappa}{\lambda} . \quad (2.78)$$

There are three components in Eq. 2.77. The first and second terms indicate the power of light propagating in the forward and backward directions, respectively. The third term is related to the wave interference effect—the power due to the interference between the forward- and backward-propagating waves. The change in irradiance in the layer,  $I_A$ , can be written as

$$I_A = I(0) - I(l) , \quad (2.79)$$

$$= \frac{1}{2} c \epsilon_0 [n (A^2 - B^2 - A^2 e^{-\alpha l} + B^2 e^{\alpha l}) \\ - 2\kappa A B \sin(2nk_0 l)] . \quad (2.80)$$

Here,  $I_A$  can be interpreted differently in various situations; i.e., as heat dissipation in a metal, light irradiance generated in a light-emitting diode, or light irradiance absorbed in a solar cell.

The time-averaged energy dissipation rate,  $Q$ , is defined as

$$Q(x) = - \frac{dI(x)}{dx} , \quad (2.81)$$

and the derivative gives

$$\begin{aligned} Q(x) = \frac{1}{2}c\epsilon_0\alpha n & [A^2e^{-\alpha x} + B^2e^{\alpha x} \\ & + 2AB\cos(2nk_0x)]. \end{aligned} \quad (2.82)$$

From the general solution for the electric field magnitude, we can calculate its absolute square as

$$|E_z|^2 = E_z E_z^*, \quad (2.83)$$

$$= (Ae^{-ikx} + Be^{ikx}) (Ae^{ik^*x} + Be^{-ik^*x}), \quad (2.84)$$

$$= A^2e^{-\alpha x} + B^2e^{\alpha x} + 2AB\cos(2nk_0x), \quad (2.85)$$

and hence, we can express  $Q$  in terms of  $E_z$  as

$$Q(x) = \frac{1}{2}c\epsilon_0\alpha n |E_z|^2. \quad (2.86)$$

Also, in the context of solar cells, including bifacial devices, the irradiance of front-incident light and back-incident light for the thin-film stack considered, denoted by  $I_0$  and  $I_{0,b}$ , respectively, are defined as

$$I_0 = \frac{1}{2}c\epsilon_0 |E_0|^2, \quad (2.87)$$

$$I_{0,b} = \frac{1}{2}c\epsilon_0 |E_{0,b}|^2, \quad (2.88)$$

with

$$I_{0,b} = R_a I_0, \quad (2.89)$$

where  $R_a$  is the spectral albedo. Different from  $I(x)$ ,  $I_0$  and  $I_{0,b}$  (and later  $I_R$  and  $I_T$ ) are irradiances for waves propagating in one direction only, and that Eq. 2.87 and 2.88 are derived from Eq. 2.77 and 2.85 by taking either the forward or backward propagating components with  $n = 1$ ,  $\kappa = 0$ , and  $k = k_0$ .

For a thin-film light-absorbing layer in solar cell, the absorptance,  $\mathfrak{A}$ , is expressed as

$$\mathfrak{A} = \frac{I_A}{I_0} = \frac{\int_0^l Q(x)dx}{I_0}, \quad (2.90)$$

which is also known as the external quantum efficiency (EQE).

In a thin-film stack with  $N$  layers, at  $x = 0$ , the irradiance reflected,  $I_R$ , takes the form

$$I_R = \frac{1}{2}c\varepsilon_0 |E_R|^2. \quad (2.91)$$

The reflectance,  $\mathfrak{R}$ , is defined as

$$\mathfrak{R} = \frac{I_R}{I_0} = \left| \frac{E_R}{E_0} \right|^2. \quad (2.92)$$

Similarly, at  $x = L_N$ , the irradiance transmitted,  $I_T$ , takes the form

$$I_T = \frac{1}{2}c\varepsilon_0 |E_T|^2. \quad (2.93)$$

The transmittance,  $\mathfrak{T}$ , is defined as

$$\mathfrak{T} = \frac{I_T}{I_0} = \left| \frac{E_T}{E_0} \right|^2. \quad (2.94)$$

## 2.2.4 Charge carrier generation

All discussions above are regarding light of a single wavelength. For a thin-film light-absorbing layer in solar cell, we need to consider a range of wavelengths; i.e.  $Q(x, \lambda)$ . With the assumption of full internal quantum efficiency, the charge carrier generation rate,  $G$ , in the light-absorbing layer takes the form

$$G(x) = \frac{1}{hc} \int_{\lambda_l}^{\lambda_u} (\lambda Q(x, \lambda)) d\lambda, \quad (2.95)$$

$$G_{avg} = \frac{1}{l} \int_0^l G(x) dx, \quad (2.96)$$

where  $\lambda_l$  and  $\lambda_u$  are the lower and upper bounds of the wavelength, and  $G_{avg}$  is the average charge carrier generation rate. The resulted current density generated in the active layer,  $i_l$ , is

$$i_l = e \int_0^l G(x) dx = \frac{e}{hc} \int_{\lambda_l}^{\lambda_u} (\lambda I_A) d\lambda. \quad (2.97)$$

The integral operators on wavelength are evaluated with Composite Simpson's rule. The interval  $(\lambda_l, \lambda_u)$  is spitted into  $M$  sub-intervals where  $M$  is an even number and the integration of a function,  $f(\lambda)$ , becomes

$$\begin{aligned} \int_{\lambda_l}^{\lambda_u} f(\lambda) d\lambda \approx & \frac{\lambda_u - \lambda_l}{3M} \left[ f(\lambda_l) + 2 \sum_{j=1}^{M/2-1} f(\lambda_{2j}) \right. \\ & \left. + 4 \sum_{j=2}^{M/2} f(\lambda_{2j-1}) + f(\lambda_u) \right]. \end{aligned} \quad (2.98)$$

### 2.2.5 Polarization and oblique incident light

Up to this point, we have examined the distributions of the optical electric field, energy dissipation, and the generation of free charge carriers within thin-film layer stacks. Before delving into the topic of incoherent light propagation, we will explore the polarization of light and its impact on the optics of thin films when subjected to non-normal incident light.

In the previous sections, we made the assumption of a uniform sinusoidal plane wave, specifically the TEM wave, where the electric and magnetic fields are mutually perpendicular and both perpendicular to the direction of wave propagation. In various optical waveguide, transmission line, and open-environment applications, including photovoltaics, two other common wave modes are frequently employed: the transverse electric (TE) or s-polarized wave and the transverse magnetic (TM) or p-polarized wave. When a wave is incident on an  $x - y$  plane, the primary distinction between TE and TM waves lies in their field orientations. The TE wave exhibits an electric field solely in the  $z$ -direction ( $E_z$ ), perpendicular to the surface, while the TM wave features a magnetic field with a  $z$ -component normal to the plane.

The concept of wave polarization becomes more significant when dealing with oblique

incident light. Take the TE wave, for example; the electric field is continuous with only a  $z-$  component, whereas calculating the magnetic field requires breaking it down into  $x-$  and  $y-$  components for incident, reflected, and refracted waves, with the incident and refracted angles as variables [47, 50]. For thin-film perovskite solar cell applications, we have considered an ASTM G173-03 Global tilt standard spectrum [51], which is measured on a receiving surface with its surface normal pointing to the sun. Therefore, our mathematical formulation's assumption of normal incident uniform plane waves remains valid, and oblique incident light is not the primary focus of this thesis. Nevertheless, ongoing research in the field of optics for photovoltaic systems with oblique incident light may be a potential avenue for future work, particularly for devices with significant rough surfaces or under different operating conditions and spectral irradiances.

## 2.3 Incoherent light propagation

In this section, our focus is on the optics related to the thick glass substrate. As previously mentioned, we consider spatially incoherent light propagation within the glass, where phase information is destroyed, and no light interference effects occur. We begin by discussing the incoherence correction term introduced in the general transfer matrix method [47, 52], which scales down the light intensity as it passes through the glass before entering the thin-film stack. Next, we introduce the phase elimination method [53], which offers a more comprehensive approach to dealing with incoherency in multilayer calculations. Finally, we conclude the chapter by verifying the calculation results for the optical systems, both with and without a glass substrate, in the context of perovskite solar cells.

### 2.3.1 Correction on incident light intensity

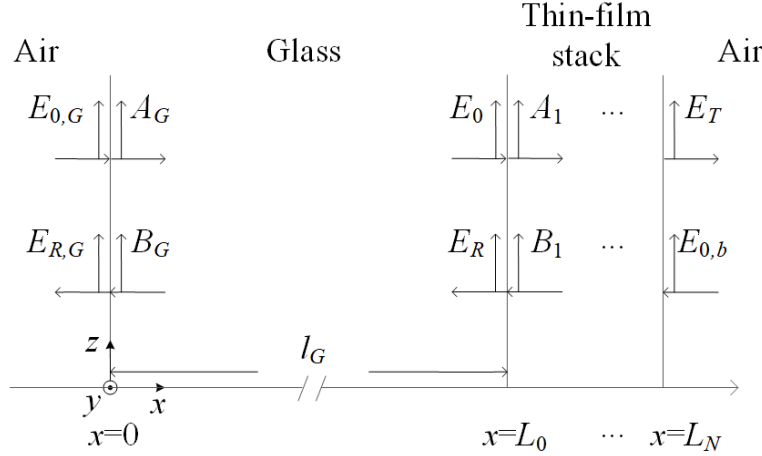


Figure 2.5: Schematic of a  $N$  layer thin-film stack bounded by glass and air.

For a  $N$  layer thin-film stack bounded by a glass layer and air, as shown in Figure 2.5, the following equations can be obtained [47, 52]:

$$|E_{0,G}|^2 = \frac{|e^{-ik^G l^G}|^2}{|t_G|^2} |E_0|^2 - \frac{|r_G e^{ik^G l^G}|^2}{|t_G|^2} |E_R|^2, \quad (2.99)$$

$$|E_{R,G}|^2 = \frac{|r_G e^{-ik^G l^G}|^2}{|t_G|^2} |E_0|^2 + \frac{(|\frac{k_0}{k_G}| |t_G|^2 - |r_G|^2) |e^{ik^G l^G}|^2}{|t_G|^2} |E_R|^2, \quad (2.100)$$

where

$$t_G = \frac{2k_G}{k_0 + k_G}, \quad (2.101)$$

$$r_G = \frac{k_0 - k_G}{k_0 + k_G}, \quad (2.102)$$

are the Fresnel's complex transmission coefficient and reflection coefficient from air to glass, respectively.

From Eq. 2.99 and 2.92, after some algebra, the relation between  $E_{0,G}$  and  $E_0$  can be

expressed as

$$E_0 = C_G E_{0,G}, \quad (2.103)$$

where

$$C_G = \sqrt{\frac{|t_G|^2}{|e^{ik^G l^G}|^2 - \Re |r_G e^{-ik^G l^G}|^2}}, \quad (2.104)$$

is the correction term which scaled down the electric field magnitude when the wave propagates through the thick glass layer. Here, note that when calculating  $\Re$  for the thin-film stack, the medium before the thin-film should be taken as glass instead of air.

### 2.3.2 The phase elimination method

The phase elimination method [53] helps thin down the thick glass layer to reduce computational cost. The glass, about 1 mm thick, is scaled down 1000 times to  $\mu\text{m}$  thickness, allowing us to adopt the system of equations in section 2.2.1 for thin-film layers. Still, further considerations are taken here to address the incoherency. There are two rounds of simulations for the optical field. We have the scaled down thickness for the glass,  $d$ , denoted as  $d'$  for the first run.  $d'$  is calculated as  $d' = l_G/1000$  and the new extinction coefficient,  $\kappa'$ , is calculated as  $\kappa' = \kappa_G l_G/d'$ , where  $\kappa' \ll n_G$ . In the second run, the scaled down glass thicknesses, denoted as  $d''$ , is calculated for each wavelength and they take the form

$$d'' = d' + \lambda/(4n_G). \quad (2.105)$$

The corresponding modified extinction coefficients are  $\kappa'' = \kappa_G l_G/d''$ . Here,  $l_G$  is the original glass thickness,  $n_G$  and  $\kappa_G$  are the refractive index and extinction coefficient for glass correspondingly. The average of the generation rates from the two rounds eliminates the optical interference effect in the thick glass layer. The total generation rate, which is a summation of  $G$  from all discrete wavelength, is compared with the generation profile obtained from the semi-analytical solution.

Here, the optical field intensity at the air/glass interface is

$$|E_z|^2 = |E_f|^2 \exp(-2\kappa^G k_0 x) + |E_b|^2 \exp(2\kappa_G k_0 x) + 2|p| \cos(2n_G k_0 l_G + \delta), \quad (2.106)$$

where  $2|p| \cos(2n_G k_0 l_G + \delta)$  is the interference term between forward and backward waves. The average of the light irradiance calculated from the two rounds eliminates the optical interference in the thick glass layer:

$$\cos(2n_G k_0 d' + \delta) + \cos(2n_G k_0 d'' + \delta) = 0. \quad (2.107)$$

## 2.4 Verifications

### 2.4.1 Thin-film layers

In this section, we verify our thin-film semi-analytical solutions. We begin by comparing the results obtained from the vectorized matrix operation with those achieved through numerical solutions using absorbing boundary conditions in COMSOL. For these verifications, we utilize optical data reported in the literature.

Verifications for the following thin-film structures have been conducted: (1) single thin-film perovskite layer bounded by air; (2) a five layer thin-film stack corresponds to a perovskite solar cell without the glass layer; and (3) a ten layer thin-film stack corresponds to a 2T tandem perovskite-on-perovskite solar cell, in which we refers to the device architecture for a state-of-the-art perovskite-on-perovskite tandem solar cell [5]. Optical data from literature for ITO [54], SnO<sub>2</sub> [55], PTAA [56], top perovskite (Cs<sub>0.2</sub>FA<sub>0.8</sub>PbI<sub>1.8</sub>Br<sub>1.2</sub>) [57], C60 [58], PEDOT:PSS [59], bottom perovskite (MA<sub>0.3</sub>FA<sub>0.7</sub>Pb<sub>0.5</sub>Sn<sub>0.5</sub>I<sub>3</sub>) [60], BCP [61], Cu [62] and MoO<sub>x</sub> [63] are adopted. The incident irradiance is chosen to be ASTM G173-03 Global tilt standard spectrum [51].

We first verify both the real and imaginary parts of the electric field at three distinct wavelengths for a perovskite layer (Cs<sub>0.2</sub>FA<sub>0.8</sub>PbI<sub>1.8</sub>Br<sub>1.2</sub> (380 nm)) bounded by air. As shown in Figure 2.6, good agreements in optical electric field are obtained.

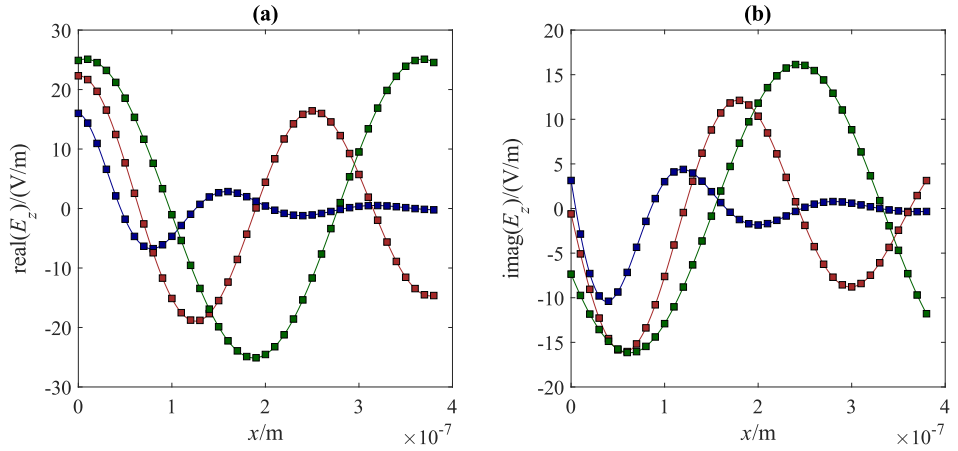


Figure 2.6: (a) Real and (b) imaginary parts of the optical electric field obtained from semi-analytical solution (lines) and solving the system of equations numerically (squares) at 400 nm (blue), 600 nm (red), and 800 nm (green) wavelengths for an one layer thin-film.

We then verify both the real and imaginary parts of the electric field at three distinct wavelengths for a thin-film stack in a sample perovskite solar cell with the structure ITO (70 nm) /PTAA (15 nm) /Cs<sub>0.2</sub>FA<sub>0.8</sub>PbI<sub>1.8</sub>Br<sub>1.2</sub> (380 nm) /C60 (20 nm) /Cu (100 nm). Here, we consider the thin-film stack to be bounded by air. Similarly, we observe good agreements between the solutions, as shown in Figure 2.7.

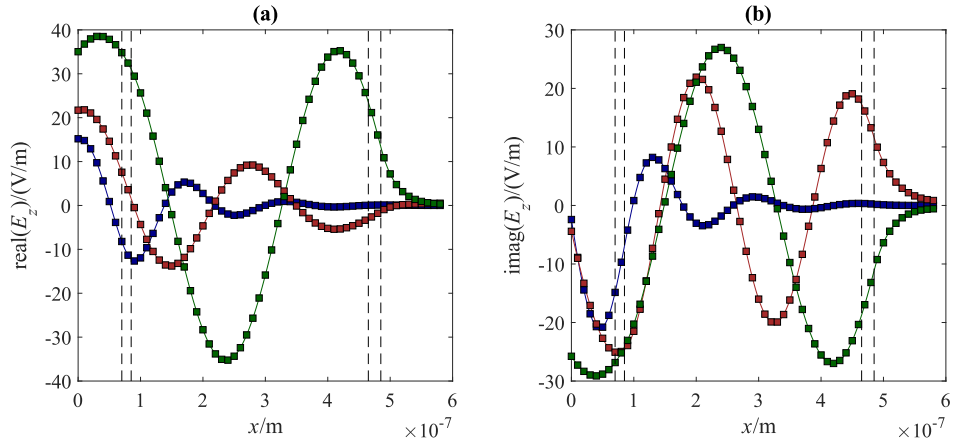


Figure 2.7: (a) Real and (b) imaginary parts of the optical electric field obtained from semi-analytical solution (lines) and solving the system of equations numerically (squares) at 400 nm (blue), 600 nm (red), and 800 nm (green) wavelengths for a five-layer thin-film stack. The vertical dashed lines indicate the interfaces between thin-film layers.

Lastly, we verify both the real and imaginary parts of the electric field at three distinct wavelengths for a thin-film stack in a sample perovskite-on-perovskite tandem solar cell

with the structure ITO (70 nm) /PTAA (15 nm) /Cs<sub>0.2</sub>FA<sub>0.8</sub>PbI<sub>1.8</sub>Br<sub>1.2</sub> (380 nm) /C60 (20 nm) /SnO<sub>2</sub> (20 nm) /PEDOT:PSS (100 nm) /MA<sub>0.3</sub>FA<sub>0.7</sub>Pb<sub>0.5</sub>Sn<sub>0.5</sub>I<sub>3</sub> (860 nm) /C60 (20 nm) /BCP (7 nm) /Cu (100 nm), similar to the state-of-the-art 2T perovskite-on-perovskite tandem solar cell in Chapter 8. We consider the thin-film stack to be bounded by air, and the optical electric fields in the top and bottom perovskite layers—layers 3 and 7—are shown in Figure 2.8.

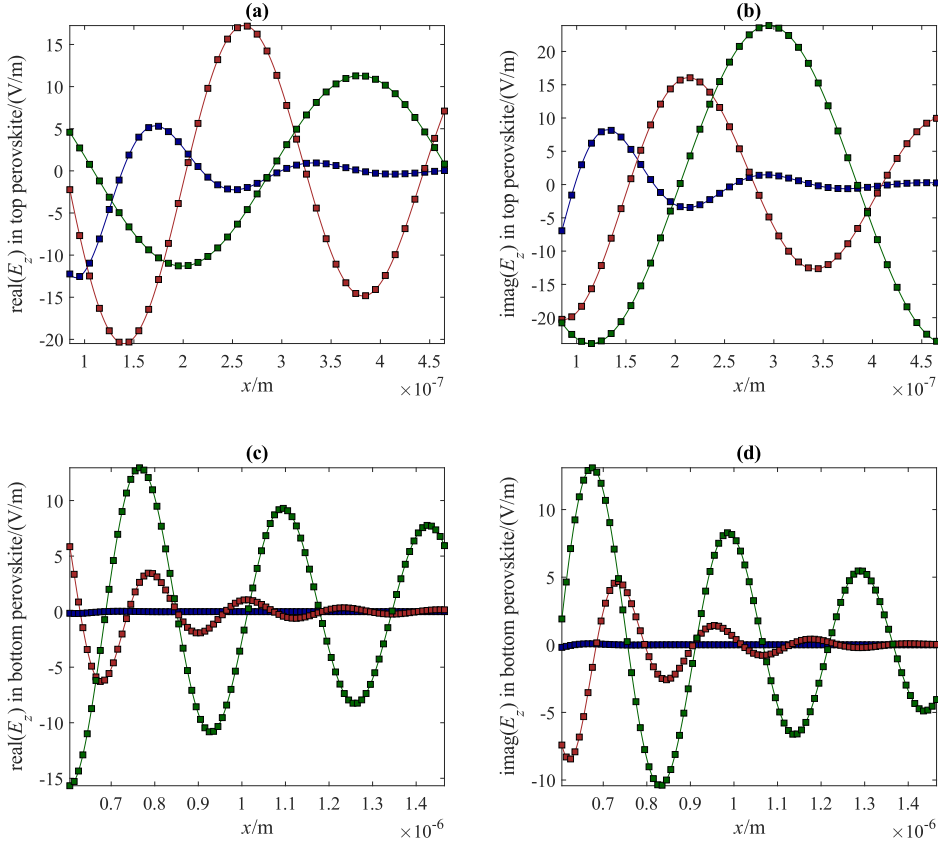


Figure 2.8: Real and imaginary parts of the optical electric field in (a-b) top perovskite layer and (c-d) bottom perovskite layer of a ten-layer thin-film stack in a 2T perovskite-on-perovskite tandem solar cell obtained from semi-analytical solution (lines) and solving the system of equations numerically (squares) at 400 nm (blue), 600 nm (red), and 800 nm (green) wavelengths.

To conclude, our derived analytical solutions for the optical electric field in thin-film layers achieve similar results compared to solving the system with absorbing boundary conditions numerically.

### 2.4.2 Thin-film layers with glass substrate

Next, we combine our derived matrix formulation and the phase elimination method, and verify it with solving the system of equations numerically with phase elimination method, as well as the general transfer matrix method. We add in the glass substrate to the sample perovskite solar cell adopted in the last sub-section, and its structure becomes Glass (1.1 mm) [64] /ITO (70 nm) /PTAA (15 nm) /Cs<sub>0.2</sub>FA<sub>0.8</sub>PbI<sub>1.8</sub>Br<sub>1.2</sub> (380 nm) /C60 (20 nm) /Cu (100 nm). For the phase elimination method, the calculated EQE and current densities are the average of two runs mentioned in section 2.3.2. We compare the EQE (see Eq. 2.90) obtained from the three methods and obtained good agreements, as shown in Figure 2.9. The slight differences in EQE from the solutions in Comsol could be due to the meshing, as the modified glass thicknesses might have different number of significant figures when being processed in Matlab and Comsol. The calculated photogenerated current densities are 175.6, 175.7, and 175.5 A/m<sup>2</sup> for the three methods, respectively.

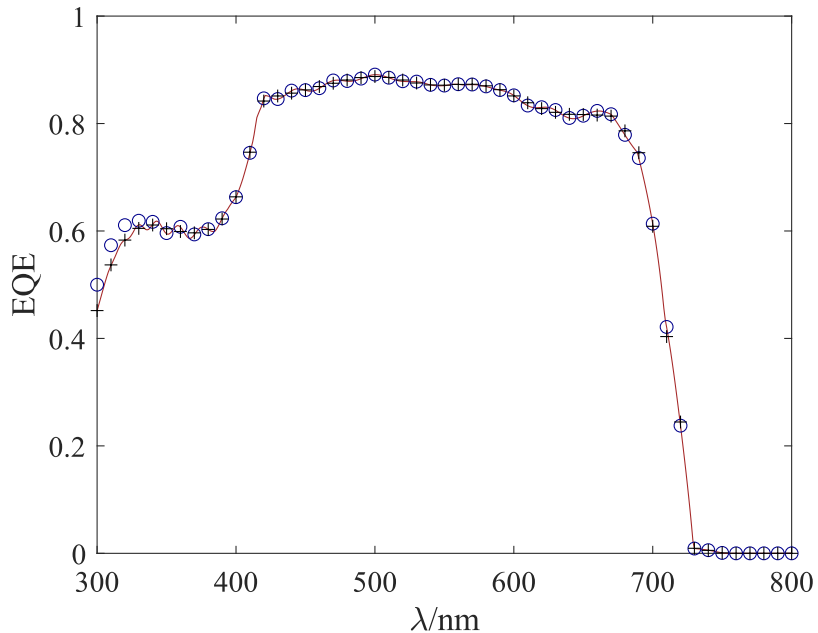


Figure 2.9: EQE calculated from semi-analytical matrix formulation with phase elimination method (red line), solving the system of equations numerically together with phase elimination method (circle), and general transfer matrix method with an incoherency correction term (plus sign).



# Chapter 3

## Electronics

In this chapter, we discuss the physics and modeling of charge carrier transport and recombination in a p-i-n type single-junction perovskite solar cell, as depicted in Figure 3.1. This electronic model can be directly coupled with the optical model by incorporating the generation rate of electron-hole pairs, serving as the source term in the active perovskite layer.

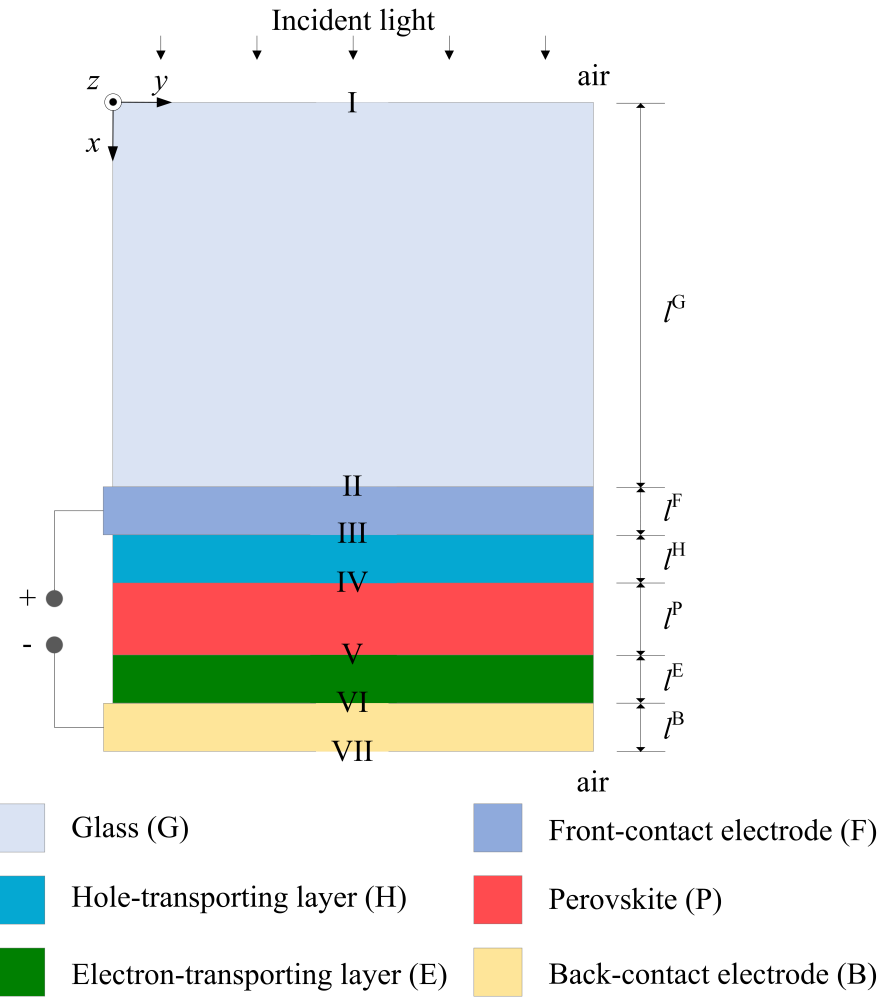


Figure 3.1: Schematic of a typical p-i-n structured planar perovskite solar cell. Here,  $l$  is the layer thickness, the roman numerals indicate the interfaces between layers, and  $\{G,F,H,P,E,B\}$  are superscripts that denote the corresponding layers.

### 3.1 Energy band level and charge carrier concentration

Energy bands are fundamental in semiconductor physics and devices, including photovoltaic technology. In semiconductor materials, we have the conduction band and the valence band, which correspond to the lowest unoccupied molecular orbital (LUMO) and the highest occupied molecular orbital (HOMO) in chemistry, respectively. The band gap represents the energy difference between the bottom of the conduction band and the top of the valence band, signifying the minimum energy required for photo-excitation to take place. Unlike conductors such as metals and conducting oxides, semiconductors

feature non-overlapping valence and conduction bands with narrow band gaps that enable electron movement between them, often triggered by excitation factors like photo-illumination. Shifting our focus to the p-i-n type single-junction perovskite solar cell illustrated in Figure 3.1, the corresponding energy band diagram is illustrated in Figure 3.2.

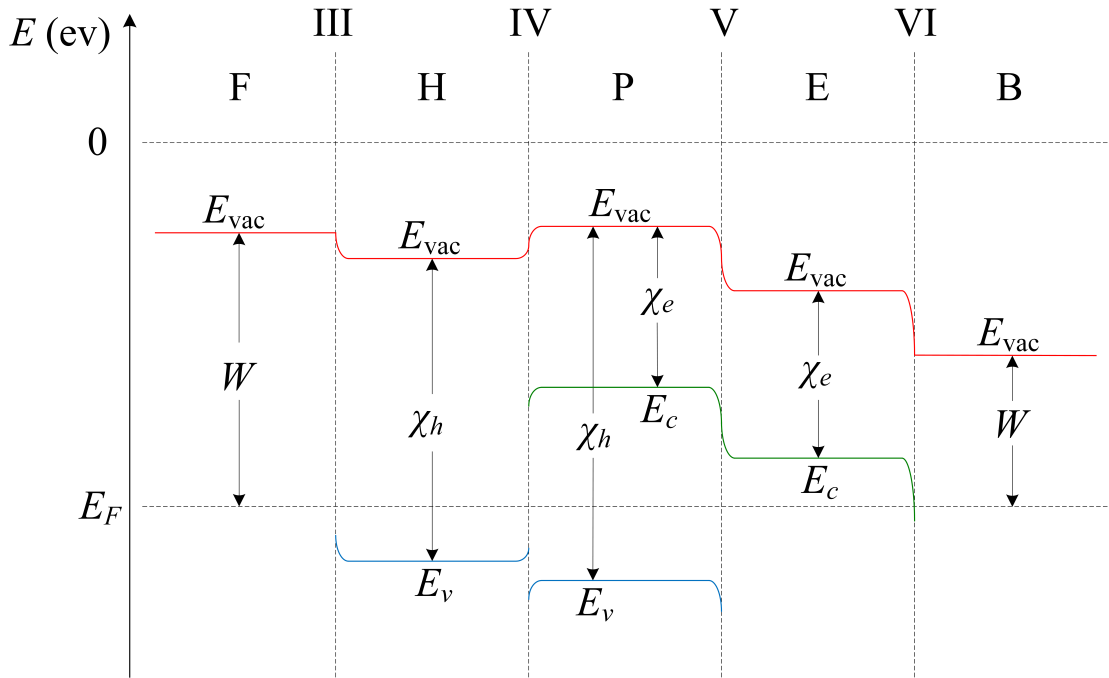


Figure 3.2: Energy band diagram for a p-i-n structured planar perovskite solar cell.

From the definition of a band gap, we can write

$$E_g = E_c - E_v, \quad (3.1)$$

$$= \chi_h - \chi_e. \quad (3.2)$$

Here,  $E_g$  is the band gap,  $E_c$  and  $E_v$  are the electron energy at the conduction band and valence band, respectively, and  $\chi_e$  and  $\chi_h$  are the electron affinity and hole ionization potential, respectively.

Let us first take a look at the built-in voltage,  $V_b$ , of the perovskite solar cell, which is defined as the potential difference between the two contacts. In the front contact in the

p-i-n device, the Fermi level,  $E_F$ , can be found as

$$E_F = E_{vac}^F - W_F^F, \quad (3.3)$$

$$E_{vac}^F = -q\phi_F^F, \quad (3.4)$$

where  $E_{vac}^F$  is the vacuum level of the front contact,  $q$  is the elementary charge, and  $\phi_F$  and  $W_F$  are the potential and work function in the front contact, respectively. Similarly, we have

$$E_F = E_{vac}^B - W_B^B, \quad (3.5)$$

$$E_{vac}^B = -q\phi_B^B, \quad (3.6)$$

for the back contact, where the superscript B denotes the properties associated with the back contact. At equilibrium, the Fermi level should match throughout the device, allowing us to find  $V_b$  as

$$V_b = \phi_B^B - \phi_F^F = (W_F^F - W_B^B)/q. \quad (3.7)$$

Next, the Fermi-Dirac distributions for electron and hole densities in a semiconductor, given that the differences between the Fermi level and conduction/valence bands are more than the thermal voltage, can be approximated as

$$c_e = N_c \exp\left(-\frac{E_c - E_F}{k_B T}\right), \quad (3.8)$$

$$c_h = N_v \exp\left(-\frac{E_F - E_v}{k_B T}\right), \quad (3.9)$$

$$E_c = E_{vac} - \chi_e, \quad (3.10)$$

$$E_v = E_{vac} - \chi_h. \quad (3.11)$$

Here,  $c_e$  and  $c_h$  are the electron and hole concentrations, respectively,  $N_c$  and  $N_v$  are the density of states in the conduction band and valence band, respectively,  $k_B$  is the Boltzmann constant and  $T$  is the temperature. At interface III between the front contact

and hole-transporting layer, Eq. 3.9 can be rewritten as

$$c_h^{\text{III}} = N_v^{\text{H}} \exp\left(-\frac{(E_{\text{vac}}^{\text{F}} - W^{\text{F}}) - (E_{\text{vac}}^{\text{H}} - \chi_h^{\text{H}})}{k_B T}\right), \quad (3.12)$$

$$= N_v^{\text{H}} \exp\left(\frac{W^{\text{F}} - \chi_h^{\text{H}}}{k_B T}\right), \quad (3.13)$$

by knowing that the vacuum levels align at the interfaces. Similarly, at interface VI between the electron-transporting layer and the back contact, Eq. 3.8 becomes

$$c_e^{\text{VI}} = N_c^{\text{E}} \exp\left(-\frac{(E_{\text{vac}}^{\text{E}} - \chi_e^{\text{E}}) - (E_{\text{vac}}^{\text{B}} - W^{\text{B}})}{k_B T}\right), \quad (3.14)$$

$$= N_c^{\text{E}} \exp\left(\frac{\chi_e^{\text{E}} - W^{\text{B}}}{k_B T}\right). \quad (3.15)$$

We then move on to the charge carrier concentrations at the two interfaces IV and V of the perovskite layer. At interface IV between the hole-transporting and perovskite layers, we have

$$c_h^{\text{IV}}|_- = N_v^{\text{H}} \exp\left(-\frac{E_F - E_v^{\text{H}}}{k_B T}\right), \quad (3.16)$$

$$c_h^{\text{IV}}|_+ = N_v^{\text{P}} \exp\left(-\frac{E_F - E_v^{\text{P}}}{k_B T}\right), \quad (3.17)$$

where the subscripts – and + here indicates properties to the left and right of the interface, respectively. Eq. 3.16 and 3.17 allow us to write the ratio of hole concentrations between the hole-transporting and perovskite layers at interface IV as

$$\frac{c_h^{\text{IV}}|_+}{c_h^{\text{IV}}|_-} = \frac{N_v^{\text{P}}}{N_v^{\text{H}}} \exp\left(\frac{E_v^{\text{P}} - E_v^{\text{H}}}{k_B T}\right), \quad (3.18)$$

$$= \frac{N_v^{\text{P}}}{N_v^{\text{H}}} \exp\left(\frac{(E_{\text{vac}}^{\text{P}} - \chi_h^{\text{P}}) - (E_{\text{vac}}^{\text{H}} - \chi_h^{\text{H}})}{k_B T}\right), \quad (3.19)$$

$$= \frac{N_v^{\text{P}}}{N_v^{\text{H}}} \exp\left(\frac{\chi_h^{\text{H}} - \chi_h^{\text{P}}}{k_B T}\right). \quad (3.20)$$

Similarly, at interface V, the ratio of electron concentrations between the perovskite and

electron-transporting layers is

$$\frac{c_e^V|_-}{c_e^V|_+} = \frac{N_c^P}{N_c^E} \exp\left(\frac{\chi_e^P - \chi_e^E}{k_B T}\right). \quad (3.21)$$

We have now obtained the charge carrier concentrations or their relations based on the energy band levels in a p-i-n structured perovskite solar cell, which could be adopted as boundary conditions in a drift and diffusion model.

## 3.2 Potential and electric field

The distribution of the electric potential across the p-i-n type single-junction device—from hole-transporting layer, to perovskite layer, and to electron-transporting layer—can be described by the Poisson's equation:

$$\epsilon \psi'' = S_\psi, \quad (\text{H,P,E}) \quad (3.22)$$

where  $\epsilon$  is the permittivity, the superscript " denotes the second-order derivative with respect to  $x$ ,  $S_\psi$  is the source term in the forms

$$S_\psi = e \begin{cases} N_a - c_h, & (\text{H}) \\ c_e - c_h, & (\text{P}) \\ c_e - N_d, & (\text{E}) \end{cases} \quad (3.23)$$

and  $N_a$  and  $N_d$  are the ionized acceptor and donor impurity concentrations in hole and electron transporting layers, respectively. By assuming the front and back contact layers as ohmic contacts, the corresponding boundary conditions at interface III and X at different applied voltages,  $V_a$ , can be written as

$$\psi^{III} = V_a - V_b, \quad \psi^{VI} = 0. \quad (3.24)$$

Here, we have set the reference electric potential to be zero at interface VI. At boundaries IV and V, we require the electrical potential and electric field to be continuous. The corresponding electric field,  $E_\psi$ , could be calculated as

$$E_\psi = \psi', \quad (3.25)$$

where the superscript ' indicates a first-order derivative with respect to  $x$ .

### 3.3 Charge carrier drift and diffusion

For transport of the charge carriers, we consider the dependent variables—hole and electron concentrations,  $c_h$  and  $c_e$ , together with the electric potential,  $\psi$ —to be spatially dependent on  $x$ . We have the following governing equations for charge carrier drift and diffusion:

$$j'_h = S_j, \text{ (H,P)} \quad (3.26)$$

$$j'_e = S_j, \text{ (E,P)} \quad (3.27)$$

where  $j_h$  and  $j_e$  are the hole and electron fluxes, respectively, and the source term,  $S_j$ , is given by

$$S_j = \begin{cases} 0, & (\text{E,H}) \\ G - R^P, & (\text{P}) \end{cases} \quad (3.28)$$

Here,  $G$  is the generation rate of electrons and holes calculated in the optics part (see Chapter 2) and  $R^P$  is the net recombination rate in the perovskite layer. The hole and electron carrier fluxes are defined as

$$j_{(e,h)} = \pm \mu_{(e,h)} c_{(e,h)} \psi' - D_{(e,h)} c'_{(e,h)}, \quad (3.29)$$

$$D_{(e,h)} = k_B T \mu_{(e,h)} / q, \quad (3.30)$$

where  $\mu$  is the carrier mobility,  $D$  is the carrier diffusion coefficient which relates to  $\mu$  by the classic Einstein relation in Eq. 3.30. For the conservation of charge carriers from interface III to VI, we have

$$c_h^{\text{III}} = c_h^0, \quad (3.31)$$

$$c_{h,+}^{\text{IV}} = \Pi_h c_{h,-}^{\text{IV}}, \quad j_{h,-}^{\text{IV}} = j_{h,+}^{\text{IV}} - j_s^{\text{IV}}, \quad j_{e,-}^{\text{IV}} = j_s^{\text{IV}}, \quad (3.32)$$

$$c_{e,-}^{\text{V}} = \Pi_e c_{e,+}^{\text{V}}, \quad j_{e,-}^{\text{V}} = j_{e,+}^{\text{V}} - j_s^{\text{V}}, \quad j_{h,+}^{\text{V}} = j_s^{\text{V}}, \quad (3.33)$$

$$c_e^{\text{VI}} = c_e^0. \quad (3.34)$$

In the above boundary conditions,  $c_h^0$  and  $c_e^0$  are the reference hole and electron concentrations at III and VI, which can be found in Eq. 3.26 and 7.2, respectively,  $\Pi$  is the ratio describing the jumps in carrier concentrations that could be derived from Eq. 3.20 and 3.21, respectively,  $j_s^{\text{IV}}$  and  $j_s^{\text{V}}$ , are the interface recombination fluxes at boundaries IV, V, respectively. The reference concentrations and concentration jumps are written as

$$c_h^0 = N_v^{\text{H}} \exp\left(-\frac{E_F - E_v^{\text{H}}}{k_B T}\right), \quad (3.35)$$

$$c_e^0 = N_c^{\text{E}} \exp\left(\frac{\chi_e^{\text{E}} - W^{\text{B}}}{k_B T}\right), \quad (3.36)$$

$$\Pi_h = \frac{N_v^{\text{P}}}{N_v^{\text{H}}} \exp\left(\frac{\chi_h^{\text{H}} - \chi_h^{\text{P}}}{k_B T}\right), \quad (3.37)$$

$$\Pi_e = \frac{N_c^{\text{P}}}{N_c^{\text{E}}} \exp\left(\frac{\chi_e^{\text{P}} - \chi_e^{\text{E}}}{k_B T}\right). \quad (3.38)$$

In addition,  $j_s^{\text{IV}}$  and  $j_s^{\text{V}}$  are the charge carrier recombination rates at the interfaces IV and V, respectively, which will be discussed further in the next section.

### 3.4 Charge carrier recombination

When electron and holes transport in the p-i-n junction, they will unavoidably undergo recombinations; i.e. radiative recombination, non-radiative recombinations including Auger recombination and Shockley-Read-Hall (SRH) recombination, and interfacial recombinations. Suppressing these recombinations, in general, could help to improve the

solar cell performances. The charge carrier recombination,  $R^P$ , in the perovskite layer in Eq. 3.28 can be expressed as

$$R^P = R_{aug} + R_{rad} + R_{srh}, \quad (3.39)$$

$$R_{aug} = (A_e c_e + A_h c_h)(c_e c_h - c_i^2), \quad (3.40)$$

$$R_{rad} = B_{rad} (c_e c_h - c_i^2), \quad (3.41)$$

$$R_{srh} = \frac{c_e c_h - c_i^2}{\tau_e (c_h + c_{h,trap}) + \tau_h (c_e + c_{e,trap})}, \quad (3.42)$$

where we have considered the Auger recombination,  $R_{aug}$ , radiative recombination,  $R_{rad}$ , and SRH recombination,  $R_{srh}$ . Here,  $A_e$  and  $A_h$  are the Auger recombination coefficient for electrons and holes, respectively,  $B_{rad}$  is the radiative recombination coefficient,  $c_i$  is the intrinsic charge carrier concentration,  $\tau$  is the charge carrier lifetime, and  $c_{h,trap}$  and  $c_{e,trap}$  are the hole and electron concentrations at the trap state, respectively. These concentrations take the forms

$$c_i = \sqrt{N_c N_v \exp[-E_g/(k_B T)]}, \quad (3.43)$$

$$c_{(e,h),trap} = N_{(c,v)} \exp[-\Delta E_{(e,h)}/(k_B T)], \quad (3.44)$$

$$\Delta E_e = E_g - \Delta E_{trap}, \Delta E_h = \Delta E_{trap}. \quad (3.45)$$

Here,  $\Delta E_{trap}$  is the energy difference between the valence band and the trap energy level,  $\Delta E_e$  is the energy difference between the trap level and the conduction band and  $\Delta E_h$  is the energy difference between the trap level and the valence band. The various recombination fluxes originated from the recombination channels are evaluated with line integers of the perovskite layer:

$$j_{aug} = \int_P R_{aug} dx, j_{rad} = \int_P R_{rad} dx, j_{srh} = \int_P R_{srh} dx. \quad (3.46)$$

In addition, the surface recombination carrier flux,  $j_s$ , can be found as

$$j_s^{\text{IV}} = v_h (c_{e,+}(c_{h,-} + c_{h,+}) - c_i^{\text{P}}(c_i^{\text{H}} + c_i^{\text{P}})), \quad (3.47)$$

$$j_s^{\text{V}} = v_e (c_{h,-}(c_{e,+} + c_{e,-}) - c_i^{\text{P}}(c_i^{\text{E}} + c_i^{\text{P}})), \quad (3.48)$$

where  $v_h$  is the effective surface recombination velocity between layers H and P and  $v_e$  is the effective surface recombination velocity between layers P and E.

We can define the total recombination carrier flux,  $j_{\text{rec}}$ , as

$$j_{\text{rec}} = j_{\text{aug}} + j_{\text{rad}} + j_{\text{srh}} + j_s^{\text{IV}} + j_s^{\text{V}}. \quad (3.49)$$

## 3.5 Summary

In this chapter, we have discussed the electronics in a planar p-i-n structured perovskite solar cell, which can be easily modified for other structures. Together with the optics discussed in Chapter 2, we have arrived at an combined optoelectronic model.

### 3.5.1 Governing equation

We have the following governing equations for the electronics part in the optoelectronic model:

$$j'_h = S_j, \quad (\text{H,P}) \quad (3.50)$$

$$j'_e = S_j, \quad (\text{P,E}) \quad (3.51)$$

$$\varepsilon \psi'' = S_\psi, \quad (\text{H,P,E}) \quad (3.52)$$

with the following source terms:

$$S_j = \begin{cases} 0, & (\text{H,E}) \\ G - R^P, & (\text{P}) \end{cases} \quad (3.53)$$

$$S_\psi = e \begin{cases} N_a - c_h, & (\text{H}) \\ c_e - c_h, & (\text{P}) \\ c_e - N_d, & (\text{E}) \end{cases} \quad (3.54)$$

where the charge carrier generation rate,  $G$ , is calculated with Eq. 2.133.

The total current density,  $i_{tot}$ , can be written as

$$i_{tot} = e(j_h - j_e). \quad (3.55)$$

### 3.5.2 Boundary conditions

We solve the governing equations subject to the following boundary conditions.

For the Poisson's equation:

$$\psi^{III} = V_a - V_b, \psi^{VI} = 0, \quad (3.56)$$

For the charge carrier transport and recombination:

$$c_h^{III} = c_h^0, \quad (3.57)$$

$$c_{h,+}^{IV} = \Pi_{h,t} c_{h,-}^{IV}, j_{h,-}^{IV} = j_{h,+}^{IV} - j_s^{IV}, j_{e,-}^{IV} = j_s^{IV}, \quad (3.58)$$

$$c_{e,-}^V = \Pi_{e,t} c_{e,+}^V, j_{e,+}^V = j_{e,-}^V - j_s^V, j_{h,+}^V = j_s^V, \quad (3.59)$$

$$c_e^{VI} = c_e^0, \quad (3.60)$$

### 3.5.3 Constitutive relations

The constitutive relations are

$$j_{(e,h)} = \pm \mu_{(e,h)} c_{(e,h)} \frac{d\psi}{dx} - D_{(e,h)} \frac{dc_{(e,h)}}{dx}, \quad (3.61)$$

$$D_{(e,h)} = k_B T \mu_{(e,h)} / e, \quad (3.62)$$

$$V_b = (W^F - W^B) / e, \quad (3.63)$$

$$c_h^0 = N_v^H \exp \left( -\frac{W^F - E_v^H}{k_B T} \right), \quad (3.64)$$

$$c_e^0 = N_c^E \exp \left( \frac{\chi_e^E - W^B}{k_B T} \right), \quad (3.65)$$

$$\Pi_h = \frac{N_v^P}{N_v^H} \exp \left( \frac{\chi_h^H - \chi_h^P}{k_B T} \right), \quad (3.66)$$

$$\Pi_e = \frac{N_c^P}{N_c^E} \exp \left( \frac{\chi_e^P - \chi_e^E}{k_B T} \right), \quad (3.67)$$

$$R^P = R_{aug} + R_{rad} + R_{srh}, \quad (3.68)$$

$$R_{aug} = (A_e c_e + A_h c_h)(c_e c_h - c_i^2), \quad (3.69)$$

$$R_{rad} = B_{rad} (c_e c_h - c_i^2), \quad (3.70)$$

$$R_{srh} = \frac{c_e c_h - c_i^2}{\tau_e (c_h + c_{h,trap}) + \tau_h (c_e + c_{e,trap})}, \quad (3.71)$$

$$j_{aug} = \int_P R_{aug} dx, j_{rad} = \int_P R_{rad} dx, j_{srh} = \int_P R_{srh} dx, \quad (3.72)$$

$$j_s^{IV} = v_h (c_{e,+}(c_{h,-} + c_{h,+}) - c_i^P (c_i^H + c_i^P)), \quad (3.73)$$

$$j_s^V = v_e (c_{h,-}(c_{e,+} + c_{e,-}) - c_i^P (c_i^E + c_i^P)), \quad (3.74)$$

$$j_{rec} = j_{aug} + j_{rad} + j_{srh} + j_s^{IV} + j_s^V, \quad (3.75)$$

$$c_i = \sqrt{N_c N_v \exp [-E_g / (k_B T)]}, \quad (3.76)$$

$$E_g = \chi_h - \chi_e, \quad (3.77)$$

$$c_{(e,h),trap} = N_{(c,v)} \exp [ -\Delta E_{(e,h)} / (k_B T) ], \quad (3.78)$$

$$\Delta E_e = E_g - \Delta E_{trap}, \Delta E_h = \Delta E_{trap}. \quad (3.79)$$

# Chapter 4

## Numerics

### 4.1 Vectorized matrix calculation for optics

For the optics, the optical electric field,  $E_z$ , across all layers considered are calculated in MATLAB R2022a with vectorized matrix operations. The charge-carrier generation rate,  $G$ , at each wavelength are then found, and averaged out with phase-elimination method. The integral operator in  $G$  is evaluated with Composite Simpson's rule. These generation profiles are then imported into COMSOL MULTIPHYSICS 5.2a via LiveLink. As such, the optics is coupled with the drift-diffusion model. In addition, EQE and  $G$  from the optics in Chapter 2 are verified using Helmholtz's equation and the phase elimination method in Comsol.

### 4.2 Finite element method

We adopt the finite element method and solve the differential equations in COMSOL MULTIPHYSICS 5.2a. The direct solver MUMPS is selected as the nonlinear solver with a  $10^{-3}$  relative convergence tolerance. The computer used to run the simulations has a CPU processor Intel® Core™ i5-7600 @ 3.50 GHz and a total installed RAM of 16.0 GB.

For the verification of optics with glass substrate, two runs of phase elimination method are conducted in Comsol. The computational domain for optical electric field

is set to six consecutive layers in one-dimensional space—glass, front-contact, hole-transporting, perovskite, electron-transporting, and back-contact layers, with a mesh size of 1 nm in the domains and 0.1 nm at the boundaries. The computational time for an auxiliary sweep of wavelength in vacuum from 300 nm to 1050 nm for the verification case takes around 8 s (wall-clock time). Here, the first run in the phase elimination method is directly conducted in Comsol, while for the second run, we use Comsol with Matlab Livelink to control the changes in wavelength and glass layer thickness, which helps avoid an implementation of parametric sweep in Comsol. The irradiance and charge carrier generation rate are then calculated from the obtained optical electric field.

For the electronic part of our model, the computational domains for charge carrier transport—hole-transporting, perovskite, and electron-transporting layers, together with the recombination junction if we are working on a two-terminal tandem device—are solved with a mesh size of 1 nm in the domains and 0.1 nm at the boundaries. Each complete run for a single applied voltage can take around 1 s (wall-clock time). Mesh independence studies were carried out with a finer mesh of 0.01 nm and similar current-voltage ( $i - V$ ) curves are obtained. The  $i - V$  data are exported out from Comsol and interpolated with cubic spline interpolation in Matlab for obtaining the PCE. The finite element method have been applied to simulation of  $i - V$  characteristics in Chapters 5 to 7.

### 4.3 Monte Carlo simulation and sensitivity analysis

In the Monte Carlo simulation, the chosen stochastic parameters, depending on the specific problem and device architecture in the later chapters, are included as the input population  $X_i$ , where the subscript  $i$  indicates the  $i$ th input parameter. In addition, we assume these parameters are independent on each others. The objective is to prepare large data that are well sampled for analysis.

In Chapter 5, for training of neural networks of perovskite solar cells, we prepared one set of training data with a sample size of one hundred thousand, and another three sets of data for validation and testing, each with a sample size of ten thousands. The

Latin hypercube sampling method was employed during data preparation.

For data used for sensitivity analysis in Chapters 6 and 7, the parameters are firstly perturbed with 10% standard deviation from their calibrated values (depending on the specific problem) based on normal distributions, and then sampled with Latin hypercube sampling method and random sampling method for checking the reproducibility of the sensitivity rankings. The parameters are varied simultaneously. For Latin hypercube and random sampling, we restrict the parameter ranges according to their upper and lower bounds obtained from the previous normally distributed data prepared. All the stochastic parameters are sampled based on the above methods to produce one thousand sets of parameter input. The critical sample size of each stochastic parameter,  $N_c$  [65], can be determined as

$$N_c = \left( \frac{z_{\alpha_s/2} \sigma_{X_i}}{\mathfrak{R} \mu_{X_i}} \right)^2, \quad (4.1)$$

where  $z_{\alpha_s/2}$  is the upper  $100(1 - \alpha_s/2)^{th}\%$  of the standard normal distribution at a significant level of  $\alpha_s$ , and  $\mathfrak{R}$  is the relative error between the sample and population means. When both  $\alpha_s$  and  $\mathfrak{R}$  are chosen to be 1%, the value of  $z_{\alpha_s/2}$  is 2.576 from the z-score table [66] and the value of  $N_c$  is calculated and rounded up to be 664. In the simulations, a sample size of one thousand that is larger than  $N_c$ , is used for every set of stochastic parameters, which ensures sufficient data for a predefined normal distribution. In addition, one-sample Kolmogoroc-Smirnov (K-S) test [66] is carried out to reject a stochastic set of  $X_i$  if one of the drawn samples is found to have significant difference from the population mean. At a significant level,  $\alpha_{ks}$ , of 5%, the difference between the sample and the population would not be statistically negligible if the degree of rarity of the result,  $p_{ks}$ , is smaller than  $\alpha_{ks}$ . While  $p_{ks}$  is smaller than 5%, the sample will be rejected and redrawn to ensure that it acts as a good representative of the population. Finally, the inputs are imported into Comsol for evaluating the  $i - V$  characteristics, and the cell performances,  $V_{oc}$ ,  $i_{sc}$ , FF, and PCE ( $\eta$ ), are returned as outputs.

After preparing the data, for the sensitivity analysis conducted in Chapter 6 and 7, the correlation between each varied parameter and each performance can be quantified

with the sigma-normalized derivative method [67] as

$$S_{X_i}^{\sigma_{(V_{oc}, i_{sc}, \text{FF}, \eta)}} = \frac{\sigma_{X_i}}{\sigma_{(V_{oc}, i_{sc}, \text{FF}, \eta)}} \frac{\partial(V_{oc}, i_{sc}, \text{FF}, \eta)}{\partial X_i}, \quad (4.2)$$

where  $\sigma_{X_i}/\sigma_{(V_{oc}, i_{sc}, \text{FF}, \eta)}$  is the normalization factor consisting of the standard deviations of the input,  $X_i$ , and one of the outputs,  $V_{oc}$ ,  $i_{sc}$ , FF, or PCE.  $\partial(V_{oc}, i_{sc}, \text{FF}, \eta)/\partial X_i$  is the partial derivative describing how sensitive an output parameter is with respect to variation in an input  $X_i$ . This derivative is evaluated with multiple linear regression fitting [67]. The purpose of adding the normalization factors is to make the derivatives comparable for different  $X_i$ .  $S_{X_i}^{\sigma}$  measures the sensitivity of the output to the input parameters. A larger absolute  $S_{X_i}^{\sigma}$  value suggests that the corresponding parameter,  $X_i$ , is more influential on the cell performance. The positive and negative signs of the  $S_{X_i}^{\sigma}$  results indicate an increasing and decreasing relationship between the input and the output, respectively.

In addition, after the mixed integer optimization in Chapter 8, we also conducted a sensitivity analysis on the optimal short-circuit current densities. The thicknesses of all layers except the glass were selected as stochastic parameters, and they were varied simultaneously based on a normal distribution with a 5% coefficient of variation from their optimal values. A sample size of ten thousand and the one-sample K-S test were employed as well.

## 4.4 Genetic algorithm

For the mixed-integer optimization in Chapter 8, we employed a genetic algorithm with a population size of one thousand, maximum generations of twenty thousand, function tolerance of  $10^{-6}$ , and a maximum stall generation of five hundred. Populations that produced short-circuit current densities within 5% of the optimum were extracted, providing information on alternative optical designs with slight loss in current outputs.

# Chapter 5

## Neural network for perovskite solar cells

### 5.1 Introduction

Due to fast development of artificial intelligence recent years, machine learning and neural network are gathering considerable interest to solve complex problems, make promising predictions and help decision makings. The usage of artificial intelligence can be multi-disciplinary, including but not limited to robotics, finance, weather forecast and so on. In the context of photovoltaics, artificial neural network could help to provide another pathway for modeling and simulation.

Researchers have applied machine learning and artificial neural network for modeling of perovskite solar cells. Oboh *et al.* [68] have trained artificial neural networks for predicting the performance of a planar perovskite solar cell. They employed the thicknesses of the perovskite layer, and the hole- and electron-transporting layers, together with the hole and electron dopant concentrations as the input parameters. The final output PCE yield is compared with numerical solutions, and has achieved good agreements. Sun *et al.* [69] focused on the optical structure design of perovskite solar cells, introduced a neural network as assistant for modeling and simulation, and obtained more than 30% enhancement in absorptance. Wu *et al.* [70] constructed and trained a neural net-

work to predict the charge-carrier recombination rates in perovskite solar cells, aiming to provide information on interface recombination, hysteresis and ionic migration through experimental validations.

The above works have contributed significantly to advanced modeling with artificial neural network in photovoltaic applications. Nonetheless, the following points regarding applying neural network to planar perovskite solar cells can be improved. The first point is about input data sampling and preparation. Varying more input parameters such as charge-carrier mobility and energy band levels can allow the artificial neural network to learn the electronic part of the numerical model. Also, a sampling method that produce even data distributions with a broad range can help on generalization of the neural network, so that it does not cater to one specific architecture. Next, it is also essential to optimize the neural network, reducing the training error and prevent over fitting problem. Lastly, introducing the concept of a digital twin—a program that simulates and predicts the photovoltaic's performance with real-time data—will grant the trained neural network on its value-add to experiment.

In this chapter, we train a general neural network model for planar p-i-n typed perovskite solar cells. The objective is to obtain a fast and computational less heavy model compared to the full electronic model, and replace it while keeping the optics part.

## 5.2 Mathematical formulation

We consider a planar perovskite solar cell with the structure shown in Figure 3.1 in Chapter 3, which consists of front- and back-contact layers, hole- and electron-transporting layers, and the perovskite active layer.

In the full optoelectronic model, the main assumptions and characteristics are:

1. The three-dimensional structure of the planar perovskite solar cell is reduced into a one-dimensional model in the  $x-$  direction, under the condition that optical field, electron and hole fluxes in the  $y-$  and  $z-$  direction are negligible.
2. All interfaces are assumed to have negligible surface roughness; all layers are

assumed to be isotropic and homogeneous.

3. Full internal quantum efficiency is assumed in charge carrier generation [14].
4. Light is treated as plane waves that incident normally from the front at interface I, and from the back at interface VII if the device is under bifacial operation.
5. We consider light propagation to be transverse electromagnetic within the coherent layers: all layers of the planar perovskite solar cell except the thick glass layer.
6. Phase elimination method [53] is used to account for incoherency of the thick glass layer.
7. The range of wavelength simulated is from 300 nm to 1200 nm, which covers the absorption range for perovskites with band gaps as low as 1 eV.
8. There is no net surface charge on the interfaces between perovskite layers and the charge carrier transport layers [71].
9. A single trap level, which can effectively describe a deep level trap distribution [72, 73], is assumed in the perovskite layers and the recombination junction.
10. The electrodes, which are current collectors, are assumed to be Ohmic [74].
11. In the perovskite layers, we consider charge carrier generation, radiative recombination, SRH recombination, and Auger recombination, whence the Auger recombination coefficient for electrons and holes are equal; and at the interfaces between the perovskite and the adjacent hole- and electron-transporting layers, interface recombination is accounted for [75].

Detailed mathematical formulations about the full optoelectronic model are described in Chapter 2 and 3, with a flowchart about the input and output parameters shown in Figure 5.1.

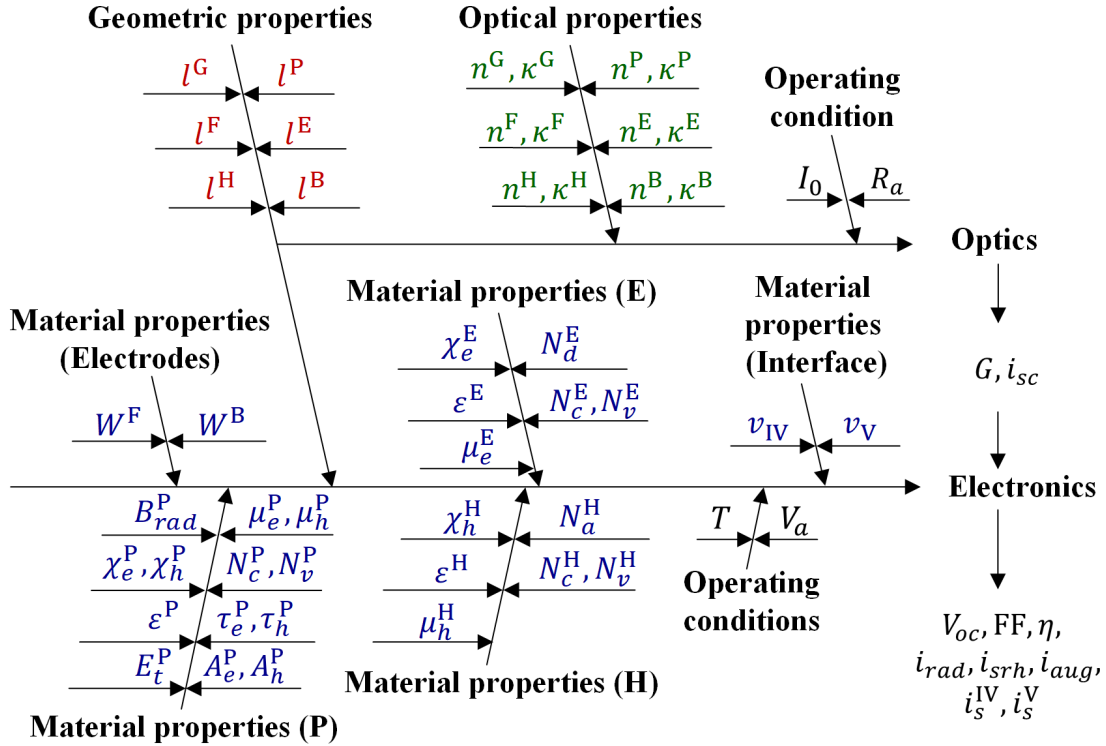


Figure 5.1: Input and output parameters of the full optoelectronic model for a planar perovskite solar cell.

For the coupled model–artificial neural network for the electronics and vectorized matrix calculation for the optics, we adopt mean square errors to quantify the model performance as compared to the results from full optoelectronic model. In essence, the optics part is retained for calculating the short-circuit current density, where as the electronics part has been replaced by three artificial neural networks for the device performances, recombination losses at maximum power point (MPP), and recombination losses at open circuit (OC). Figure 5.2 provides illustrations of the neural networks.

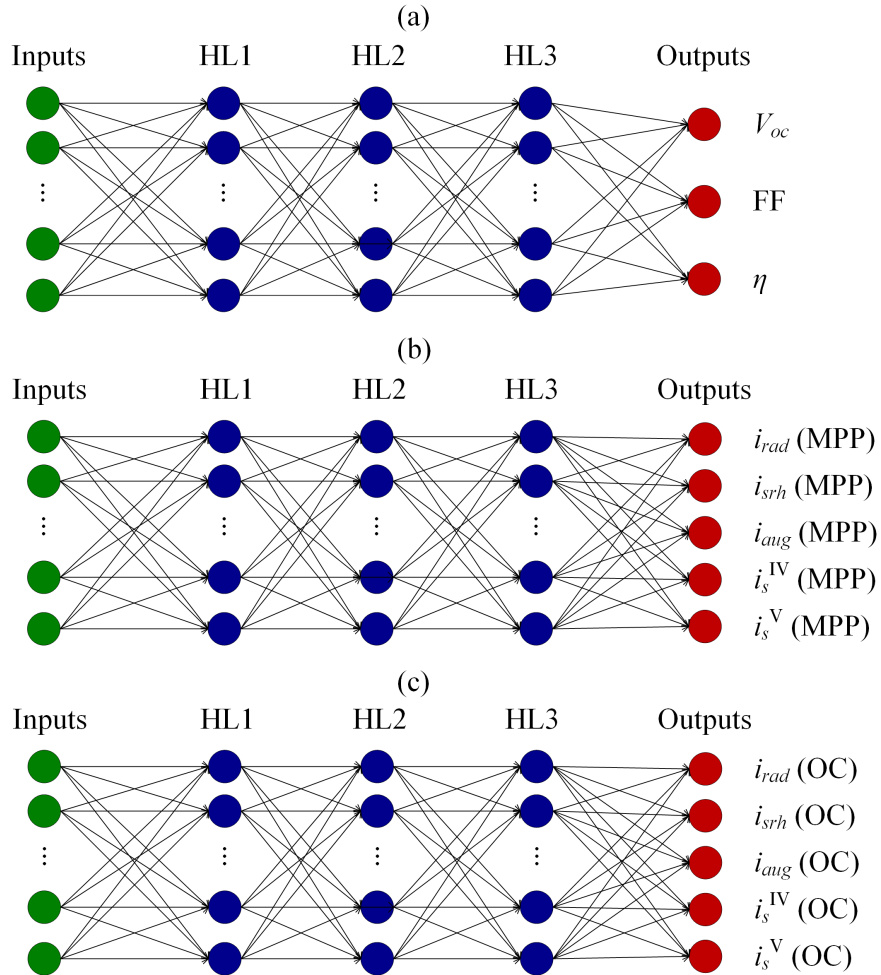


Figure 5.2: Neural network architectures for a planar perovskite solar cell with three hidden layers—HL1, HL2, and HL3, and with the outputs being (a) the device performances, (b) recombination losses at MPP, and (c) recombination losses at OC. Here, not all the nodes in the inputs and hidden layers are shown for the sake of simplicity.

Furthermore, the number of parameters inside a shallow neural network trained by Bayesian regularization [76] is calculated as the summation of the weights and bias components:

$$N_{ANN} = N_W + N_B, \quad (5.1)$$

$$N_W = N_{input} \times N_1 + N_1 \times N_2 + N_2 \times N_3 + N_3 \times N_{output}, \quad (5.2)$$

$$N_B = N_1 + N_2 + N_3 + N_{output}, \quad (5.3)$$

for a neural network with three hidden layers as an example, where  $N_{ANN}$ ,  $N_W$ ,  $N_B$ ,  $N_{input}$ ,  $N_{output}$ ,  $N_1$  to  $N_3$  are the total number of parameters in the neural network, number of

weights, number of bias, number of inputs, number of outputs, and number of neurons in hidden layers 1 to 3, respectively. For a good generalization, the sample size should be at least ten times of the total number of parameters in the neural network [77]. This is known as the Widrow's rule of thumb, which supports the employment of a neural network with one hundred thousand sample size and three hidden layers in the later sections.

For coupling the optics and electronics, we use the average generation rate,  $G_{avg}$ , as an input parameter for the neural network. Here, we assume the short-circuit current density to be from 120 to 360 A m<sup>-2</sup>, which is a wide enough range and can cover the output current densities for most of the planar perovskite solar cells. The average generation rate is calculated based on the short-circuit current density as

$$G_{avg} = \frac{i_{sc}}{el^P}. \quad (5.4)$$

## **5.3 Methodology**

### **5.3.1 Types of neural networks**

Neural networks can be broadly classified into three types: artificial neural networks including multilayer perceptrons, convolutional neural networks and recurrent neural networks. An artificial neural network is the one of the basic algorithms, which is suitable for regression problems. In contrast, convolutional neural networks have significant advantage when treating two-dimensional images with spatial relations among pixels while recurrent neural networks is powerful for time-series data or sequence prediction problems involving multiple output layers. For a regression problem in our case, adopting convolutional or recurrent neural networks might be an overkill. we will thus focus on artificial neural networks for predicting the perovskite solar cell performances. Nevertheless, convolutional, recurrent and deep neural networks can be potential future work with full  $i - V$  curves/characteristics involved.

### 5.3.2 Data preparation

	Lower bound	Upper bound	Units	Scale
<i>Inputs</i>				
$A_{(e,h)}$	-41	-37	$\text{m}^6 \text{s}^{-1}$	Logarithmic
$B_{rad}$	-19	-15	$\text{m}^3 \text{s}^{-1}$	Logarithmic
$\chi_e^E$	4	4.3	eV	Linear
$\chi_e^H$	2	3	eV	Linear
$\chi_e^P$	3.8	4.2	eV	Linear
$\chi_h^E$	5	7	eV	Linear
$\chi_h^H$	5	5.3	eV	Linear
$\chi_h^P$	5.2	5.8	eV	Linear
$\varepsilon^{(\text{H},\text{E})}$	3	6		Linear
$\varepsilon^P$	3	10		Linear
$G_{avg}$	26.878	28.078	$\text{m}^{-4} \text{s}^{-1}$	Logarithmic
$l^{(\text{H},\text{E})}$	20	300	nm	Linear
$l^P$	200	1000	nm	Linear
$\mu_e^{(P,E)}$	-6	-2	$\text{m}^2 \text{V}^{-1} \text{s}^{-1}$	Logarithmic
$\mu_h^{(H,P)}$	-6	-2	$\text{m}^2 \text{V}^{-1} \text{s}^{-1}$	Logarithmic
$N_{(c,v)}^{(\text{H},\text{P},\text{E})}$	22	28	$\text{m}^{-3}$	Logarithmic
$\tau_{(e,h)}$	-8	-2	s	Logarithmic
$v_{(e,h)}$	-28	-22	$\text{m}^4 \text{s}^{-1}$	Logarithmic
$W^B$	4.2	4.4	eV	Linear
$W^F$	4.6	5.0	eV	Linear
<i>Outputs</i>				
$V_{oc}$	0.160	1.564	V	Linear
$\mathfrak{F}$	0.064	0.944		Linear
$\eta$	0.005	0.435		Linear
$i_{rad}(\text{MPP})$	-6.724	2.437	$\text{A m}^{-2}$	Logarithmic
$i_{srh}(\text{MPP})$	-9.744	2.443	$\text{A m}^{-2}$	Logarithmic
$i_{aug}(\text{MPP})$	-9.442	2.445	$\text{A m}^{-2}$	Logarithmic
$i_s^{\text{IV}}(\text{MPP})$	-11.670	2.471	$\text{A m}^{-2}$	Logarithmic
$i_s^{\text{V}}(\text{MPP})$	-11.920	2.471	$\text{A m}^{-2}$	Logarithmic
$i_{rad}(\text{OC})$	-5.818	2.554	$\text{A m}^{-2}$	Logarithmic
$i_{srh}(\text{OC})$	-8.945	2.546	$\text{A m}^{-2}$	Logarithmic
$i_{aug}(\text{OC})$	-7.213	2.555	$\text{A m}^{-2}$	Logarithmic
$i_s^{\text{IV}}(\text{OC})$	-6.956	2.564	$\text{A m}^{-2}$	Logarithmic
$i_s^{\text{V}}(\text{OC})$	-7.312	2.557	$\text{A m}^{-2}$	Logarithmic

Table 5.1: Input and output parameters collected from the full optoelectronics model for training of neural network.

To train an artificial neural network that can be applied to various p-i-n typed perovskite solar cells, we include in total thirty-one parameters as the input, and they are summarized in Table 5.1 with lower and upper bounds. The bounds are based on literature

values [15, 17, 75, 78, 79], and are set to be wide for a general model for devices with various performances. Here, the trap energy level for SRH recombination is fixed to be 0.16 eV [80] for perovskite materials. When the lower and upper bounds have more than one order of magnitude difference, we apply a logarithmic scale during data preparation so that the data are not clustered towards one side of the bounds. For the input data sampling, we prepare one hundred thousand samples based on Latin Hypercube sampling method. This set of data is employed as the training data. Another three sets of data, all with a sampling size of ten thousand but different seeds, are prepared as the testing data (testing data A), validation data, and second set of testing data (testing data B), respectively. In addition, after the data are sampled, we remove samples that do not allow smooth charge-carrier transport due to alignments of the energy bands; i.e.

$$E_v^P < E_v^H < W^F, \quad (5.5)$$

$$W^B < E_c^E < E_c^P. \quad (5.6)$$

The inputs are imported into the optoelectronic model, and thirteen outputs are generated, including the open-circuit voltage, fill factor, power conversion efficiency and various recombination losses, and they are shown in Table 5.1 as well. As the input and output parameters can have large order of magnitude differences between each other, we normalize all inputs and outputs to be within -1 to 1, which can help train the neural networks more efficiently. Illustrations of the final inputs and outputs can be found in Figure 5.3 in the later sections.

### **5.3.3 Training of neural network**

Training of the neural networks are conducted in Matlab with Bayesian regularization [76], which automatically updates and optimizes the weights and bias during training. Instead of dividing samples randomly, we fix the training data (one hundred thousand samples), validating data (ten thousand samples) and testing data (ten thousand samples, testing data A). This is to help ensure even sampling of the data and obtain consistent

training results. The number of hidden layers is chosen to be three. The transfer function at the output layer is set to be linear (purelin). The maximum number of failures—number of successive iterations when the mean squared error for the validating data increases while that for the training data increases—is set to be ten to prevent over fitting. The rest of the hyperparameters, namely the number of neurons and transfer functions in hidden layers, initial learning rate, initial momentum, number of epochs and minimum gradient are found from Bayesian optimization.

### 5.3.4 Optimization of hyperparameters

We employ the in-built Bayesian optimization in Matlab which efficiently utilizes a Gaussian process regression to find the optimized hyperparameters. The hyperparameters and their bounds are summarized below. For the hidden layer sizes, the minimum and maximum number of neurons are set to be 2 and 100, respectively. The maximum number of epochs is 500. The initial learning rate, minimum gradient, and momentum have minimum values of 0.01,  $10^{-8}$ , and 0.5, respectively, and maximum values of 1,  $10^{-6}$ , and 0.98, respectively. For the transfer functions in the three hidden layers, we employ the following commonly found transfer functions in Matlab for classification problems: hyperbolic tangent sigmoid (tansig), radial basis (radbas), log-sigmoid (logsig), and linear (purelin). Regarding termination of the optimization, the returned objective function is set to be the mean squared error of the training data in the neural network, and the maximum number of objective iterations is  $10^4$ , the maximum time is three days, with the number of initial seed points being 500. The Bayesian optimization is coupled with the neural network training to find the best performing neural network model.

## 5.4 Results and discussions

### 5.4.1 Visualization of data

We look at the data distributions for the inputs and outputs, which are crucial in neural network developments.

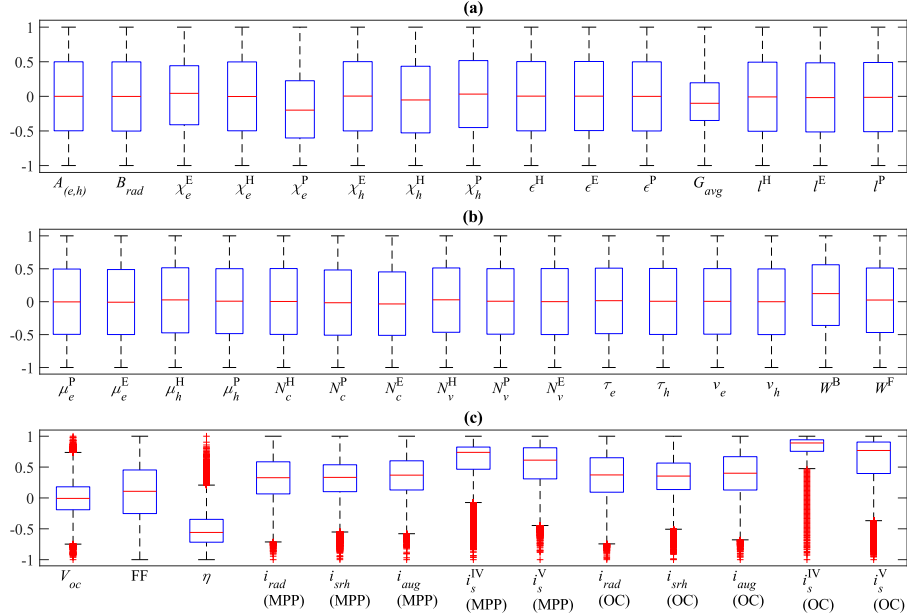


Figure 5.3: Distributions of the inputs (a-b) and outputs (c) parameters. Here, all inputs and outputs are normalized between -1 and 1. The horizontal red line inside of each box denotes the sample median, the top and bottom edge of each box represents the upper and lower quartiles, and the red plus signs are the outliers with values more than 1.5 times of the interquartile range away from the box.

As shown in Figure 5.3(a) and (b), most of the input data are evenly distributed with the median being 0 and the interquartile range from -0.5 to 0.5, except  $G_{avg}$  and the energy band levels  $\chi$  and work function  $W$ . For  $G_{avg}$ , we attribute the narrower interquartile to the calculation of  $G_{avg}$  in Equation 5.4. The generation rate is calculated based on evenly distributed short-circuit current densities and perovskite layer thicknesses. Regarding the energy levels, since we have removed the samples that may cause misalignment of energy levels, their distributions are not exactly even. Nevertheless, all input data are close to uniformly distributed data set without outliers, indicating a successful sampling of inputs.

For the output shown in Figure 5.3(c), the open-circuit voltage is close to a normal distribution, the fill factor is close to an even distribution, the power conversion efficiency is positively skewed, and the recombination losses are negatively skewed. The maximum power conversion efficiency reached is 43.5% (see Table 5.1), which has exceeded the SQ limit, and identified as an outlier. Nonetheless, since our objective is to have a general neural network model, the data points that are larger than the SQ limit can be considered as bifacial equivalent PCE for bifacial devices. From the distributions of the recombination losses, we find the losses at interface IV–between hole-transporting layer and perovskite layer—are more negatively skewed at both MPP and OC compared with the losses at interface V–between electron-transporting and perovskite layer. This can be due to the energy band levels and high charge carrier concentration at the interface.

#### 5.4.2 Neural network performance

The performance of the three optimized neural networks for predicting device performances ( $V_{oc}$ , FF,  $\eta$ ), recombination losses at MPP and OC are shown and discussed in this section, which also acts as verification of the neural networks with the full opto-electronic model. We adopt the coefficient of correlation and the means squared error to quantify the quality of the neural networks.

### 5.4.2.1 Baseline model: predicting all outputs

Hyperparameters	Results	Neural network performances	Results
Number of epoch	165	Coefficient of correlation (training data)	0.99910
Initial learning rate	0.0122	Coefficient of correlation (validating data)	0.99828
Minimum gradient	$8.1763 \times 10^{-8}$	Coefficient of correlation (testing data A)	0.99834
Momentum	0.8625	Mean squared error (training data)	$4.190 \times 10^{-4}$
HL1 transfer function	tansig	Mean squared error (testing data)	$7.150 \times 10^{-4}$
HL2 transfer function	radbas	$N_{ANN}$	9162
HL3 transfer function	logsig		
$N_1$	88		
$N_2$	39		
$N_3$	54		

Table 5.2: Optimized hyperparameters and neural network performances for predicting all thirteen device performances ( $V_{oc}$ , FF,  $\eta$ , and recombination losses at MPP and OC). The mean squared errors are calculated based on the normalized data.

Before moving on to train the three neural network with structures illustrated in Figure 5.2, we adopt similar methodology, optimize and train a baseline reference model with all outputs included, namely  $V_{oc}$ , FF,  $\eta$ , and ten recombination losses at MPP and OC. Here, one set of data with ten thousand samples is adopted as the training data, and another two sets of data, each with one thousand samples and different seed number, are employed as validation and testing data, respectively. The found hyperparameters and neural network performances are summarized in Table 5.2, and the comparisons between the true and predicted values are shown in Figure 5.4 to 5.6.

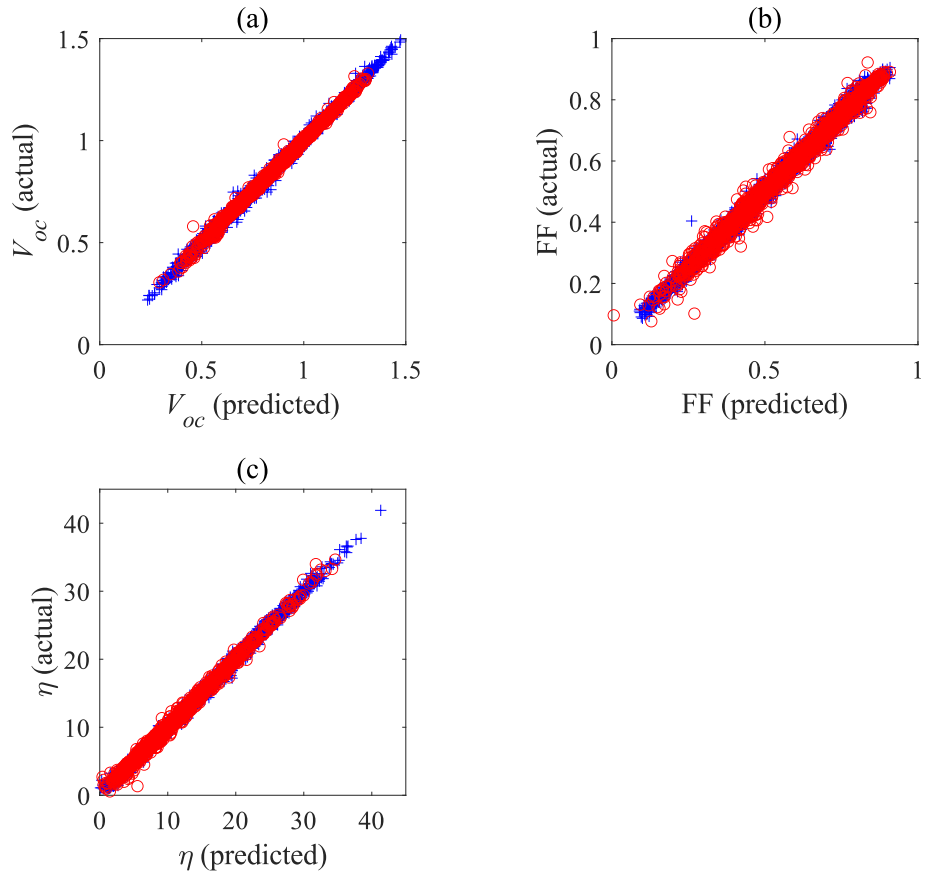


Figure 5.4: Actual values from full optoelectronic model and results from baseline neural network prediction for the (a) open-circuit voltage, (b) fill factor, and (c) power conversion efficiency. The blue plus signs and red circles represent the training data and testing data, respectively.

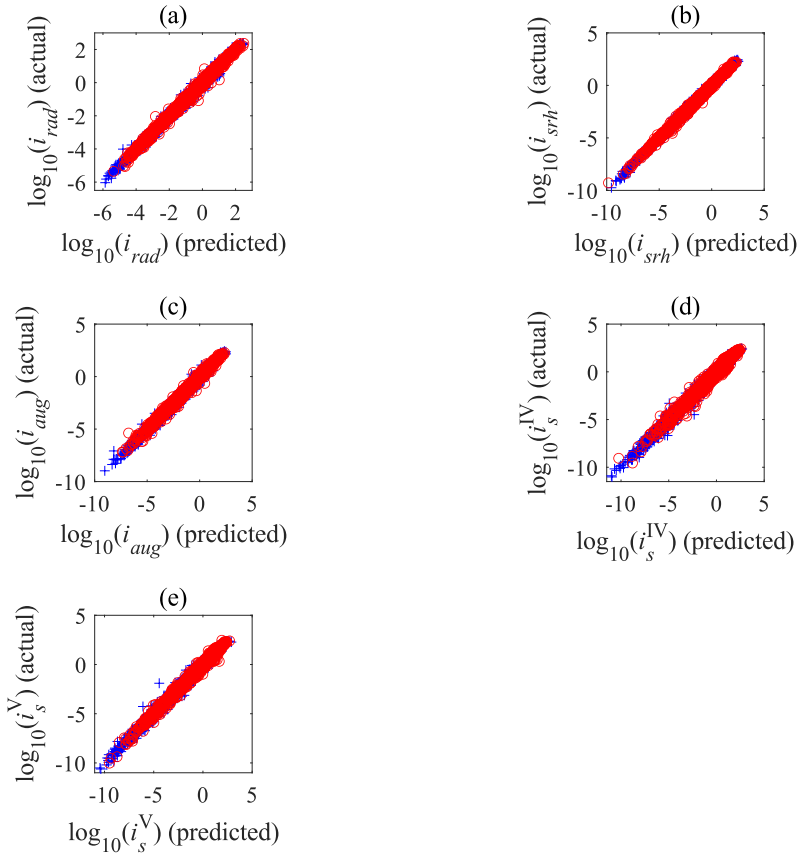


Figure 5.5: Actual values from full optoelectronic model and results from baseline neural network prediction for the (a) radiative recombination loss, (b) SRH recombination loss, (c) auger recombination loss, (d) surface recombination loss at interface IV, and (e) surface recombination loss at interface V at the MPP. The blue plus signs and red circles represent the training data and testing data, respectively.

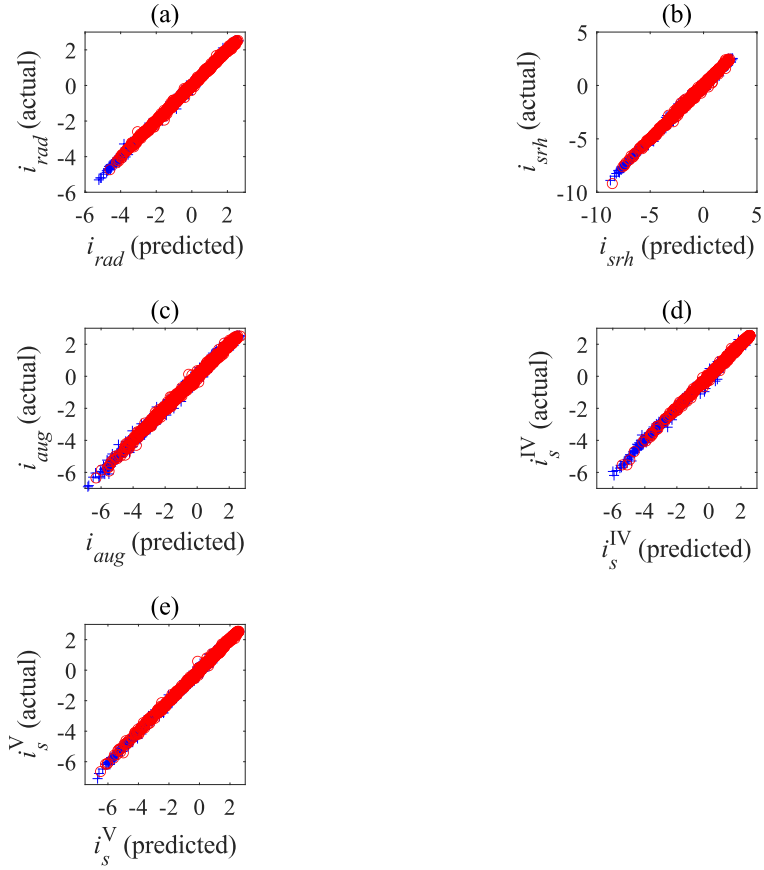


Figure 5.6: Actual values from full optoelectronic model and results from baseline neural network prediction for the (a) radiative recombination loss, (b) SRH recombination loss, (c) auger recombination loss, (d) surface recombination loss at interface IV, and (e) surface recombination loss at interface V at the OC. The blue plus signs and red circles represent the training data and testing data, respectively.

The baseline neural network is capable of predicting the outputs with mean squared errors less than  $10^{-3}$  with no obvious outliers. However, we find the testing error is about 70% higher than the training error, indicating the rise of over fitting problem when treating new and unseen data. Therefore, we propose a strategy to train three neural networks separately, each with one group of distinct outputs as shown in Figure 5.2.

There are a few advantages for adopting this approach. Firstly, by reducing the number of outputs, it is expected that the performances of the neural networks to improve. Secondly, the usage of the neural networks has become more specific. For predicting key metrics of a perovskite solar cell, only one neural network predicting  $V_{oc}$ , FF and PCE will be used, while the other two neural networks can be employed to help prob-

lems related to loss analysis. This also makes retraining of the first neural network with new experiment and simulation data easier, since recombination losses are hard to be measured experimentally.

Last but not least, it is reasonable to have these three groups of outputs, which look at different aspects of  $i - V$  characteristics.  $V_{oc}$ , FF and PCE focus on the  $i - V$  curve itself, providing key information on the short-circuit current density, maximum power generation, and open-circuit voltage point. For the five recombination losses at MPP, they are outputs that need to be optimized for higher FF, and they focus on one specific point in the  $i - V$  curve. Regarding the recombination losses at OC, they play a crucial role in bringing down the current to zero, and the sum of the losses will be equal to the short-circuit current density.

In addition, the number of neural network parameter is found to be 9162, indicating the need for more data points according to Widrow's rule of thumb [77]. Therefore, we train three neural networks separately in the next subsections, with training data comprising one hundred thousand samples. This larger data size is expected to alleviate the problem of over fitting as well.

#### **5.4.2.2 Predicting device performance ( $V_{oc}$ , FF, $\eta$ )**

Together with the short-circuit current density predicted from the optical model, creating a neural network for the electronic part that can efficiently predict the performance matrix—open-circuit voltage, fill factor, and PCE—of p-i-n perovskite solar cells could add extra values during device characterization; that is, provide a method to quickly calibrate the electronic parameters and thus find out the rooms for improvements.

Hyperparameters	Results	Neural network performances	Results
Number of epoch	266	Coefficient of correlation (training data)	0.99943
Initial learning rate	0.0118	Coefficient of correlation (validating data)	0.99902
Minimum gradient	$7.8261 \times 10^{-8}$	Coefficient of correlation (testing data A)	0.99897
Momentum	0.5395	Mean squared error (training data)	$2.307 \times 10^{-4}$
HL1 transfer function	tansig	Mean squared error (testing data B)	$3.362 \times 10^{-4}$
HL2 transfer function	logsig	$N_{ANN}$	8722
HL3 transfer function	radbas		
$N_1$	65		
$N_2$	55		
$N_3$	51		

Table 5.3: Optimized hyperparameters and neural network performances for predicting the device performance ( $V_{oc}$ , FF,  $\eta$ ).

After Bayesian optimization of the hyperparameters for the neural network in Figure 5.2(a), the found hyperparameters and neural network performance are summarized in Table 5.3. The coefficients of correlation are close to 1 with mean squared errors at an order of magnitude of  $10^{-4}$  for both training and testing data. These mean squared errors are considered to be small as compared to the normalized output data from -1 to 1. Figure 5.7(a) to (c) show the differences between the predicted and actual open-circuit voltage, fill factor, and PCE, respectively, and the predicted and actual data are close to each other. Comparing with the baseline model, the decrease in the mean squared errors are significant, especially the errors for the unseen data, which has been reduced by more than 50%.

We notice that among the one hundred thousand samples in the training data, there are still a small amount (less than 10 samples) that do not meet the expected performance for predicting the fill factor. This could be because of numerical issues. Nevertheless, this sample size is less than 0.1% of the total training data, indicating good overall performance of the neural network.

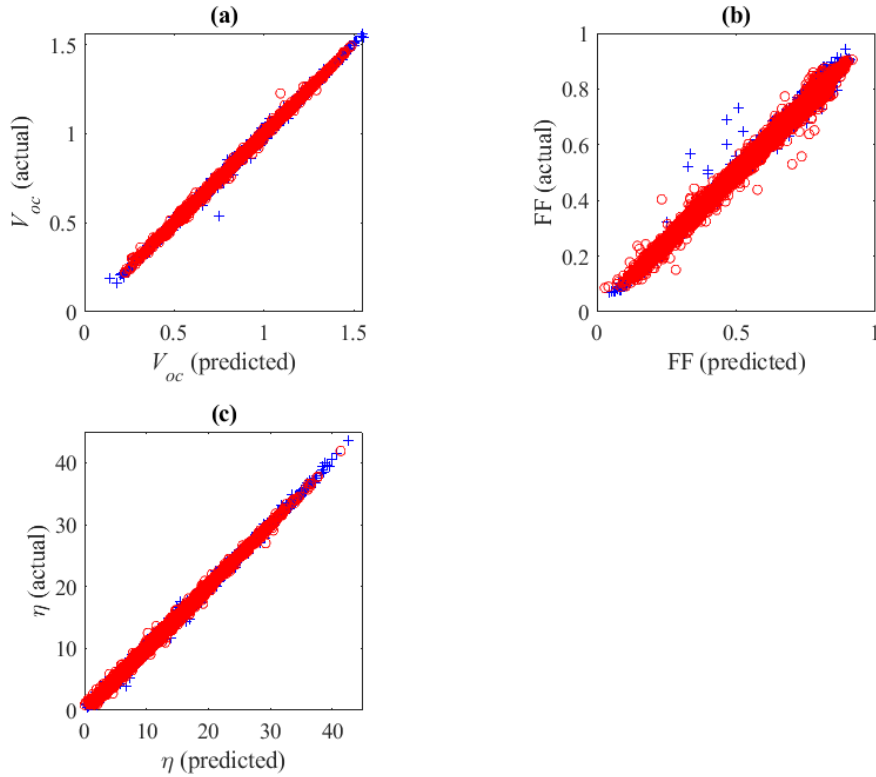


Figure 5.7: Actual values from full optoelectronic model and results from neural network prediction for the (a) open-circuit voltage, (b) fill factor, (c) power conversion efficiency. The blue plus signs and red circles represent the training dataset and testing dataset B, respectively.

### 5.4.2.3 Predicting recombination losses at MPP

Hyperparameters	Results	Neural network performances	Results
Number of epoch	313	Coefficient of correlation (training data)	0.99806
Initial learning rate	0.0135	Coefficient of correlation (validating data)	0.99773
Minimum gradient	$7.0826 \times 10^{-8}$	Coefficient of correlation (testing data A)	0.99775
Momentum	0.7267	Mean squared error (training data)	$4.8924 \times 10^{-4}$
HL1 transfer function	logsig	Mean squared error (testing data B)	$5.8206 \times 10^{-4}$
HL2 transfer function	radbas	$N_{ANN}$	6895
HL3 transfer function	tansig		
$N_1$	61		
$N_2$	39		
$N_3$	56		

Table 5.4: Optimized hyperparamters and neural network performances for predicting the recombination losses at MPP.

Next, other than the device performance, a neural network that can predict the recombination losses can bring more insights during device characterization. Since artificial neural network models are much more computational efficient than common optoelectronic models, conducting quick device calibration and loss analysis can be made possible. The optimized hyperparamters and neural network performance for the network architecture in Figure 5.2(b) for predicting the recombination losses at MPP are shown in Table 5.4.

The neural network demonstrates a coefficient of correlation of close to 1, small mean squared error (around  $5 \times 10^{-4}$  with normalized data from -1 to 1), together with predicted and actual values that are close to each other as illustrated in Figure 5.8. Although the training error is slightly higher than that of the baseline model, the testing error for unseen data has been reduced and approaches the training error, indicating smaller possibility for over fitting problem.

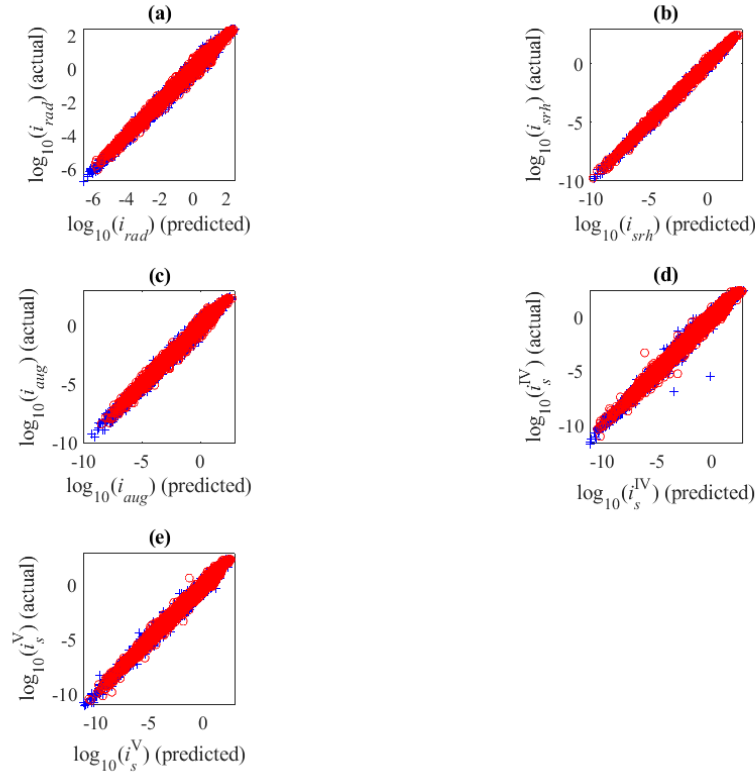


Figure 5.8: Actual values from full optoelectronic model and results from neural network prediction for the (a) radiative recombination loss, (b) SRH recombination loss, (c) Auger recombination loss, (d) interfacial recombination loss at IV, (e) interfacial recombination loss at V at MPP. The blue plus signs and red circles represent the training dataset and testing dataset B, respectively.

#### 5.4.2.4 Predicting recombination losses at OC

Hyperparameters	Results	Neural network performances	Results
Number of epoch	276	Coefficient of correlation (training data)	0.99984
Initial learning rate	0.0194	Coefficient of correlation (validating data)	0.99983
Minimum gradient	$6.0789 \times 10^{-8}$	Coefficient of correlation (testing data A)	0.99974
Momentum	0.8734	Mean squared error (training data)	$5.0788 \times 10^{-5}$
HL1 transfer function	logsig	Mean squared error (testing data B)	$5.0144 \times 10^{-5}$
HL2 transfer function	radbas	$N_{ANN}$	8163
HL3 transfer function	tansig		
$N_1$	40		
$N_2$	46		
$N_3$	96		

Table 5.5: Optimized hyperparamters and neural network performances for predicting the recombination losses at OC.

The recombination losses at MPP could provide information on how to improve the fill factor. On the other hand, having one more neural network that can predict the recombination losses at OC could help suggest pathways for enhancing the open-circuit voltage. For the third neural network (see Figure 5.2(c)), the optimized hyperparameters and neural network performance are summarized in Table 5.5.

We note that the neural network for the recombination losses at OC, compared to previous two, has the best coefficients of correlation and lowest mean squared errors. Figure 5.9 compares the predicted and actual values, which excellently agree with each other except three outliers for the interfacial recombination losses at interface IV (see Figure 5.9(d)). We attribute these outliers to numerical issues from a huge data with one hundred thousand sample size. Moreover, the errors are one order of magnitude smaller compared to the baseline model.

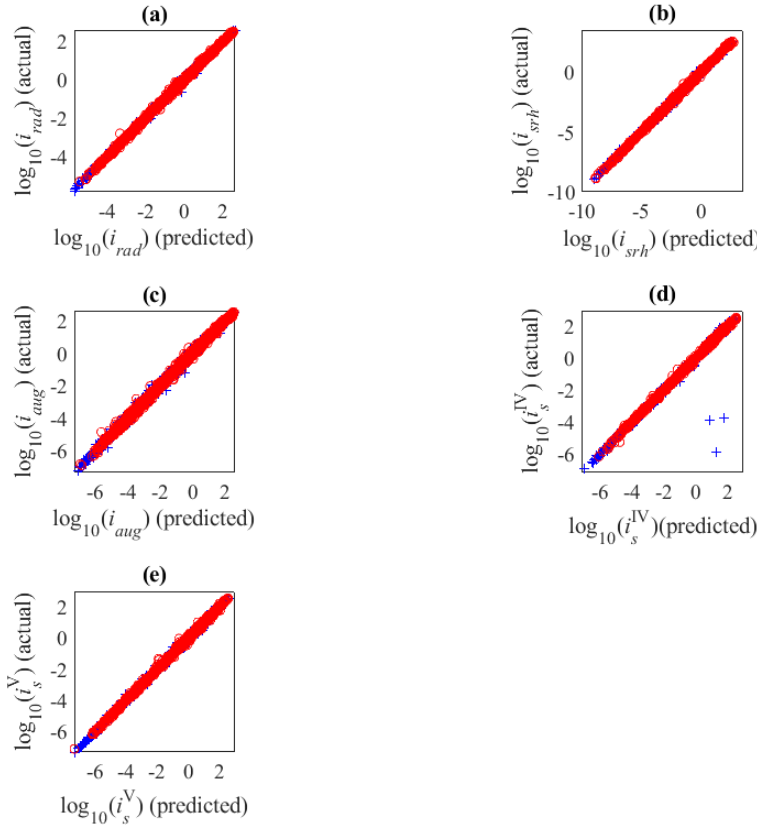


Figure 5.9: Actual values from full optoelectronic model and results from neural network prediction for the (a) radiative recombination loss, (b) SRH recombination loss, (c) Auger recombination loss, (d) interfacial recombination loss at IV, (e) interfacial recombination loss at V at OC. The blue plus signs and red circles represent the training dataset and testing dataset B, respectively.

Moreover, with the found optimal number of neurons in the hidden layers, the total parameters inside the neural networks are calculated to be 8722, 6895 and 8163 for the three neural networks with Eq. 5.1. According to Widrow's rule of thumb [77], the preferred sample size is less than one hundred thousand, indicating our training data size is sufficient. Also, this result indicates that if a larger number of hidden layers; i.e. four hidden layers, is adopted, an one hundred thousand sample size may not be sufficient.

### 5.4.3 Calibration and validation

In solar cell applications, the key metrics are the  $i_{sc}$ ,  $V_{oc}$ , FF and PCE, and they are commonly adopted to help compare the performances among various devices, instead of looking at full  $i - V$  curves. After testings and verification, our first trained neural

network model could be applied to validate with a perovskite solar cell, conduct characterization of physical parameters and estimate the recombination losses together with the other two neural network models.

To calibrate and validation the model, we take three literature reported perovskite solar cells (Cells A [5], B [5], and C [27]), and source the corresponding material parameters from literature. The remaining unknown parameters regarding device recombination rates are either assumed or fitted. In detail, a list of parameters is presented in Table 5.6 to 5.8 for Cells A to C, followed by assumptions and procedures for calibration.

	Cell A	Units
$A_{(e,h)}$	$1 \times 10^{-41}$ (assumed)	$\text{m}^6 \text{s}^{-1}$
$B_{rad}$	$3.03 \times 10^{-18}$ (fitted)	$\text{m}^3 \text{s}^{-1}$
$\chi_e^E$	4.2 [81]	eV
$\chi_e^H$	2.32 [82]	eV
$\chi_e^P$	4.02 [83]	eV
$\chi_h^E$	5.94 [81]	eV
$\chi_h^H$	5.27 [82]	eV
$\chi_h^P$	5.77 [83]	eV
$\epsilon^{(H,E)}$	3 [84], 3.03 [42]	
$\epsilon^P$	5.56 [80]	
$G_{avg}$	$2.84 \times 10^{27}$ (From Eq. 5.4)	$\text{m}^{-4} \text{s}^{-1}$
$l^{(H,E)}$	20, 20 (SEM)	nm
$l^P$	380 (SEM)	nm
$\mu_e^{(P,E)}$	$5.5 \times 10^{-4}$ [83], $1.6 \times 10^{-4}$ [25]	$\text{m}^2 \text{V}^{-1} \text{s}^{-1}$
$\mu_h^{(H,P)}$	$1 \times 10^{-6}$ [85], $5.5 \times 10^{-4}$ [83]	$\text{m}^2 \text{V}^{-1} \text{s}^{-1}$
$N_c^{(H,P,E)}$	$5 \times 10^{25}$ [86], $1.7 \times 10^{22}$ [87], $1 \times 10^{22}$ [88]	$\text{m}^{-3}$
$N_v^{(H,P,E)}$	$5 \times 10^{25}$ [86], $1.8 \times 10^{25}$ [75], $1 \times 10^{22}$ [88]	$\text{m}^{-3}$
$\tau_{(e,h)}$	$1 \times 10^{-5}$ (assumed)	s
$v_{(e,h)}$	$3.39 \times 10^{-27}$ , $4.04 \times 10^{-24}$ (fitted)	$\text{m}^4 \text{s}^{-1}$
$W^B$	4.3 [89]	eV
$W^F$	4.9 [90]	eV
<i>Performances</i>		
$V_{oc}$	1.21	V
$\mathfrak{F}$	0.768	
$\eta$	0.161	

Table 5.6: Parameters for the calibration of the first neural network model for Cell A [5]. Here, SEM stands for scanning electron microscopy.

	Cell B	Units
$A_{(e,h)}$	$1 \times 10^{-41}$ (assumed)	$\text{m}^6 \text{s}^{-1}$
$B_{\text{rad}}$	$6.79 \times 10^{-18}$ (fitted)	$\text{m}^3 \text{s}^{-1}$
$\chi_e^{\text{E}}$	4.2 [81]	eV
$\chi_e^{\text{H}}$	3.2 [91]	eV
$\chi_e^{\text{P}}$	3.83 [92]	eV
$\chi_h^{\text{E}}$	5.94 [81]	eV
$\chi_h^{\text{H}}$	5 [91]	eV
$\chi_h^{\text{P}}$	5.05 [92]	eV
$\varepsilon^{(\text{H,E})}$	3 [84], 3.03 [42]	
$\varepsilon^{\text{P}}$	6.17 [80]	
$G_{\text{avg}}$	$2.28 \times 10^{27}$ (From Eq. 5.4)	$\text{m}^{-4} \text{s}^{-1}$
$l^{(\text{H,E})}$	80, 20 (SEM)	nm
$l^{\text{P}}$	860 (SEM)	nm
$\mu_e^{(\text{P,E})}$	$7.9 \times 10^{-3}$ [5], $1.6 \times 10^{-4}$ [25]	$\text{m}^2 \text{V}^{-1} \text{s}^{-1}$
$\mu_h^{(\text{H,P})}$	$7.7 \times 10^{-5}$ [93], $7.9 \times 10^{-3}$ [5]	$\text{m}^2 \text{V}^{-1} \text{s}^{-1}$
$N_c^{(\text{H,P,E})}$	$3 \times 10^{26}$ [93], $1.7 \times 10^{22}$ [87], $1 \times 10^{22}$ [88]	$\text{m}^{-3}$
$N_v^{(\text{H,P,E})}$	$3 \times 10^{26}$ [93], $1.8 \times 10^{25}$ [75], $1 \times 10^{22}$ [88]	$\text{m}^{-3}$
$\tau_{(e,h)}$	$1 \times 10^{-5}$ (assumed)	s
$v_{(e,h)}$	$8.91 \times 10^{-23}$ , $6.01 \times 10^{-27}$ (fitted)	$\text{m}^4 \text{s}^{-1}$
$W^{\text{B}}$	4.3 [89]	eV
$W^{\text{F}}$	4.9 [90]	eV
<i>Performances</i>		
$V_{\text{oc}}$	0.831	V
$\mathfrak{F}$	0.808	
$\eta$	0.211	

Table 5.7: Parameters for the calibration of the first neural network model for Cell B [5].

	Cell C	Units
$A_{(e,h)}$	$1 \times 10^{-41}$ (assumed)	$\text{m}^6 \text{s}^{-1}$
$B_{rad}$	$5.48 \times 10^{-18}$ (fitted)	$\text{m}^3 \text{s}^{-1}$
$\chi_e^E$	4.2 [81]	eV
$\chi_e^H$	2.22 [94]	eV
$\chi_e^P$	3.87 [95]	eV
$\chi_h^E$	5.94 [81]	eV
$\chi_h^H$	5.2 [94]	eV
$\chi_h^P$	5.66 [95]	eV
$\varepsilon^{(H,E)}$	11.7, 3 [78]	
$\varepsilon^P$	5.56 [78]	
$G_{avg}$	$4.14 \times 10^{27}$ (From Eq. 5.4)	$\text{m}^{-4} \text{s}^{-1}$
$l^{(H,E)}$	35, 30 (SEM)	nm
$l^P$	270 (SEM)	nm
$\mu_e^{(P,E)}$	$5.5 \times 10^{-4}$ [83], $1.6 \times 10^{-4}$ [96]	$\text{m}^2 \text{V}^{-1} \text{s}^{-1}$
$\mu_h^{(H,P)}$	$2.8 \times 10^{-4}$ [97], $5.5 \times 10^{-4}$ [83]	$\text{m}^2 \text{V}^{-1} \text{s}^{-1}$
$N_c^{(H,P,E)}$	$1 \times 10^{24}$ [98], $1.7 \times 10^{22}$ [78], $1 \times 10^{22}$ [88]	$\text{m}^{-3}$
$N_v^{(H,P,E)}$	$1 \times 10^{24}$ [98], $6.9 \times 10^{22}$ [78], $1 \times 10^{22}$ [88]	$\text{m}^{-3}$
$\tau_{(e,h)}$	$1 \times 10^{-5}$ (assumed)	s
$v_{(e,h)}$	$9.38 \times 10^{-26}$ , $2.72 \times 10^{-25}$ (fitted)	$\text{m}^4 \text{s}^{-1}$
$W^B$	4.3 [89]	eV
$W^F$	4.9 [90]	eV
<i>Performances</i>		
$V_{oc}$	1.26	V
$\mathfrak{F}$	0.791	
$\eta$	0.178	

Table 5.8: Parameters for the calibration of the first neural network model for Cell C [27].

We find the parameters  $B_{rad}$ ,  $v_e$ , and  $v_h$  for each cell by minimizing the following mean squared error (MSE):

$$\text{MSE} = \frac{(\hat{V}_{oc} - V_{oc}^{exp})^2 + (\hat{\mathfrak{F}} - \mathfrak{F}^{exp})^2 + (\hat{\eta} - \eta^{exp})^2}{3}, \quad (5.7)$$

where  $\hat{V}_{oc}$ ,  $\hat{\mathfrak{F}}$ , and  $\hat{\eta}$  are the normalized open circuit voltage, FF and PCE, respectively. Here, The particle swarm optimization algorithm is employed for this optimization problem in Matlab. Default option with a swarm size of two hundred is applied.

Here, certain assumptions are made. The auger recombination coefficients are set to

be at the lower bound by assuming that auger recombination is not the dominant loss channel. The charge carrier lifetimes for electrons and holes are equal to each other, and assumed to be about  $10^{-5}$  s [99]. Indeed, charge carrier lifetime could be found from experiment, but could vary with perovskite film quality [87]. As such, this value is pre-assumed here and could be fixed after measurements. With these assumptions, the number of fitting parameters is reduced to three.

After calibration, our neural network model predicts the  $V_{oc}$ , FF and PCE to be 1.21 V, 0.769, 0.161 for Cell A, 0.834 V, 0.809, 0.210 for Cell B, and 1.26 V, 0.792, 0.177 for Cell C. The corresponding MSEs are  $4.87 \times 10^{-7}$ ,  $1.53 \times 10^{-5}$ , and  $7.85 \times 10^{-6}$ , respectively. The time taken for each calibration is about 24 s (wall-clock time). The trained neural network models, can then be used for fast device characterization, predicting key device performances and estimating recombination losses.

To validate the model, we import the parameters in Table 5.6 to 5.8 back to Comsol to generate the  $i - V$  curves, and compare with experiments. Figure 5.10 depicts the differences among simulated and experimental  $i - V$  curves. We notice that although there are good agreements among most of the current-voltage points, some simulated points close to the MPP shows differences compared to experiments—around maximum absolute errors of 0.1 V and  $30 \text{ A/m}^2$  when looking at the  $x-$  and  $y-$  axis in Figure 5.10, respectively. This could be due to the difficulty in locating the MPP position with limited swarm size and information on the  $i - V$  curve. Nevertheless, consider the small MSEs for the predicted device performances around order of magnitude of  $10^{-7}$  to  $10^{-5}$ , as well as errors and uncertainty that can arise from training of neural network and model calibration, the model demonstrates reasonable capability in predicting device performances.

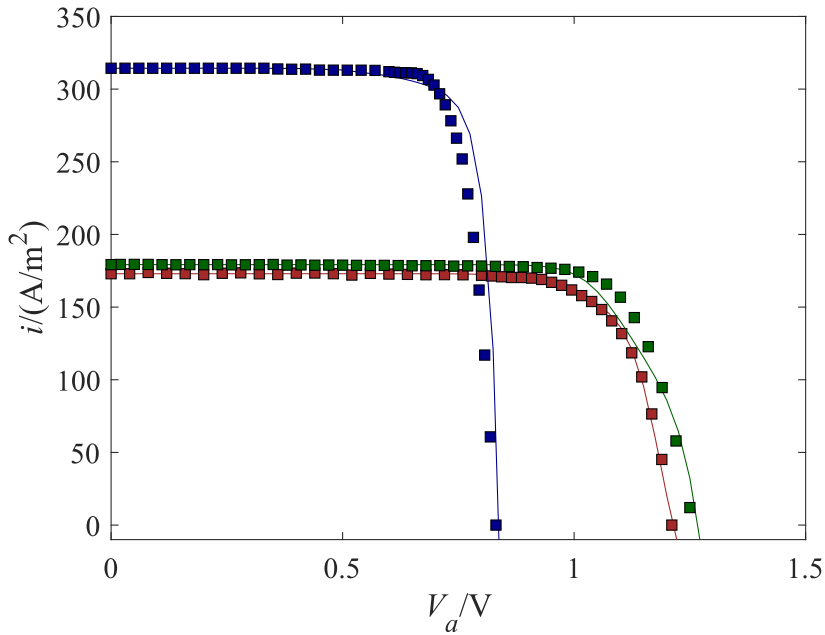


Figure 5.10: Simulated (lines) and experimental (symbols)  $i - V$  curves for Cells A (red), B (blue) and C (green).

A key advantage of this neural network model is the time taken for calibration and characterization, a 24 s calibration time allows rapid predictions that can provide information on influential layers and dominant recombination losses. In this way, continuous adjustments on device structure can be done. In order to further improve the neural network performances towards digital twins applications, methodologies such as training with k-fold cross validation, including extra current-voltage points as inputs, and switch to convolutional neural network for the full  $i - V$  curves could be used, and they are potential future work.

In terms of scalability, the trained neural network has a wide input and output parameter bounds as shown in Table 5.1, including material properties, recombination coefficients, layer thicknesses. As such, the model can account for improved properties of thin-film layers and newer materials. The neural network model is suitable for bifacial devices as well. It acts as a stand-alone replacement of the electronics model, and the optics part can be modeled with our matrix method or directly calculated according to Eq. 5.4. In addition, since the optics part is segregated, the neural network can be applied to 4T perovskite-on-perovskite tandem solar cells by predicting the performances

of the subcells separately. Once more experimental or simulated data are available, re-training of the model can be done by either adopting the current model as starting point, or combining the current model with newly trained models.

On the other hand, the current model can only be applied to a p-i-n structured perovskite solar cell since the neural network is trained based on data from p-i-n structured perovskite solar cells, which is a main disadvantage of the model. By adding in new data that consider n-i-p structured devices, retraining of the neural network can help solve this problem. Still, for 2T tandem devices, new data and model need to be prepared and trained.

## 5.5 Summary

Through replacing the electronic part in the optoelectronic model with artificial neural network for planar p-i-n structured perovskite solar cells, this coupled model enables efficient prediction of the device performances and recombination losses. The hyperparameters for training these neural network models have been optimized through a Bayesian optimization and the optimized neural networks can predict the wanted results with means squared errors lower than  $10^{-3}$ . By adopting the neural network models during device characterization, when measuring the  $i - V$  characteristics, device calibration, estimation of electronic parameters, sensitivity and loss analysis, and optimizations of device performances could be conducted more efficiently compared to using optoelectronic models. The device architecture can then be improved based on the simulation results. An iterative process that combines device fabrication and simulations will allow continuous developments of the perovskite solar cells, which places the coupled neural networks with optics a valuable tool towards digital twin applications.

# Chapter 6

## 2T perovskite-on-perovskite tandem solar cells

We develop an optoelectronic model for a 2T perovskite-on-perovskite tandem solar cell comprising a top cell, a bottom cell, and an interconnecting layer in between that connects the two sub-cells in series electrically. In short, the model considers incoherent and coherent light propagation in the glass and thin-film layers respectively, as well as charge carrier transport, generation, and recombination. After calibrating the model to the state of the art 2T perovskite-on-perovskite tandem solar cell with an efficiency of 24.5%, we first focus on the interconnecting layer, study the current matching behavior and S-shaped current-voltage curve. Next, the light interference effect is investigated. Layer thicknesses are adjusted to increase the short circuit current. From a loss analysis, the leading order recombination channels are the surface and SRH recombinations. Moreover, we show that the PCE of this calibrated tandem model can reach 30.5% by adjusting the layer thicknesses, increasing carrier mobility, and reducing recombination loss. Finally, after switching to bifacial operation, the model predicts a PCE of around 35%.

## 6.1 Introduction

In this work, based on the mathematical formulations for a single-junction perovskite solar cell in Chapter 2 and 3, we present an optoelectronic model for a 2T perovskite-on-perovskite tandem solar cell that couples the top and bottom sub-cells with an interconnecting layer in between. The model considers key characteristics including the light interference effects, recombination in the bulk perovskite layers, the interconnecting layer, and at the interfaces. Model calibration and validation are conducted with the state-of-the-art 2T perovskite-on-perovskite tandem solar cell of 24.5% PCE (backward sweep) from Lin *et al.* [5]. Since the 2T perovskite-on-perovskite tandem solar cells adopted for model calibration have inverted structures for both top and bottom sub-cells, this work focus on this inverted (p-i-n) cell architecture.

A key difference from modeling single-junction perovskite solar cell and 2T tandem solar cell is the presence of an interconnecting layer. There are several stand-alone interconnecting layer models, including Tsu-Esaki based models and recombination based models [100]. These stand-alone models, that output the current density, can be used for post-processing calculations, but are difficult to be coupled with an optoelectronic model directly. Alternatively, Hurkx *et al.* has proposed recombination based models for band-to-band and trap-assisted recombination which can be coupled with a drift-diffusion model [101], and thus integrated into an optoelectronic model for a 2T perovskite-on-perovskite tandem solar cell.

After establishing model fidelity through calibration and validation, we investigate how the interconnecting layer, and the geometrical and carrier transport properties can affect the performance of a 2T perovskite-on-perovskite tandem solar cell. Through light management to enhance the short-circuit current density,  $i_{sc}$ , together with loss analysis to obtain high open-circuit voltage,  $V_{oc}$ , and fill factor (FF), we predict a more than 30.5% PCE based on a calibrated 2T perovskite-on-perovskite tandem solar cell model. In addition, we extend our model for bifacial operation and identify the potential for achieving a bifacial equivalent PCE of 35.1%. Our work provides a deeper understanding of the recombination mechanisms and the light interference effect in a 2T

perovskite-on-perovskite tandem solar cell. Leading order parameters that can affect the cell performance are identified to provide a realistic guideline for fabrication, therefore contributing to the development and commercialization of 2T perovskite-on-perovskite tandem solar cell.

## 6.2 Mathematical formulation

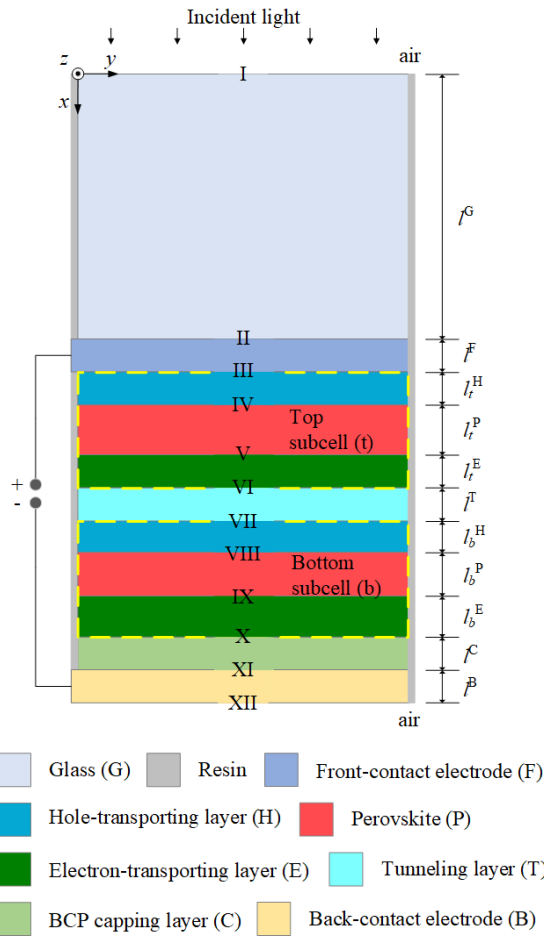


Figure 6.1: Schematic diagram for the 2T perovskite-on-perovskite tandem solar cell considered. The interfaces are denoted by the roman numerals.  $l$  is the layer thickness. The superscripts G, F, H, P, E, T, and B denotes the glass, front contact, hole-transporting, perovskite, electron-transporting, interconnecting/tunneling layer, and the back contact layers, respectively. The subscripts  $t$  and  $b$  denote the top and bottom sub-cells, respectively.

We consider a 2T perovskite-on-perovskite tandem solar cell with the structure shown in Fig. 6.1, which consists of top and bottom sub-cells with the interconnecting layer in between.

The main assumptions and characteristics for the optics in our model are:

1. The three-dimensional structure of the 2T perovskite-on-perovskite tandem solar cell is reduced into a one-dimensional model in the  $x$ -direction, under the condition that optical electric field, electron and hole fluxes in the  $y$ - and  $z$ - directions are negligible.
2. All interfaces are assumed to have negligible surface roughness; all layers are assumed to be isotropic and homogeneous.
3. Full internal quantum efficiency is assumed in charge carrier generation [14].
4. Light is treated as monochromatic plane waves that incident normally from the front at interface I and from the back at interface XII; there is no back-incident light at interface XII for a non-bifacial 2T perovskite-on-perovskite tandem solar cell.
5. We consider light propagation to be transverse electromagnetic (TEM) within the layers.
6. An incoherency correction term [52] that treats the incident optical field is used to account for the loss of light power through the thick glass layer, such that it is not spatially resolved. The semi-analytical solution from general transfer matrix method with this correction term was verified by solving the Helmholtz equation numerically in all layers including the glass with a phase-elimination numerical technique [53].
7. The range of wavelength simulated is from 300 nm to 1050 nm, which covers the absorption range obtained from the experimental data that are used for verification and validation of the optics part [5].

The main assumptions and characteristics for the electronics in our model are:

1. There is no net surface charge on the interfaces between perovskite layers and the charge carrier transport layers [71].

2. A single trap level, which can effectively describe a deep level trap distribution [72, 73], is assumed in the perovskite layers and the interconnecting layer.
3. The BCP capping layer acts as ohmic contact between the charge carrier transport layer and the electrode [17, 102, 103].
4. The electrodes, which are current collectors, are assumed to be ohmic [74].
5. In the perovskite layers, we consider charge carrier generation, radiative recombination, Auger recombination, and SRH recombination; and at the interfaces between the perovskite and the adjacent hole-transporting and electron-transporting layers, interface recombination is accounted for [75].
6. At the interconnecting layer, we consider an electric field dependent trap-assisted recombination [101].

We extend the optics and electronics discussed in Chapter 2 and 3 to the 2T perovskite-on-perovskite tandem solar cell device, and they are summarized as follows.

### 6.2.1 Governing equations

$$\dot{j}_h = S_j, \quad (\text{H,P,T}) \quad (6.1)$$

$$\dot{j}_e = S_j, \quad (\text{P,E,T}) \quad (6.2)$$

$$\varepsilon \psi'' = S_\psi, \quad (\text{H,P,E,T}) \quad (6.3)$$

where the source terms,  $S_j$  and  $S_\psi$ , are given by

$$S_j = \begin{cases} 0, & (\text{H,E}) \\ G - R^P, & (\text{P}) \\ -R^T, & (\text{T}) \end{cases} \quad (6.4)$$

$$S_\psi = e \begin{cases} N_a - c_h, & (\text{H}) \\ c_e - c_h, & (\text{P,T}) \\ c_e - N_d. & (\text{E}) \end{cases} \quad (6.5)$$

The current density,  $i_{tot}$ , can be written as

$$i_{tot} = e(j_h - j_e), \quad (6.6)$$

and the power conversion efficiency,  $\eta$ , can be expressed as

$$\eta = \max(p)/p_{sun}, \quad (6.7)$$

where  $p$  is the output power density at a voltage applied and  $p_{sun}$  is the normalized one sun power density which is equivalent to 1000 W/m<sup>2</sup>.

### 6.2.2 Boundary conditions

For the Poisson's equation, by assuming the front and back contact layers as ohmic contacts, the corresponding boundary conditions at interface III and X at different applied voltages,  $V_a$ , can be written as

$$\psi^{III} = V_a - V_b, \psi^X = 0, \quad (6.8)$$

where  $V_b$  is the built-in voltage.

For the conservation of charge carriers in the top cell from interface III to VI, we

have

$$c_h^{\text{III}} = c_h^0, \quad (6.9)$$

$$c_{h,+}^{\text{IV}} = \Pi_{h,t} c_{h,-}^{\text{IV}}, j_{h,-}^{\text{IV}} = j_{h,+}^{\text{IV}} - j_s^{\text{IV}}, j_{e,-}^{\text{IV}} = j_s^{\text{IV}}, \quad (6.10)$$

$$c_{e,-}^{\text{V}} = \Pi_{e,t} c_{e,+}^{\text{V}}, j_{e,+}^{\text{V}} = j_{e,-}^{\text{V}} - j_s^{\text{V}}, j_{h,+}^{\text{V}} = j_s^{\text{V}}, \quad (6.11)$$

$$j_{e,-}^{\text{VI}} = j_{e,+}^{\text{VI}}. \quad (6.12)$$

Similarly, in the bottom cell from interface VII to X, we have

$$j_{h,+}^{\text{VII}} = j_{h,-}^{\text{VII}}, \quad (6.13)$$

$$c_{h,+}^{\text{VIII}} = \Pi_{h,b} c_{h,-}^{\text{VIII}}, j_{h,-}^{\text{VIII}} = j_{h,+}^{\text{VIII}} - j_s^{\text{VIII}}, j_{e,-}^{\text{VIII}} = j_s^{\text{VIII}}, \quad (6.14)$$

$$c_{e,-}^{\text{IX}} = \Pi_{e,b} c_{e,+}^{\text{IX}}, j_{e,+}^{\text{IX}} = j_{e,-}^{\text{IX}} - j_s^{\text{IX}}, j_{h,+}^{\text{IX}} = j_s^{\text{IX}}, \quad (6.15)$$

$$c_e^{\text{X}} = c_e^0. \quad (6.16)$$

In addition, in the interconnecting layer from interface VI to VII, we have

$$c_{e,+}^{\text{VI}} = \Pi_e^T c_{e,-}^{\text{VI}}, j_{e,+}^{\text{VI}} = j_{e,-}^{\text{VI}}, j_{h,+}^{\text{VI}} = 0, \quad (6.17)$$

$$c_{h,-}^{\text{VII}} = \Pi_h^T c_{h,+}^{\text{VII}}, j_{h,-}^{\text{VII}} = j_{h,+}^{\text{VII}}, j_{e,-}^{\text{VII}} = 0. \quad (6.18)$$

### 6.2.3 Constitutive relations

The built-in voltage and the reference carrier concentrations at interface III and X are calculated as

$$V_b = (W^F - W^B)/e, \quad (6.19)$$

$$c_h^0 = N_{v,t}^H \exp \left[ (W^F - \chi_{h,t}^H)/(k_B T) \right], \quad (6.20)$$

$$c_e^0 = N_{c,b}^E \exp \left[ (\chi_{e,b}^E - W^B)/(k_B T) \right]. \quad (6.21)$$

At boundaries IV to IX, the ratios describing the jumps in carrier concentrations,  $\Pi$ ,

are defined as

$$\Pi_{h,(t,b)} = (N_{v,(t,b)}^P / N_{v,(t,b)}^H) \exp \left[ (\chi_{h,(t,b)}^H - \chi_{h,(t,b)}^P) / (k_B T) \right], \quad (6.22)$$

$$\Pi_h^T = (N_{v,b}^H / N_v^T) \exp \left[ (\chi_{h,b}^H - \chi_h^T) / (k_B T) \right], \quad (6.23)$$

$$\Pi_e^T = (N_{c,t}^E / N_c^T) \exp \left[ (\chi_{e,t}^E - \chi_e^T) / (k_B T) \right]. \quad (6.24)$$

For the recombination inside the 2T perovskite-on-perovskite tandem solar cell, we consider Auger recombination, radiative recombination and SRH recombination in the perovskite layers:

$$R^P = R_{aug} + R_{rad} + R_{SRH}, \quad (6.25)$$

$$R_{aug} = (A_e c_e + A_h c_h) (c_e c_h - c_i^2), \quad (6.26)$$

$$R_{rad} = B_{rad} (c_e c_h - c_i^2), \quad (6.27)$$

$$R_{srh} = \frac{c_e c_h - c_i^2}{\tau_e (c_h + c_{h,trap}) + \tau_h (c_e + c_{e,trap})}. \quad (6.28)$$

The various recombination fluxes originated from the recombination channels are evaluated as

$$j_{aug} = \int_P R_{aug} dx, \quad j_{rad} = \int_P R_{rad} dx, \quad j_{srh} = \int_P R_{srh} dx. \quad (6.29)$$

In addition, the surface recombination carrier flux,  $j_s$ , can be found as

$$j_s^{(IV,VIII)} = v_h \left( c_{e,+} (c_{h,-} + c_{h,+}) - c_{i,(t,b)}^P (c_{i,(t,b)}^H + c_{i,(t,b)}^P) \right), \quad (6.30)$$

$$j_s^{(V,IX)} = v_e \left( c_{h,-} (c_{e,+} + c_{e,-}) - c_{i,(t,b)}^P (c_{i,(t,b)}^E + c_{i,(t,b)}^P) \right). \quad (6.31)$$

During the loss analysis, we define the total recombination carrier flux,  $j_{rec}$ , as

$$j_{rec} = j_{aug,t} + j_{aug,b} + j_{rad,t} + j_{rad,b} + j_{srh,t} + j_{srh,b} + j_s^{IV} + j_s^{VIII} + j_s^V + j_s^IX. \quad (6.32)$$

In the interconnecting layer, we adopt the trap-assisted recombination based model from

Hurkx *et al.* [101] and the trap-assisted recombination rate,  $R^T$ , is calculated as

$$R^T = \frac{c_e c_h - c_i^2}{\tau_e^T(c_h + c_{h,trap})/(1 + \Gamma_e) + \tau_h^T(c_e + c_{e,trap})/(1 + \Gamma_h)}, \quad (6.33)$$

where  $\tau^T$  is the trap-assisted tunneling coefficient and the field effect function,  $\Gamma$ , is expressed as follows

$$\Gamma_{(e,h)} = \begin{cases} (2\sqrt{3\pi} \left| \frac{d\psi}{dx} \right| / F_\Gamma) \exp \left[ (\frac{d\psi}{dx} / F_\Gamma)^2 \right] & \Lambda_{(e,h)} > \frac{2\Delta E_{(e,h)}}{3k_B T}, \\ \sqrt{2\pi/(3\Lambda_{(e,h)})} \frac{\Delta E_{(e,h)} F_\gamma}{k_B T} \exp \left[ \frac{\Delta E_{(e,h)}}{k_B T} - \Lambda_{(e,h)} \right] & \Lambda_{(e,h)} \leq \frac{2\Delta E_{(e,h)}}{3k_B T} \end{cases}, \quad (6.34)$$

$$F_\Gamma = 2\pi \sqrt{24m^*(k_B T)^3 / (eh)}, \quad (6.35)$$

$$\Lambda_{(e,h)} = 8\pi \sqrt{2m^*(\Delta E_{(e,h)})^3} / (3eh \left| \frac{d\psi}{dx} \right|), \quad (6.36)$$

$$m^* = 0.25m_0, \quad (6.37)$$

$$F_\gamma = a_1 \gamma_{(e,h)} + a_2 \gamma_{(e,h)}^2 + a_3 \gamma_{(e,h)}^3, \quad (6.38)$$

$$\gamma_{(e,h)} = \left[ \left( 1 + \beta \left( \frac{\Delta E_{(e,h)}}{k_B T} - \frac{3}{2} \Lambda_{(e,h)} \right) \right) \sqrt{\frac{3}{2} \Lambda_{(e,h)}} \right]^{-1}. \quad (6.39)$$

Here, the filed effect function describes the ratio between the emission probability at a given electrical potential to the probability in the absence of an electrical potential,  $m^*$  is the effective mass of the majority charge carrier,  $h$  is the Planck's constant,  $a_1$ ,  $a_2$ ,  $a_3$  and  $\beta$  are constants taken from Hurkx *et al* [101, 104].

### 6.3 Verification and validation (optics)

The model is applied to a 2T perovskite-on-perovskite tandem solar cell with the structure glass ( $5.4 \times 10^{-4}$  m) /ITO (70 nm) /PTAA (15 nm) /Cs<sub>0.2</sub>FA<sub>0.8</sub>PbI<sub>1.8</sub>Br<sub>1.2</sub> (380 nm) /C60 (20 nm) /SnO<sub>2</sub> (20 nm) /PEDOT:PSS (80 nm) /MA<sub>0.3</sub>FA<sub>0.7</sub>Pb<sub>0.5</sub>Sn<sub>0.5</sub>I<sub>3</sub> (860 nm) /C60 (20 nm) /BCP (7 nm) /Cu (100 nm) [5], under 1000 W/m<sup>2</sup> solar irradiance, 25°C cell temperature, AM1.5, and ASTM G173-03 standard spectrum [51]. Here, the layer thicknesses indicated in the parentheses are estimated from the scanning electron microscopy (SEM) diagram by Lin *et.al* [5] and the glass thickness is assumed. The

optical properties for different materials are sourced from published data with a wavelength ranged from 300 nm to 1050 nm. The optical constants for  $\text{SnO}_2$  and BCP are extrapolated from 1001 to 1050 nm as the literature data we adopted are only up to 1000 nm wavelength. In addition, the optical properties for bottom cell perovskite are from similar constituent materials [60].

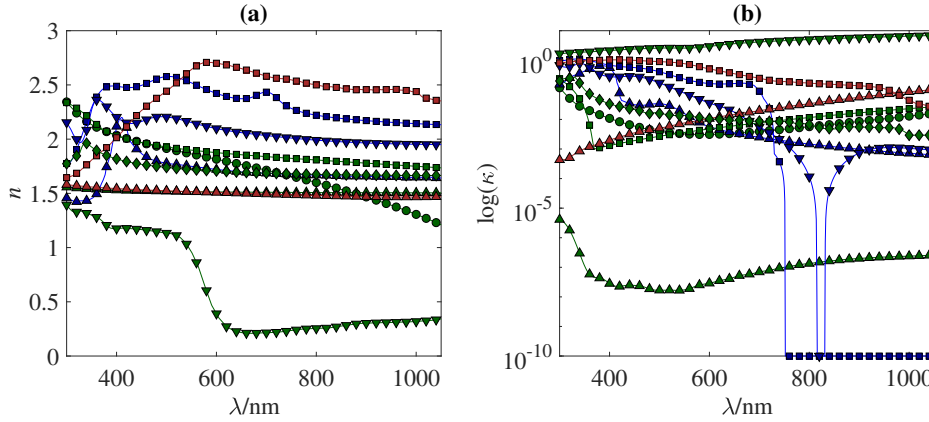


Figure 6.2: (a) Refractive index and (b) extinction coefficient for glass (green line with upper triangle), ITO (green line with circle), PTAA (blue line with upper triangle), top cell perovskite (blue line with square), C60 (blue line with lower triangle),  $\text{SnO}_2$  (green line with square), PEDOTPSS (red line with upper triangle), bottom cell perovskite (red line with square), BCP (green line with diamond) and Cu (green line with lower triangle). Here, C60 in the bottom cell shares the same optical properties with the top cell C60.

The corresponding  $n$  and  $\kappa$  data are shown in Figure 6.2. Here, we consider optical data from literature for glass [64], ITO [54],  $\text{SnO}_2$  [55], PTAA [56], top perovskite ( $\text{Cs}_{0.2}\text{FA}_{0.8}\text{PbI}_{1.8}\text{Br}_{1.2}$ ) [57], C60 [58], PEDOT:PSS [59], bottom perovskite ( $\text{MA}_{0.3}\text{FA}_{0.7}\text{Pb}_{0.5}\text{Sn}_{0.5}\text{I}_3$ ) [60], BCP [61] and Cu [62].

For optical verification, we compare the generation profiles obtained from the semi-analytical solution and solving the Helmholtz equation numerically with phase elimination method [53]. In Figure 6.3(a), there is good agreement between the generation profiles and the relative errors are less than 1% for both top and bottom subcells. In comparison between the simulated photogenerated current,  $i_p$ , from the semi-analytical solution and Lin *et al.*'s experimental results [5] for validation, we obtain  $i_p$  as 16.0 mA/cm<sup>2</sup> (semi-analytical solution), and 15.7 mA/cm<sup>2</sup> (experiment) for top subcell and 15.8 mA/cm<sup>2</sup> (semi-analytical solution), and 15.5 mA/cm<sup>2</sup> (experiment) for bottom

subcell with their differences within  $0.3 \text{ mA/cm}^2$ . Furthermore, the external quantum efficiency (EQE) from simulation and experiment are shown in Figure 6.3(b). Overall, good agreement between the EQE ranged from 300 nm to 1050 nm for the top and bottom cells is obtained.

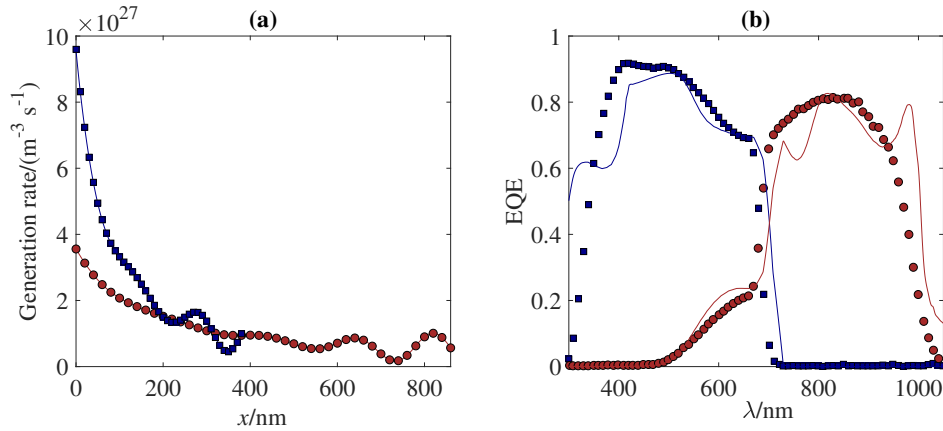


Figure 6.3: (a) Generation profiles from the phase elimination method (symbols) and from the semi-analytical solution (lines) for top subcell (blue) and bottom subcell (red); (b) EQE from the semi-analytical solution (lines) and from experiment (symbols) for top subcell (blue) and bottom subcell (red).

## 6.4 Calibration and validation (electronics)

Similar to the optics part, the model is applied to the same 2T perovskite-on-perovskite tandem solar cell under  $1000 \text{ W/m}^2$  solar irradiance,  $25^\circ\text{C}$  cell temperature, AM1.5, and ASTM G173-03 standard spectrum [51]. We perform calibration for the two single-junction perovskite solar cells separately. For each subcell, there are in total twenty-seven parameters required for the simulation for the electronics with the layer thicknesses excluded. Here, twenty parameters are sourced from literature and the remaining seven parameters for the recombination mechanisms in each cell are calibrated with forty  $i - V$  data points extracted from experiment  $i - V$  curve reported by Lin *et al.* [5]. The calibration is conducted using particle swarm optimization algorithm in Matlab R2019a. Default options are employed for the optimization despite the swarm size is set to be two hundred for sufficient samples. For all simulations, we assume  $A_e = A_h$  and  $\tau_e = \tau_h$  in

the perovskite layers. We find the parameters,

$$\Phi = (A_e, A_h, B, \tau_e, \tau_h, v_e, v_h), \quad (6.40)$$

for each subcell by minimizing the least squared error:

$$\min_{\Phi} |i_{tot}(\Phi, V_a) - i_{tot}^{exp}(\Phi, V_a)|^2, \quad (6.41)$$

where  $i_{tot}$  and  $i_{tot}^{exp}$  are the total current densities from simulation and experiment respectively.

	TC	BC	ICL	Units	TC	BC	ICL
$A_e$	$2.5 \times 10^{-38}$	$1.3 \times 10^{-38}$		$\text{m}^6 \text{s}^{-1}$	Fit	Fit	
$A_h$	$2.5 \times 10^{-38}$	$1.3 \times 10^{-38}$		$\text{m}^6 \text{s}^{-1}$	Fit	Fit	
$a_1$			0.3480242				[101]
$a_2$			-0.0948798				[101]
$a_3$			0.7478556				[101]
$B_{rad}$	$2.3 \times 10^{-16}$	$2.4 \times 10^{-16}$		$\text{m}^3 \text{s}^{-1}$	Fit	Fit	
$\beta$			0.61685				[101]
$c$	$2.998 \times 10^8$			$\text{m s}^{-1}$			
$\chi_e^E$	4.2	4.2		eV	[81]	[81]	
$\chi_h^H$	5.27	5		eV	[82]	[91]	
$\chi_e^{(P,T)}$	4.02	3.83		eV	[83]	[92]	
$\chi_h^{(P,T)}$	5.77	5.05		eV	[83]	[92]	
$\Delta E_{trap}$	0.16	0.16	1	eV	[80]	[80]	[105]
$e$	$1.602 \times 10^{-19}$			C			
$\epsilon_0$	$8.854 \times 10^{-12}$			$\text{F m}^{-1}$			
$\epsilon^E$	$3.03\epsilon_0$	$3.03\epsilon_0$		$\text{F m}^{-1}$	[42]	[42]	
$\epsilon^H$	$3\epsilon_0$	$3\epsilon_0$		$\text{F m}^{-1}$	[84]	[42]	
$\epsilon^{(P,T)}$	$5.56\epsilon_0$	$6.17\epsilon_0$	9.86 $\epsilon_0$	$\text{F m}^{-1}$	[80]	[80]	[106]
$h$	$6.626 \times 10^{-34}$			J s			
$k_B$	$1.38 \times 10^{-23}$			$\text{J K}^{-1}$			
$m_0$				$9.11 \times 10^{-31}$	kg		
$m^*$				$0.25m_0$	kg		[101]
$\mu_e^E$	$1.6 \times 10^{-4}$	$1.6 \times 10^{-4}$		$\text{m}^2 \text{V}^{-1}$	[25]	[25]	
$\mu_h^H$	$1 \times 10^{-6}$	$7.7 \times 10^{-5}$		$\text{m}^2 \text{V}^{-1}$	[85]	[93]	
$\mu_e^{(P,T)}$	$5.5 \times 10^{-4}$	$7.9 \times 10^{-3}$	$4.2 \times 10^{-2}$	$\text{m}^2 \text{V}^{-1}$	[83]	[5]	[107]
$\mu_h^{(P,T)}$	$5.5 \times 10^{-4}$	$7.9 \times 10^{-3}$	$4.2 \times 10^{-2}$	$\text{m}^2 \text{V}^{-1}$	[83]	[5]	[107]
$N_c^E$	$1 \times 10^{22}$	$1 \times 10^{22}$		$\text{m}^{-3}$	[88]	[88]	
$N_c^H$	$5 \times 10^{25}$	$3 \times 10^{26}$		$\text{m}^{-3}$	[86]	[93]	
$N_c^{(P,T)}$	$1.7 \times 10^{22}$	$1.7 \times 10^{22}$	$9.38 \times 10^{18}$	$\text{m}^{-3}$	[87]	[87]	[80]
$N_v^E$	$1 \times 10^{22}$	$1 \times 10^{22}$		$\text{m}^{-3}$	[88]	[88]	
$N_v^H$	$5 \times 10^{25}$	$3 \times 10^{26}$		$\text{m}^{-3}$	[86]	[93]	
$N_v^{(P,T)}$	$1.8 \times 10^{25}$	$1.8 \times 10^{25}$	$9.38 \times 10^{18}$	$\text{m}^{-3}$	[75]	[75]	[80]
$\tau_e$	$1.3 \times 10^{-8}$	$3.8 \times 10^{-8}$	$1 \times 10^{-12}$	s	Fit	Fit	Fit
$\tau_h$	$1.3 \times 10^{-8}$	$3.8 \times 10^{-8}$	$1 \times 10^{-12}$	s	Fit	Fit	Fit
$v_e$	$1.7 \times 10^{-26}$	$2.5 \times 10^{-26}$		$\text{m}^4 \text{s}^{-1}$	Fit	Fit	
$v_h$	$3.5 \times 10^{-29}$	$1.2 \times 10^{-25}$		$\text{m}^4 \text{s}^{-1}$	Fit	Fit	
$W^B$	4.3	4.3		eV	[89]	[89]	
$W^F$	4.9	4.9		eV	[90]	[90]	

Table 6.1: Parameters for the top subcell (TC), bottom subcell (BC) and the interconnecting layer (ICL). The references are stated in the last three columns. Some of the parameters are fitted (Fit) based on calibration.

After calibration of the two single-junction subcells, the model of top and bottom subcells are then coupled electrically by an interconnecting layer in which ten parameters are sourced from literature and two parameters describing the trap-assisted recombination are calibrated with the experiment  $i - V$  curve of the 2T perovskite-on-perovskite tandem solar cell. All parameter and their values considered here are shown in Table 6.1. Forty  $i - V$  data points are extracted from the experiment 2T perovskite-on-perovskite tandem solar cell  $i - V$  curve [5], in which twenty points are used for calibration and the rest are used for validation. In the tandem configuration, we also assume that  $\tau_e = \tau_h$  in the interconnecting layer.

As shown in Figure 6.4, good agreement is obtained between the simulated and measured  $i - V$  curves. For validation, the twenty  $i - V$  data points preserved align with the simulated 2T perovskite-on-perovskite tandem solar cell  $i - V$  curve. In detail, the simulated  $i_{sc}$  are 17.7, 31.3, and 15.8mA/cm<sup>2</sup> while experimental ones are 17.4, 31.4, and 15.6 mA/cm<sup>2</sup> for the top, bottom and tandem cells respectively. Similarly, for  $V_{oc}$ , we have 1.21, 0.81, and 1.96 V from simulation and 1.21, 0.83, and 1.96 V from experiment. For PCE, we have 16.3%, 21.8%, and 24.1% from simulation and 16.1%, 21.1%, and 24.5% from experiment. Through validation and establishing of model fidelity, we proceed to use our model for further analysis.

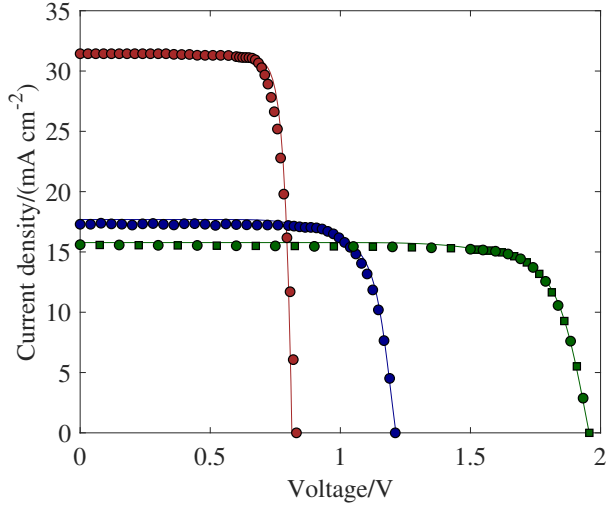


Figure 6.4: Predicted (lines) and experimental measured (circles for calibration and squares for validation) current-voltage curves for top perovskite cell (blue), bottom perovskite cell (red), and 2T perovskite-on-perovskite tandem solar cell (green).

## 6.5 Results and discussions

Through verifications and validations with experimental results from literature, model fidelity has been established. From the developed 2T perovskite-on-perovskite tandem solar cell model, we are then able to analyze the effects of optical losses and interferences, recombination losses, together with the functionality of the interconnecting layer on the cell performances.

In this chapter, we present key insights derived from our optoelectronic model. Firstly, we confirm the vital role of the interconnecting layer in achieving current matching in a 2T perovskite-on-perovskite tandem solar cell. Secondly, we delve into light management within the cell and investigate the impact of layer thicknesses on  $i_{sc}$  and PCE. Moving forward, we perform a loss analysis, pinpointing the primary recombination mechanisms and quantifying their correlation with overall cell performance. As a result, our predictions suggest the potential for this 2T perovskite-on-perovskite tandem solar cell to achieve a PCE of 30.5% and a bifacial equivalent PCE of 35.1% when extended under bifacial operation. These analyses rely on calibrated parameter values obtained from experiments (see Table 6.1) and the corresponding PCE as baselines.

### 6.5.1 The interconnecting layer

Our model incorporates trap-assisted recombination at the interconnecting layer. This junction helps to match the current in top and bottom subcells by conservation of charge carriers. To capture this current matching behavior in the 2T perovskite-on-perovskite tandem solar cell, we alter the charge carrier generation rates and compare the resulted top and bottom cell photogenerated current densities,  $i_{p,t}$  and  $i_{p,b}$  respectively, together with  $i_{sc}$ . As shown in Figure 6.5(a),  $i_{sc}$  is limited by the lower  $i_p$  from the top and bottom subcells. Owing to the good agreement between  $i_{sc}$  and the limiting  $i_p$ , it indicates the recombination model we adapted can achieve automatic current matching in the 2T perovskite-on-perovskite tandem solar cell. From Figure 6.5(a), the red dashed lines indicate how the current is automatically limited by the current from the bottom subcell, for the case with the parameters from calibration.

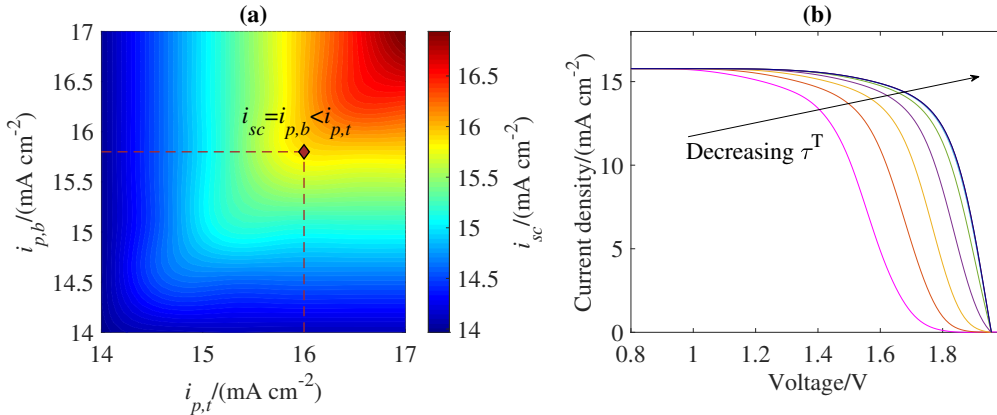


Figure 6.5: (a) Current limiting behavior of a 2T perovskite-on-perovskite tandem solar cell achieved by ICL in the model, with the red dotted lines showing how current is limited for the calibrated parameters (red diamond); (b) Current-voltage curves when trap-assisted recombination coefficient is varied from  $\tau^T = 10^{-12}$  s to  $\tau^T = 10^{-5}$  s.

Moreover, our model explains a possible origin of an S-shaped  $i - V$  characteristic. In the paper by Lin *et al.* [5] where experimental results are taken for model calibration, an S-shape  $i - V$  behavior near  $V_{oc}$  has been reported for cell with a poorly fabricated interconnecting layer. When an ultra thin Au layer has been deposited on SnO<sub>2</sub> in the interconnecting layer, the S-shape is found to disappear. They attribute this result to increased charge carrier recombination by the Au layer.

Our model is able to predict this S-shape behavior. As shown in Figure 6.5(b), by increasing the trap-assisted recombination coefficient,  $\tau^T$ , from  $10^{-12}$  to  $10^{-5}$  s, clear S-shape is found in the  $i - V$  curve. When  $\tau^T$  increases, the trap-assisted recombination rate,  $R^T$ , decreases (see Eq. 7.35). Since the model is recombination based [101], decreasing  $R^T$  leads to a smaller majority carrier recombination flux and a lower limit on how much current can pass through the junction at a given electrical potential. This gives rise to the S-shape and causes a drop in FF and thus PCE. On the other hand,  $i_{sc}$  and  $V_{oc}$  are not affected. The layer connecting the two subcells in a 2T configuration thus may need to be fabricated in a way to facilitate charge carrier recombination.

We also conduct an investigation into the impact of varying charge carrier mobility and density of states for the  $\text{SnO}_2$  material used in the interconnecting layer on the  $i - V$  characteristics of the tandem device. The results are presented in Figure 6.6. In our analysis, we assume equal carrier mobility and density of states for both electrons and holes, and we individually sweep these parameters over a range from  $10^{-6}$  to  $10^{-1}$   $\text{m}^2/\text{V}/\text{s}$  and from  $10^{18}$  to  $10^{20}$   $1/\text{m}^3$ , respectively. We observe that changes in charge carrier mobility within the interconnecting layer have no significant impact on device performance. This outcome may be attributed to the ultra-thin nature of the layer (under 20 nm), where the transport of electrons and holes is already sufficiently rapid. Next, the density of states in the material of the interconnecting layer are more influential in device performance. A substantial improvement in  $V_{oc}$  from 1.85 to 2.05 V is observed, emphasizing the importance of the density of states in the interconnecting layer. This quantity is linked to charge carrier concentrations and energy level distributions within the layer, and increasing it might have enhanced the smoothness of charge carrier transport and recombination in this specific system.

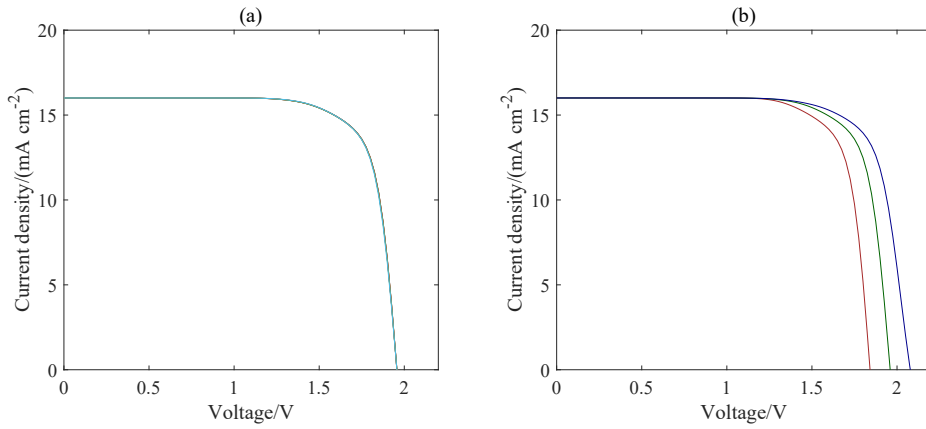


Figure 6.6: Simulated  $i - V$  curves of the tandem devices with (a) the charge carrier mobility in the interconnecting layer changed from  $10^{-6}$  to  $10^{-1} \text{ m}^2/\text{V}\cdot\text{s}$  and (b) density of states in the interconnecting layer being  $10^{18}$  (red),  $10^{19}$  (green), and  $10^{20}$  (blue)  $1/\text{m}^3$ . Here, there is no obvious perturbations of  $i - V$  curves with changes in charge carrier mobility in (a).

Furthermore, in our model, we switch the material in the interconnecting layer from  $\text{SnO}_2$  to IZO, with its calibrated parameter values in Chapter 7 (see Table 7.1)—charge carrier mobility of  $2.4 \times 10^{-3} \text{ m}^2 \text{ V}^{-1} \text{ s}^{-1}$ , density of states of  $1.5 \times 10^{21} \text{ m}^{-3}$ , thickness of 4 nm, and recombination coefficient of  $1.1 \times 10^{-15} \text{ s}$ . The differences between the simulated  $i - V$  curves are shown in Figure 6.7. We notice that by changing to an IZO interconnecting layer, there is no significant improvement in PCE, and a S-shape near  $V_{oc}$  appears. Possible reasons can be that the IZO layer is not properly calibrated for this perovskite-on-perovskite tandem device, and therefore more experiments for calibration can be a potential future work. As one limitation of our model, the interconnecting layer needs to be calibrated again in a particular device for more accurate predictions if the material is switched. With more experimental data available, we present investigations on the interconnecting layer calibrated with different materials in Chapter 7 for a 2T perovskite-on-organic tandem solar cell.

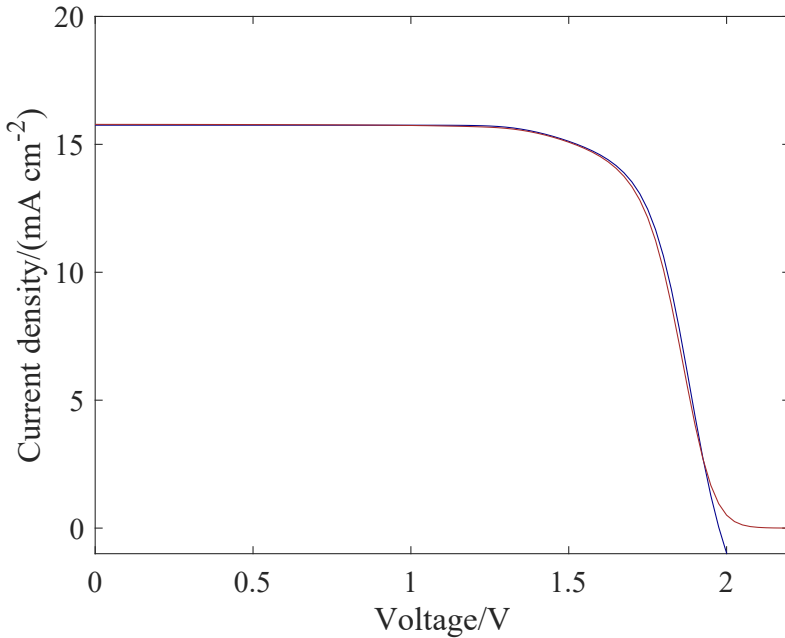


Figure 6.7: Simulated  $i$  –  $V$  curves of the 2T perovskite-on-perovskite tandem solar cells with  $\text{SnO}_2$  (blue) and IZO (red).

### 6.5.2 Light management

Effective light management is a crucial factor in achieving a high PCE in 2T perovskite-on-perovskite tandem solar cells. It involves minimizing total reflection and parasitic absorption while optimizing light absorption within the two perovskite layers by taking into account light interference effects in thin-film layers. Our investigation focuses on the optical system of 2T perovskite-on-perovskite tandem solar cells, with specific variations in the front contact thickness,  $l^F$ , top cell perovskite thickness,  $l_t^P$ , and bottom cell perovskite thickness,  $l_b^P$ .  $l^F$  is considered here since the front contact should be responsible for the most reflection and parasitic loss.  $l_t^P$  and  $l_b^P$  are chosen since they are the active layer thicknesses.

We begin by assessing the impact of front contact thickness,  $l^F$ , ranging from 20 to 120 nm. Our findings reveal that a 30 nm front contact yields the highest  $i_{sc}$  of 16.3 mA/cm<sup>2</sup>. Next, we simultaneously vary  $l_t^P$  and  $l_b^P$  at two different front contact thicknesses ( $l^F = 70$  nm and  $l^F = 30$  nm). As illustrated in Figure 6.8, the highest predicted PCE is 24.6% for  $l^F = 70$  nm, while a PCE of 25.2% can be achieved with  $l_t^P = 420$  nm

and  $l_b^P = 940$  nm when  $l^F=30$  nm. These results suggest that maintaining a thin front contact is advisable. However, with regard to the perovskite layer thicknesses, thicker is not necessarily better. Careful design is needed to optimize light absorption in both perovskite layers by considering light interference effects. Specifically,  $l_t^P$  cannot be too large to allow sufficient light to enter the bottom cell, and we should aim for constructive wave interference to enhance light absorption in both perovskite layers.

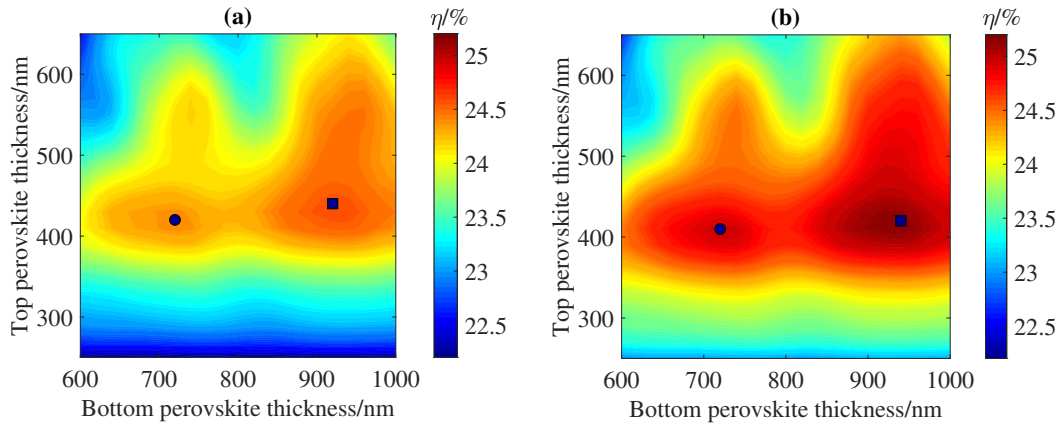


Figure 6.8: PCE, represented by the symbol  $\eta$ , of the 2T perovskite-on-perovskite tandem solar cell at different top and bottom perovskite thicknesses with (a) 70 nm and (b) 30 nm front contact, showing the first (blue square) and second (blue circle) local highest PCE points for the parameter ranges considered here.

Besides, two local highest PCE points marked by the blue squares are found in both Figure 6.8(a) and (b). Here, in Figure 6.8(a), with  $l^F = 70$  nm, the cell has a  $i_{sc}$  of 16.2 mA/cm<sup>2</sup> at the first local highest PCE point and 15.6 mA/cm<sup>2</sup> at the second local highest PCE point. In Figure 6.8(b), with  $l^F = 30$  nm, these  $i_{sc}$  values are 16.3 mA/cm<sup>2</sup> and 15.9 mA/cm<sup>2</sup> respectively. We attribute these results to the light interference effect. As mentioned above, the respective layer thicknesses should be chosen for constructive wave interference. This constructive interference effect can take place at different thickness combinations. As such, it is possible to make a 2T perovskite-on-perovskite tandem solar cell that has thinner perovskite layers without lowering too much on  $i_{sc}$  and PCE.

Additionally, we have identified two local peaks in PCE marked by blue squares in both Figure 6.8(a) and (b). In Figure 6.8(a), with  $l^F = 70$  nm, the cell has a  $i_{sc}$  of 16.2 mA/cm<sup>2</sup> at the first local PCE peak and 15.6 mA/cm<sup>2</sup> at the second local PCE peak. In Figure 6.8(b), with  $l^F = 30$  nm, these  $i_{sc}$  values are 16.3 mA/cm<sup>2</sup> and 15.9 mA/cm<sup>2</sup>

respectively. We attribute these findings to the light interference effect. The choice of layer thicknesses to achieve constructive wave interference can vary, allowing for the design of 2T perovskite-on-perovskite tandem solar cells with thinner perovskite layers without significant reductions in  $i_{sc}$  and PCE.

### 6.5.3 Loss analysis

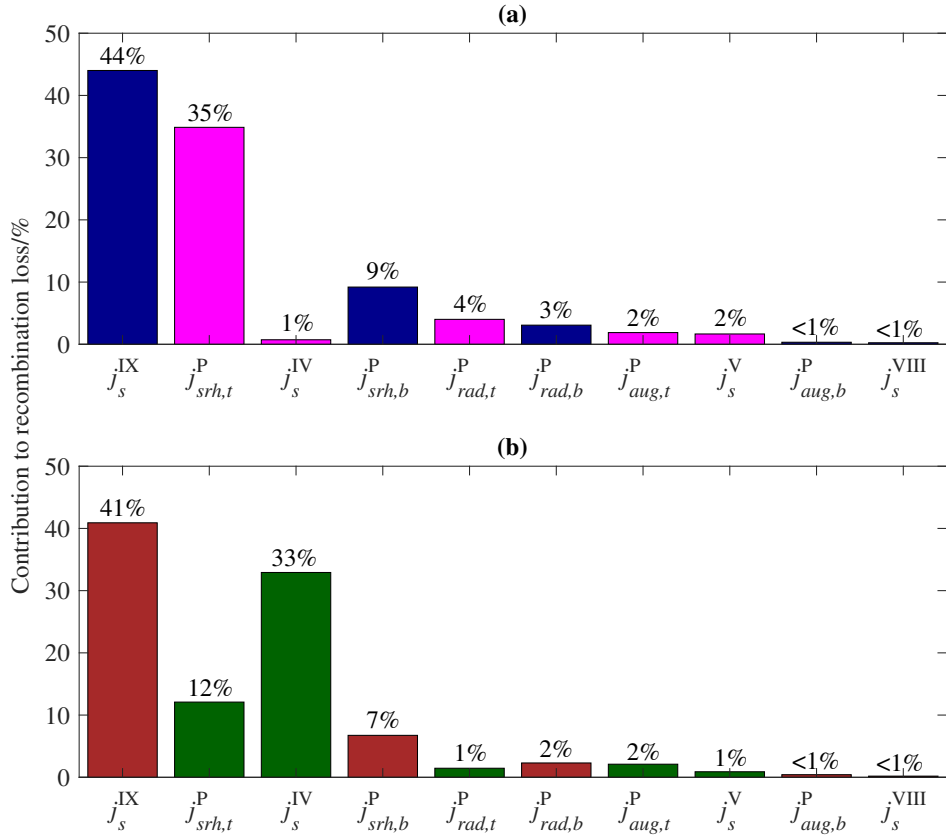


Figure 6.9: Loss due to radiative, auger and SRH recombinations in the perovskite layers and interface recombinations between perovskite layers and their adjacent carrier transporting layers at (a) MPP (in top subcell: magenta square; in bottom subcell: blue square); and (b)  $V_{oc}$  (in top subcell: green square; in bottom subcell: red square). The percentage loss is calculated as each individual recombination loss divided by the total recombination loss for the parameters considered here.

On the electronic side, our model accounts for radiative, Auger, and SRH recombinations within the bulk perovskite, as well as surface recombinations at the interfaces between the perovskite layer and its adjacent electron- and hole-transporting layers in both subcells. It is important to identify the leading order recombination channels responsible

for current losses in 2T perovskite-on-perovskite tandem solar cells to achieve high efficiency. The loss analysis is conducted at the Maximum Power Point (MPP) and  $V_{oc}$ . In Figure 6.9, we present the percentage contribution of ten recombination channels to the total recombination carrier flux,  $j_{rec}$ , at various positions within the cell.

Our findings reveal that surface recombinations at interfaces IV and XI, along with SRH recombination in the top and bottom perovskite layers, are the predominant contributors to losses in 2T perovskite-on-perovskite tandem solar cells. At MPP, these four recombination channels account for 1%, 44%, 35%, and 9%, respectively. At  $V_{oc}$ , their contributions are 33%, 41%, 12%, and 7%, respectively. These results align with experimental observations where SRH and interface recombinations, stemming from defects in the perovskite, significantly impact the performance of single-junction perovskite solar cells [108, 109, 110]. Moreover, Tong *et al.* [87] concluded that an increase in perovskite defect carrier lifetime, related to SRH recombination, enhances the PCE of all-perovskite tandem devices. Thus, our loss analysis findings are consistent with existing literature.

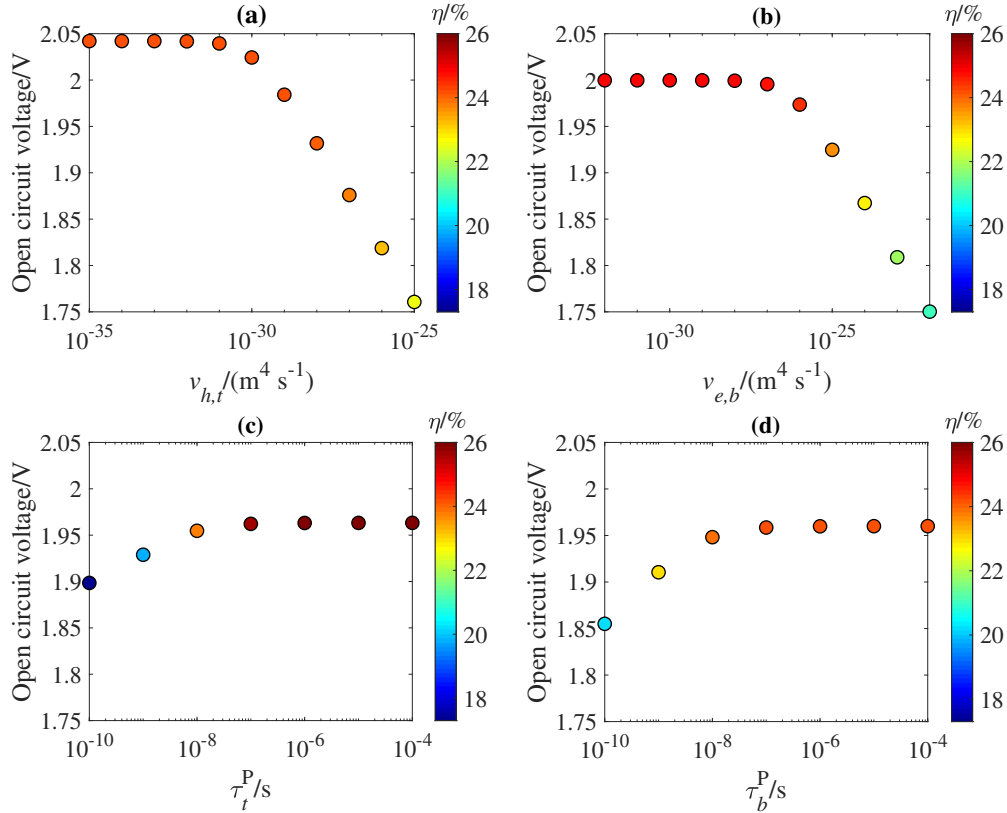


Figure 6.10:  $V_{oc}$  and PCE of the 2T perovskite-on-perovskite tandem solar cell when the effective surface recombination velocities at (a) interface IV; (b) interface IX; and trap-assisted recombination lifetime in (c) top perovskite; (d) bottom perovskite are varied.

Parametric studies are conducted to provide detailed insights into how the primary recombination channels influence the performance of the 2T perovskite-on-perovskite tandem solar cell. The parameters under investigation include the effective surface recombination velocities at interfaces IV and XI, denoted as  $v_{h,t}$  and  $v_{e,b}$ , and the SRH recombination lifetimes, represented by  $\tau_t^P$  and  $\tau_b^P$ .

As depicted in Figure 6.10(a), within the explored parameter range, a higher  $v_{h,t}$  value, which results in increased surface recombination at IV, significantly reduces the  $V_{oc}$  from the calibrated value of 1.96 V to 1.76 V. Consequently, the PCE is predicted to decrease to 22.5%. Conversely, a reduction in  $v_{h,t}$  leads to an increase in  $V_{oc}$ , approaching 2.05 V, while the PCE remains stable at 24.2%. This adjustment results in a decrease in the FF due to the increase in  $V_{oc}$ .

Similarly, in 6.10(b), when  $v_{e,b}$  is reduced, resulting in decreased surface recombination at IX,  $V_{oc}$  increases to around 2 V with a PCE of 24.6%. On the other hand,

when surface recombination dominates at higher values of  $v_{e,b}$ , a drop of more than 3% in PCE is observed. These findings align with experimental results from Wolff et al. and Correa-Baena *et al.* [108, 109], indicating the significant impact of surface defects and interface recombination on the performance of single-junction perovskite solar cells. Based on these findings, we predict that these effects from surface recombination apply to 2T perovskite-on-perovskite tandem solar cells as well.

High SRH recombination due to defects in the bulk perovskite is another significant source of losses in both single-junction perovskite solar cells and perovskite-on-perovskite tandem solar cells, as reported by Leijtens *et al.* and Tong *et al.* [87, 110]. Our results, as illustrated in Figure 6.10(c) and (d), corroborate this conclusion. Compared to the effects of surface recombination, the reduction in  $V_{oc}$  due to SRH recombination is less pronounced. However, the FF and PCE are significantly penalized, particularly evident in 6.10(c) when SRH recombination in the top perovskite is high. The maximum difference in PCE is approximately 8%, underscoring the importance of avoiding low carrier lifetimes in the perovskite layers.

In comparing the losses at the MPP and  $V_{oc}$ , we find that surface recombination plays a more prominent role than SRH recombination. The percentage contribution from the top cell SRH recombination flux,  $j_{srh,t}^P$ , decreases from 35% at MPP to 12% at  $V_{oc}$ , while the surface recombination flux,  $j_s^{IV}$ , at interface IV increases from 1% at MPP to 33% at  $V_{oc}$ . At  $V_{oc}$ , surface recombination dominates at interfaces IV (35%) and IX (40%). SRH recombination in the top perovskite remains significant at MPP. Taking into account our previous results where surface recombination's impact on  $V_{oc}$  is more pronounced and SRH recombination exerts greater influence on the FF, we recommend that these identified surface recombinations should be closely examined if a fabricated 2T perovskite-on-perovskite tandem solar cell exhibits a low  $V_{oc}$ , while SRH recombinations should be investigated if the cell has a low FF.

### 6.5.4 Towards higher PCE

Building upon the insights gathered from our previous discussions on both optics and electronics, we aim to identify a path toward achieving a 30% PCE for the 2T perovskite-on-perovskite tandem solar cell. Our starting point is the baseline data obtained from model calibration, as presented in Table 6.1. We make modifications to three geometric properties and five carrier transport parameters to enhance the PCE. The values of these parameters, both from calibration and after adjustments, are listed in Table 6.2, and the performance predictions for the 2T perovskite-on-perovskite tandem solar cell are summarized in Table 6.3. The changes in  $V_{oc}$ , FF, and PCE resulting from these parameter adjustments are depicted in Figure 6.11(a), and the corresponding i-V curves can be found in Figure 6.11(b).

In detail, we begin by adopting the layer thicknesses outlined in the light management section, which gives optimized short-circuit current densities of 16.2 and 16.3 mA/cm<sup>2</sup> with 70 and 30 nm front contacts, respectively. This initial adjustment boosts the PCE to 25.2%. Next, we mitigate surface recombinations at interfaces IV and XI by reducing  $v_{h,t}$  and  $v_{e,b}$ . This intervention leads to a substantial increase in  $V_{oc}$  from 1.96 V to approximately 2.1 V, aligning with our loss analysis. By extending the SRH carrier lifetimes,  $\tau_t^P$  and  $\tau_b^P$ , to  $10^{-5}$  s, the FF is increased to nearly 84% and the PCE to around 29%. This modification is based on findings from Tong *et al.*, which reported carrier lifetimes exceeding 1  $\mu$ s for perovskite [87]. Lastly, by enhancing the carrier mobility in the top perovskite layer,  $\mu^P$ , to a value of  $5.5 \times 10^{-3}$  m<sup>2</sup>V<sup>-1</sup>s<sup>-1</sup>, we further enhance the FF to nearly 88%, resulting in a PCE of 30.5%. Experiments have reported perovskite with carrier mobility greater than 10<sup>-3</sup> m<sup>2</sup>V<sup>-1</sup>s<sup>-1</sup> [111, 112], and our chosen value is within a similar range. The modifying layer thicknesses are also feasible in practice.

The following guidelines outline potential experimental actions to implement the proposed improvements. Firstly, applying surface passivation techniques [37, 102] to interfaces IV and XI can help mitigate current loss caused by surface recombination. Utilizing more efficient thin-film passivation or buffer layers, such as BCP [74], can also effectively suppress this type of recombination. To address SRH recombination within

the bulk perovskites, introduce additives like guanidinium thiocyanate (GuaSCN), following the approach proposed by Tong *et al.* [87]. These additives can help extend the charge carrier lifetime, thereby reducing losses due to SRH recombination. Regarding the charge carrier mobility, depositing a perovskite layer with small effective masses of anti-bonding band-edge states [111] could help improve charge carrier transport. Lastly, optimization of the optics can be achieved through our modeling, followed by making slight adjustments to layer thicknesses and deposition techniques. However, it is important to note that while a 30 nm ITO layer is feasible for fabrication and can reduce parasitic absorption, the small thickness may compromise on the conductivity of the front contact. As an alternative, a 70 nm ITO layer might result in a slightly lower photogenerated current density but offers advantages for experimentation.

Consequently, our proposed enhancements to the calibrated 2T perovskite-on-perovskite tandem solar cell are not only achievable but hold promising potential. With reduced surface recombination during fabrication, the 2T perovskite-on-perovskite tandem solar cell has a strong likelihood of achieving a PCE exceeding 30% in accordance with the outlined guidelines.

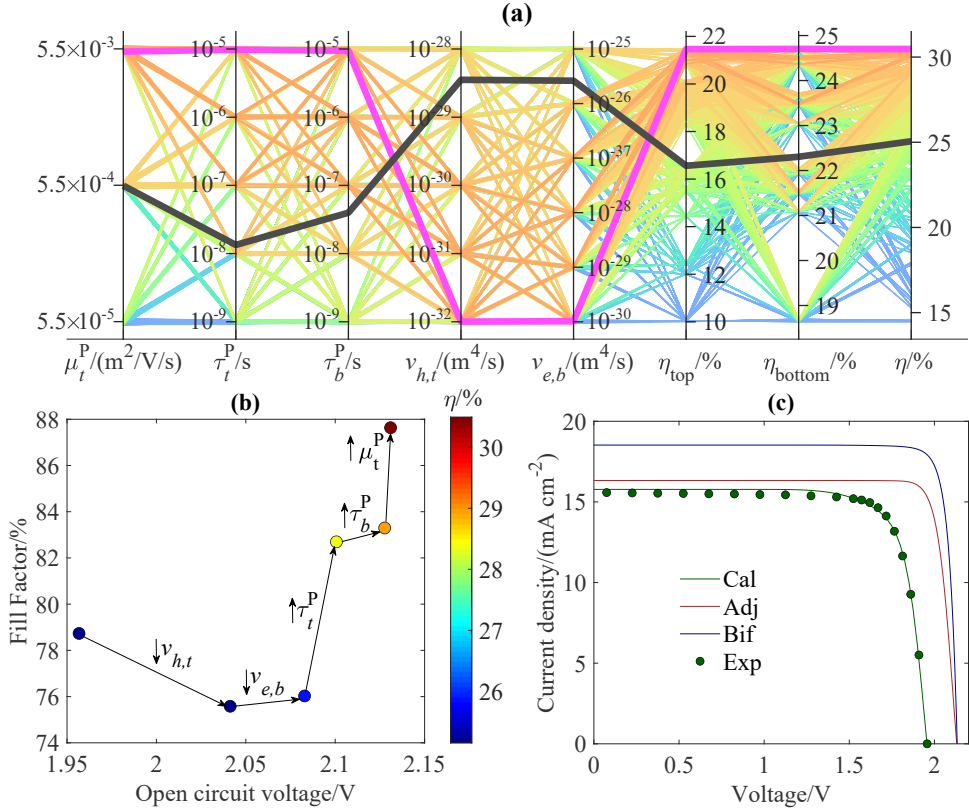


Figure 6.11: Pathway to improve the PCE of the 2T perovskite-on-perovskite tandem solar cell, (a) showing the change in  $V_{oc}$ , FF and PCE when intrinsic transport properties are adjusted based on Table 2 and (b) the corresponding current-voltage curves from experiment (Exp), calibration (Cal), model prediction with adjusted parameters (Adj) in Table 6.2, together with model predication from bifacial operation (Bif).

Parameters	TC (Cal)	BC (Cal)	TC (Adj)	BC (Adj)	Units
$l^F$	70		30		nm
$l^P$	380	860	420	940	nm
$\mu^P$	$5.5 \times 10^{-4}$		$5.5 \times 10^{-3}$		$m^2 V^{-1} s^{-1}$
$\tau^P$	$1.3 \times 10^{-8}$	$3.8 \times 10^{-8}$	$1 \times 10^{-5}$	$1 \times 10^{-5}$	s
$v_e$		$2.5 \times 10^{-26}$		$1 \times 10^{-30}$	$m^4 s^{-1}$
$v_h$	$3.5 \times 10^{-29}$		$1 \times 10^{-32}$		$m^4 s^{-1}$

Table 6.2: Parameters from calibrated model (Cal) and from adjusted parameter set (Adj) in the top subcell (TC) and bottom subcell (BC) for achieving a 30.5% PCE 2T perovskite-on-perovskite tandem solar cell.

	$i_{sc}/(\text{mA}/\text{cm}^2)$	$V_{oc}/\text{V}$	FF/%	$\eta/\%$
Exp	15.6	1.96	80.2	24.5
Cal	15.8	1.96	77.9	24.1
Adj	16.3	2.13	87.6	30.5
Bif	18.5	2.13	88.8	35.1

Table 6.3:  $i - V$  characteristics, FF and PCE of the 2T perovskite-on-perovskite tandem solar cell from experiment (Exp), model calibration (Cal), model prediction with adjusted parameter values (Adj) and the bifacial operation (Bif).

### 6.5.5 Levelized cost of electricity

The levelized cost of electricity (LCOE) is an important metric widely used in the energy and renewables industry to assess and compare the cost of generating electricity over the entire life cycle of a system, including photovoltaic modules and power plants. LCOE is calculated as the ratio of the total life cycle costs to the total electricity generated over the system's lifetime.

In photovoltaic applications, the costs comprise materials, utilities, depreciation and maintenance, labor, overhead, and other expenses, as described by Li *et al.* [113]. They estimated the LCOE for various solar cell technologies, including traditional silicon solar cells, planar perovskite solar cells, 2T perovskite-on-silicon tandem solar cells, and 2T perovskite-on-perovskite tandem solar cells. The LCOE values for these technologies were 5.50, 4.34, 5.22, and 4.22 US cents per kilowatt-hour (kWh), respectively. Among these, 2T perovskite-on-perovskite tandem solar cell modules are expected to be the most cost-efficient, assuming a mass production power conversion efficiency (PCE) of 22%.

Additionally, when the PCE of 2T perovskite-on-perovskite tandem solar cell modules reaches 24.5%—matching the PCE of our calibrated device—the LOCE can be further reduced to approximately 3.79 US cents per kWh. This assumes that the fabrication techniques and costs remain constant. Furthermore, by aiming for a PCE of 30.5% in the optimized device structure, the LCOE is expected to decrease to about 3.04 US cents per kWh in the future. This notably low LCOE underscores the considerable potential

of 2T perovskite-on-perovskite solar cells for commercial applications. An extention of our model includes associating each material and fabrication processes with the costs involved. Nonetheless, the model and the methodologies to improve the PCE are crucial for determining the architecture guidelines of the solar cell, as well as its potential towards next generation highly efficient photovoltaic device.

### 6.5.6 Bifacial operation

Despite the adjustments to our parameters, the PCE of the 2T perovskite-on-perovskite tandem solar cell remains below the SQ limit of 33.7%. To potentially exceed this limit, one approach is the use of bifacial solar cells. Extending our model for bifacial operation is straightforward by modifying the optical boundary conditions in our mathematical formulation. We assume a constant effective spectral responsive albedo, denoted as  $R_a$ , which represents the ratio of rear-side incident light power to front-side incident light power across all wavelengths. We set  $R_a$  to 0.2 based on experimental data for common rear-side ground materials such as green grass, red brick, and dark sand, where albedos around 0.2 have been reported [114, 115]. Other parameters remain the same as those in the adjusted parameter set, except for changes in the thicknesses of the two perovskite layers, which are adjusted to increase the  $i_{sc}$  for the bifacial 2T perovskite-on-perovskite tandem solar cell. The material of the last back contact layer is switched from Cu to ITO to make the rear side semi-transparent. The work function at the back contact,  $W^B$ , is maintained at 4.3 eV [116]. The calculation of bifacial equivalent PCE for a bifacial 2T perovskite-on-perovskite tandem solar cell is performed using Eq. 7.7, as described by Russell *et al.* [115]

By increasing the top perovskite thickness to 700 nm while keeping the bottom perovskite thickness at 940 nm, we achieved  $i_{p,t}$ ,  $i_{p,b}$  and  $i_{sc}$ , all around 18.5 mA/cm<sup>2</sup>. This  $i_{sc}$  is significantly higher compared to those in the non-bifacial 2T perovskite-on-perovskite tandem solar cell cases we have looked at. In this bifacial operation, the bottom cell primarily receives the rear-incident light power. As the bottom perovskite exhibits broad absorption characteristics, a substantial portion of the rear-side light power

is absorbed by it, reducing the light that reaches the top cell. To address this, we increased the top perovskite thickness from 440 nm to 700 nm, resulting in a higher  $i_{p,t}$  for effective current matching. The predicted  $i - V$  curve for the extended bifacial 2T perovskite-on-perovskite tandem solar cell model is shown in Figure 6.11(b). According to the data presented in Table 6.3, the predicted bifacial equivalent PCE has reached 35.1%.

The enhancement in PCE for bifacial 2T devices is substantial. However, several challenges in bifacial operation and device setups must be addressed. Inconsistent environmental conditions, including factors like heavy wind, rain, snow, and seasonal changes, can significantly affect the spectral albedo,  $R_a$ . Even slight perturbations in rear-incident light power can disrupt the current matching condition, leading to a decrease in PCE. Additionally, there's a challenge related to the spacing between solar cell modules in a bifacial setup. These modules need to be adequately spaced to capture sufficient power reflected from the ground, but this can reduce the total area available for electricity generation in a power station, for example. Moreover, rear-incident light consists of diffused light due to ground reflection, so changes in ground surface conditions caused by environmental factors can also influence rear side incident angle and device performance. Furthermore, once the modules are optimized for layer thicknesses and fabricated, they cannot adapt to maintain current matching conditions under varying environmental conditions, which is another concern to consider in bifacial setups. Nevertheless, research on 2T devices under bifacial operation remains preferable due to their highly attractive PCE and significant potential in high albedo conditions, such as those found in white sandy areas and snowy regions.

### 6.5.7 Sensitivity analysis

In the previous section, a 2T perovskite-on-perovskite tandem solar cell model calibrated to the state of the art 2T perovskite-on-perovskite tandem solar cell is presented. Based on the model, several parametric studies are done involving either a single or maximum two parameter(s). In order to further examine the potential of a 2T perovskite-on-

perovskite tandem solar cell to have a better performance, a Monte Carlo simulation is conducted to study the sensitivities of twenty-eight parameters on  $V_{oc}$ ,  $i_{sc}$ , FF and PCE ( $\eta$ ).

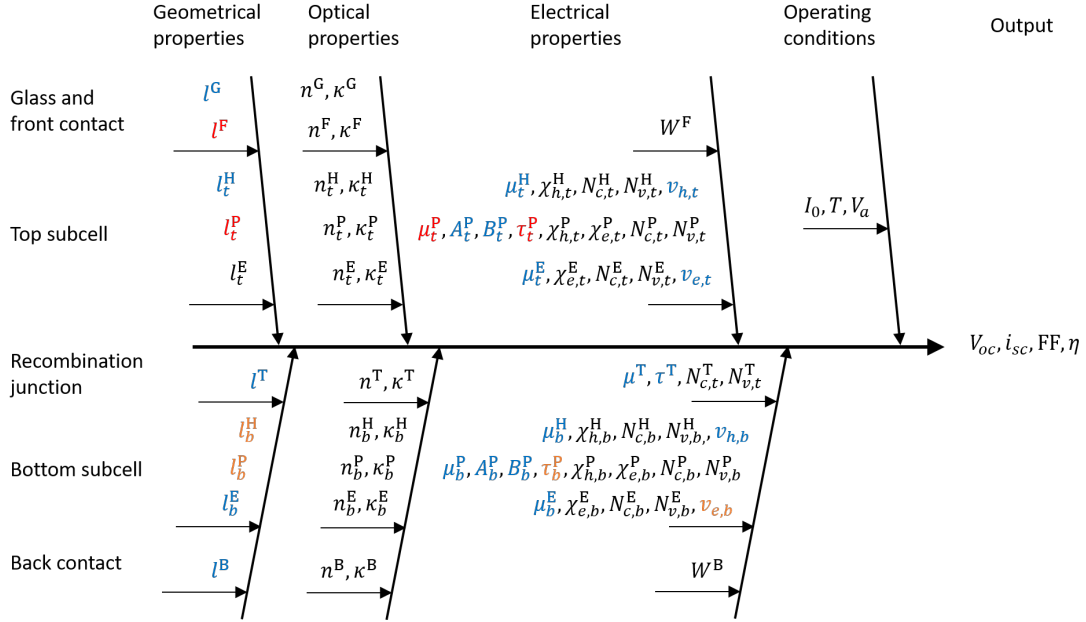


Figure 6.12: Fishbone diagram for the parameters involved in the 2T perovskite-on-perovskite tandem solar cell modeling, with the twenty eight chosen stochastic parameters for Monte Carlo simulation in blue, top four determined most sensitive parameters in red, and next four influential parameters in yellow.

There are three different parametric spaces prepared by random normal sampling, Latin Hypercube sampling, and random sampling to investigate the effects of the stochastic parameters on the cell performance. The parameters are varied simultaneously and their partial correlations to the output performances are evaluated through the sigma-normalized derivative method. Figure 6.12 shows the fishbone diagram for most of the parameters involved in the 2T perovskite-on-perovskite tandem solar cell model with the twenty eight chosen stochastic parameters highlighted in blue, top four most sensitive parameters highlighted in red, and four more parameters that can be more influential compared to the rest in yellow. The top four parameters are the top perovskite mobility,  $\mu_t^P$ , top perovskite layer thickness,  $l_t^P$ , front contact thickness,  $l^F$ , and top perovskite SRH recombination lifetime,  $\tau_t^P$ . The next four parameters identified that can still be influential are the bottom perovskite layer thickness,  $l_b^P$ , bottom hole-transporting layer thickness,  $l_b^H$ , bottom perovskite SRH recombination lifetime,  $\tau_b^P$ , and net recombination

velocity at the interface between bottom subcell perovskite and electron-transporting layer,  $v_{e,b}$ . These identified parameters that can have significant effect on the cell performance are similar to the parameters studied in the previous 2T perovskite-on-perovskite tandem solar cell modeling section.

#### 6.5.7.1 Correlation from normal distribution

How effective the parameters are on the cell performances are ranked according to their partial correlations to the outputs. For the case of normally distributed parameter space, the sensitivities,  $S_X^\sigma$ , for the top ten most influential parameters on the  $V_{oc}$ ,  $i_{sc}$ , FF and PCE are shown in Figure 6.13.

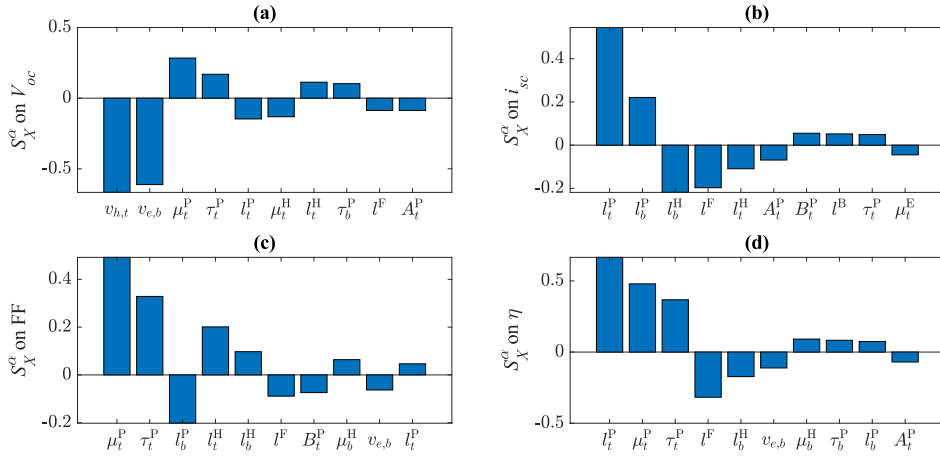


Figure 6.13: Sensitivity rankings of the stochastic parameters involved in the 2T perovskite-on-perovskite tandem solar cell from a normally distributed input for (a)  $V_{oc}$ ; (b)  $i_{sc}$ ; (c) FF; and (d) PCE.

From Figure 6.13(a), for  $V_{oc}$ , most of the effective parameters are involved in charge carrier transport. The top two parameters are the net surface recombination velocities,  $v_{h,t}$  and  $v_{e,b}$ , which aligned with how these surface recombinations affect  $V_{oc}$  in the previous section. This is because  $V_{oc}$  is related to the recombination losses in the 2T perovskite-on-perovskite tandem solar cell. A decrease in recombination rate results in less current loss at a high applied voltage, which gives a higher  $V_{oc}$ . On the other hand, for  $i_{sc}$ , the geometrical parameters, especially the perovskite layer thicknesses, play an important role, as shown in Figure 6.13(b). The maximum photo current that can be

generated depends more on the active layer thicknesses. At zero applied voltage, the recombination loss is neglectable, and thus the carrier transport properties do not have significant effect on  $i_{sc}$ . In Figure 6.13(c), for FF, we observe a mix of geometrical and electrical parameters since the calculation of FF involves both  $V_{oc}$  and  $i_{sc}$ . The bottom perovskite thickness,  $l_b^P$  is a crucial parameter in affecting  $i_{sc}$  as well as FF. It has a positive correlation to  $i_{sc}$  but a negative correlation to FF, both with similar magnitude of 0.2. As such, an increase in  $l_b^P$  is beneficial on an optical aspect, however, results in larger recombination in the bottom subcell and a lower FF. The combination of these two effects makes  $l_b^P$  cease to be identified as a key factor in affecting the PCE, as shown in Figure 6.13(d). For PCE, the most influential parameters are the top subcell perovskite thickness, carrier mobility and SRH recombination lifetime, together with the front contact thickness. Hence, the top subcell is relatively more important in the overall design of the 2T perovskite-on-perovskite tandem solar cell, while the front contact thickness is also crucial since it can contribute significantly to reflection loss and parasitic absorption.

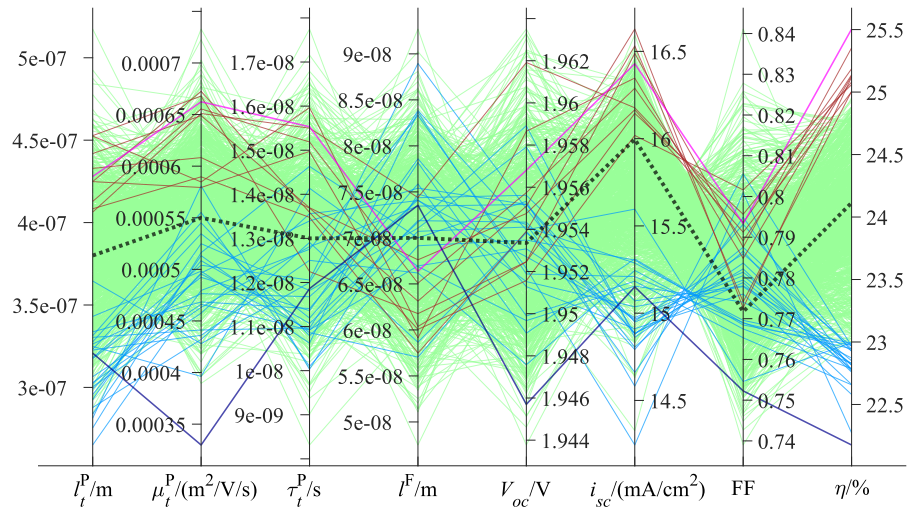


Figure 6.14: Input and output parametric space including the top four parameters for the case of normal distribution, with dataset for the highest PCE (magenta line); PCE larger than 25% (red line); PCE within 23% to 25% (green line); PCE smaller than 23% (cyan line); the lowest PCE (blue line); and the calibration case (dotted line) shown.

The input and output data space including the top four parameters for the PCE is shown in Figure 6.14. There is a strong correlation between the top perovskite thickness and  $i_{sc}$  as well as PCE by observing the distributions of the data set according to high

and low PCE. Besides, the charge carrier transport system is relatively more complicated compared to the optical system, because the data for high, medium, and low PCE are more clustered together by looking at the  $V_{oc}$  and FF. This is because both geometrical and electrical parameters can influence these output. This non-linearity in the numerical model indicates a difficulty to simplify the model to a linear regression model. A neural network model could be more helpful in this case as a more effective tool compared to simple regressions. From the parametric space, we found the maximum and minimum PCEs to be around 25.5% and 22%, respectively, and the maximum improvement in PCE from the calibrated case is around 1.5% for this set of data. Comparing to the calibrated values and the parameter values that give the highest PCE of 25.5%, the top perovskite layer thickness is increased from 380 to 430 nm, the top perovskite mobility is increased from  $5.5 \times 10^{-4}$  to more than  $6.5 \times 10^{-4} \text{ m}^2/\text{V}\cdot\text{s}$ , the top perovskite SRH lifetime is increased from about  $1.3 \times 10^{-8}$  to near  $1.6 \times 10^{-8} \text{ s}$ , and the front contact thickness is slightly decreased. Small perturbations of the system is able to give a near to 1.5% increase in PCE.

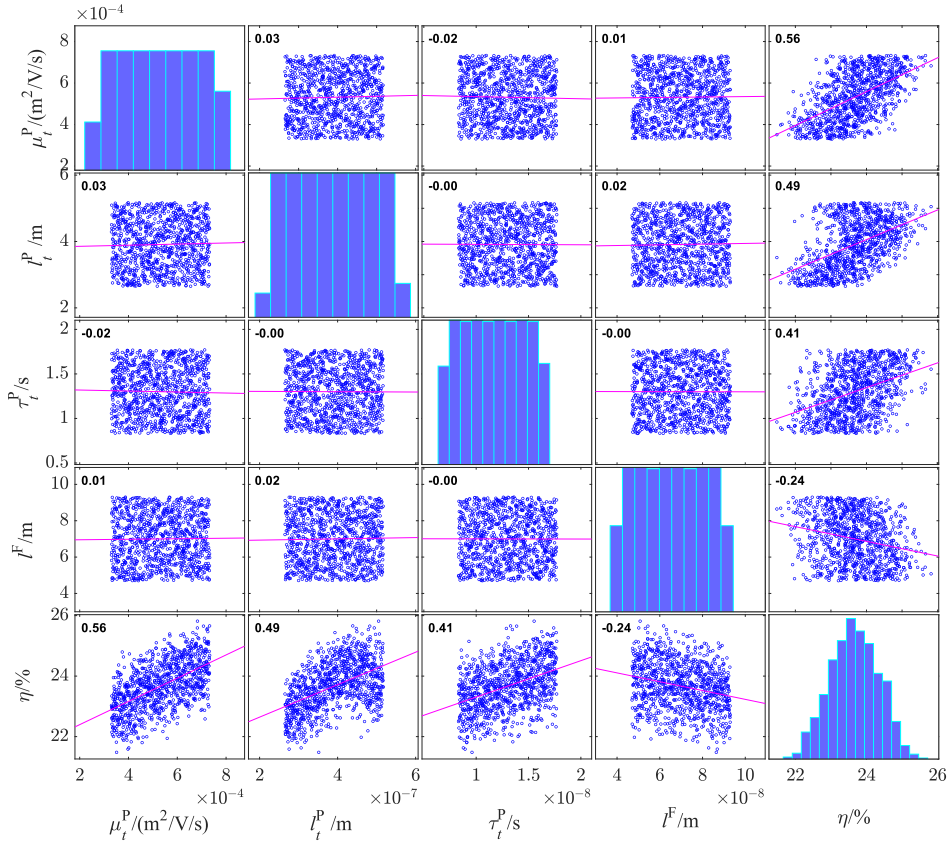


Figure 6.15: Correlation matrix for the relations among the top four most sensitive parameters and the PCE, in the case of normal distribution.

In addition, it is found that for the top perovskite thickness, which is ranked as the first most influential parameter, its largest and smallest values do not guarantee the highest and lowest PCE outputs. This could be because of the light interference effect. The top perovskite thickness should always be coupled with a bottom perovskite thickness for optimum current matching. Also, increase the perovskite layer thickness can lead to more recombination, and therefore not the thicker the better. For the second most influential parameter, the charge carrier mobility in top perovskite layer, it is found that its smallest value corresponds to the lowest PCE for this data space. This mobility cannot be too low in order to avoid small carrier diffusion length. Its largest value, however, does not match with the highest PCE, since the effects from the other influential factors such as the perovskite and front contact layer thicknesses, and the SRH recombination lifetime should be considered as well.

The correlation matrix involving the top four parameters and the PCE is shown in

Figure 6.15. The distributions of the parameters are close to normal distributions as expected. The larger the sensitivity value,  $S_X^\sigma$ , the stronger the correlation between the parameter and the output PCE. There will be less dispersion and stronger linear relationship with the PCE for a more influential parameter, which can be inferred from the correlation between  $l_t^P$  and the PCE. There is no correlation between the input parameters as we assumed they are independent on each other. The output PCE might not follow an exact normal distribution due to the complexity of the optical and carrier transport systems in the 2T perovskite-on-perovskite tandem solar cell.

### 6.5.7.2 Correlation from Latin hypercube and random sampling

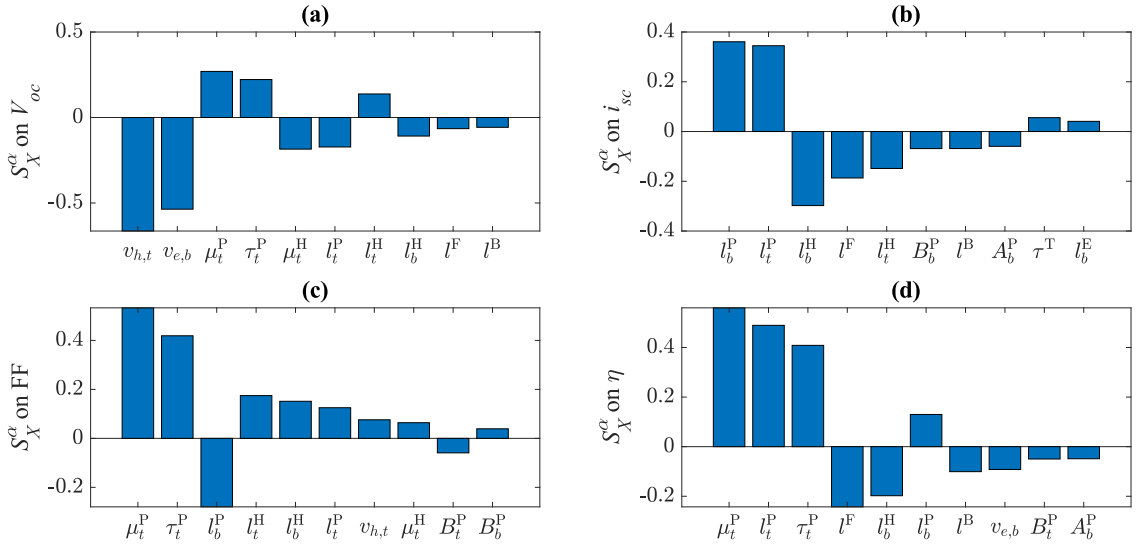


Figure 6.16: Sensitivity rankings of the stochastic parameters involved in the 2T perovskite-on-perovskite tandem solar cell from a Latin hypercube sampled input for (a)  $V_{oc}$ ; (b)  $i_{sc}$ ; (c) FF; and (d) PCE.

To confirm on the sensitivity analysis results, two more data space with Latin hypercube and random sampling are employed in the Monte Carlo simulation. In the case of Latin hypercube sampling, the parameter sensitivity rankings are shown in Figure 6.16. Comparing to the first case with normally distributed parameters, the sensitivity rankings are found to be similar with the top four most sensitive parameters being the same. The top perovskite mobility has surpassed the layer thickness as the most influential parameter. This could be due to the different parameter ranges in preparing the data as shown in

the parametric space in Figure 6.17. The top perovskite mobility could have a larger net effect when the data is more widely distributed. The data distribution and correlation matrix are shown in Figure 6.18.

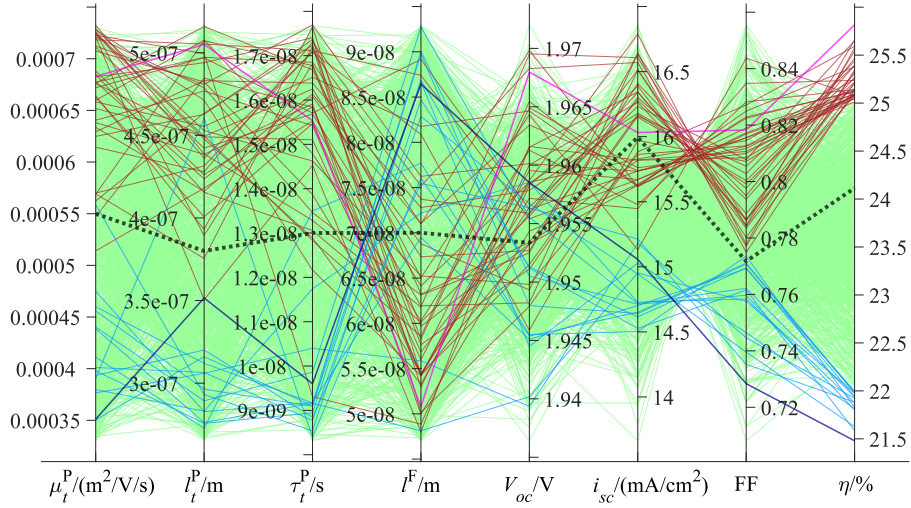


Figure 6.17: Input and output parametric space including the top four parameters for the case of Latin hypercube sampling, with dataset for the highest PCE (magenta line); PCE larger than 25% (red line); PCE within 22% to 25% (green line); PCE smaller than 22% (cyan line); the lowest PCE (blue line); and the calibration case (dotted line) shown.

From the parametric space, the ranges for the PCEs are wider compared to the results from normal distribution. This is because for the later sampling methods, the data are more dispersed as seen in the correlation matrices. The highest and lowest PCEs are around 26% and 21.5% respectively, which gives a near 2% increase from the calibrated PCE with small variations of the parameters (10% standard derivations from the mean values). Comparing to the calibrated values and the parameter values that give the highest PCE of near 26%, the top perovskite mobility is increased from  $5.5 \times 10^{-4}$  to near  $7 \times 10^{-4} \text{ m}^2/\text{V/s}$ , the top perovskite layer thickness is increased from 380 to more than 500 nm, the top perovskite SRH lifetime is increased from about  $1.3 \times 10^{-8}$  to near  $1.6 \times 10^{-8} \text{ s}$ , and the front contact thickness is decreased from 70 to 50 nm. Comparing to the normal distribution case, a slightly larger perturbations of the system, but still within the same parameter ranges, is able to give a near to 2% increase in PCE. This is because in the Latin hypercube sampling case, more data with parameters near their lower and upper bounds are included. Similar to the case of normally distributed input,

a low top perovskite carrier mobility should be avoided and the layer thicknesses should be optimized for current matching.

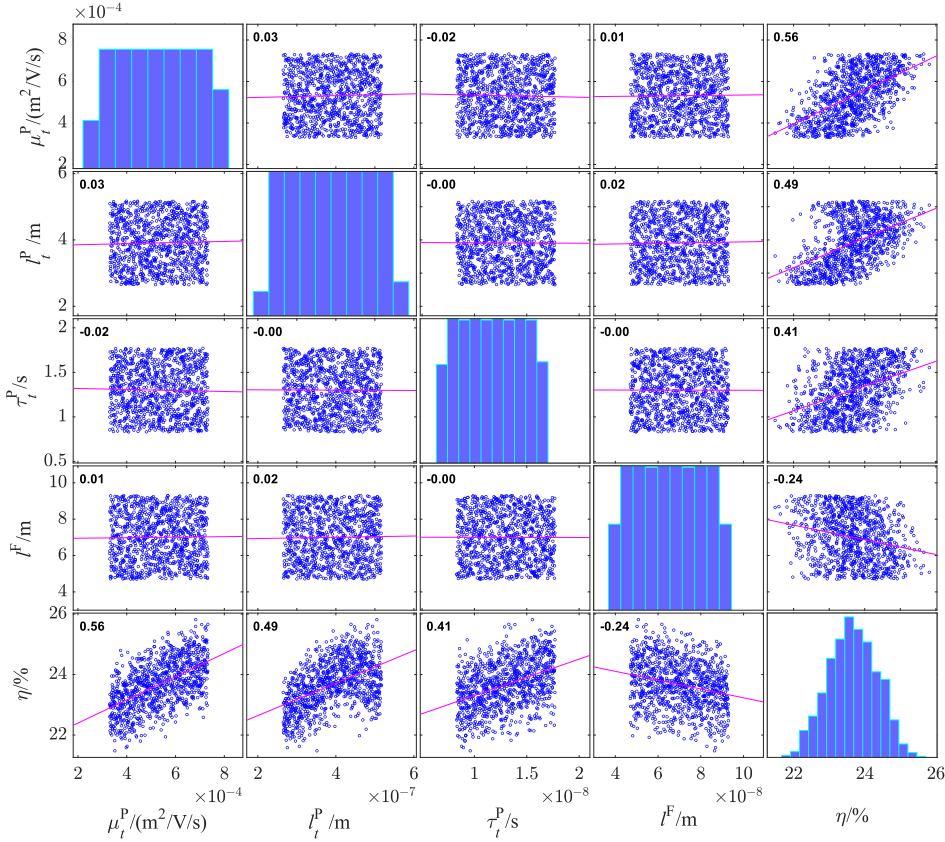


Figure 6.18: Correlation matrix for the relations among the top four most sensitive parameters and the PCE, in the case of Latin hypercube sampling.

From the correlation matrix, the PCE output, compared to the normal distribution case, is more widely spread and follows a normal distribution better. The Latin hypercube sampling, different from normal distribution, covers the parametric spaces for the parameter values and their lower and upper bounds, which can be seen from the rectangular shaped correlation in between each pair of the input parameters. This helps to include those extreme parameter combinations which we are also interested for an optimum PCE. The weight in this distribution is shifted more away from the mean value towards the bounds, as compared to the normal distribution case, and this may result in a wider and more normally distributed PCE from 21.5% to 26%. Besides, from the correlation matrix, it is found that the relation between  $l_t^P$  and the PCE is slightly different

from the rest. There is an elliptical empty space on the left where only a few data can be seen. This is because once the top perovskite layer thickness is higher than about 400 nm, the resulted matched current has been increased. Therefore, there is less chance for the PCE to fall below 23%. There are only few data PCE points that are lower than 22% when  $l_t^P$  is larger than 400 nm.

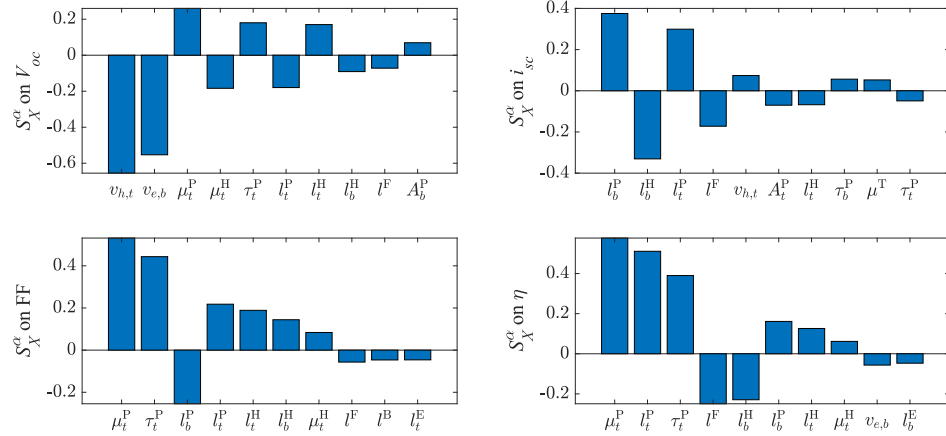


Figure 6.19: Sensitivity rankings of the stochastic parameters involved in the 2T perovskite-on-perovskite tandem solar cell from a random sampling input for (a)  $V_{oc}$ ; (b)  $i_{sc}$ ; (c) FF; and (d) PCE.

For random sampling, the rankings are mostly identical to the case of Latin hypercube sampling with the top four parameters being the same, as shown in Figure 6.19

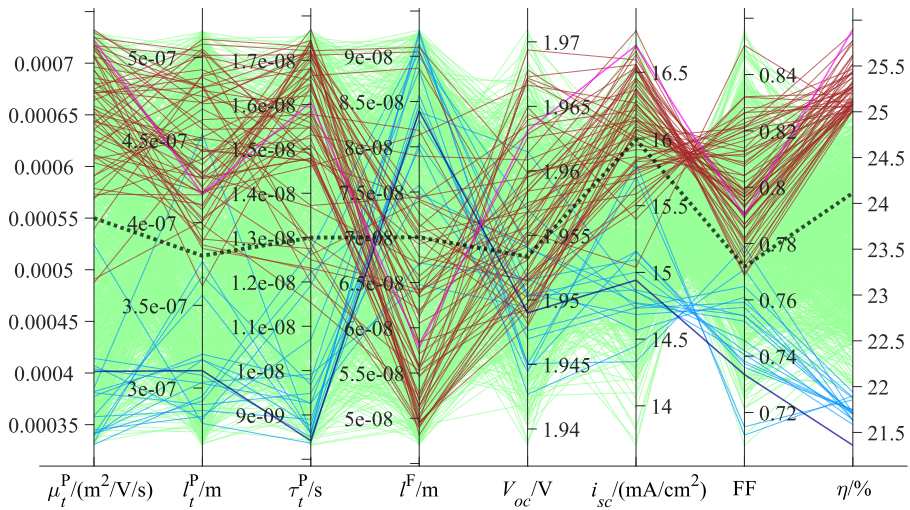


Figure 6.20: Input and output parametric space including the top four parameters for the case of random sampling, with dataset for the highest PCE (magenta line); PCE larger than 25% (red line); PCE within 22% to 25% (green line); PCE smaller than 22% (cyan line); the lowest PCE (blue line); and the calibration case (dotted line) shown.

The corresponding parametric space and correlation matrix are shown in Figure 6.20 and 6.21, respectively. From both Latin hypercube and random sampling, although the data are still clustered together for  $V_{oc}$ , high top perovskite mobility, long top perovskite lifetime and a thin front contact layer results in a high FF, and vice versa. The results between the Latin hypercube sampling and random sampling cases are mostly identical due to the similarity in the data distribution. Nevertheless, since the data are randomly sampled, some parameter combinations can be missed out as compared to the Latin hypercube sampling case. The output PCE is no longer normally distributed.

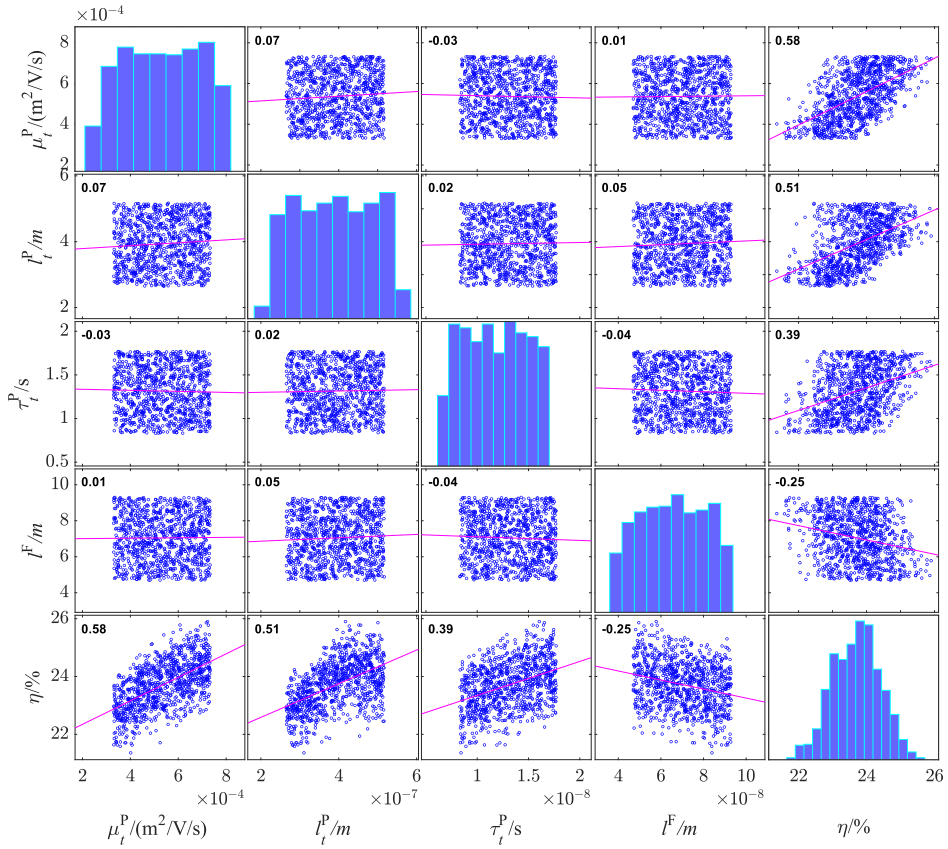


Figure 6.21: Correlation matrix for the relations among the top four most sensitive parameters and the PCE, in the case of random sampling.

From all three data sets, we confirmed from the Monte Carlo simulation that  $\mu_t^P$ ,  $l_t^P$ ,  $l^F$ , and  $\tau_t^P$  are the most crucial factors in determining the performance of the 2T perovskite-on-perovskite tandem solar cell from all three prepared data sets. The next four parameters chosen that can still be influential are  $l_b^P$ ,  $l_b^H$ ,  $\tau_b^P$ , and  $v_{e,b}$ , which are always ranked as the top ten parameters and are identified to be important.

## 6.6 Summary

We present an optoelectronic model for a 2T perovskite-on-perovskite tandem solar cell that considers coherent and incoherent light propagation, optical interference effect, charge carrier conservation including various recombination mechanisms, and trap-assisted tunneling at the interconnecting layer. We calibrate the model to the world record 2T perovskite-on-perovskite tandem solar cell with 24.5% PCE. From the in-

sights we gained from light management and loss analysis, together with increasing the carrier mobility in the top perovskite layer, we predict a 6% increase in the PCE towards 30.5%. Extending to bifacial operation, our results show the possibility for a bifacial 2T perovskite-on-perovskite tandem solar cell to reach a 35.1% PCE in this paper, which exceeds the Shockley–Queisser limit.

The model can also be easily applied to other 2T perovskite-on-perovskite tandem solar cell with different planar top and bottom perovskite solar cell structures, different layer materials and thicknesses, and under different incident light spectrum. Other than this, it can be further extended towards multi-terminal perovskite-on-perovskite tandem solar cell. Hence, our model can be widely adopted and calibrated to different fabricated 2T perovskite-on-perovskite tandem solar cells, and provide sound insights towards achieving a higher PCE.

Additionally, we conducted Monte Carlo simulations and sensitivity analyses using different sampling methods. Eight parameters were identified as relatively more influential than the rest:  $l^F$ ,  $l_t^P$ ,  $l_b^P$ , and  $l_b^H$  as geometrical parameters, and  $\mu_t^P$ ,  $\tau_t^P$ ,  $\tau_b^P$ , and  $v_{e,b}$  as electrical parameters. The top and bottom perovskite layer thicknesses play a crucial role in maximizing the photogenerated current collected from the top and bottom subcells, while the front contact layer thickness affects reflection loss and parasitic absorption. The thickness of the bottom hole-transporting layer can also be influential due to parasitic absorption. Moreover, the top perovskite carrier mobility influences the diffusion length and recombination loss in the bulk. The SRH recombination lifetime in both perovskite layers significantly contributes to the overall recombination loss, as observed in the previous loss analysis. Finally, surface recombination at the bottom perovskite and electron-transporting layer interface should not be neglected as it affects  $V_{oc}$ . By analyzing the sensitivity, we identified the key parameters affecting cell performance. Furthermore, by studying the positive or negative correlations between these parameters and output performance, we can offer valuable suggestions for enhancing cell efficiency through adjustments in layer thicknesses or slight tuning of material properties.

# Chapter 7

## 2T perovskite-on-organic tandem solar cells

### 7.1 Introduction

2T perovskite-based thin-film tandem solar cells have garnered increasing interest as cost-effective photovoltaic devices, driven by rapid advancements in PCEs in recent years [28]. These tandem solar cells encompass various configurations, including perovskite-on-silicon, perovskite-on-perovskite, perovskite-on-copper indium gallium selenide, and perovskite-on-organic tandem solar cells, boasting respective record PCEs of 33.7% [12], 28.0% [29], 24.2% [30], and 24.0% [31]. While the PCE of 2T perovskite-on-organic tandem solar cells may lag behind, it has made significant progress, increasing from 18% to 24% in the past two years [27, 31, 34, 35, 36, 37, 38, 39]. This type of tandem solar cell continues to show promise, offering advantages like tunable broad band-gap characteristics [40, 41] and fewer challenges in solution processing [37] compared to perovskite-on-perovskite tandem solar cells.

The interplay between the interconnecting layer and the top and bottom sub-cells is critical for the performance of a 2T perovskite-on-organic tandem solar cell. In terms of optics, the interconnecting layer connects the sub-cells in series, restricting the current in the device to that of the subcell producing the lower current. On the electronic side,

recombination losses from both sub-cells can reduce the overall PCE of the 2T device. An ideal interconnecting layer must exhibit high transparency, excellent electrical conductivity, and a sufficient number of recombination sites [27] to minimize optical and voltage losses while promoting effective charge carrier recombination between the sub-cells. Consequently, the performance of a 2T perovskite-on-organic tandem solar cell is influenced by both the sub-cells and the interconnecting layer, and it is unclear which physical parameter has the most significant impact. To bridge this knowledge gap, we employ optoelectronic modeling of the 2T device to identify the sensitive parameters, elucidate the underlying physics, and provide guidance for achieving a higher PCE.

To elucidate the underlying physics, we have developed an optoelectronic model for 2T perovskite-on-organic tandem solar cells. This model is based on our previously developed single-junction models for both perovskite solar cells and organic solar cells [15, 17, 117]. Within this model, we have taken into account the interplay of optics, charge carrier transport, and recombination, creating a fully coupled representation of the tandem device. Calibration and validation of the model are performed using experimental data from 2T perovskite-on-organic tandem solar cells with a PCE of 23.6% [27]. Sensitivity and loss analyses are carried out to identify influential parameters and key recombination losses. In particular, we have explored the impact of surface coverage, bulk and sheet resistances on charge carrier recombination in the interconnecting layer. Additionally, we have investigated scenarios where the interconnecting layer fails as an efficient recombination junction. Moreover, we have identified a pathway for enhancing the PCE of 2T perovskite-on-organic tandem solar cells to achieve 30% by focusing on improving charge carrier dissociation, transport, and recombination.

## 7.2 Mathematical formulation

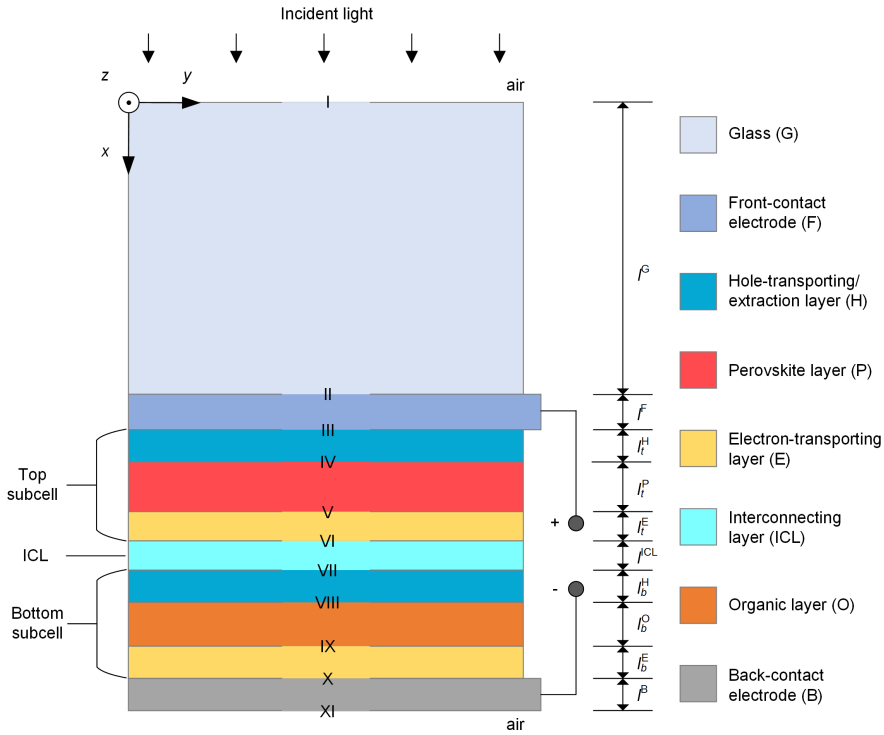


Figure 7.1: Schematic diagram of a 2T perovskite-on-organic tandem solar cell.

Our optoelectronic model for a 2T perovskite-on-organic tandem solar cell is based on the structure in Figure 7.1, where the Roman numerals denote the interfaces.  $l$  is the layer thickness. G, F, H, P, E, ICL, O, and B are superscripts that denote the glass, front-contact, hole-transporting/extraction, perovskite, electron-transporting, interconnecting, organic, and back-contact layers, respectively. The subscripts  $t$  and  $b$  represent the top and bottom sub-cells, respectively. The model comprises a top perovskite subcell and a bottom organic subcell electrically connected via ICL in between. We consider the device under  $1000 \text{ W/m}^2$  solar irradiance,  $25^\circ\text{C}$  cell temperature, and ASTM G173-03 Global tilt standard spectrum [51]. Although both subcells are in p-i-n configuration, this model can easily accommodate and simulate other designs. The semi-analytical solution for the charge carrier generation rate and most model characteristics and assumptions can be found in our previous work [78]. Additional features and assumptions are listed below.

1. Radiative recombination and SRH recombination are considered in the perovskite

layer, while the non-dominant Auger recombination is not considered.

2. In the organic layer, electron-hole pairs undergo the charge transfer state, and the Langevin recombination is considered [118].
3. For an interconnecting layer with charge carrier recombination as the mechanism, Hurkx's trap-assisted recombination model is adopted [101]. The recombination lifetime,  $\tau_{(e,h)}^{\text{ICL}}$ , for electrons and holes are equal.
4. When the interconnecting thickness increases, it can fail as an efficient recombination junction. We propose that charge carrier transport instead of charge carrier recombination should be the mechanism. In this case, there is no recombination inside the interconnecting layer. Instead, interface recombination is considered at its adjacent interfaces.

We extend the optics and electronics discussed in Chapter 2, 3 and 6 to the 2T perovskite-on-organic tandem solar cell device, and they are summarized in the following subsections.

### 7.2.1 Governing equations

$$j'_h = S_j, \text{ (H,P,ICL,O)} \quad (7.1)$$

$$j'_e = S_j, \text{ (P,E,ICL,O)} \quad (7.2)$$

$$\varepsilon\psi'' = S_\psi, \text{ (H,P,E,ICL,O)} \quad (7.3)$$

where the source terms,  $S_j$  and  $S_\psi$ , are given by

$$S_j = \begin{cases} 0, & (\text{H,E}) \\ G - R^P, & (\text{P}) \\ PG - k_{en}(1 - P)R^O, & (\text{O}) \\ -R^{\text{ICL}}, & (\text{ICL}) \end{cases} \quad (7.4)$$

$$S_\psi = e \begin{cases} N_a - c_h, & (\text{H}) \\ c_e - c_h, & (\text{P,ICL,O}) \\ c_e - N_d, & (\text{E}) \end{cases} \quad (7.5)$$

where  $P$  is the exciton dissociation probability in the charge transfer state and  $k_{en}$  is the recombination reduction factor.

The current density,  $i_{tot}$ , can be written as

$$i_{tot} = e(j_h - j_e), \quad (7.6)$$

and the power conversion efficiency,  $\eta$ , can be expressed as

$$\eta = \max(p)/p_{\text{sun}}, \quad (7.7)$$

where  $p$  is the output power density at a voltage applied and  $p_{\text{sun}}$  is the normalized one sun power density which is equivalent to 1000 W/m<sup>2</sup>.

### 7.2.2 Boundary conditions

For the Poisson's equation, by assuming the front and back contact layers as ohmic contacts, the corresponding boundary conditions at interface III and X at different applied voltages,  $V_a$ , can be written as

$$\psi^{\text{III}} = V_a - V_b, \psi^{\text{X}} = 0, \quad (7.8)$$

where  $V_b$  is the built-in voltage.

For the conservation of charge carriers in the top cell from interface III to VI, we have

$$c_h^{\text{III}} = c_h^0, \quad (7.9)$$

$$c_{h,+}^{\text{IV}} = \Pi_{h,t} c_{h,-}^{\text{IV}}, j_{h,-}^{\text{IV}} = j_{h,+}^{\text{IV}} - j_s^{\text{IV}}, j_{e,-}^{\text{IV}} = j_s^{\text{IV}}, \quad (7.10)$$

$$c_{e,-}^{\text{V}} = \Pi_{e,t} c_{e,+}^{\text{V}}, j_{e,+}^{\text{V}} = j_{e,-}^{\text{V}} - j_s^{\text{V}}, j_{h,+}^{\text{V}} = j_s^{\text{V}}, \quad (7.11)$$

$$j_{e,-}^{\text{VI}} = j_{e,+}^{\text{VI}}. \quad (7.12)$$

Similarly, in the bottom cell from interface VII to X, we have

$$j_{h,+}^{\text{VII}} = j_{h,-}^{\text{VII}}, \quad (7.13)$$

$$c_{h,+}^{\text{VIII}} = \Pi_{h,b} c_{h,-}^{\text{VIII}}, j_{h,-}^{\text{VIII}} = j_{h,+}^{\text{VIII}} - j_s^{\text{VIII}}, j_{e,-}^{\text{VIII}} = j_s^{\text{VIII}}, \quad (7.14)$$

$$c_{e,-}^{\text{IX}} = \Pi_{e,b} c_{e,+}^{\text{IX}}, j_{e,+}^{\text{IX}} = j_{e,-}^{\text{IX}} - j_s^{\text{IX}}, j_{h,+}^{\text{IX}} = j_s^{\text{IX}}, \quad (7.15)$$

$$c_e^X = c_e^0. \quad (7.16)$$

In addition, in the recombination junction from interface VI to VII, we have

$$c_{e,+}^{\text{VI}} = \Pi_e^{\text{ICL}} c_{e,-}^{\text{VI}}, j_{e,+}^{\text{VI}} = j_{e,-}^{\text{VI}}, j_{h,+}^{\text{VI}} = 0, \quad (7.17)$$

$$c_{h,-}^{\text{VII}} = \Pi_h^{\text{ICL}} c_{h,+}^{\text{VII}}, j_{h,-}^{\text{VII}} = j_{h,+}^{\text{VII}}, j_{e,-}^{\text{VII}} = 0. \quad (7.18)$$

### 7.2.3 Constitutive relations

The built-in voltage and the reference carrier concentrations at interface III and X are calculated as

$$V_b = (W^F - W^B)/e, \quad (7.19)$$

$$c_h^0 = N_{v,t}^H \exp \left[ (W^F - \chi_{h,t}^H)/(k_B T) \right], \quad (7.20)$$

$$c_e^0 = N_{c,b}^E \exp \left[ (\chi_{e,b}^E - W^B)/(k_B T) \right]. \quad (7.21)$$

At boundaries IV to IX, the ratios describing the jumps in carrier concentrations,  $\Pi$ , are defined as

$$\Pi_{h,(t,b)} = (N_{v,(t,b)}^P / N_{v,(t,b)}^H) \exp \left[ (\chi_{h,(t,b)}^H - \chi_{h,(t,b)}^P) / (k_B T) \right], \quad (7.22)$$

$$\Pi_h^{ICL} = (N_{v,b}^H / N_v^{ICL}) \exp \left[ (\chi_{h,b}^H - \chi_h^{ICL}) / (k_B T) \right], \quad (7.23)$$

$$\Pi_e^{ICL} = (N_{c,t}^E / N_c^{ICL}) \exp \left[ (\chi_{e,t}^E - \chi_e^{ICL}) / (k_B T) \right]. \quad (7.24)$$

For the recombination inside the 2T perovskite-on-organic tandem solar cell, we consider Auger recombination, radiative recombination and SRH recombination in the perovskite layers:

$$R^P = R_{aug} + R_{rad} + R_{SRH}, \quad (7.25)$$

$$R_{aug} = (A_e c_e + A_h c_h) (c_e c_h - c_i^2), \quad (7.26)$$

$$R_{rad} = B_{rad} (c_e c_h - c_i^2), \quad (7.27)$$

$$R_{srh} = \frac{c_e c_h - c_i^2}{\tau_e (c_h + c_{h,trap}) + \tau_h (c_e + c_{e,trap})}; \quad (7.28)$$

and Langevin recombination in the organic layer:

$$R^O = R_{Lan}, \quad (7.29)$$

$$R_{Lan} = \frac{e c_e c_h (\mu_e + \mu_h)}{\epsilon} \quad (7.30)$$

The various recombination fluxes originated from the recombination channels are evaluated as

$$j_{aug} = \int_P R_{aug} dx, j_{rad} = \int_P R_{rad} dx, j_{srh} = \int_P R_{srh} dx, j_{Lan} = \int_O R_{Lan} dx \quad (7.31)$$

In addition, the surface recombination carrier flux,  $j_s$ , can be found as

$$j_s^{(\text{IV,VIII})} = v_h \left( c_{e,+}(c_{h,-} + c_{h,+}) - c_{i,(t,b)}^{\text{P}}(c_{i,(t,b)}^{\text{H}} + c_{i,(t,b)}^{\text{P}}) \right), \quad (7.32)$$

$$j_s^{(\text{V,IX})} = v_e \left( c_{h,-}(c_{e,+} + c_{e,-}) - c_{i,(t,b)}^{\text{P}}(c_{i,(t,b)}^{\text{E}} + c_{i,(t,b)}^{\text{P}}) \right). \quad (7.33)$$

During the loss analysis, we define the total recombination carrier flux,  $j_{rec}$ , as

$$j_{rec} = j_{aug} + j_{aug} + j_{rad} + j_{Lan} + j_s^{\text{IV}} + j_s^{\text{VIII}} + j_s^{\text{V}} + j_s^{\text{IX}}. \quad (7.34)$$

In the interconnecting layer we adopt the trap-assisted recombination based model from Hurkx *et al.* [101] and the trap-assisted recombination rate,  $R^{\text{ICL}}$ , is calculated as

$$R^{\text{ICL}} = \frac{c_e c_h - c_i^2}{\tau_e^{\text{ICL}}(c_h + c_{h,trap})/(1 + \Gamma_e) + \tau_h^{\text{ICL}}(c_e + c_{e,trap})/(1 + \Gamma_h)}, \quad (7.35)$$

where  $\tau^{\text{ICL}}$  is the trap-assisted tunneling coefficient and the field effect function,  $\Gamma$ , is expressed as follows

$$\Gamma_{(e,h)} = \begin{cases} (2\sqrt{3\pi} \left| \frac{d\psi}{dx} \right| / F_\Gamma) \exp \left[ (\frac{d\psi}{dx} / F_\Gamma)^2 \right] & \Lambda_{(e,h)} > \frac{2\Delta E_{(e,h)}}{3k_B T} \\ \sqrt{2\pi/(3\Lambda_{(e,h)})} \frac{\Delta E_{(e,h)} F_\gamma}{k_B T} \exp \left[ \frac{\Delta E_{(e,h)}}{k_B T} - \Lambda_{(e,h)} \right] & \Lambda_{(e,h)} \leq \frac{2\Delta E_{(e,h)}}{3k_B T} \end{cases}, \quad (7.36)$$

$$F_\Gamma = 2\pi \sqrt{24m^*(k_B T)^3} / (eh), \quad (7.37)$$

$$\Lambda_{(e,h)} = 8\pi \sqrt{2m^*(\Delta E_{(e,h)})^3} / (3eh \left| \frac{d\psi}{dx} \right|), \quad (7.38)$$

$$m^* = 0.25m_0, \quad (7.39)$$

$$F_\gamma = a_1 \gamma_{(e,h)} + a_2 \gamma_{(e,h)}^2 + a_3 \gamma_{(e,h)}^3, \quad (7.40)$$

$$\gamma_{(e,h)} = \left[ \left( 1 + \beta \left( \frac{\Delta E_{(e,h)}}{k_B T} - \frac{3}{2} \Lambda_{(e,h)} \right) \right) \sqrt{\frac{3}{2} \Lambda_{(e,h)}} \right]^{-1}. \quad (7.41)$$

Here, the filed effect function describes the ratio between the emission probability at a given electrical potential to the probability in the absence of an electrical potential,  $m^*$  is the effective mass of the majority charge carrier,  $h$  is the Planck's constant,  $a_1$ ,  $a_2$ ,  $a_3$  and  $\beta$  are constants taken from Hurkx *et al* [101, 104].

If the interconnecting layer is not thin enough as an efficient charge carrier recombination center, we consider interfacial recombinations at interfaces VI and VII instead:

$$j_s^{(\text{VI,VII})} = v_{(e,h)} c_{e,-} c_{h,+}. \quad (7.42)$$

### 7.3 Calibration and validation

Model calibration and validation are essential to test whether the 2T model can capture and reproduce experimental results. In this section, we demonstrate that our simulation results agree well with experiment. All experimental  $i - V$  curves are adopted from Chen *et al* [27].

We first calibrated the single-junction perovskite solar cell model with a stand-alone single-junction perovskite top cell. This perovskite solar cell has the following architecture: glass/ ITO/ NiO<sub>x</sub>/ perovskite/ C60/ BCP/ Ag. The fitted parameters are the perovskite radiative recombination coefficient and the surface recombination velocities at the interfaces between the perovskite active layer and its adjacent hole- and electron-transporting layers. The rest of the parameters are sourced from literature as listed in Table 7.1. Since the 2T perovskite-on-organic tandem solar cell is fabricated with the perovskite top cell using similar fabrication techniques and substrates, the fitted parameter values from the first step mentioned above could be employed in the tandem device.

Parameters	Values	Units	References
<i>Top subcell</i>			
$B_{rad}$	$5.0 \times 10^{-16}$	$\text{m}^{-3} \text{s}^{-1}$	Fitted
$\chi_e^E, \chi_h^H, \chi_e^P, \chi_h^P$	4.2, 5.2, 3.87, 5.66	eV	[94], [81], [95], [95]
$l^E, l^H, l^P$	$3.5 \times 10^{-8}, 3 \times 10^{-8}, 2.7 \times 10^{-7}$	m	SEM [27]
$\mu_e^E, \mu_h^H, \mu_e^P, \mu_h^P$	$1.6 \times 10^{-4}, 2.8 \times 10^{-4},$ $5.5 \times 10^{-4}, 5.5 \times 10^{-4}$	$\text{m}^2 \text{V}^{-1} \text{s}^{-1}$	[96], [97], [78], [78]
$N_c^E, N_c^H, N_c^P$	$1 \times 10^{22}, 1 \times 10^{24}, 1.7 \times 10^{22}$	$\text{m}^{-3}$	[88], [98], [78]
$N_v^E, N_v^H, N_v^P$	$1 \times 10^{22}, 1 \times 10^{24}, 6.9 \times 10^{22}$	$\text{m}^{-3}$	[88], [98], [78]
$\tau_{(e,h)}^P$	$1 \times 10^{-6}$	s	[99]
$\epsilon^E, \epsilon^H, \epsilon^P$	3, 11.7, 5.56		[78]
$v_e^{\text{IV}}, v_h^{\text{V}}$	$2.8 \times 10^{-25}, 3.5 \times 10^{-26}$	$\text{m}^4 \text{s}^{-1}$	Fitted
<i>Bottom subcell</i>			
$\chi_e^E, \chi_h^H, \chi_e^O, \chi_h^O$	3.93, 5.3, 4.2, 5.56	eV	[119], [120], [27], [27]
$k_{en}$	0.10		Fitted
$l^E, l^H, l^O$	$1 \times 10^{-8}, 2.5 \times 10^{-8}, 1.1 \times 10^{-7}$	m	SEM[27]
$\mu_e^E, \mu_h^H, \mu_e^O, \mu_h^O$	$2.5 \times 10^{-8}, 2.5 \times 10^{-4},$ $7.1 \times 10^{-8}, 1.9 \times 10^{-7}$	$\text{m}^2 \text{V}^{-1} \text{s}^{-1}$	[119], [121], [122], [122]
$N_c^E, N_c^H, N_c^O$	$1 \times 10^{27}, 1 \times 10^{26}, 1 \times 10^{26}$	$\text{m}^{-3}$	[123], [121], [124]
$N_v^E, N_v^H, N_v^O$	$1 \times 10^{27}, 1 \times 10^{26}, 1 \times 10^{26}$	$\text{m}^{-3}$	[123], [121], [124]
$P$	0.983		[34]
$\epsilon^E, \epsilon^H, \epsilon^O$	10, 3.37, 4.66		[125], [121], [97]
$v_e^{\text{VIII}}, v_h^{\text{IX}}$	$8.0 \times 10^{-30}, 1.0 \times 10^{-28}$	$\text{m}^4 \text{s}^{-1}$	Fitted
<i>Interconnecting layer, glass, front and back contacts</i>			
$l^B, l^F, l^G, l^{\text{ICL}}$	$1 \times 10^{-7}, 1.6 \times 10^{-7}, 1.1 \times 10^{-3},$ $1 \times 10^{-9}$	m	SEM [27]
$\mu_{(e,h)}^{\text{ICL}}$	$2.4 \times 10^{-3}$	$\text{m}^2 \text{V}^{-1} \text{s}^{-1}$	[126]
$N_{(c,v)}^{\text{ICL}}$	$1.5 \times 10^{21}$	$\text{m}^{-3}$	Assumed
$\tau_{(e,h)}^{\text{ICL}}$	$5.0 \times 10^{-12}$	s	Fitted
$v_h^{\text{VI}}, v_e^{\text{VII}}$	0,0	$\text{m}^4 \text{s}^{-1}$	Assumed
$\epsilon^{\text{ICL}}$	11.5		[127]
$W^B, W^F$	4.13, 4.9	eV	[128], [78]
<i>Constants and operating condition</i>			
$e$	$1.602 \times 10^{-19}$	C	
$h$	$6.626 \times 10^{-34}$	J s	
$k_B$	$1.38 \times 10^{-23}$	$\text{J K}^{-1}$	
$p_{in}$	1000	$\text{W m}^{-2}$	
$T$	300	K	

Table 7.1: Mathematical model parameters for the stand-alone single junction perovskite top cell and the 2T perovskite-on-organic tandem solar cell with Ag as interconnecting layer. The layer thicknesses are estimated from scanning electron microscopy diagram (SEM).

Subsequently, we calibrated the developed 2T perovskite-on-organic tandem solar

cell model to a tandem device with the architecture glass/ ITO/ NiO<sub>x</sub>/ perovskite/ C60/ BCP/ Ag/ MoO<sub>x</sub>/ organic layer/ PNDIT-F3N/ Ag. The recombination reduction factor in the organic layer and the surface recombination velocities at interfaces between the active organic layer and its adjacent hole-extraction and electron-transporting layers are fitted for the bottom subcell, while the other parameters sourced from literature. For the interconnecting layer, the recombination lifetime is fitted. All parameters and their values considered here are shown in Table 7.1, and the optical constants are sourced from literature (see Table 7.2).

Materials	References	Materials	References
Glass	[64]	MoO <sub>x</sub>	[63]
ITO	[129]	Organic compound	[130]
NiO <sub>x</sub>	[131]	PNDIT-F3N	[132]
Perovskite	[78]	Ag(Interconnecting layer)	[133]
C60	[58]	Ag(Back-contact electrode)	[131]
BCP	[61]	IZO	[131]

Table 7.2: Optical data for the materials considered.

The champion 2T perovskite-on-organic tandem solar cell with a 4 nm IZO as interconnecting layer and a record PCE of 23.6% is employed for model validation. An interconnecting layer fabricated from IZO instead of Ag has better surface coverage and less parasitic absorption. While all other parameters remain unchanged, the organic layer recombination reduction factor and the recombination lifetime in interconnecting layer are decreased for a better deposited organic active layer and a more efficient recombination junction, respectively.

We applied our model to another batch of tandem solar cells with different IZO thicknesses: 2, 4, 6, and 20 nm. We further validated our model with this second batch of cells. All top and bottom subcell parameters are unchanged except the perovskite thickness, which accounts for the current mismatch since the cells are from a different batch of tandem solar cells. The recombination lifetime in the interconnecting layer is fitted for the tandem solar cells with IZO thicknesses of 2, 4, and 6 nm. For the tandem solar cell with 20 nm IZO, if we only consider modifying the parameters in the interconnecting layer, our model with charge carrier recombination as the interconnecting layer mecha-

nism cannot reproduce the experimental results. However, the simulation results match the experimental  $i - V$  curve when the mechanism is switched to charge carrier transport and the interface recombination velocities at VI and VII are fitted. Table 7.3 summarizes the parameter values different from Table 7.1 for this batch of cells.

Cell index	Parameters	Values	Units
3	$k_{en}$	0.01	
	$\tau_{(e,h)}^{\text{ICL}}$	$1.1 \times 10^{-15}$	s
4, 5, 6	$l^P$	$3 \times 10^{-7}$	m
	$\tau_{(e,h)}^{\text{ICL}}$	$8.4 \times 10^{-9}, 1.9 \times 10^{-11}, 1.2 \times 10^{-9}$	s
7	$l^P$	$2.9 \times 10^{-7}$	m
	$v_h^{\text{VI}}, v_e^{\text{VII}}$	$1 \times 10^{-27}, 1 \times 10^{-28}$	$\text{m}^4 \text{s}^{-1}$

Table 7.3: Mathematical model parameters that are different from Table 7.1 for the champion tandem solar cell with IZO as interconnecting layer (cell 3), and the second batch of tandem solar cell with 2, 4, 6, and 20 nm IZO as interconnecting layer (cell 4 to 7).

The experimental and simulated  $i - V$  curves are shown in Figure 7.2. In Figure 7.2(a), the maximum absolute errors observed between model predicted and experimentally measured cell performances are around 0.01 V, 0.4 mA/cm<sup>2</sup>, 0.02, and 0.1% for open-circuit voltage, short-circuit current density, fill factor, and PCE respectively. In Figure 7.2(b), these errors are around 0.03 V, 0.4 mA/cm<sup>2</sup>, 0.02, and 0.4% respectively. The predicted  $i - V$  curves follow the shapes of the experimentally measured curves. In conclusion, we have obtained good agreements between the simulated and experimental  $i - V$  curves.

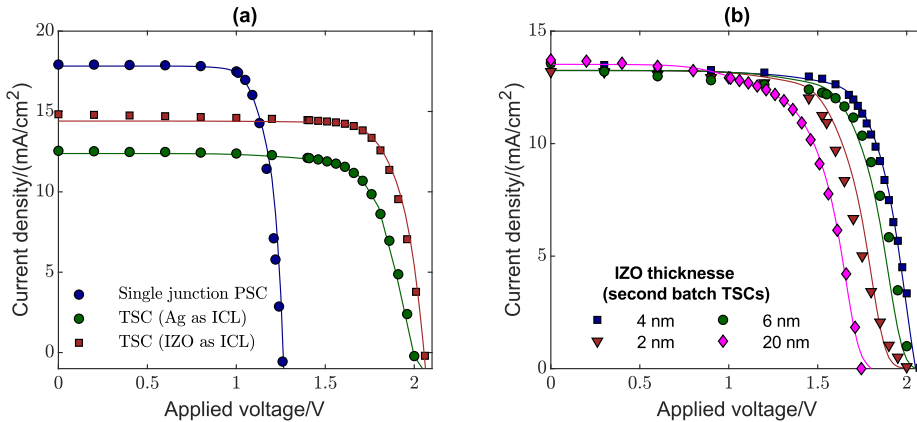


Figure 7.2: (a) Simulated and experimental  $i - V$  curves for cells calibrated; (b) experimental  $i - V$  curves for 2T perovskite-on-organic tandem solar cells with different interconnecting layer thicknesses.

In addition, we evaluate the total photogenerated current densities for the subcells in the 2T perovskite-on-organic tandem solar cells to determine which subcell is limiting the current. For the 2T perovskite-on-organic tandem solar cell with Ag as interconnecting layer, the photogenerated current densities are  $15.6$  and  $12.5 \text{ mA/cm}^2$  for the perovskite and organic subcells, respectively. For the champion 2T perovskite-on-organic tandem solar cell with IZO as interconnecting layer, these photogenerated current densities are  $15.6$  and  $14.5 \text{ mA/cm}^2$  for its subcells. The bottom organic subcell limits the current in both tandem devices, which agrees with the experimental results from Chen *et al* [27]. Comparing the two tandem devices, by switching the material of interconnecting layer from Ag to a more transparent IZO, more light can enter the organic subcell, and better current matching is achieved, leading to an increase in the short current density from around  $12.5$  to  $14.5 \text{ mA/cm}^2$ . The current in the champion tandem solar cell is still not perfectly matched, indicating possible room for improvement. A sensitivity analysis can help to determine the parameters that should be fine-tuned for even better current matching in the 2T perovskite-on-organic tandem solar cells.

Furthermore, we have calculated the total photogenerated current densities in the subcells identify the one responsible for limiting the current. In the 2T perovskite-on-organic tandem solar cell utilizing Ag as the interconnecting layer, the photogenerated current densities are  $15.6 \text{ mA/cm}^2$  for the perovskite subcell and  $12.5 \text{ mA/cm}^2$  for the organic subcell. In the leading 2T perovskite-on-organic tandem solar cell with IZO as the interconnecting layer, these photogenerated current densities are  $15.6 \text{ mA/cm}^2$  for the perovskite subcell and  $14.5 \text{ mA/cm}^2$  for the organic subcell. In both tandem devices, the current limitation stems from the bottom organic subcell, corroborating findings by Chen *et al* [27]. When comparing these two tandem devices, the switch from Ag to the more transparent IZO as the interconnecting layer enables more light to enter the organic subcell, resulting in improved current matching and an increase in short-circuit current density from approximately  $12.5$  to  $14.5 \text{ mA/cm}^2$ . Although current matching is enhanced in the champion tandem solar cell, it is not yet ideal, leaving room for potential improvements. A sensitivity analysis can help identify the parameters that require fine-

tuning to achieve even better current matching in 2T perovskite-on-organic tandem solar cells.

## 7.4 Sensitivity analysis

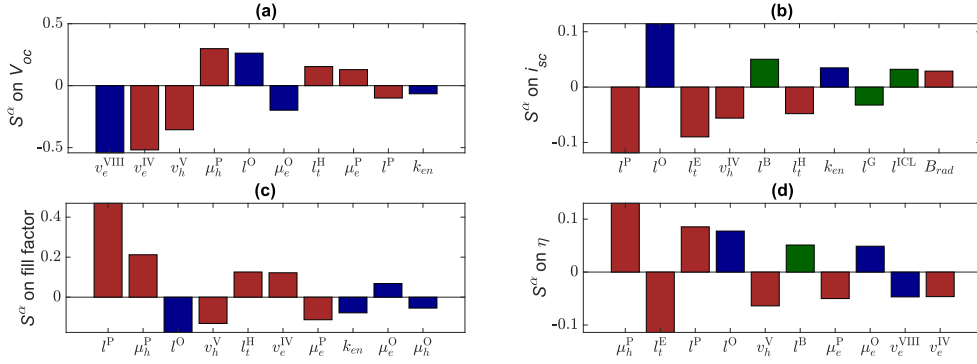


Figure 7.3: Sensitivity rankings of the stochastic parameters involved in the 2T perovskite-on-organic tandem solar cell for (a) open-circuit voltage ( $V_{oc}$ ), (b) short-circuit current density ( $i_{sc}$ ), (c) fill factor, and (d) PCE ( $\eta$ ).

We performed a sensitivity analysis using the parameters of the 23.6% PCE champion tandem solar cell to identify the most influential factors for further enhancing the performance of this cutting-edge 2T perovskite-on-organic tandem solar cell. All stochastic parameters were varied based on their calibrated values listed in Table 7.1 and 7.3. In Figure 7.3, we present the sensitivities of the top ten most crucial parameters concerning open-circuit voltage, short-circuit current density, fill factor, and PCE. The red, blue, and green bars represent the sensitivities of parameters associated with the top sub-cell, bottom sub-cell, and other layers, including the interconnecting layer, respectively.

In Figure 7.3(a), the recombination velocities at interfaces VIII, IV, and V are identified as the top three most influential parameters on the open-circuit voltage. Interfacial recombination is a critical factor that limits the open-circuit voltage, consistent with the findings of Brinkmann *et al.* [31]. Implementing further surface passivation at these interfaces is expected to reduce the interfacial recombination rates and subsequently raise the open-circuit voltage. On the contrary, the recombination velocity at interface IX has a minimal effect and does not rank within the top ten, indicating an already effective

surface contact between the organic and bottom electron-transporting layers. Moreover, increasing the charge carrier mobility of the perovskite layer contributes to an enhanced open-circuit voltage. This is due to the fact that higher charge carrier mobility facilitates faster charge carrier transport, reducing charge carrier recombination near the open-circuit voltage. Conversely, increasing the electron mobility in the organic layer leads to a decrease in voltage, indicated by the negative  $S^\sigma$  value. This is because higher electron mobility results in more significant Langevin recombination rates, outweighing the benefits of faster charge carrier transport. Furthermore, the thicknesses of the organic, top hole-transporting, and perovskite layers have an impact on the open-circuit voltage since they influence charge carrier concentrations and, consequently, recombination rates.

Regarding the short-circuit current density, as shown in Figure 7.3(b), most of the sensitive parameters are the layer thicknesses. In a 2T tandem solar cell, achieving current matching between subcells is more critical than simply increasing the photogenerated current in a single subcell. The highest absolute  $S^\sigma$  value is slightly above 0.1, which is significantly lower than that for the open-circuit voltage. This suggests that increasing the open-circuit voltage is relatively more straightforward in this tandem solar cell. Secondly, the optics is close to the current matching condition for the band gaps and parameters considered here. Nevertheless, there is still room for improvement by fine-tuning the layer thicknesses. The top perovskite and electron-transporting layer thicknesses should be decreased to transmit more light to the bottom organic layer. Increasing the organic layer thickness will also yield better absorption of light. The remaining parameters have smaller absolute sensitivity values of less than 0.05, and their sensitivities are close to each other; therefore, they are not identified as influential parameters.

Sensitive parameters on the fill factor are shown and ranked in Figure 7.3(c). We focus on the top three ranked parameters because the rest of the parameters are relatively less influential and have  $S^\sigma$  values close to each other. Since the fill factor calculation includes the open-circuit voltage and short-circuit current, which are not fixed while the parameters are perturbed, when investigating the physics behind the sensitivities, the effect of open-circuit voltage and short-circuit current should be considered. The top

perovskite layer thickness is the most influential parameter. Increasing the top perovskite thickness decreases the overall current output because less light is passed to the bottom subcell. In contrast, the open-circuit voltage is not affected much by the perovskite thickness, according to Figure 7.3(a). This also suggests the overall recombination loss is decreased because of a lower photogenerated current density. As a result, the fill factor increases. Similarly, reducing the organic layer thickness gives a lower overall current and higher fill factor. Another influential parameter is the top perovskite hole mobility, which can lead to improvements in both the open-circuit voltage and fill factor and a shift of the  $i - V$  curve to the right. As this charge carrier mobility increases, there should be more minor recombination losses in the perovskite layer and at the interfaces. The top perovskite hole mobility is, therefore, a crucial parameter.

For the PCE, as shown in Figure 7.3(d), the sensitive parameters identified are the hole mobility in perovskite, top electron-transporting, perovskite, and organic layer thicknesses, which have relatively higher  $S^\sigma$  values of close to 0.1 compared to the rest of the ranked parameters. Due to the combined effects on the open-circuit voltage and fill factor, the top perovskite hole mobility becomes the most influential parameter for device efficiency. On the other hand, the top perovskite electron mobility is not a significant parameter. We attribute this to the following reason. The hole mobility and electron mobility are related to the hole concentration and electron concentration respectively, which are critical parameters in determining the recombination losses at V and IV. As shown in the loss analysis later, the surface recombination rate is much more significant at interface V than IV. Hence, the top perovskite electron mobility less affects the interfacial recombination loss. Regarding the layer thicknesses, the top electron-transporting layer thickness is more effective on the PCE than the perovskite and organic active layer thicknesses, despite being ranked after the active layer thicknesses for the short-circuit current in Figure 7.3(b). This is because the active layer thicknesses affect both the open-circuit current and fill factor, and these effects balance each other out. Still, the active layer thicknesses should be increased for better current matching, higher fill factor, and a more efficient tandem solar cell. We also conclude that the top perovskite subcell should

be the focus for improving the PCE according to the ranking.

## 7.5 Loss analysis

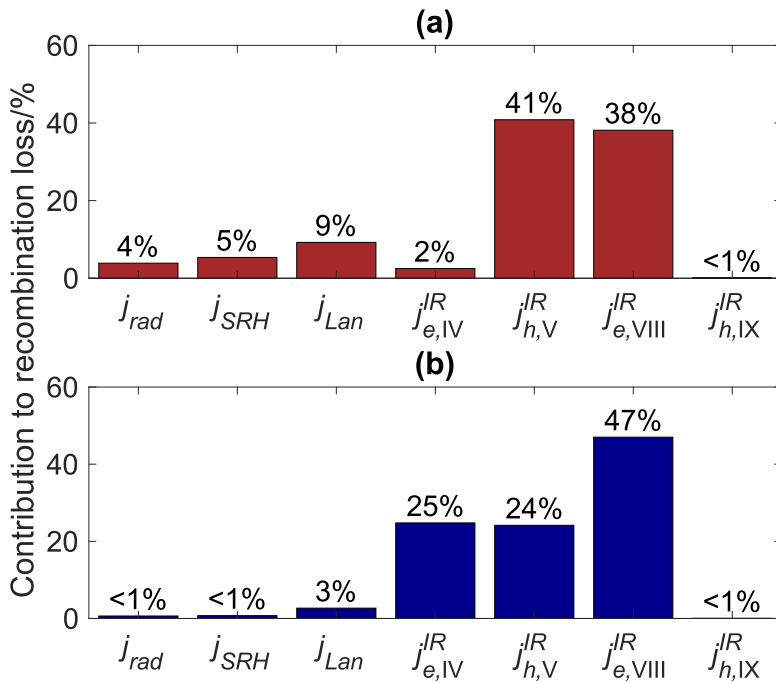


Figure 7.4: Percentage contributions to the total recombination loss due to different loss channels at (a) MPP and (b) open-circuit voltage.

Besides current matching, reducing recombination losses in a 2T perovskite-on-organic tandem solar cell is crucial to improving the PCE. Loss analysis is conducted for the champion 2T perovskite-on-organic tandem solar cell with IZO as interconnecting layer to determine the most significant recombination losses. There are seven loss channels identified. They are the recombination losses due to radiative recombination, SRH recombination, Langevin recombination in the organic layer, and interfacial recombination at IV, V, VIII, and IX respectively. The contributions of each recombination to the total loss at the max power point (MPP) and the open-circuit voltage are shown in Figure 7.4. Here,  $j_{rad}$ ,  $j_{SRH}$ , and  $j_{Lan}$  are the total radiative, SRH, and Langevin recombination fluxes respectively, and  $j^{IR}$  is the interface recombination flux.

The most considerable losses at MPP are the interfacial recombinations at interfaces

V and VIII, followed by the Langevin recombination in the organic layer. At open-circuit voltage, there are significant losses due to interfacial recombinations at interfaces IV, V, and VIII. Compared to the top perovskite, the recombination in the bottom organic layer is more critical as the Langevin recombination depends on both the charge carrier mobility and concentrations. A higher charge carrier mobility results in faster charge carrier transport but more considerable recombination. Thus, a balance between charge carrier transport and recombination needs to be achieved. In conclusion, the interfacial recombinations at interfaces IV, V, and VIII are the major losses in this 2T perovskite-on-organic tandem solar cell, followed by the recombination in the bottom organic layer. Reducing these losses is therefore critical to improving the PCE.

## 7.6 Interconnecting layer

This section discusses the relationship between the surface coverage, resistances, and charge carrier recombination in the interconnecting layer to provide more insights into the 2T perovskite-on-organic tandem solar cell fabrication. The surface coverage, bulk and sheet resistances are taken from Chen *et al* [27]. For the performances of the 2T perovskite-on-organic tandem solar cells shown in Figure 7.2(a), the PCE increases from 18.6% to 23.6% when the interconnecting layer material is changed from Ag to IZO. We attributed this PCE improvement to the improved current matching and increased charge carrier recombination. Table 7.1 and 7.3 show that the champion tandem solar cell has a lower recombination lifetime of  $1.1 \times 10^{-15}$  s than the tandem device with Ag as interconnecting layer of  $5.0 \times 10^{-12}$  s. We found the surface coverage of the IZO and Ag interconnecting layers to be 95.7% and 53.7% respectively. Due to a lack of surface coverage, the Ag interconnecting layer can result in insufficient recombination sites for the charge carriers from the top and bottom subcells to recombine. Therefore, it should have a higher recombination lifetime and smaller total recombination current flux. It is also found that an interconnecting layer that results in continuous and broad surface coverage between the perovskite and organic subcells can prevent short circuits and insufficient charge carrier recombination [27, 36], which aligns with our simulation

results.

We also observe that the low recombination lifetime of  $1.1 \times 10^{-15}$  s in the champion device has provided sufficient recombination sites for a high charge carrier flux to pass through. Decreasing the recombination lifetime further would have no effect on the device's performance, as supported by our sensitivity analysis results where  $\tau^{\text{ICL}}$  is not a local sensitive factor. This is because the recombination flux that is allowed to pass through has already exceeded the charge carrier flux from the subcells at all electric potentials. In this case, the IZO interconnecting layer with its specific band energy levels has been optimized.

To gain more insights, we investigate how different material properties can affect the I-V curve. Similar to Chapter 6, we switch the material in the interconnecting layer from IZO to  $\text{SnO}_2$ , with higher charge carrier mobility of  $4.2 \times 10^{-2} \text{ m}^2 \text{ V}^{-1} \text{ s}^{-1}$ , density of states of  $9.38 \times 10^{18} \text{ m}^{-3}$ , thickness of 20 nm, and recombination coefficient of  $1 \times 10^{-12}$  s. The differences in the  $i - V$  curves are shown in Figure 7.5. A slight decrease in  $i_{sc}$  due to more parasitic absorption and a significant decrease in  $V_{oc}$  are observed. We attribute the change in  $V_{oc}$  to the lower density of states that decreases charge carrier recombination. Our analysis suggests that for a specific material chosen for the interconnecting layer, one should consider its density of states if the tandem device exhibits a low combined  $V_{oc}$  and focus on providing sufficient recombination charge carrier flux if the device has a lower than expected FF.

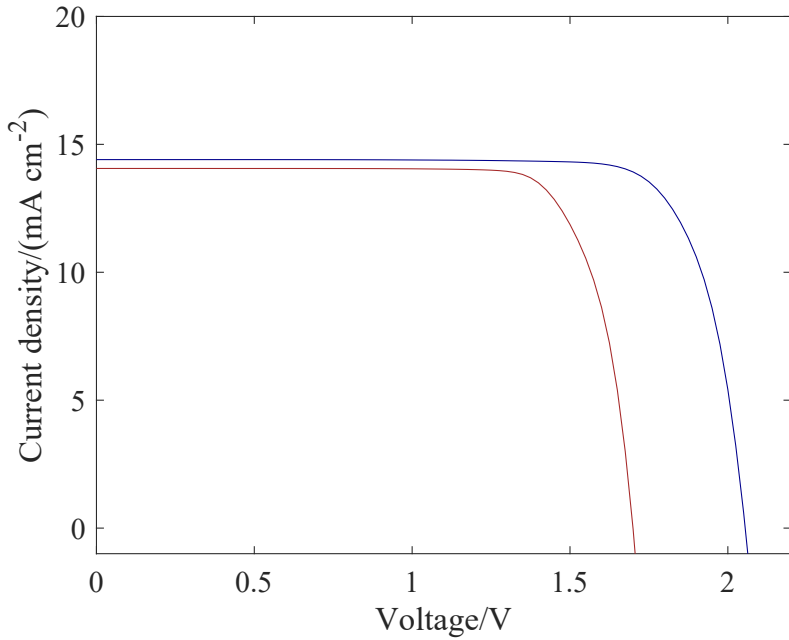


Figure 7.5: Simulated  $i$  –  $V$  curves of the 2T perovskite-on-organic tandem solar cells with IZO (blue) and SnO<sub>2</sub> (red).

Moreover, low bulk and high sheet resistance of the interconnecting layer can avoid charge carrier accumulation [38] and current leakage [27]. The bulk resistances are 2100, 0.05, and 0.03 Ωcm for the 2, 4, and 6 nm IZO layers in the second batch of tandem solar cells. The 2 nm thin IZO layer is not continuous; therefore, its experimental measured bulk resistance is much higher than the others. Next, the corresponding sheet resistances are  $1.1 \times 10^{10}$ ,  $1.2 \times 10^5$ , and  $4.9 \times 10^4$  Ω/sq. From model calibration, the recombination lifetimes in these interconnecting layers are  $8.4 \times 10^{-9}$ ,  $1.9 \times 10^{-11}$ , and  $1.2 \times 10^{-9}$  s respectively. As such, interconnecting layer in the 2T device that results in the largest charge carrier recombination and highest PCE is the 4 nm IZO, followed by 6 nm IZO and 2 nm IZO. For the cell with 6 nm IZO, although its interconnecting layer has the lowest bulk resistance, its PCE is smaller than the 4 nm IZO cell. This is due to the lowest sheet resistance in the interconnecting layer, which results in more considerable current leakage in the  $y$ – and  $z$ – directions and therefore fewer charge carriers that recombine in the  $x$ – direction.

In conclusion, the second batch tandem solar cells with 4 nm IZO as interconnecting layer has the lowest charge carrier recombination lifetime and highest PCE, which agrees

with the experimental  $i - V$  curves in Figure 7.2(b). For the second batch of devices with 2, 4, and 6 nm IZO, the whole interconnecting layer can act as a recombination junction, which allows recombination-based current flux to pass through. Once the thickness of the IZO layer is increased to 20 nm in the tandem solar cell, we demonstrate it no longer behaves as a recombination junction but as a charge carrier transporting layer instead. As shown in Figure 7.2(b), the  $i - V$  curve for this tandem solar cell differs from the 2, 4, and 6 nm IZO  $i - V$  curves. It has a much lower open-circuit voltage of 1.75 V. The electrons from the top subcell need to be transported through the entire interconnecting layer to recombine with the holes from the bottom subcell at an interface 20 nm apart. Compared to the recombination junctions, the 20 nm IZO as a charge carrier transporting layer has less total charge carrier recombination and thus limited charge carrier flux that can be passed through. This reduced flux results in a significant drop of the open-circuit voltage from 2 V to 1.75 V. An interconnecting layer that functions as a recombination junction is therefore preferred for a 2T perovskite-on-organic tandem solar cell.

## 7.7 Towards a more efficient device

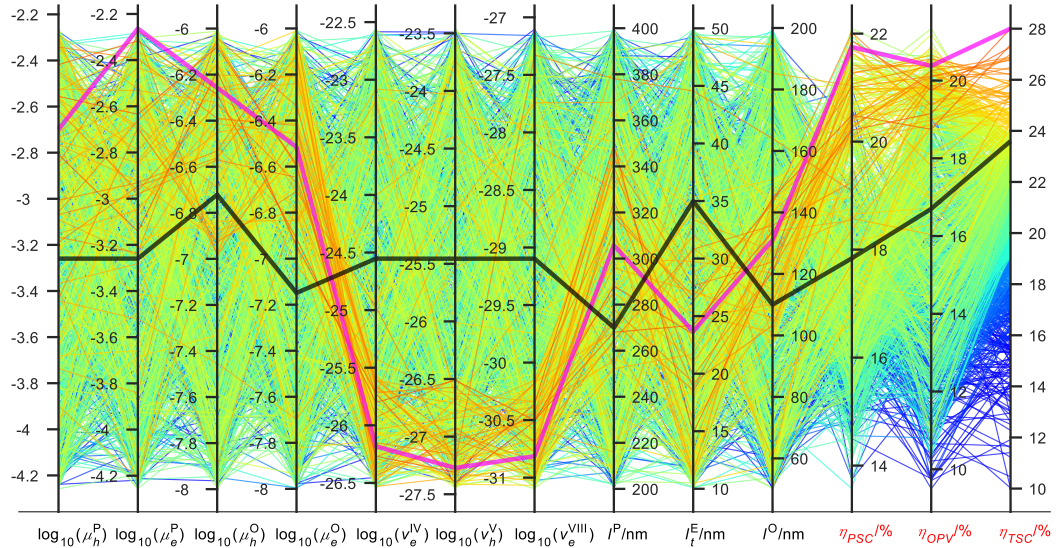


Figure 7.6: Relationship between the charge carrier mobility, interfacial recombination velocities, layer thicknesses, and the output PCEs from the parametric sweep study.

After identifying the sensitive parameters and the main recombination losses in the champion 2T perovskite-on-organic tandem solar cell, a parametric sweep is conducted to provide a pathway toward higher PCE. Based on the sensitivity analysis and the loss analysis results, we chose the following parameters: the charge carrier mobility in the perovskite and organic layer, the surface recombination velocities, and the perovskite, top electron-transporting, and organic layer thicknesses. These parameters are varied simultaneously from their calibrated values in Table 7.1. The charge carrier mobility is perturbed based on literature reported values [134, 135, 136], and the bounds for the layer thicknesses are based on the literature reported 2T perovskite-on-organic tandem solar cells [27, 35, 36]. Figure 7.6 shows the perturbed parameters and output PCEs for the perovskite and organic single-junction cell,  $\eta_{PSC}$  and  $\eta_{OPV}$ , together with the PCE for the 2T perovskite-on-organic tandem solar cell,  $\eta_{TSC}$ .

From the simulation result, we found that the PCE of the 2T perovskite-on-organic tandem solar cell can be improved further from 23.6% to 28%, which are indicated by the black and magenta lines in Figure 7.6. Here, the pathway suggests increasing the charge carrier mobility, reducing the interfacial recombination velocities, increasing both active layer thicknesses, and decreasing the top electron-transporting layer thickness, as shown in Figure 7.6 by the black and magenta lines. These changes in parameter values align with the results from our sensitivity analysis. A charge carrier mobility of around  $5 \times 10^{-3} \text{ m}^2/\text{V}\cdot\text{s}$  results in efficient charge carrier transport in the perovskite layer. As discussed, the charge carrier mobility in the organic layer affects charge carrier transport and recombination rate. Their optimal values here are about  $5 \times 10^{-7} \text{ m}^2/\text{V}\cdot\text{s}$ . Better surface passivation should be made at the interfaces between the perovskite layer and its adjacent transporting layers and between the organic layer and its adjacent hole-extraction layer to reduce the interfacial recombination. Our predictions here have shown the device's potential towards higher efficiency, however, certain modifications such as interface passivations are not straightforward during device fabrications, and as such, fabrications and model calibrations can be conducted iteratively for continuous developments of the solar cell.

For the perovskite layer, top electron-transporting layer, and organic layer, their optimum thicknesses are around 300 nm, 25 nm, and 130 nm respectively. The best predicted 2T perovskite-on-organic tandem solar cell requires the single junction perovskite solar cell and organic solar cell to have PCEs of around 22.7% and 20.4%, respectively. We can estimate the practical efficiency with the SQ limit [137]. Single junction solar cells with band gaps of 1.5 eV and 1.79 eV have PCE limits of about 32% and 28% respectively. The certified PCE for a perovskite solar cell with around 1.5 eV band gap is 25.7% [138] – 80% of its SQ limit. From here, for a 1.79 eV perovskite solar cell as the top cell, its PCE can be estimated as 80% of the corresponding 28% SQ limit. This results in a 22.4% practical efficiency for the top cell considered here, which is very close to our predicted value of 22.7%.

On the other hand, the predicted PCE for the single junction organic device is higher than its certified PCE of 18.2% [139]. Although the top perovskite solar cell is more influential on the 2T PCE according to the sensitivity analysis results, a breakthrough in the organic solar cell efficiency is critical for the 2T device to reach the predicted 28% PCE. Lastly, in addition to the above-mentioned improvements to the device, what else could be required toward the practical 30% PCE limit [35] of this 2T perovskite-on-organic tandem solar cell? Having an organic solar cell with a smaller band gap can be one possible solution [31]. Once the perovskite cell reaches the 80% SQ limit, developing efficient, narrower band gap of less than 1.36 eV organics becomes the next driving force to bring the PCE of perovskite-on-organic tandem solar cells to above 30%.

We have discussed and provided possible pathways for 2T perovskite-on-perovskite and perovskite-on-organic tandem solar cells towards higher PCE in Chapter 6 and 7, respectively. Both tandem configurations have potential to reach 30% PCE, in which the former—with its advantages mentioned in Chapter 6—demonstrates a higher record PCE and predicted optimized PCE. The reason is mainly the better current matching with a narrower bandgap bottom device, and at the same time, a high enough  $V_{oc}$  is retained. Current state-of-the-art organic solar cell commonly has a bandgap from 1.3 to 1.6 eV [140], which is at disadvantage compared to a 1.13 eV perovskite solar cell as the

bottom device in 2T configuration. Nevertheless, 2T perovskite-on-organic tandem solar cells still have their advantages over 2T perovskite-on-perovskite tandem solar cells, such as lead-free, and in terms of flexibility and stability according to Wu *et al.* [141]. By them, recent progresses have shown improved thermal and chemical stability of organic compounds. Also, Organic blend can offer higher mechanical performance, and is more sophisticated compared to perovskite in flexible solar cells. However, the cost-effectiveness of organic solar cell as bottom subcell is still lower than that of perovskite bottom device. Hence, for future industrialization, the problems on bottom cell bandgap and cost-effectiveness are to be addressed.

## 7.8 Summary

We have developed an optoelectronic model for 2T perovskite-on-organic tandem solar cell, capturing charge carrier transport, generation, and recombination within the device.

Through a sensitivity analysis, the critical parameters affecting the PCE are identified as the hole mobility in the perovskite layer and the top electron-transporting, perovskite, and organic layer thicknesses. The interfacial recombinations between the top perovskite layer and its adjacent charge carrier transporting layers and between the bottom organic layer and hole-extraction layer are key recombination losses.

For the interconnecting layer, the interplay between surface coverage, bulk resistance, and charge carrier recombination is investigated. In addition, increasing the thickness of the IZO interconnecting layer from a few to 20 nm will result in a charge carrier transporting layer instead of a recombination junction, thus significantly lowering the PCE.

Furthermore, we have investigated the effects of layer thicknesses, charge carrier mobility, and recombination rates on the single-junction and tandem PCEs. From here, a guideline for the 2T perovskite-on-organic tandem solar cell to reach a 28% PCE is provided, where the PCEs for the corresponding single-junction perovskite solar cell and organic solar cell are 22.7% and 20.4%, respectively. The proposed guideline includes improving the charge carrier transport in the active layers, reducing interfacial recom-

bination, increasing both the active layer thicknesses, and decreasing the top electron-transporting layer thickness. Developing efficient, narrower band gap organics is the next step toward a 30% 2T perovskite-on-organic tandem device.



# Chapter 8

## Mixed-integer optimization on bifacial tandem solar cells

### 8.1 Introduction

Tandem solar cells are promising candidates for highly efficient photovoltaic devices [28], with world record PCEs of 33.7% [12] and 28.0% [29] for 2T perovskite-on-silicon and perovskite-on-perovskite tandem solar cells, respectively. To further improve their efficiencies, bifacial 2T tandem solar cells have been developed, which can absorb both front and rear incident light to enhance short-circuit current densities. In addition, band gap engineering has been employed in perovskites on top subcells to enhance the performance of bifacial perovskite-on-perovskite [142] and perovskite-on-silicon [143] tandem solar cells. To achieve optimal performance, it is crucial to design 2T tandem devices that maximize short-circuit current densities while ensuring current matching between the subcells. This requires careful selections of materials and tuning of layer thicknesses.

Modeling and simulating the optics in 2T tandem solar cells offer cost-effective designs, performance prediction, and optimization. Kim *et al.* [144] optimized planar perovskite-on-silicon tandem solar cells and determined the maximum theoretical current by varying the perovskite band gap and layer thickness in the top subcell; the sil-

icon bottom subcell, however, was not optimized for consistent fabrication. Soldera *et al.* [44] found an optimal short-circuit current density of approximately  $185 \text{ A/m}^2$  for ideal 2T perovskite-on-perovskite tandem solar cells, assuming no parasitic absorption in the transparent contact layers. They explored four different transparent oxides for the conductive layer and different materials such as  $\text{NiO}_x$  and PEDOT:PSS for hole-transporting layers, and  $\text{SnO}_2$  and PCBM for electron-transporting layers while keeping the perovskite materials fixed. Moreover, Chantana *et al.* [45] optimized the band gaps of the subcells in ideal 2T tandem solar cells under bifacial operation using the SQ limit. They found that there is a trade-off between the optimal band gaps of the two subcells and both band gaps approach approximately 1.5 eV under high albedo values. Hörantner and Snaith [46] optimized 2T tandem solar cell performance by improving current matching under various solar spectrum. Currently, there is no study that accounts for the simultaneous consideration of material choice, layer thickness, and spectral albedos for the optimal design of a 2T tandem solar cell.

In this work, we carry out mixed-integer optimization of an optics model for the short-circuit current densities in 2T perovskite-on-perovskite tandem solar cells, considering material selections and layer thicknesses under different spectral albedos. The optics model is validated with experiments [145] for monofacial and bifacial tandem cells consisting of various top perovskite materials. We consider over a million material combinations for the two subcells, varying thicknesses of the thin-film layers in the tandem solar cell, and several albedos; and apply constraints for energy-level matching to ensure that the material combinations give rise to smooth charge-carrier transport. Comprehensive guidelines on the choices of materials and thicknesses in the thin-film layers are then provided. After optimization, a sensitivity analysis quantifies the variations in the optimal short-circuit current densities. Finally, we discuss the achieved short-circuit current density, theoretical maximum open-circuit voltages and fill factors, and PCEs.

## 8.2 Mathematical formulation

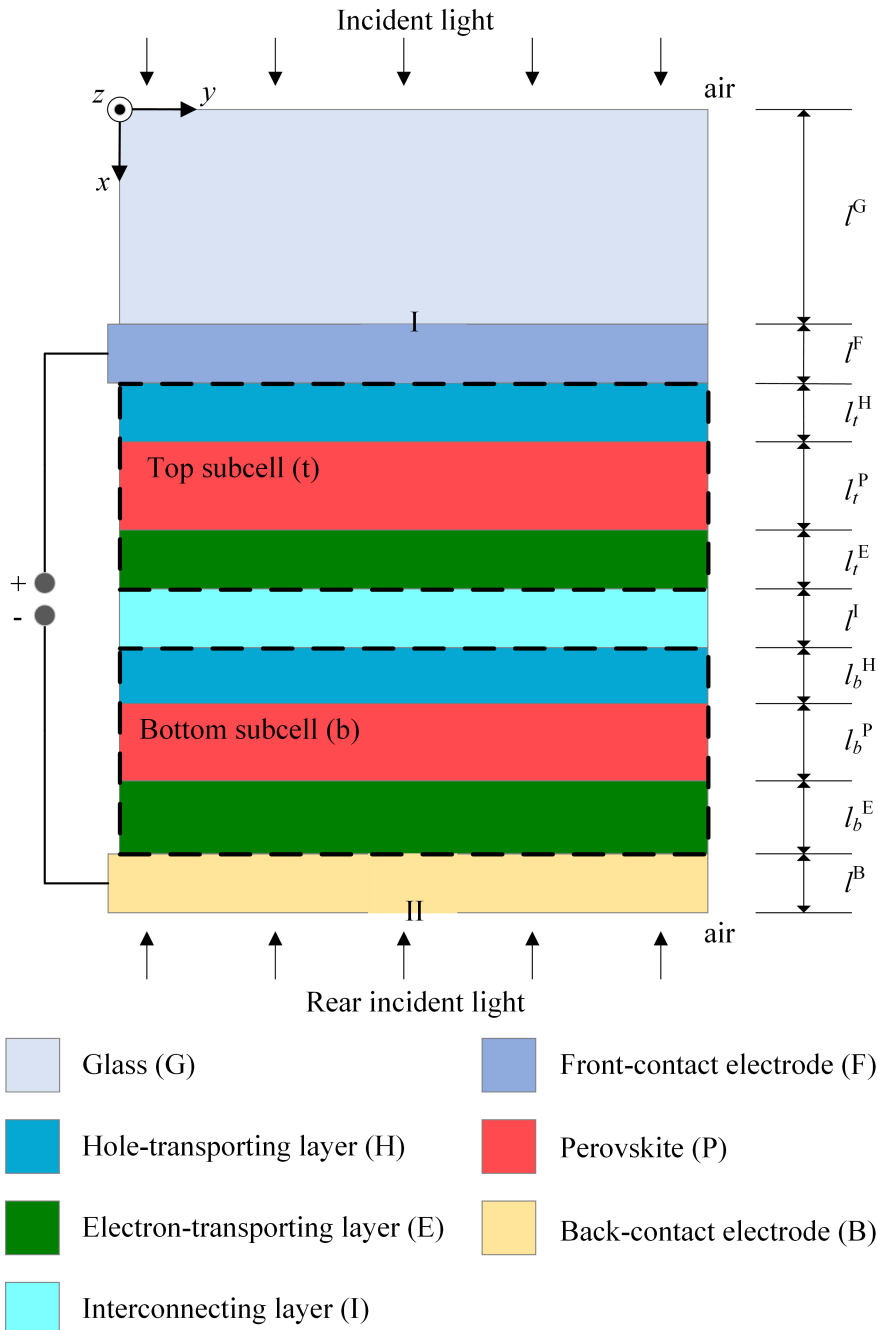


Figure 8.1: Schematic of a 2T perovskite-on-perovskite tandem solar cell. Here, the Roman numerals denote the interfaces,  $l$  is the layer thickness; and G, F, H, P, E, I, and B denote the glass, front-contact, hole-transporting, perovskite, electron-transporting, interconnecting, and back-contact layers, respectively. The subscripts  $t$  and  $b$  denote the top and bottom subcells, respectively.

Our optics model for a 2T perovskite-on-perovskite tandem solar cell is based on the structure shown in Figure 8.1. The model assumes that the layers have no surface rough-

ness and the incident light is normal to the solar cell, allowing us to capture the optics with a one-dimensional geometry. For the front incident light, 1000 W/m<sup>2</sup> solar irradiance, and ASTM G173-03 Global tilt standard spectrum [51] is adopted. For the rear incident light, we consider five different spectral albedos [115]. During the optimization, a 25 °C cell temperature is assumed for all albedo conditions.

In the mixed-integer optimization, we consider the materials and thicknesses of the nine thin-film layers (not the front glass layer) as illustrated in Figure 8.1. The thicknesses are continuous while the materials are represented by integers. We denote the material in layer  $j$  as an integer value  $m_j$ , where  $j$  starts from one at the front-contact electrode, and increases up to nine for the back-contact electrode. We further let the number of materials that can be chosen for layer  $j$  be  $M_j$ , with each material having its own set of optical data and energy band levels. The optimization problem is then as follows:

$$\max i_{sc}(m_1, m_2, \dots, m_9, l^F, l_{(t,b)}^H, l_{(t,b)}^P, l_{(t,b)}^E, l^I, l^B) \quad (8.1)$$

$$\text{s.t. } m_j \in \{1, 2, \dots, M_j\}, \forall j = 1, 2, \dots, 9$$

$$80 \text{ nm} \leq l^F \leq 250 \text{ nm}$$

$$20 \text{ nm} \leq l_{(t,b)}^H \leq 250 \text{ nm}$$

$$200 \text{ nm} \leq l_{(t,b)}^P \leq 1000 \text{ nm}$$

$$20 \text{ nm} \leq l_{(t,b)}^E \leq 250 \text{ nm}$$

$$1 \text{ nm} \leq l^I \leq 20 \text{ nm}$$

$$80 \text{ nm} \leq l^B \leq 250 \text{ nm}$$

$$E_{v,t}^H - W^F \leq 0$$

$$E_{v,t}^P - E_{v,t}^H \leq 0$$

$$E_{c,t}^E - E_{c,t}^P \leq 0$$

$$E_{v,b}^P - E_{v,b}^H \leq 0$$

$$E_{c,b}^E - E_{c,b}^P \leq 0$$

$$W^B - E_{c,b}^E \leq 0$$

where  $i_{sc}$  is the short-circuit current density,  $W$  is the work function, and  $E_c$  and  $E_v$  are the conduction band and valance band energy levels respectively. Here, the glass layer thickness is set at 1 mm [146]. We have assumed a perfect interconnecting layer with energy levels allowing for efficient charge carrier recombination or tunneling.

A summary about the mixed-integer optimization process is shown in Figure 8.2. Here, we pass the solar spectrum, albedo, layer thicknesses, energy levels and optical data (from each material) into the mixed-integer optimization with genetic algorithm as input parameters. The final output is the optimized short-circuit current density, together with the corresponding materials and layer thicknesses. There are inequality constraints on the energy levels (see Eq. 8.1) made during the optimization process with genetic algorithm. If any of the inequality constraints are violated, the individual, or the material combination in particular, in the current generation is not allowed to survive to the next generation, and vice versa.

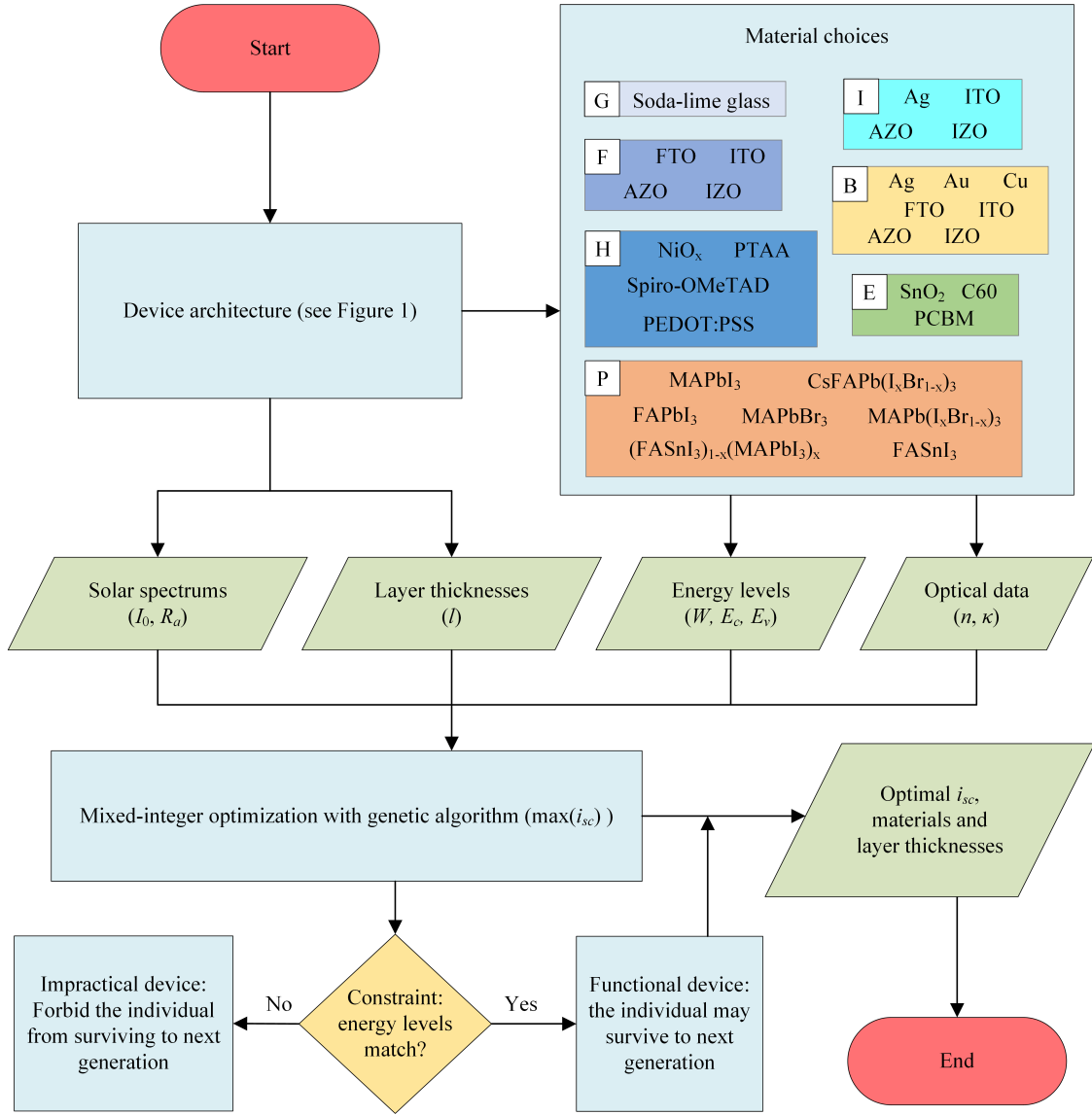


Figure 8.2: Inputs, constraints, and outputs considered in the mixed integer optimization for 2T perovskite-on-perovskite tandem solar cells. Here,  $I_0$  is the solar irradiance of the front incident light,  $R_a$  is the spectral albedo,  $n$  is the refractive index, and  $\kappa$  is the extinction coefficient.

We have the following choices of materials with different properties (see Table 8.1) represented by integer values as  $m_j$  in the optimization problem formulation:

- Glass (G): Soda-lime glass [64];
- Front contact (F): FTO, ITO, AZO, IZO;
- Hole-transporting layer (H): spiro-OMeTAD,  $\text{NiO}_x$ , PEDOT:PSS, PTAA;
- Perovskite layer:  $\text{MAPbI}_3$ ,  $\text{FAPbI}_3$ ,  $\text{FASnI}_3$ ,  $\text{MAPbBr}_3$ ,  $\text{MAPb}(\text{I}_{1-x}\text{Br}_x)_3$  with

1.68, 1.85, and 2.03 eV band gaps,  $\text{CsFAPb}(\text{I}_{1-x}\text{Br}_x)_3$  with 1.62, 1.67, 1.70, 1.73, 1.75 and 1.80 eV bandgaps,  $(\text{FASnI}_3)_{1-x}(\text{MAPbI}_3)_x$  with 1.07, 1.13, 1.25, and 1.30 eV bandgaps; here, the bandgaps vary due to different chemical doping concentrations and halide ion compositions indicated by the subscript x;

- Electron-transporting layer (E):  $\text{SnO}_2$ , PCBM, C60;
- Interconnecting layer (I): IZO, ITO, AZO, Ag;
- Back contact (B): FTO, ITO, AZO, IZO, Ag, Au, Cu.

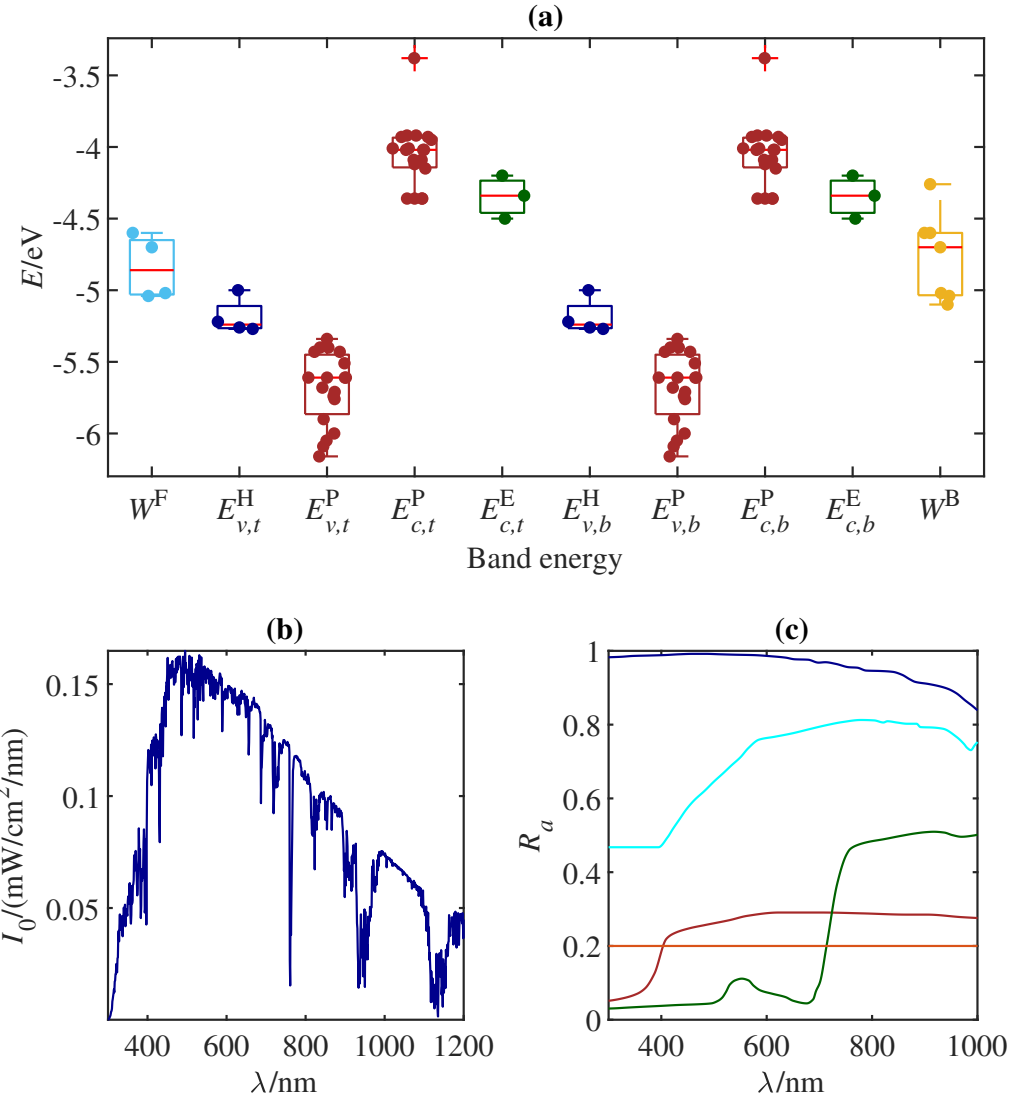


Figure 8.3: (a) Energy band diagrams for the materials for the 2T perovskite-on-perovskite tandem solar cells; (b) front incident light based on the ASTM G173-03 global tilt solar spectrum; and (c) albedo values for roof shingle (red), green grass (green), white sand (cyan), snow (blue), and 0.2 albedo (orange).

The materials and bounds for the layer thicknesses are based on earlier studies [147] and our previous calibrated perovskite based solar cell models [78, 79, 80]. We set the upper bound for the perovskite layer thickness to 1000 nm since further increasing the thickness could compromise the quality of the thin-film layer [148, 149]. We also impose constraints on the material work functions and energy levels (summarized in Table 8.1 and Figure 8.3(a)) to ensure smooth charge-carrier transport in the optimized 2T perovskite-on-perovskite tandem solar cells. For bifacial tandem solar cells,

we consider a 0.2 albedo and four commonly found spectral albedos for roof shingle, green grass, white sand, and snow, which provide additional solar irradiance of approximately 200-940 W/m<sup>2</sup> across a range of wavelengths from 300 to 1200 nm. The ASTM G173-03 Global tilt solar spectrum and the chosen albedo values are depicted in Figure 8.3(b-c). The optical properties of the materials considered are presented in Figure 8.4.

Materials	$n, \kappa$	$E_c/\text{eV}$	$E_v/\text{eV}$	$W/\text{eV}$
<i>Perovskite layer</i>				
MAPbI <sub>3</sub>	[150]	-3.93[151]	-5.43[152]	...
MAPbBr <sub>3</sub>	[131]	-3.38[153]	-5.4[153]	...
FAPbI <sub>3</sub>	[131]	-3.92[154]	-5.68[154]	...
FASnI <sub>3</sub>	[57]	-4.12[155]	-5.34[155]	...
MAPb(I <sub>1-x</sub> Br <sub>x</sub> ) <sub>3</sub>	[131]	-4.08 to -3.97[156]	-6.28 to -5.67[156]	...
CsFAPb(I <sub>1-x</sub> Br <sub>x</sub> ) <sub>3</sub>	[57]	-4.15 o -3.95[83]	-6.09 to -5.51[83]	...
(FASnI <sub>3</sub> ) <sub>1-x</sub> (MAPbI <sub>3</sub> ) <sub>x</sub>	[60]	-4.36[157]	-5.61[157]	...
<i>Electron-transporting layer</i>				
SnO <sub>2</sub>	[150]	-4.34[158]	...	...
PCBM	[131]	-4.2[98]	...	...
C60	[150]	-4.5[96]	...	...
<i>Hole-transporting layer</i>				
spiro-OMeTAD	[159]	...	-5.22[158]	...
NiO <sub>x</sub>	[131]	...	-5.26[94]	...
PEDOT:PSS	[160]	...	-5[24]	...
PTAA	[56]	...	-5.27[82]	...
<i>Interconnecting and contact layers</i>				
FTO	[131]	...	...	-4.6[158]
ITO	[132]	...	...	-4.7[96]
AZO	[131]	...	...	-5.04[161]
IZO	[131]	...	...	-5.02[162]
Ag	(B)[131],(I)[133]	...	...	-4.26[94]
Au	[163]	...	...	-5.1[158]
Cu	[62]	...	...	-4.6[164]

Table 8.1: Sources of optical data (refractive index,  $n$ , and extinction coefficient,  $\kappa$ ), energy levels, and work functions for the materials considered for the mixed-integer optimization.

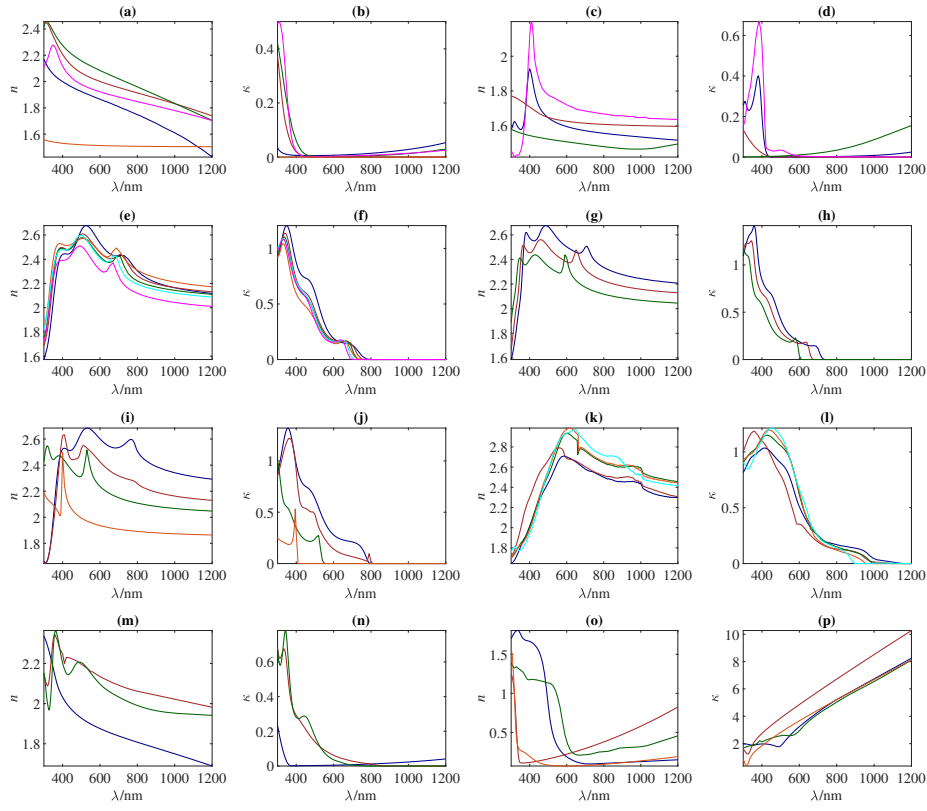


Figure 8.4: Refractive indices ( $n$ ) and extinction coefficients ( $\kappa$ ) for the materials in the optimization: (a-b) FTO (blue), ITO (red), IZO (green), AZO (magenta) and Soda-lime glass (orange); (c-d) spiro-OMeTAD (blue), NiO<sub>x</sub> (red), PEDOT-PSS (green) and PTAA (magenta); (e-f) CsFAPb(I<sub>1-x</sub>Br<sub>x</sub>)<sub>3</sub> with bandgaps of 1.62 eV (blue), 1.67 eV (red), 1.70 eV (green), 1.73 eV (orange), 1.75 eV (cyan), and 1.80 eV (magenta); (g-h) MAPb(I<sub>1-x</sub>Br<sub>x</sub>)<sub>3</sub> with bandgaps of 1.68 eV (blue), 1.85 eV (red), and 2.03 eV (green); (i-j) MAPbI<sub>3</sub> (blue), FAPbI<sub>3</sub> (red), MAPbBr<sub>3</sub> (green), and MAPbCl<sub>3</sub> (orange); (k-l) (FASnI<sub>3</sub>)<sub>1-x</sub>(MAPbI<sub>3</sub>)<sub>x</sub> with bandgaps of 1.07 eV (blue), 1.13 eV (red), 1.25 eV (green), and 1.30 eV (orange), together with FASnI<sub>3</sub> (cyan); (m-n) SnO<sub>2</sub> (blue), PCBM (red) and C60 (green); (o-p) Au (blue), Ag (red for back contact, orange for interconnecting layer), and Cu (green).

Furthermore, we predict the open-circuit voltages,  $V_{oc}$ , based on theoretical estimations according to perovskite bandgaps,  $E_g$ , with the following estimated relation from the classical diode equation for a single-junction perovskite solar cell [165]:

$$qV_{oc} \approx 0.84E_g - 0.08\text{eV}, \quad (8.2)$$

where  $q$  is the elementary charge. For a 2T perovskite-on-perovskite tandem solar cell,

its open-circuit voltage can be estimated as the sum of the open-circuit voltages of the corresponding single-junction perovskite solar cells. By assuming a theoretical optimum fill factor [165],  $\mathfrak{F}$ , the PCE,  $\eta$ , is

$$\eta = p_{out}/p_{in}, \quad (8.3)$$

$$p_{out} = V_{oc}i_{sc}\mathfrak{F}. \quad (8.4)$$

Here,  $p_{out}$  is the output power density and  $p_{in}$  is the input power density that takes the value of 1000 W/m<sup>2</sup>. For device under bifacial operation, we consider the bifacial equivalent power conversion efficiency [166], which can be calculated with the input power density still taken on the value of one sun at 1000 W/m<sup>2</sup>. By doing so, we can compare the output power density among devices under various albedo.

### 8.3 Validation

Our optics model was validated with experiments [145] for 2T perovskite-on-perovskite tandem solar cells under 0 and 0.3 albedo. These devices have structures of Glass/ITO (70 nm)/ NiO<sub>x</sub> (20 nm)/ CsFAPb(I<sub>1-x</sub>Br<sub>x</sub>)<sub>3</sub> (500 nm)/ C60 (26 nm)/ SnO<sub>2</sub> (20 nm)/ PEDOT:PSS (20 nm)/ (FASnI<sub>3</sub>)<sub>1-x</sub>(MAPbI<sub>3</sub>)<sub>x</sub> (1000 nm)/ C60 (26 nm)/ SnO<sub>2</sub> (20 nm) followed by Au (150 nm) for monofacial cells and ITO (70 nm) for bifacial cells. The layer thicknesses were approximated from SEM image. We adopted the perovskite materials CsFAPb(I<sub>1-x</sub>Br<sub>x</sub>)<sub>3</sub> in Table 8.1 with the closest bandgap to those found in experiments.

Band gap/eV	Albedo	Experiment $i_{sc}/(\text{A/m}^2)$	Simulation $i_{sc}/(\text{A/m}^2)$
1.77(MF)	0	$158.5 \pm 1.2$	156
	0.3	$146.7 \pm 3.8$	146
1.77	0.3	$157.6 \pm 2.5$	156
	0	$129.9 \pm 4.7$	140
1.73	0.3	$175.3 \pm 3.1$	163
	0	$122.3 \pm 3.9$	127
1.68	0.3	$184.8 \pm 4.0$	176
	0	$112.0 \pm 3.3$	121
1.62	0.3	$187.1 \pm 3.8$	182

Table 8.2: Experimental [145] and simulated short-circuit current densities for monofacial (MF) and bifacial 2T perovskite-on-perovskite tandem solar cells with various top perovskite bandgaps and under two different albedos.

As can be inferred from Table 8.2, we have good agreement between experimental and simulated short-circuit current densities, with the maximum difference within 10  $\text{A/m}^2$  when including the experimental error margins.

## 8.4 Results and discussions

### 8.4.1 Mixed-integer optimization

The optimization is conducted for monofacial 2T perovskite-on-perovskite tandem solar cells as well as devices under five spectral albedos. The resulting perovskite material selections, layer thicknesses and corresponding short-circuit current densities are presented in Figure 8.5, and the complete optimization results are listed in Table 8.4.

For brevity, the six albedo conditions are arranged into three categories: monofacial, low albedos (0.2 albedo, roof shingle and green grass), and high albedos (white sand and snow). We find that the optimal and close-to-optimal short-circuit current densities range from 172 to 181  $\text{A/m}^2$  for the monofacial devices, 195 to 206  $\text{A/m}^2$  for bifacial tandem cells under low albedos, and 291 to 342  $\text{A/m}^2$  for bifacial devices under high albedos.

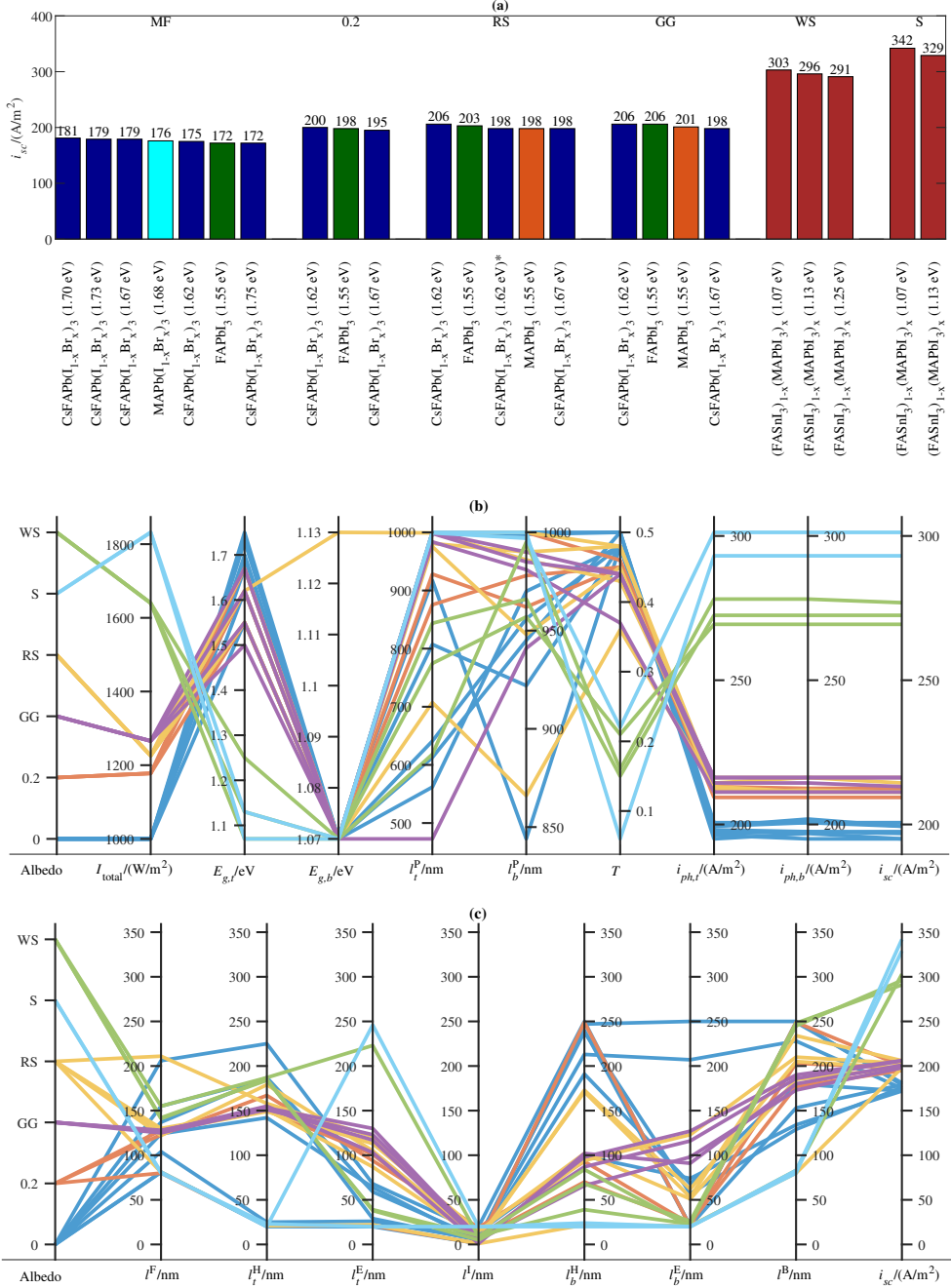


Figure 8.5: (a) Optimized top perovskite materials and their best short-circuit current densities in the optimized 2T perovskite-on-perovskite tandem solar cells under different albedo conditions: monofacial (MF, 0 albedo), 0.2 albedo (0.2), roof shingle (RS), green grass (GG), white sand (WS) and snow (S). Here, the bottom perovskite material is  $(\text{FASnI}_3)_{1-x}(\text{MAPbI}_3)_x$  for all cases, with a bandgap of 1.07 eV except the one marked by \* in RS, where the bandgap is 1.13 eV. (b) Optimal perovskite bandgaps and layer thicknesses for the top and bottom subcells with the corresponding photogenerated current densities and short-circuit current density in the 2T perovskite-on-perovskite tandem solar cells. Here,  $I_{total}$  is the total irradiance,  $E_{g,t}$  and  $E_{g,b}$  are the top and bottom perovskite bandgaps respectively,  $T$  is the average transmittance from the top subcell entering the bottom subcell, and  $i_{ph,t}$  and  $i_{ph,b}$  are the top and bottom photogenerated current densities, respectively; and (c) optimal thicknesses of the remaining layers.

Albedo	Cell architecture	Layer	$i_{sc}/(\text{A/m}^2)$
		thickness/nm	
	ITO/ spiro-OMeTAD/ CsFAPb( $I_{1-x}Br_x$ ) <sub>3</sub> (1.70 eV)/ C60/ ITO/ NiO <sub>x</sub> / (FASnI <sub>3</sub> ) <sub>1-x</sub> (MAPbI <sub>3</sub> ) <sub>x</sub> (1.07 eV)/ C60/ Au	81, 21, 999, 20, 20, 250, 1000, 20, 250	181
MF	ITO/ PTAA/ CsFAPb( $I_{1-x}Br_x$ ) <sub>3</sub> (1.73 eV)/ SnO <sub>2</sub> / IZO/ NiO <sub>x</sub> / (FASnI <sub>3</sub> ) <sub>1-x</sub> (MAPbI <sub>3</sub> ) <sub>x</sub> (1.07 eV)/ C60/ Cu	81, 20, 999, 20, 2, 247, 999, 250, 250	179
	ITO/ NiO <sub>x</sub> / CsFAPb( $I_{1-x}Br_x$ ) <sub>3</sub> (1.67 eV)/ C60/ ITO/ NiO <sub>x</sub> / (FASnI <sub>3</sub> ) <sub>1-x</sub> (MAPbI <sub>3</sub> ) <sub>x</sub> (1.07 eV)/ C60/ Au	155, 186, 605, 29, 5, 240, 956, 21, 153	179
	ITO/ NiO <sub>x</sub> / MAPb( $I_{1-x}Br_x$ ) <sub>3</sub> (1.68 eV)/ PCBM/ AZO/ NiO <sub>x</sub> / (FASnI <sub>3</sub> ) <sub>1-x</sub> (MAPbI <sub>3</sub> ) <sub>x</sub> (1.07 eV)/ C60/ Au	137, 187, 788, 59, 7, 238, 922, 57, 129	176
	ITO/ PTAA/ CsFAPb( $I_{1-x}Br_x$ ) <sub>3</sub> (1.62 eV)/ SnO <sub>2</sub> / IZO/ PTAA/(FASnI <sub>3</sub> ) <sub>1-x</sub> (MAPbI <sub>3</sub> ) <sub>x</sub> (1.07 eV)/ C60/ Au	104, 25, 518, 26, 6, 213, 970, 207, 228	175
	ITO/ NiO <sub>x</sub> / FAPbI <sub>3</sub> (1.55 eV) / PCBM/ ITO/ NiO <sub>x</sub> / (FASnI <sub>3</sub> ) <sub>1-x</sub> (MAPbI <sub>3</sub> ) <sub>x</sub> (1.07 eV)/ C60/ Au	206, 225, 574, 68, 14, 99, 945, 74, 134	172
	ITO/ NiO <sub>x</sub> / CsFAPb( $I_{1-x}Br_x$ ) <sub>3</sub> (1.75 eV)/ SnO <sub>2</sub> / IZO/ NiO <sub>x</sub> / (FASnI <sub>3</sub> ) <sub>1-x</sub> (MAPbI <sub>3</sub> ) <sub>x</sub> (1.07 eV)/ C60/ Au	124, 142, 909, 64, 3, 191, 844, 68, 180	172
0.2	ITO/ spiro-OMeTAD/ CsFAPb( $I_{1-x}Br_x$ ) <sub>3</sub> (1.62 eV)/ SnO <sub>2</sub> / IZO/ NiO <sub>x</sub> / (FASnI <sub>3</sub> ) <sub>1-x</sub> (MAPbI <sub>3</sub> ) <sub>x</sub> (1.07 eV)/ C60/ ITO	80, 21, 999, 21, 1, 249, 1000, 20, 249	200

	ITO/ NiO <sub>x</sub> / FAPbI <sub>3</sub> (1.55 eV)/ PCBM/	123, 167, 863,	198
	ITO/ NiO <sub>x</sub> / (FASnI <sub>3</sub> ) <sub>1-x</sub> (MAPbI <sub>3</sub> ) <sub>x</sub> (1.07 eV)/ C60/ AZO	94, 19, 93, 978, 23, 203	
	ITO/ NiO <sub>x</sub> / CsFAPb(I <sub>1-x</sub> Br <sub>x</sub> ) <sub>3</sub> (1.67 eV)/ C60/ AZO/ NiO <sub>x</sub> / (FASnI <sub>3</sub> ) <sub>1-x</sub> (MAPbI <sub>3</sub> ) <sub>x</sub> (1.07 eV)/ C60/ ITO	128, 150, 921, 101, 7, 70, 962, 24, 177	195
Roof shingle	ITO/ NiO <sub>x</sub> / CsFAPb(I <sub>1-x</sub> Br <sub>x</sub> ) <sub>3</sub> (1.62 eV)/ SnO <sub>2</sub> / ITO/ NiO <sub>x</sub> / (FASnI <sub>3</sub> ) <sub>1-x</sub> (MAPbI <sub>3</sub> ) <sub>x</sub> (1.07 eV)/ C60/ AZO	130, 151, 999, 87, 6, 171, 986, 53, 234	206
	FTO/ NiO <sub>x</sub> / FAPbI <sub>3</sub> (1.55 eV)/ C60/ ITO/ PEDOT:PSS/ (FASnI <sub>3</sub> ) <sub>1-x</sub> (MAPbI <sub>3</sub> ) <sub>x</sub> (1.07 eV)/ C60/ ITO	122, 179, 979, 105, 7, 94, 990, 123, 210	203
	ITO/ spiro-OMeTAD/ CsFAPb(I <sub>1-x</sub> Br <sub>x</sub> ) <sub>3</sub> (1.62 eV)/ SnO <sub>2</sub> / AZO/ spiro-OMeTAD/ (FASnI <sub>3</sub> ) <sub>1-x</sub> (MAPbI <sub>3</sub> ) <sub>x</sub> (1.13 eV)/ C60/ ITO	81, 21, 999, 22, 1, 22, 1000, 21, 80	198
	ITO/ spiro-OMeTAD/ MAPbI <sub>3</sub> (1.55 eV)/ C60/ Ag/ NiO <sub>x</sub> / (FASnI <sub>3</sub> ) <sub>1-x</sub> (MAPbI <sub>3</sub> ) <sub>x</sub> (1.07 eV)/ C60/ ITO	211, 158, 678, 121, 4, 173, 866, 62, 205	198
Green grass	ITO/ NiO <sub>x</sub> / CsFAPb(I <sub>1-x</sub> Br <sub>x</sub> ) <sub>3</sub> (1.67 eV)/ C60/ ITO/ NiO <sub>x</sub> / (FASnI <sub>3</sub> ) <sub>1-x</sub> (MAPbI <sub>3</sub> ) <sub>x</sub> (1.07 eV)/ C60/ ITO	127, 149, 973, 113, 15, 102, 948, 51, 185	198
	ITO/ NiO <sub>x</sub> / CsFAPb(I <sub>1-x</sub> Br <sub>x</sub> ) <sub>3</sub> (1.62 eV)/ C60/ ITO/ NiO <sub>x</sub> / (FASnI <sub>3</sub> ) <sub>1-x</sub> (MAPbI <sub>3</sub> ) <sub>x</sub> (1.07 eV)/ C60/ ITO	127, 153, 1000, 130, 5, 98, 990, 127, 190	206
	ITO/ NiO <sub>x</sub> / FAPbI <sub>3</sub> (1.55 eV)/ C60/ ITO/ NiO <sub>x</sub> / (FASnI <sub>3</sub> ) <sub>1-x</sub> (MAPbI <sub>3</sub> ) <sub>x</sub> (1.07 eV)/ C60/ ITO	128, 151, 998, 123, 9, 87, 985, 116, 186	206

	ITO/ NiO <sub>x</sub> / MAPbI <sub>3</sub> (1.55 eV)/ C60/ ITO/ NiO <sub>x</sub> / (FASnI <sub>3</sub> ) <sub>1-x</sub> (MAPbI <sub>3</sub> ) <sub>x</sub> (1.07 eV)/ C60/ IZO	127, 155, 420, 103, 1, 102, 941, 91, 180	201
	ITO/ NiO <sub>x</sub> / CsFAPb(I <sub>1-x</sub> Br <sub>x</sub> ) <sub>3</sub> (1.67 eV)/ PCBM/ Ag/ NiO <sub>x</sub> / (FASnI <sub>3</sub> ) <sub>1-x</sub> (MAPbI <sub>3</sub> ) <sub>x</sub> (1.07 eV)/ C60/ ITO	125, 152, 982, 117, 5, 66, 981, 98, 173	198
White sand	ITO/ NiO <sub>x</sub> / (FASnI <sub>3</sub> ) <sub>1-x</sub> (MAPbI <sub>3</sub> ) <sub>x</sub> (1.07 eV)/ C60/ Ag/ NiO <sub>x</sub> / (FASnI <sub>3</sub> ) <sub>1-x</sub> (MAPbI <sub>3</sub> ) <sub>x</sub> (1.07 eV)/ C60/ FTO	155, 187, 580, 22, 9, 84, 995, 20, 83	303
	ITO/ NiO <sub>x</sub> / (FASnI <sub>3</sub> ) <sub>1-x</sub> (MAPbI <sub>3</sub> ) <sub>x</sub> (1.13 eV)/ C60/ Ag/ spiro-OMeTAD/ (FASnI <sub>3</sub> ) <sub>1-x</sub> (MAPbI <sub>3</sub> ) <sub>x</sub> (1.07 eV)/ C60/ ITO	142, 184, 828, 39, 10, 39, 966, 23, 245	296
	ITO/ NiO <sub>x</sub> / (FASnI <sub>3</sub> ) <sub>1-x</sub> (MAPbI <sub>3</sub> ) <sub>x</sub> (1.25 eV)/ C60/ Ag/ PTAA/ (FASnI <sub>3</sub> ) <sub>1-x</sub> (MAPbI <sub>3</sub> ) <sub>x</sub> (1.07 eV)/ C60/ ITO	141, 185, 752, 38, 5, 68, 957, 26, 248	291
Snow	ITO/ NiO <sub>x</sub> / (FASnI <sub>3</sub> ) <sub>1-x</sub> (MAPbI <sub>3</sub> ) <sub>x</sub> (1.07 eV)/ C60/ IZO/ spiro-OMeTAD/ (FASnI <sub>3</sub> ) <sub>1-x</sub> (MAPbI <sub>3</sub> ) <sub>x</sub> (1.07 eV)/ C60/ FTO	81, 20, 999, 246, 20, 24, 997, 20, 80	342
	ITO/ NiO <sub>x</sub> / (FASnI <sub>3</sub> ) <sub>1-x</sub> (MAPbI <sub>3</sub> ) <sub>x</sub> (1.13 eV)/ C60/ Ag/ spiro-OMeTAD/ (FASnI <sub>3</sub> ) <sub>1-x</sub> (MAPbI <sub>3</sub> ) <sub>x</sub> (1.07 eV)/ C60/ FTO	80, 23, 1000, 20, 20, 20, 1000, 20, 83	329

Table 8.4: Material combinations and layer thicknesses in monofacial (MF) and bifacial 2T perovskite-on-perovskite tandem solar cells for optimal short-circuit current.

### 8.4.1.1 Monofacial devices

For monofacial devices,  $\text{CsFAPb}(\text{I}_{1-x}\text{Br}_x)_3$  is the best-performing perovskite material for the top subcells. This material has a range of halide ion concentrations and bandgaps between 1.62 to 1.75 eV, as illustrated in Figure 8.5(a). The 2T tandem device, which includes the 1.70 eV perovskite in its top subcell, achieves the highest short-circuit current density of  $181 \text{ A/m}^2$ , which is close to the predicted  $185 \text{ A/m}^2$ , for an ideal device with no parasitic absorption in the transparent contact layers [44]. By fine-tuning the perovskite bandgap, short-circuit current densities within  $10 \text{ A/m}^2$  of the optimum can be achieved; for example,  $\text{MAPb}(\text{I}_{1-x}\text{Br}_x)_3$  and  $\text{FAPbI}_3$  are alternative perovskite materials for the top subcell, with bandgaps of 1.68 and 1.55 eV, respectively.

As shown in Figure 8.5(b), the optimized layer thicknesses for  $\text{CsFAPb}(\text{I}_{1-x}\text{Br}_x)_3$  with bandgaps from 1.7 to 1.75 eV are close to 1000 nm, while the thicknesses for  $\text{FAPbI}_3$  and  $\text{CsFAPb}(\text{I}_{1-x}\text{Br}_x)_3$  with bandgaps from 1.62 to 1.67 eV are only about 500 to 600 nm. Although these narrower bandgap perovskites provide lower short-circuit current densities of 172 to  $179 \text{ A/m}^2$  in tandem devices, there are substantial reductions in the perovskite thicknesses of the top subcells.

For the bottom perovskite layer, the best material is  $(\text{FASnI}_3)_{1-x}(\text{MAPbI}_3)_x$ , which has the narrowest bandgap among the perovskite materials considered. Its optimal thickness falls within the range of 850 to 1000 nm.

In addition, compared to the state-of-the-art 2T perovskite-on-perovskite tandem solar cell with a short-circuit current density of  $164 \text{ A/m}^2$  [149], our optimized optics structures have similar materials for the thin-film layers except the bottom hole-transporting and back-contact layers. On top of that, more than  $15 \text{ A/m}^2$  increases in the short-circuit current densities are predicted by having thicker perovskite layers up to 1000 nm, showing the potential for a better performing tandem solar cell.

### 8.4.1.2 Low albedos

$\text{CsFAPb}(\text{I}_{1-x}\text{Br}_x)_3$  remains the best choice for the top perovskite layers in bifacial 2T perovskite-on-perovskite tandem solar cells under low albedo values, as depicted in

Figure 8.5(a). The perovskite bandgaps of  $\text{CsFAPb}(\text{I}_{1-x}\text{Br}_x)_3$  range from 1.62 to 1.67 eV, which are narrower compared to those in the optimized monofacial tandem solar cells.  $\text{CsFAPb}(\text{I}_{1-x}\text{Br}_x)_3$  with various halide ion concentrations are thus suitable choices for the top perovskite layer in both monofacial and low albedo conditions. Their thicknesses, however, which range from 900 to 1000 nm (see Figure 8.5(b)) in devices under low albedos, are larger than that in the monofacial devices. This is because the top subcells need to generate higher photogenerated current densities for current matching in bifacial 2T devices.

Moreover,  $\text{FAPbI}_3$  is another promising candidate with the second best short-circuit current densities for devices under low albedo conditions. As alternatives,  $\text{MAPbI}_3$  is also a possible perovskite material in the top subcells for devices under albedos for roof shingle and green grass. For the bottom subcells,  $(\text{FASnI}_3)_{1-x}(\text{MAPbI}_3)_x$  with bandgap ranged from 1.07 to 1.13 eV are preferred as the perovskite material.

#### **8.4.1.3 High albedos**

At high albedo values, such as white sand and snow,  $(\text{FASnI}_3)_{1-x}(\text{MAPbI}_3)_x$  is the optimal perovskite material for both the top and bottom subcells, as depicted in Figure 8.5(a). These perovskites have narrow bandgaps ranging from 1.07 to 1.25 eV by tuning the chemical compositions. The optimized bifacial 2T perovskite-on-perovskite tandem solar cells have short-circuit current densities up to  $342 \text{ A/m}^2$ . Therefore, for these bifacial devices operating under high albedos, we suggest using narrow bandgap perovskites for both the top and bottom layers to achieve optimal short-circuit current densities. This guideline can also be applied to other types of tandem solar cells, including 4T perovskite-on-perovskite tandem solar cells, 2T perovskite-on-silicon and perovskite-on-organic tandem solar cells.

Similar optimal perovskite materials are identified for both white sand and snow, although their optimal thicknesses differ, as illustrated in Figure 8.5(b-c). In the case of snow albedo, the perovskite layer thicknesses of the top subcells are approximately 1000 nm, whereas they are around 600 to 800 nm for the white sand albedo. The optimal

thicknesses for the front-contact and top hole-transporting layers are around 150 nm and 180 nm, respectively, for devices under white sand albedo. In contrast, under the snow albedo, these decrease to 80 nm and 20 nm, respectively. Additionally, we observe that C60 is the best material for the bottom electron-transporting layer, with its thickness kept at 20 nm for all the optimized structures for high albedo conditions.

#### 8.4.1.4 Transmittance

Figure 8.5(b) demonstrates that the average transmittance of the top subcells decreases as the total irradiance increases. Specifically, for monofacial devices, the transmittance is around 0.5. For the low albedos, the transmittance ranges from 0.36 to 0.48. In contrast, for the high albedos, the transmittance is less than 0.25. In other words, the top subcells should be less semi-transparent at higher albedo values. Additionally, all optimized tandem devices exhibit good current matching between subcells, with the maximum differences in top and bottom photogenerated current densities being less than 5 A/m<sup>2</sup>.

#### 8.4.1.5 Further guidelines for materials and thicknesses

Across all albedos considered, the top subcells have an optimized perovskite layer thickness ranging from 400 to 1000 nm, while the bottom subcells have a range of around 850 to 1000 nm. In optimized tandem devices, the top subcells have more choices of perovskite materials than the bottom subcells, resulting in more variations in perovskite layer thicknesses for optimal transmittance and current matching.  $(\text{FASnI}_3)_{1-x}(\text{MAPbI}_3)_x$  with a thickness from 850 to 1000 nm is always preferred for the bottom perovskite layer.

Regarding the thin-film layers except for perovskite layers, optimal thicknesses can range from 20 nm to over 200 nm, depending on variations in materials and albedo conditions. However, certain trends can still be identified. For the top hole-transporting layer, most optimal thicknesses are either 20 nm or between 140 and 180 nm. The thicknesses of the two electron-transporting layers are generally below 140 nm. Additionally, most optimal thicknesses for the front-contact layer are either 80 nm or between 120 and 160 nm.

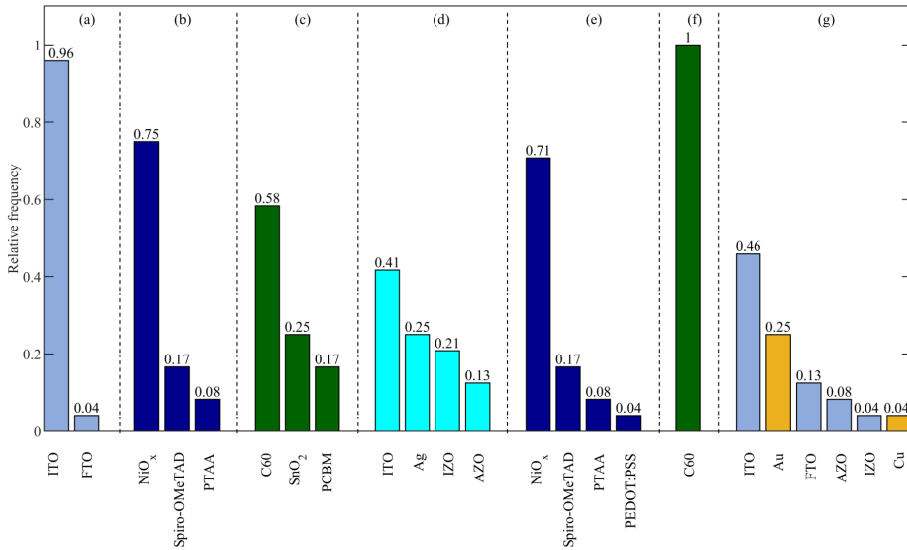


Figure 8.6: Relative frequencies of the materials that have been identified as the best choice in (a) the front-contact, (b) top hole-transporting, (c) top electron-transporting, (d) interconnecting, (e) bottom hole-transporting, (f) bottom electron-transporting and (g) back-contact layers of the twenty-four optimized 2T perovskite-on-perovskite tandem solar cells.

Moreover, Figure 8.6 presents the relative frequencies of materials that appear in these thin-film layers of the twenty-four optimized tandem solar cell structures. ITO stands out as the best transparent oxide for the front- and back-contact layers in most of the identified optimal tandem cell structures, while Au is a promising candidate for the metal back contact in monofacial tandem solar cells. NiO<sub>x</sub> is the best choice for the hole-transporting layers because of its low extinction coefficients (see Figure 8.4(d)), allowing minimal parasitic absorption. Similarly, C60 is identified as the optimal material for the bottom electron-transporting layers in all optimized cases due to its low extinction coefficients from 600 to 1200 nm wavelength (see Figure 8.4(n)).

We notice that although SnO<sub>2</sub> has the lowest extinction coefficients among the electron-transporting materials considered in the design space, it is not identified as the best material for the bottom electron-transporting layer. This is because its conduction band energy level (-4.34 eV) is higher than that of (FASnI<sub>3</sub>)<sub>1-x</sub>(MAPbI<sub>3</sub>)<sub>x</sub> (-4.36 eV), which violates our constraints set during the optimization process.

In addition, although the material combinations spiro-OMeTAD/ perovskite/ C60

and spiro-OMeTAD/ perovskite/  $\text{SnO}_2$  produce high short-circuit current densities in some of the tandem devices (see Table 8.4), it could be difficult to deposit an extreme thin spiro-OMeTAD layer of around 20 nm. On the one hand, the optimal thickness of spiro-OMeTAD is about 200 to 370 nm on perovskite, further reducing it may lead to a reduced uniformity of coverage on the perovskite layer [18]. On the other hand, this material as hole-transporting layer can lead to stability problems such as deterioration due to oxidation and humidity in perovskite solar cells [19, 20]. As such, replacing spiro-OMeTAD by  $\text{NiO}_x$  or PTAA is a better option for experimental implementation [18, 22]. These two alternatives can be also used as an extra thin hole-transporting layer of around 20 nm thick in efficient tandem devices [26, 27]. Some of the alternative architectures are provided in Table 8.4, which do not require extra thin spiro-OMeTAD layers of around 20 nm, and still produce close-to-optimal short-circuit current densities.

#### 8.4.2 External quantum efficiency

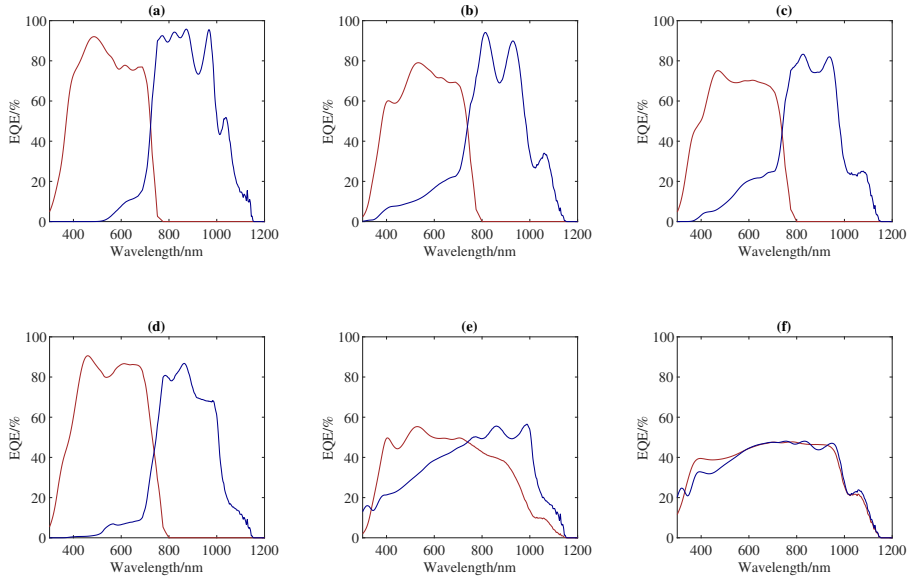


Figure 8.7: External quantum efficiencies (EQEs) of the top subcells (red) and bottom subcells (blue) for the optimized 2T perovskite-on-perovskite tandem solar cells: (a) monofacial, (b) 0.2 albedo, (c) roof shingle, (d) green grass, (e) white sand and (f) snow.

Next, it is worthwhile to evaluate the EQEs for the optimized 2T perovskite-on-perovskite tandem solar cells with the highest short-circuit current densities. Compared to the monofacial device, we observe two changes in EQEs when the solar cells are operating under bifacial conditions. First, the EQEs for the bottom subcell increase at short wavelengths ranging from 300 nm to 500 nm due to the rear incident light in bifacial tandem solar cells, as shown in Figure 8.7(a-d). Second, for high albedo values, the EQEs for both top and bottom subcells start to overlap for wavelengths from 300 to 1200 nm, as illustrated in Figure 8.7(e-f). For the snow albedo, which has an incident power density of 940 W/m<sup>2</sup> from the rear side, the irradiance is almost evenly distributed between the two subcells for all the wavelengths considered here. This occurs due to the decrease in perovskite bandgap and average transmittance in the top subcell. In contrast to other optimizations on bifacial tandem solar cells that considered only semi-transparent top perovskite subcells [45, 145, 167], we recommend non-semi-transparent top subcells for optimal optical designs under high albedo conditions.

#### **8.4.3 Sensitivity analysis**

The thicknesses of the layers in a solar cell can vary depending on fabrication conditions [168, 169]. Our sensitivity analysis aims to quantify the variability of the short-circuit current densities due to variations in the design space. The distributions of the short-circuit current densities for each albedo are presented in Figure 8.8(a-f). Here, we observe that the output distributions are negatively skewed for all cases, except for snow, which displays a bimodal normal distribution.

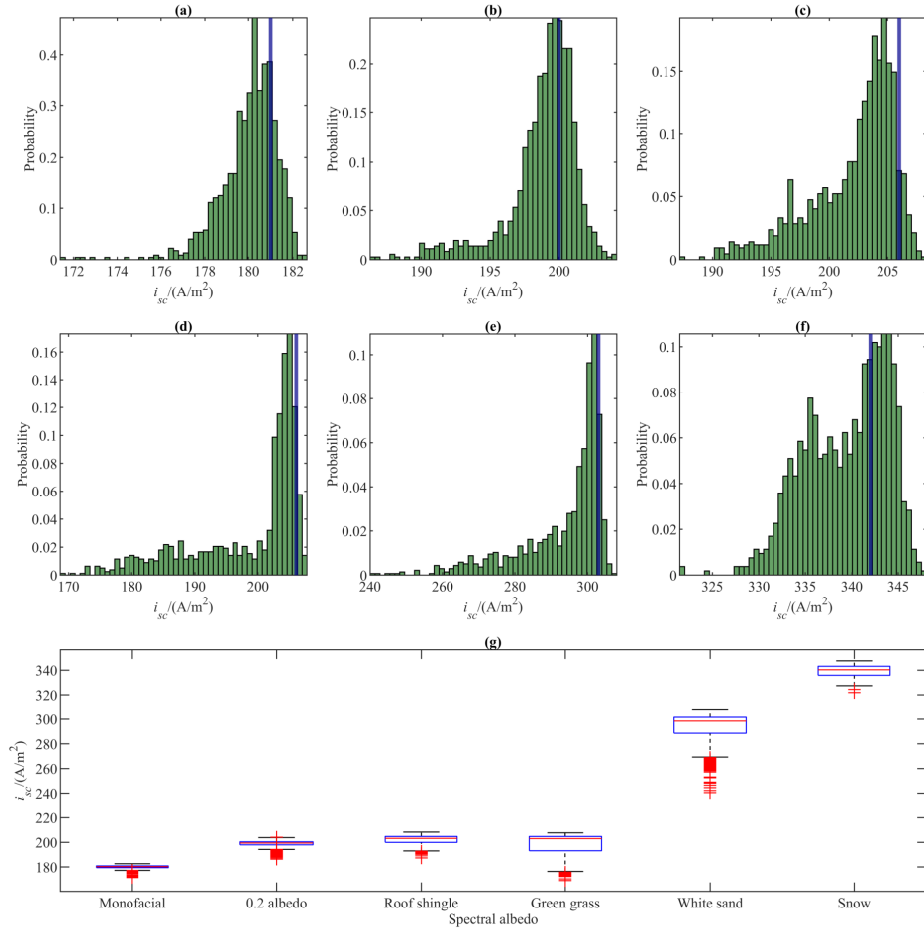


Figure 8.8: Probability distribution functions for the short-circuit current densities from the sensitivity analysis for 2T perovskite-on-perovskite tandem solar cells under different albedo conditions: (a) monofacial, (b) 0.2 albedo, (c) roof shingle, (d) green grass, (e) white sand and (f) snow. The statistics of the short-circuit current densities under various operation spectral albedos are highlighted in (g); and the short-circuit current densities from mixed-integer optimizations are indicated by blue vertical lines in (a)-(f).

For the monofacial device, all the short-circuit current densities are within 10 A/m<sup>2</sup> from the optimal value (181 A/m<sup>2</sup>), and less than 1% of the data are below 175 A/m<sup>2</sup>. For bifacial devices, more than 99%, 90%, 70%, 67% and 95% of the short-circuit current densities are within 10 A/m<sup>2</sup> of the optimum for 0.2 albedo, roof shingle, green grass, white sand and snow, respectively. This indicates that the majority of the short-circuit current densities remain close to the optimal point, demonstrating the robustness of the design with regards to small variations in the fabricated layer thicknesses.

To further assess the variability in the short-circuit current densities, we computed the medians and interquartile ranges for the first five albedos, as their distributions are non-normal [170]. The medians range from 180 to 300 A/m<sup>2</sup> (see Figure 8.8(g)), while the interquartile ranges are one order of magnitude smaller, ranging from 1 to 13 A/m<sup>2</sup>. For snow albedo, we fit the bimodal distributed data with a Gaussian mixture distribution model [171] and split them into two sets. The coefficients of variation for the two sets of data are 1.06% and 0.48%, respectively, which are significantly lower than the 5% coefficient of variation for layer thicknesses. Across all six albedo conditions, the output distributions are therefore narrower and more certain than the input distributions, and the optimal short-circuit current densities have low sensitivities to changes in layer thicknesses.

In addition, we note that the maximum short-circuit current densities may surpass the optimized values due to the absence of practical constraints imposed during the mixed-integer optimization. This implies that perovskite layer thicknesses exceeding 1000 nm can be used to achieve even higher short-circuit current densities; however, the marginal gains in short-circuit current densities are minimal, less than 5 A/m<sup>2</sup> compared to the optimal values ranging from 181 to 342 A/m<sup>2</sup>. Moreover, further increasing the thickness could compromise the quality of the thin-film layer [148, 149].

Based on the sensitivity analysis, we have found that the optimal short-circuit current densities are not significantly affected by small changes in layer thicknesses. This suggests that when a batch of solar cells is produced using our optimized conditions, their short-circuit current density values are likely to be very close to optimal—provided that the material properties do not vary significantly.

#### **8.4.4 Device performance**

Finally, we turn our attention towards the device performance in terms of open-circuit voltage and power-conversion efficiency. According to the bandgaps shown in Figure 8.5, the estimated open-circuit voltages are 2.25 V for the optimized monofacial device, 2.18 V for bifacial cells at low albedos, and 1.72 V for bifacial cells under high albedos.

For the fill factor of a 2T tandem device, we estimate it to be the lowest value among the corresponding single-junction subcells. The theoretical optimum fill factor is about 0.85 for a device with narrow bandgap of 1 to 1.1 eV, and increases when the bandgap becomes wider [165]. We therefore consider a theoretical optimum fill factor of 0.85 for our optimized 2T perovskite-on-perovskite tandem solar cells under various spectral albedos.

With these open-circuit voltages and fill factor, the power conversion efficiency for the optimized monofacial device is estimated to be 34.6%, and the bifacial equivalent power conversion efficiencies for the optimized bifacial devices are estimated to be 37.1%, 38.2%, 38.2%, 45.1% and 50.9% under 0.2 albedo and the albedos for roof shingle, green grass, white sand and snow, respectively.

#### 8.4.5 Cost consideration

As discussed in Chapter 6, a 2T perovskite-on-perovskite tandem solar cell has an advantage on its LOCE as compared to single junction silicon and perovskite solar cells, as well as perovskite-on-silicon solar cell. Our methodology here for a mixed-integer optimization can be applied to involve material and fabrication costs, which can be a potential future work to provide a multi-objective mixed-integer pareto front optimization. This could help to determine the most cost-efficient device architecture under various spectral albedos. Nevertheless, in order to provide more comprehensive suggestions, installation and labour costs at different albedo conditions need to be considered, which could be a possible limitation and challenge.

### 8.5 Summary

We have identified the best material combinations, layer thicknesses, and optimal short-circuit current densities for both monofacial and bifacial 2T perovskite-on-perovskite tandem solar cells through a mixed-integer optimization of a validated optics model. Among the materials considered, the best perovskite material in the top subcells for a

monofacial devices is  $\text{CsFAPb}(\text{I}_{1-x}\text{Br}_x)_3$  with a bandgap of 1.70 eV. For bifacial devices under 0.2 albedo and albedos for roof shingle and green grass, the optimal top perovskite material is still  $\text{CsFAPb}(\text{I}_{1-x}\text{Br}_x)_3$ , but with different halide ion concentrations and a 1.62 eV bandgap. In contrast, under albedos for white sand and snow,  $(\text{FASnI}_3)_{1-x}(\text{MAPbI}_3)_x$  with a bandgap of 1.07 eV is preferred. The optimal designs no longer require semi-transparent top subcells at high albedo values.

The sensitivity analysis shows that small perturbations in layer thicknesses will not significantly affect the short-circuit current densities of the optimized devices provided the material properties do not vary significantly during fabrication.

We further estimate that the power conversion efficiency for the optimized monofacial 2T perovskite-on-perovskite tandem solar cell can reach 34.6%. With additional rear-side irradiance, the bifacial equivalent efficiencies surpass 50% for bifacial 2T perovskite-on-perovskite tandem solar cells under high albedo values.

Our work provides a comprehensive optimization of the optics system in 2T perovskite-on-perovskite tandem solar cells and offers guidelines for material selection and thicknesses for thin-film layers. To gain more insights into the open-circuit voltage, fill factor, and power conversion efficiency, the optimization can be extended to include charge carrier transport and recombination parameters with an optoelectronic model.

# Chapter 9

## Conclusion

In this thesis, we have discussed the mathematical modeling and simulations of thin-film perovskite-based solar cells, including single-junction perovskite solar cells and perovskite-based 2T tandem solar cells. The mathematical modeling part includes detailed descriptions of thin-film optics and formulations on charge carrier transport and recombination with respect to energy band levels. This forms an optoelectronic model adaptable to single-junction perovskite and organic solar cells, and extendable for tandem devices, such as perovskite-on-perovskite and perovskite-on-organic tandem solar cells.

In Chapter 5, we developed artificial neural network models to replace the electronic part of the optoelectronic model for planar p-i-n structured perovskite solar cells. Through Bayesian optimization, we optimized the hyperparameters of these neural networks, resulting in good predictions of the device performances with mean squared errors much lower than  $10^{-3}$ , while the outputs were normalized between -1 and 1. Integrating these neural network models into device characterization, i-V measurements, device calibration, estimation of electronic parameters, sensitivity and loss analysis, and performance optimizations can be conducted more efficiently compared to using optoelectronic models. This enables us to improve the device architecture based on simulation results, fostering an iterative process that combines device fabrication and simulations for continuous development of perovskite solar cells. The incorporation of coupled neural networks with optics can become a valuable tool for digital twin applications.

In Chapter 6, we introduced an optoelectronic model for a 2T perovskite-on-perovskite tandem solar cell, taking into account coherent and incoherent light propagation, optical interference effects, charge carrier conservation, various recombination mechanisms, and trap-assisted tunneling at the interconnecting layer. By calibrating the model to the world record 2T perovskite-on-perovskite tandem solar cell with 24.5% PCE, we gained valuable insights into light management and loss analysis. Leveraging these insights and enhancing the carrier mobility in the top perovskite layer, we predict a significant 6% increase in the PCE, achieving a promising efficiency of 30.5%. Moreover, exploring the potential of bifacial operation, our results indicate the possibility of a bifacial 2T perovskite-on-perovskite tandem solar cell to achieve a bifacial equivalent PCE of 35.1% under 0.2 albedo, surpassing the SQ limit. These findings demonstrate the potential of our optoelectronic model to provide practical pathways for enhancing the performance of 2T perovskite-based tandem solar cells.

In Chapter 7, we developed an optoelectronic model for the 2T perovskite-on-organic tandem solar cell, focusing on charge carrier transport, generation, and recombination within the device. Our sensitivity analysis identified critical parameters influencing the PCE, such as hole mobility in the perovskite layer and the thicknesses of the top electron-transporting, perovskite, and organic layers. Key recombination losses occur at the interfaces between the top perovskite layer and its adjacent charge carrier transporting layers, as well as between the bottom organic layer and the hole-extraction layer. We also investigated the interconnecting layer, finding that increasing its thickness to 20 nm transforms it into a charge carrier transporting layer, significantly reducing the PCE. Furthermore, by studying layer thicknesses, charge carrier mobility, and recombination rates, we formulated a guideline for the 2T perovskite-on-organic tandem solar cell to achieve a 28% PCE, compared to 22.7% for the corresponding single-junction perovskite solar cell and 20.4% for the organic solar cell. The proposed guideline includes improving charge carrier transport in the active layers, reducing interfacial recombinations, increasing active layer thicknesses, and decreasing the top electron-transporting layer thickness. Future efforts will focus on developing efficient, narrower band gap

organics to move towards a 30% 2T perovskite-on-organic tandem device.

Chapter 8 focuses on a mixed-integer optimization to identify the best material combinations, layer thicknesses, and optimal short-circuit current densities for both monofacial and bifacial 2T perovskite-on-perovskite tandem solar cells. Using a validated optics model, we made significant findings regarding material choices. Notably, high albedo values no longer necessitate semi-transparent top subcells. Through a sensitivity analysis, we demonstrated that slight variations in layer thicknesses will not significantly impact the optimized short-circuit current densities, given that material properties remain relatively constant during fabrication. We estimate that the optimized monofacial 2T perovskite-on-perovskite tandem solar cell can achieve a 34.6% PCE. With additional rear-side irradiance, the bifacial equivalent efficiencies surpass 50% under high albedo conditions. This study presents a comprehensive optimization of the optics system for 2T perovskite-on-perovskite tandem solar cells, providing valuable guidelines for material selection and layer thicknesses. Future research can extend the optimization to include charge carrier transport and recombination parameters using an optoelectronic model, offering insights into the open-circuit voltage, fill factor, and PCE.



# Chapter 10

## Outlook

Several extensions can be made to our current work to better achieve the objectives mentioned above and provide more robust suggestions to enhance the performance of perovskite-based thin-film solar cells.

Firstly, a validated real solar cell performance predictions with our trained neural networks in Chapter 5 will allow consistent developments of the solar cells over time. This work should help conduct fast characterizations of the device, identify influential parameters to enhance cell performance through sensitivity and loss analyses, and provide an optimized device architecture and its performance for fabricating the next batch of solar cells. An iterative process can be formed, where the model utilizes real-time data to help improve device structures. Other than employing artificial neural networks, other types of deep learning algorithms such as deep, convolutional and recurrent neural networks can be explored on their potential improvements on the neural network performances. Also, artificial neural networks that cater to a device architecture with material and fabrication costs considered can be trained. This could be helpful on characterization purposes and performance predictions of specific photovoltaic devices. Our trained neural network, which targets p-i-n perovskite solar cells in general, can be one base case for comparing with the newly trained neural networks.

Secondly, for the optoelectronic models for 2T tandem devices in Chapters 6 and 7, similar artificial neural networks could be trained for more efficient simulations. Additionally, the model can be modified for 2T thin-film devices with more than two sub-

cells. For the interconnecting layer, we have investigated the effect of its resistivity and thickness on PCE; however, our validation is conducted for one batch of devices with limited material choices and samples. To further elucidate the physics and provide sound suggestions for real-world scenarios, more calibration and validation with experiments under various operating and environment conditions could be beneficial. In addition, we have considered room operating temperature in our simulations. Temperature considerations could be added into our models as one future work. One way to achieve that is to add in Fermi-Dirac statistics involving temperature as variable in the drift-diffusion model. Nonetheless, modeling of temperature's effects on material stability, deformation and interface qualities remains a challenge, and might require more calibrations and validations with experiments. As another future work, a cost-benefit analysis for 2T perovskite-based thin-film tandem solar cells can be conducted to provide insights on the economic gain and feasibilities for small- and large-scale mass productions.

Thirdly, other approaches, such as electrical models for 2T perovskite-based thin-film solar cells, can be considered. Electrical models, although not involving device electronic parameters such as charge carrier mobility and density of state, consider i-V characteristics, saturation current, resistances, and ideality factors for fitting. They have certain advantages, such as efficient computational cost and the ability to calibrate series and shunt resistances. However, due to a lack of key parameters like layer thicknesses, electrical models may not provide sound suggestions to improve device architecture. As an extension to our work, a comparison between optoelectronic models and electrical models can be done. The objective is to link these two different models and find functional forms that formulate electrical parameters like shunt resistance and ideality factor with electronic and geometrical parameters.

Lastly, for the mixed-integer optimization presented in Chapter 8, this work can be more meaningful when coupled with a full optoelectronic model or artificial neural network model. Considering the computational cost, artificial neural network models are preferred for 2T tandem solar cells. By doing so, the best material combinations and thicknesses for both optimized optical and electronic systems can be found. Moreover,

the methodology here can be extended into a multi-objective mixed-integer optimization for providing a pareto front on device LOCE and PCE. By doing so, the cost-effectiveness of a device could be optimized. The overall objective is to provide a more comprehensive guideline on device fabrication and suggest paths to improve device performances, including short-circuit current density, open-circuit voltage, fill factor, PCE, and cost.



# Bibliography

- [1] Christian Breyer et al. “On the role of solar photovoltaics in global energy transition scenarios”. In: *Progress in Photovoltaics: Research and Applications* 25.8 (Mar. 2017), pp. 727–745. DOI: [10.1002/pip.2885](https://doi.org/10.1002/pip.2885).
- [2] Nam-Gyu Park. “Perovskite solar cells: an emerging photovoltaic technology”. In: *Materials Today* 18.2 (Mar. 2015), pp. 65–72. DOI: [10.1016/j.mattod.2014.07.007](https://doi.org/10.1016/j.mattod.2014.07.007).
- [3] S. D. Stranks et al. “Electron-Hole Diffusion Lengths Exceeding 1 Micrometer in an Organometal Trihalide Perovskite Absorber”. In: *Science* 342.6156 (Oct. 2013), pp. 341–344. DOI: [10.1126/science.1243982](https://doi.org/10.1126/science.1243982).
- [4] Mohammed Istafaul Haque Ansari, Ahsanulhaq Qurashi, and Mohammad Khaja Nazeeruddin. “Frontiers, opportunities, and challenges in perovskite solar cells: A critical review”. In: *Journal of Photochemistry and Photobiology C: Photochemistry Reviews* 35 (June 2018), pp. 1–24. DOI: [10.1016/j.jphotochemrev.2017.11.002](https://doi.org/10.1016/j.jphotochemrev.2017.11.002).
- [5] Renxing Lin et al. “Monolithic all-perovskite tandem solar cells with 24.8% efficiency exploiting comproportionation to suppress Sn(ii) oxidation in precursor ink”. In: *Nature Energy* 4.10 (Sept. 2019), pp. 864–873. DOI: [10.1038/s41560-019-0466-3](https://doi.org/10.1038/s41560-019-0466-3).
- [6] Terry Chien-Jen Yang et al. “High-Bandgap Perovskite Materials for Multijunction Solar Cells”. In: *Joule* 2.8 (Aug. 2018), pp. 1421–1436. DOI: [10.1016/j.joule.2018.05.008](https://doi.org/10.1016/j.joule.2018.05.008).

- [7] Qingfeng Dong et al. “Electron-hole diffusion lengths > 175  $\mu\text{m}$  in solution-grown  $\text{CH}_3\text{NH}_3\text{PbI}_3$  single crystals”. In: *Science* 347.6225 (Jan. 2015), pp. 967–970. DOI: [10.1126/science.aaa5760](https://doi.org/10.1126/science.aaa5760).
- [8] G. Xing et al. “Long-Range Balanced Electron- and Hole-Transport Lengths in Organic-Inorganic  $\text{CH}_3\text{NH}_3\text{PbI}_3$ ”. In: *Science* 342.6156 (Oct. 2013), pp. 344–347. DOI: [10.1126/science.1243167](https://doi.org/10.1126/science.1243167).
- [9] Qianqian Lin et al. “Electro-optics of perovskite solar cells”. In: *Nature Photonics* 9.2 (Dec. 2014), pp. 106–112. DOI: [10.1038/nphoton.2014.284](https://doi.org/10.1038/nphoton.2014.284).
- [10] Valerio D’Innocenzo et al. “Excitons versus free charges in organo-lead trihalide perovskites”. In: *Nature Communications* 5.1 (Apr. 2014). DOI: [10.1038/ncomms4586](https://doi.org/10.1038/ncomms4586).
- [11] Christian Wehrenfennig et al. “High Charge Carrier Mobilities and Lifetimes in Organolead Trihalide Perovskites”. In: *Advanced Materials* 26.10 (Dec. 2013), pp. 1584–1589. DOI: [10.1002/adma.201305172](https://doi.org/10.1002/adma.201305172).
- [12] NREL. *Best Research-Cell Efficiencies*. Oct. 2023. URL: <https://www.nrel.gov/pv/assets/pdfs/best-research-cell-efficiencies.20200925.pdf>.
- [13] Sven Ruehle. “Tabulated values of the Shockley–Queisser limit for single junction solar cells”. In: *Solar Energy* 130 (June 2016), pp. 139–147. DOI: [10.1016/j.solener.2016.02.015](https://doi.org/10.1016/j.solener.2016.02.015).
- [14] Bin Yang et al. “Perovskite Solar Cells with Near 100% Internal Quantum Efficiency Based on Large Single Crystalline Grains and Vertical Bulk Heterojunctions”. In: 137.29 (July 2015), pp. 9210–9213. DOI: [10.1021/jacs.5b03144](https://doi.org/10.1021/jacs.5b03144).
- [15] Hansong Xue et al. “Modelling and loss analysis of meso-structured perovskite solar cells”. In: *Journal of Applied Physics* 122.8 (Aug. 2017), p. 083105. DOI: [10.1063/1.4986115](https://doi.org/10.1063/1.4986115).

- [16] Hansong Xue, Erik Birgersson, and Rolf Stangl. “Correlating variability of modeling parameters with photovoltaic performance: Monte Carlo simulation of a meso-structured perovskite solar cell”. In: *Applied Energy* 237 (Mar. 2019), pp. 131–144. DOI: [10.1016/j.apenergy.2018.12.066](https://doi.org/10.1016/j.apenergy.2018.12.066).
- [17] Hansong Xue, Rolf Stangl, and Erik Birgersson. “Elucidating the functional form of the recombination losses in a planar perovskite solar cell: A scaling analysis”. In: *Journal of Applied Physics* 128.12 (Sept. 2020), p. 123102. DOI: [10.1063/5.0013741](https://doi.org/10.1063/5.0013741).
- [18] Florine M. Rombach, Saif A. Haque, and Thomas J. Macdonald. “Lessons learned from spiro-OMeTAD and PTAA in perovskite solar cells”. In: *Energy & Environmental Science* 14.10 (2021), pp. 5161–5190. DOI: [10.1039/d1ee02095a](https://doi.org/10.1039/d1ee02095a).
- [19] Ajay Kumar Jena et al. “Role of spiro-OMeTAD in performance deterioration of perovskite solar cells at high temperature and reuse of the perovskite films to avoid Pb-waste”. In: *Journal of Materials Chemistry A* 6.5 (2018), pp. 2219–2230. DOI: [10.1039/c7ta07674f](https://doi.org/10.1039/c7ta07674f).
- [20] Ernestas Kasparavicius et al. “Oxidized Spiro-OMeTAD: Investigation of Stability in Contact with Various Perovskite Compositions”. In: *ACS Applied Energy Materials* 4.12 (Dec. 2021), pp. 13696–13705. DOI: [10.1021/acsaem.1c02375](https://doi.org/10.1021/acsaem.1c02375).
- [21] Qifan Xue et al. “Improving Film Formation and Photovoltage of Highly Efficient Inverted-Type Perovskite Solar Cells through the Incorporation of New Polymeric Hole Selective Layers”. In: *Advanced Energy Materials* 6.5 (Dec. 2015), p. 1502021. DOI: [10.1002/aenm.201502021](https://doi.org/10.1002/aenm.201502021).
- [22] Md. Bodil Islam et al. “NiOx Hole Transport Layer for Perovskite Solar Cells with Improved Stability and Reproducibility”. In: *ACS Omega* 2.5 (May 2017), pp. 2291–2299. DOI: [10.1021/acsomega.7b00538](https://doi.org/10.1021/acsomega.7b00538).

- [23] Jiaxing Song et al. “Low-temperature SnO<sub>2</sub>-based electron selective contact for efficient and stable perovskite solar cells”. In: *Journal of Materials Chemistry A* 3.20 (2015), pp. 10837–10844.
- [24] Dong Yang et al. “Stable Efficiency Exceeding 20.6% for Inverted Perovskite Solar Cells through Polymer-Optimized PCBM Electron-Transport Layers”. In: *Nano Letters* 19.5 (Apr. 2019), pp. 3313–3320. DOI: [10.1021/acs.nanolett.9b00936](https://doi.org/10.1021/acs.nanolett.9b00936).
- [25] W. Ke et al. “Efficient planar perovskite solar cells using roomtemperature vacuum-processed C<sub>60</sub> electron selective layers”. In: *J. Mater. Chem. A* 3 (2015), p. 17971. DOI: [10.1039/C5TA04313A](https://doi.org/10.1039/C5TA04313A).
- [26] Renxing Lin et al. “Monolithic all-perovskite tandem solar cells with 24.8% efficiency exploiting comproportionation to suppress Sn (II) oxidation in precursor ink”. In: *Nature Energy* 4.10 (2019), pp. 864–873.
- [27] Wei Chen et al. “Monolithic perovskite/organic tandem solar cells with 23.6% efficiency enabled by reduced voltage losses and optimized interconnecting layer”. In: *Nature Energy* 7.3 (Jan. 2022), pp. 229–237. DOI: [10.1038/s41560-021-00966-8](https://doi.org/10.1038/s41560-021-00966-8).
- [28] Hui Li and Wei Zhang. “Perovskite Tandem Solar Cells: From Fundamentals to Commercial Deployment”. In: *Chemical Reviews* 120.18 (Aug. 2020), pp. 9835–9950. DOI: [10.1021/acs.chemrev.9b00780](https://doi.org/10.1021/acs.chemrev.9b00780).
- [29] Martin A. Green et al. “Solar cell efficiency tables (Version 60)”. In: *Progress in Photovoltaics: Research and Applications* 30.7 (June 2022), pp. 687–701. DOI: [10.1002/pip.3595](https://doi.org/10.1002/pip.3595).
- [30] Marko Jošt et al. “Perovskite/CIGS Tandem Solar Cells: From Certified 24.2% toward 30% and Beyond”. In: *ACS Energy Letters* 7.4 (Mar. 2022), pp. 1298–1307. DOI: [10.1021/acsenergylett.2c00274](https://doi.org/10.1021/acsenergylett.2c00274).

- [31] K. O. Brinkmann et al. “Perovskite–organic tandem solar cells with indium oxide interconnect”. In: *Nature* 604.7905 (Apr. 2022), pp. 280–286. DOI: [10.1038/s41586-022-04455-0](https://doi.org/10.1038/s41586-022-04455-0).
- [32] Ke Xiao et al. “All-perovskite tandem solar cells with 24.2% certified efficiency and area over 1 cm<sup>2</sup> using surface-anchoring zwitterionic antioxidant”. In: *Nature Energy* 5.11 (Oct. 2020), pp. 870–880. DOI: [10.1038/s41560-020-00705-5](https://doi.org/10.1038/s41560-020-00705-5).
- [33] A De Vos. “Detailed balance limit of the efficiency of tandem solar cells”. In: *Journal of Physics D: Applied Physics* 13.5 (May 1980), pp. 839–846. DOI: [10.1088/0022-3727/13/5/018](https://doi.org/10.1088/0022-3727/13/5/018).
- [34] Shenkun Xie et al. “Efficient monolithic perovskite/organic tandem solar cells and their efficiency potential”. In: *Nano Energy* 78 (Dec. 2020), p. 105238. DOI: [10.1016/j.nanoen.2020.105238](https://doi.org/10.1016/j.nanoen.2020.105238).
- [35] Xu Chen et al. “Efficient and Reproducible Monolithic Perovskite/Organic Tandem Solar Cells with Low-Loss Interconnecting Layers”. In: *Joule* 4.7 (July 2020), pp. 1594–1606. DOI: [10.1016/j.joule.2020.06.006](https://doi.org/10.1016/j.joule.2020.06.006).
- [36] Weijie Chen et al. “Surface Reconstruction for Stable Monolithic All-Inorganic Perovskite/Organic Tandem Solar Cells with over 21% Efficiency”. In: *Advanced Functional Materials* 32.5 (Oct. 2021), p. 2109321. DOI: [10.1002/adfm.202109321](https://doi.org/10.1002/adfm.202109321).
- [37] Yue-Min Xie et al. “Homogeneous Grain Boundary Passivation in Wide-Bandgap Perovskite Films Enables Fabrication of Monolithic Perovskite/Organic Tandem Solar Cells with over 21% Efficiency”. In: *Advanced Functional Materials* 32.19 (Feb. 2022), p. 2112126. DOI: [10.1002/adfm.202112126](https://doi.org/10.1002/adfm.202112126).
- [38] Pang Wang et al. “Tuning of the Interconnecting Layer for Monolithic Perovskite/Organic Tandem Solar Cells with Record Efficiency Exceeding 21%”. In: *Nano Letters* 21.18 (Sept. 2021), pp. 7845–7854. DOI: [10.1021/acs.nanolett.1c02897](https://doi.org/10.1021/acs.nanolett.1c02897).

- [39] Shucheng Qin et al. “Constructing Monolithic Perovskite/Organic Tandem Solar Cell with Efficiency of 22.0% via Reduced Open-Circuit Voltage Loss and Broadened Absorption Spectra”. In: *Advanced Materials* 34.11 (Feb. 2022), p. 2108829. DOI: [10.1002/adma.202108829](https://doi.org/10.1002/adma.202108829).
- [40] Cenqi Yan et al. “Non-fullerene acceptors for organic solar cells”. In: *Nature Reviews Materials* 3.3 (Feb. 2018). DOI: [10.1038/natrevmats.2018.3](https://doi.org/10.1038/natrevmats.2018.3).
- [41] Lingxian Meng et al. “Organic and solution-processed tandem solar cells with 17.3% efficiency”. In: *Science* 361.6407 (Sept. 2018), pp. 1094–1098. DOI: [10.1126/science.aat2612](https://doi.org/10.1126/science.aat2612).
- [42] Ajay Singh and Alessio Gagliardi. “Efficiency of all-perovskite two-terminal tandem solar cells: A drift-diffusion study”. In: *Solar Energy* 187 (July 2019), pp. 39–46. DOI: [10.1016/j.solener.2019.05.006](https://doi.org/10.1016/j.solener.2019.05.006).
- [43] Neelima Singh, Alpana Agarwal, and Mohit Agarwal. “Numerical simulation of highly efficient lead-free all-perovskite tandem solar cell”. In: *Solar Energy* 208 (Sept. 2020), pp. 399–410. DOI: [10.1016/j.solener.2020.08.003](https://doi.org/10.1016/j.solener.2020.08.003).
- [44] Marcos Soldera, Alejandro Koffman-Frischknecht, and Kurt Taretto. “Optical and electrical optimization of all-perovskite pin type junction tandem solar cells”. In: *Journal of Physics D: Applied Physics* 53.31 (June 2020), p. 315104. DOI: [10.1088/1361-6463/ab8851](https://doi.org/10.1088/1361-6463/ab8851).
- [45] Jakapan Chantana et al. “Optimized bandgaps of top and bottom subcells for bifacial two-terminal tandem solar cells under different back irradiances”. In: *Solar Energy* 220 (May 2021), pp. 163–174. DOI: [10.1016/j.solener.2021.03.034](https://doi.org/10.1016/j.solener.2021.03.034).
- [46] Maximilian T. Häßlertner and Henry J. Snaith. “Predicting and optimising the energy yield of perovskite-on-silicon tandem solar cells under real world conditions”. In: *Energy & Environmental Science* 10.9 (2017), pp. 1983–1993. DOI: [10.1039/c7ee01232b](https://doi.org/10.1039/c7ee01232b).

- [47] David J. Griffiths and Colin Ingfield. “Introduction to Electrodynamics”. In: *American Journal of Physics* 73.6 (June 2005), pp. 574–574. DOI: [10.1119/1.4766311](https://doi.org/10.1119/1.4766311).
- [48] Axel Donges. “The coherence length of black-body radiation”. In: *European Journal of Physics* 19.3 (May 1998), pp. 245–249. DOI: [10.1088/0143-0807/19/3/006](https://doi.org/10.1088/0143-0807/19/3/006).
- [49] Puhan et al. “Irradiance in Mixed Coherent/Incoherent Structures: An Analytical Approach”. In: *Coatings* 9.9 (Aug. 2019), p. 536. DOI: [10.3390/coatings9090536](https://doi.org/10.3390/coatings9090536).
- [50] keqian Zhang and Dejie Li. *Electromagnetic Theory for Microwaves and Optoelectronics*. Springer Berlin Heidelberg, 2008. DOI: [10.1007/978-3-540-74296-8](https://doi.org/10.1007/978-3-540-74296-8).
- [51] C.A. Gueymard, D. Myers, and K. Emery. “Proposed reference irradiance spectra for solar energy systems testing”. In: *Solar Energy* 73.6 (Dec. 2002), pp. 443–467. DOI: [10.1016/s0038-092x\(03\)00005-7](https://doi.org/10.1016/s0038-092x(03)00005-7).
- [52] Sungyeop Jung et al. “Optical Modeling and Analysis of Organic Solar Cells with Coherent Multilayers and Incoherent Glass Substrate Using Generalized Transfer Matrix Method”. In: *Japanese Journal of Applied Physics* 50 (Nov. 2011), p. 122301. DOI: [10.1143/jjap.50.122301](https://doi.org/10.1143/jjap.50.122301).
- [53] Andrej Campa, Janez Krc, and Marko Topic. “Two approaches for incoherent propagation of light in rigorous numerical simulations”. In: *Progress In Electromagnetics Research* 137 (2013), pp. 187–202. DOI: [10.2528/pier13010407](https://doi.org/10.2528/pier13010407).
- [54] Zachary C. Holman et al. “Infrared light management in high-efficiency silicon heterojunction and rear-passivated solar cells”. In: *Journal of Applied Physics* 113.1 (Jan. 2013), p. 013107. DOI: [10.1063/1.4772975](https://doi.org/10.1063/1.4772975).
- [55] Jan Isidorsson et al. “Ellipsometry on sputter-deposited tin oxide films: optical constants versus stoichiometry, hydrogen content, and amount of electrochemically intercalated lithium”. In: *Applied Optics* 37.31 (Nov. 1998), p. 7334. DOI: [10.1364/ao.37.007334](https://doi.org/10.1364/ao.37.007334).

- [56] Rudi Santbergen et al. “Minimizing optical losses in monolithic perovskite/c-Si tandem solar cells with a flat top cell”. In: *Optics Express* 24.18 (Aug. 2016), A1288. DOI: [10.1364/oe.24.0a1288](https://doi.org/10.1364/oe.24.0a1288).
- [57] Jérémie Werner et al. “Complex Refractive Indices of Cesium–Formamidinium-Based Mixed-Halide Perovskites with Optical Band Gaps from 1.5 to 1.8 eV”. In: *ACS Energy Letters* 3.3 (Feb. 2018), pp. 742–747. DOI: [10.1021/acsenergylett.8b00089](https://doi.org/10.1021/acsenergylett.8b00089).
- [58] Horiba. *C60 and C70 Optical Constants Study by Ellipsometry*. (accessed 25 August 2020).
- [59] K. Bittkau, T. Kirchartz, and U. Rau. “Optical design of spectrally selective interlayers for perovskite/silicon heterojunction tandem solar cells”. In: *Optics Express* 26.18 (July 2018), A750. DOI: [10.1364/oe.26.00a750](https://doi.org/10.1364/oe.26.00a750).
- [60] Kiran Ghimire et al. “Optical response of mixed methylammonium lead iodide and formamidinium tin iodide perovskite thin films”. In: *AIP Advances* 7.7 (July 2017), p. 075108. DOI: [10.1063/1.4994211](https://doi.org/10.1063/1.4994211).
- [61] Z.T. Liu et al. “The characterization of the optical functions of BCP and CBP thin films by spectroscopic ellipsometry”. In: *Synthetic Metals* 150.2 (Apr. 2005), pp. 159–163. DOI: [10.1016/j.synthmet.2005.02.001](https://doi.org/10.1016/j.synthmet.2005.02.001).
- [62] H.-J. Hagemann, W. Gudat, and C. Kunz. “Optical constants from the far infrared to the x-ray region: Mg, Al, Cu, Ag, Au, Bi, C, and Al<sub>2</sub>O<sub>3</sub>”. In: *J. Opt. Soc. Am.* 65.6 (June 1975), pp. 742–744. DOI: [10.1364/JOSA.65.000742](https://doi.org/10.1364/JOSA.65.000742). URL: <http://www.osapublishing.org/abstract.cfm?URI=josa-65-6-742>.
- [63] B. Macco et al. “Low-temperature atomic layer deposition of MoO<sub>x</sub> for silicon heterojunction solar cells”. In: 9.7 (June 2015), pp. 393–396. DOI: [10.1002/pssr.201510117](https://doi.org/10.1002/pssr.201510117).
- [64] Malte Ruben Vogt et al. “Measurement of the Optical Constants of Soda-Lime Glasses in Dependence of Iron Content and Modeling of Iron-Related Power

- Losses in Crystalline Si Solar Cell Modules”. In: *IEEE Journal of Photovoltaics* 6.1 (Jan. 2016), pp. 111–118. DOI: [10.1109/jphotov.2015.2498043](https://doi.org/10.1109/jphotov.2015.2498043).
- [65] Patrick O’Connor and Andre Kleyner. *Practical reliability engineering*. John Wiley & Sons, 2012.
- [66] Robert S Witte and John S Witte. *Statistics, 11th Edition*. Wiley, 2017.
- [67] Raj S. Chhikara. “Communications in statistics”. In: *Communications in Statistics - Theory and Methods* 13.23 (Jan. 1984), pp. 7–8. DOI: [10.1080/03610928408828867](https://doi.org/10.1080/03610928408828867).
- [68] Innocent O. Oboh, Uchechukwu H. Offor, and Nsikakabasi D. Okon. “Artificial neural network modeling for potential performance enhancement of a planar perovskite solar cell with a novel TiO<sub>2</sub> electron transport bilayer using nonlinear programming”. In: *Energy Reports* 8 (Nov. 2022), pp. 973–988. DOI: [10.1016/j.egyr.2021.12.010](https://doi.org/10.1016/j.egyr.2021.12.010).
- [69] Shuren Sun et al. “Light trapping nano structures with over 30% enhancement in perovskite solar cells”. In: *Organic Electronics* 75 (Dec. 2019), p. 105385. DOI: [10.1016/j.orgel.2019.105385](https://doi.org/10.1016/j.orgel.2019.105385).
- [70] Jionghua Wu et al. “Using hysteresis to predict the charge recombination properties of perovskite solar cells”. In: *Journal of Materials Chemistry A* 9.10 (2021), pp. 6382–6392. DOI: [10.1039/d0ta12046d](https://doi.org/10.1039/d0ta12046d).
- [71] J. M. Foster et al. “A Model for the Operation of Perovskite Based Hybrid Solar Cells: Formulation, Analysis, and Comparison to Experiment”. In: *SIAM Journal on Applied Mathematics* 74.6 (Jan. 2014), pp. 1935–1966. DOI: [10.1137/130934258](https://doi.org/10.1137/130934258).
- [72] J. G. Simmons and G. W. Taylor. “Nonequilibrium Steady-State Statistics and Associated Effects for Insulators and Semiconductors Containing an Arbitrary Distribution of Traps”. In: *Physical Review B* 4.2 (July 1971), pp. 502–511. DOI: [10.1103/physrevb.4.502](https://doi.org/10.1103/physrevb.4.502).

- [73] Tejas S. Sherkar et al. “Recombination in Perovskite Solar Cells: Significance of Grain Boundaries, Interface Traps, and Defect Ions”. In: *ACS Energy Letters* 2.5 (May 2017), pp. 1214–1222. DOI: [10.1021/acsenergylett.7b00236](https://doi.org/10.1021/acsenergylett.7b00236).
- [74] Chuanliang Chen et al. “Effect of BCP buffer layer on eliminating charge accumulation for high performance of inverted perovskite solar cells”. In: 7.57 (2017), pp. 35819–35826. DOI: [10.1039/c7ra06365b](https://doi.org/10.1039/c7ra06365b).
- [75] Hansong Xue, Erik Birgersson, and Rolf Stangl. “A spatially smoothed device model for meso-structured perovskite solar cells”. In: *Journal of Applied Physics* 124.19 (Nov. 2018), p. 193103. DOI: [10.1063/1.5045379](https://doi.org/10.1063/1.5045379).
- [76] Frank Burden and Dave Winkler. “Bayesian Regularization of Neural Networks”. In: *Methods in Molecular Biology*™. Humana Press, 2008, pp. 23–42. DOI: [10.1007/978-1-60327-101-1\\_3](https://doi.org/10.1007/978-1-60327-101-1_3).
- [77] Simon Haykin. *Neural Networks. A Comprehensive Foundation (3rd Edition)*. Prentice Hall, 2007, p. 842. ISBN: 9780131471399.
- [78] Xinhai Zhao et al. “Elucidating the underlying physics in a two-terminal all-perovskite tandem solar cell: A guideline towards 30% power conversion efficiency”. In: *Solar Energy* 231 (Jan. 2022), pp. 716–731. DOI: [10.1016/j.solener.2021.11.029](https://doi.org/10.1016/j.solener.2021.11.029).
- [79] Xinhai Zhao et al. “Modeling and sensitivity analysis of a two-terminal perovskite on organic tandem solar cell”. In: *Cell Reports Physical Science* 3.9 (Sept. 2022), p. 101038. DOI: [10.1016/j.xcrp.2022.101038](https://doi.org/10.1016/j.xcrp.2022.101038).
- [80] Hu Quee Tan et al. “Optoelectronic modeling and sensitivity analysis of a four-terminal all-perovskite tandem solar cell – Identifying pathways to improve efficiency”. In: *Solar Energy* 216 (Mar. 2021), pp. 589–600. DOI: [10.1016/j.solener.2021.01.021](https://doi.org/10.1016/j.solener.2021.01.021).
- [81] T. Golubev et al. “Understanding the impact of C60 at the interface of perovskite solar cells via drift-diffusion modeling”. In: *AIP Advances* 9 (2019), p. 035026. DOI: [10.1063/1.5068690](https://doi.org/10.1063/1.5068690).

- [82] A. Intaniwet et al. “Achieving a stable time response in polymeric radiation sensors under charge injection by X-rays”. In: *ACS Appl Mater Interfaces* 2.6 (2010), pp. 1692–1969. DOI: [10.1021/am100220y](https://doi.org/10.1021/am100220y).
- [83] Sateesh Prathapani, Parag Bhargava, and Sudhanshu Mallick. “Electronic band structure and carrier concentration of formamidinium–cesium mixed cation lead mixed halide hybrid perovskites”. In: *Applied Physics Letters* 112.9 (2018), p. 092104. DOI: [10.1063/1.5016829](https://doi.org/10.1063/1.5016829).
- [84] M. Sendner, J. Trollmann, and A. Pucci. “Dielectric function and degradation process of poly(triarylamine) (PTAA)”. In: *Organic Electronics* 15.11 (2014), pp. 2959–2963. DOI: [10.1016/j.orgel.2014.08.037](https://doi.org/10.1016/j.orgel.2014.08.037).
- [85] P. Vivo, J. K. Salunke, and A. Priimagi. “Hole-transporting materials for printable perovskite solar cells”. In: *Materials* 10 (2017), p. 1087. DOI: [10.3390/ma10091087](https://doi.org/10.3390/ma10091087).
- [86] S. Hunter, A. D. Mottram, and T. D. Anthopoulos. “Temperature and composition-dependent density of states in organic small-molecule/polymer blend transistors”. In: *J. Appl. Phys.* 120 (2016), p. 025502. DOI: [10.1063/1.4955282](https://doi.org/10.1063/1.4955282).
- [87] Jinhui Tong et al. “Carrier lifetimes of  $> 1 \mu\text{s}$  in Sn-Pb perovskites enable efficient all-perovskite tandem solar cells”. In: *Science* 364.6439 (2019), pp. 475–479. DOI: [10.1126/science.aav7911](https://doi.org/10.1126/science.aav7911).
- [88] Zakarya Berkai et al. “Monte Carlo simulation of electric conductivity for pure and doping fullerene (C<sub>60</sub>)”. In: *Physics Letters A* 383.17 (2019), pp. 2090–2092. DOI: [10.1016/j.physleta.2019.04.011](https://doi.org/10.1016/j.physleta.2019.04.011).
- [89] T. Sakurai et al. “Influence of gap states on electrical properties at interface between bathocuproine and various types of metals”. In: *J. Appl. Phys.* 107 (2010), p. 043707. DOI: [10.1063/1.3309278](https://doi.org/10.1063/1.3309278).
- [90] Wei-Chih Lai et al. “Perovskite-based solar cells with inorganic inverted hybrid planar heterojunction structure”. In: *AIP Advances* 8.1 (2018), p. 015109. DOI: [10.1063/1.5010951](https://doi.org/10.1063/1.5010951).

- [91] Subramani Thiyagu et al. “Hybrid organic-inorganic heterojunction solar cells with 12% efficiency by utilizing flexible film-silicon with a hierarchical surface”. In: *Nanoscale* 6.6 (2014), p. 3361. DOI: [10.1039/c3nr06323b](https://doi.org/10.1039/c3nr06323b).
- [92] A. Rajagopal et al. “High efficient perovskite-perovskite tandem solar cells reaching 80% of the theoretical limit in photovoltage”. In: *Adv. Mater.* 29.24 (2017), p. 1702140. DOI: [10.1002/adma.201702140](https://doi.org/10.1002/adma.201702140).
- [93] Masatsugu Yamashita et al. “Nondestructive measurement of carrier mobility in conductive polymer PEDOT: PSS using terahertz and infrared spectroscopy”. In: *2011 XXXth URSI General Assembly and Scientific Symposium*. IEEE. 2011, pp. 1–4. DOI: [10.1109/URSIGASS.2011.6050616](https://doi.org/10.1109/URSIGASS.2011.6050616).
- [94] Menglei Feng et al. “High-Efficiency and Stable Inverted Planar Perovskite Solar Cells with Pulsed Laser Deposited Cu-Doped NiOsubix/i/sub Hole-Transport Layers”. In: *ACS Applied Materials & Interfaces* 12.45 (Oct. 2020), pp. 50684–50691. DOI: [10.1021/acsami.0c15923](https://doi.org/10.1021/acsami.0c15923).
- [95] Amran Al-Ashouri et al. “Monolithic perovskite/silicon tandem solar cell with >29% efficiency by enhanced hole extraction”. In: *Science* 370.6522 (Dec. 2020), pp. 1300–1309. DOI: [10.1126/science.abd4016](https://doi.org/10.1126/science.abd4016).
- [96] Heetae Yoon et al. “Hysteresis-free low-temperature-processed planar perovskite solar cells with 19.1% efficiency”. In: *Energy & Environmental Science* 9.7 (2016), pp. 2262–2266. DOI: [10.1039/c6ee01037g](https://doi.org/10.1039/c6ee01037g).
- [97] Pandeng Li et al. “Synergistic Effect of Dielectric Property and Energy Transfer on Charge Separation in Non-Fullerene-Based Solar Cells”. In: *Angewandte Chemie International Edition* 60.27 (May 2021), pp. 15054–15062. DOI: [10.1002/anie.202103357](https://doi.org/10.1002/anie.202103357).
- [98] Xiaolan Wang et al. “Device Modeling and Design of Inverted Solar Cell Based on Comparative Experimental Analysis between Effect of Organic and Inorganic Hole Transport Layer on Morphology and Photo-Physical Property of Per-

- ovskite Thin Film”. In: *Materials* 14.9 (Apr. 2021), p. 2191. DOI: [10.3390/ma14092191](https://doi.org/10.3390/ma14092191).
- [99] Pietro Caprioglio et al. “On the Origin of the Ideality Factor in Perovskite Solar Cells”. In: 10.27 (June 2020), p. 2000502. DOI: [10.1002/aenm.202000502](https://doi.org/10.1002/aenm.202000502).
- [100] N. Moulin et al. “Tunnel junction I(V) characteristics: Review and a new model for p-n homojunctions”. In: *Journal of Applied Physics* 126.3 (July 2019), p. 033105. DOI: [10.1063/1.5104314](https://doi.org/10.1063/1.5104314).
- [101] G.A.M. Hurkx, D.B.M. Klaassen, and M.P.G. Knuvers. “A new recombination model for device simulation including tunneling”. In: *IEEE Transactions on Electron Devices* 39.2 (1992), pp. 331–338. DOI: [10.1109/16.121690](https://doi.org/10.1109/16.121690).
- [102] Shivam Singh et al. “Investigation on Organic Molecule Additive for Moisture Stability and Defect Passivation via Physisorption in CH<sub>3</sub>NH<sub>3</sub>PbI<sub>3</sub> Based Perovskite”. In: *ACS Applied Energy Materials* 1.5 (Apr. 2018), pp. 1870–1877. DOI: [10.1021/acsaem.8b00350](https://doi.org/10.1021/acsaem.8b00350).
- [103] D. Mateus Torres-Herrera et al. “Thermal co-evaporated MoO<sub>x</sub>:Au thin films and its application as anode modifier in perovskite solar cells”. In: *Solar Energy* 206 (Aug. 2020), pp. 136–144. DOI: [10.1016/j.solener.2020.05.105](https://doi.org/10.1016/j.solener.2020.05.105).
- [104] J. Howlett, Milton Abramowitz, and Irene A. Stegun. “Handbook of Mathematical Functions”. In: *The Mathematical Gazette* 50.373 (Oct. 1966), p. 358. DOI: [10.2307/3614753](https://doi.org/10.2307/3614753).
- [105] F. Trani et al. “Density functional study of oxygen vacancies at the SnO<sub>2</sub> surface and subsurface sites”. In: *Physical Review B* 77 (2008), p. 245410. DOI: [10.1103/PhysRevB.77.245410](https://doi.org/10.1103/PhysRevB.77.245410).
- [106] AZoM. *Tin Dioxide (SnO<sub>2</sub>) Semiconductors* (2013). (accessed 28 August 2020).
- [107] Weijun Ke et al. “Effects of annealing temperature of tin oxide electron selective layers on the performance of perovskite solar cells”. In: *Journal of Materials Chemistry A* 3.47 (2015), pp. 24163–24168. DOI: [10.1039/C5TA06574G](https://doi.org/10.1039/C5TA06574G).

- [108] Christian M. Wolff et al. “Nonradiative Recombination in Perovskite Solar Cells: The Role of Interfaces”. In: *Advanced Materials* 31.52 (Oct. 2019), p. 1902762. DOI: [10.1002/adma.201902762](https://doi.org/10.1002/adma.201902762).
- [109] Juan-Pablo Correa-Baena et al. “Identifying and suppressing interfacial recombination to achieve high open-circuit voltage in perovskite solar cells”. In: *Energy & Environmental Science* 10.5 (2017), pp. 1207–1212. DOI: [10.1039/c7ee00421d](https://doi.org/10.1039/c7ee00421d).
- [110] Tomas Leijtens et al. “Carrier trapping and recombination: the role of defect physics in enhancing the open circuit voltage of metal halide perovskite solar cells”. In: *Energy & Environmental Science* 9.11 (2016), pp. 3472–3481. DOI: [10.1039/c6ee01729k](https://doi.org/10.1039/c6ee01729k).
- [111] Youwei Wang et al. “High intrinsic carrier mobility and photon absorption in the perovskite CH<sub>3</sub>NH<sub>3</sub>PbI<sub>3</sub>”. In: *Physical Chemistry Chemical Physics* 17.17 (2015), pp. 11516–11520. DOI: [10.1039/c5cp00448a](https://doi.org/10.1039/c5cp00448a).
- [112] Hikaru Oga et al. “Improved Understanding of the Electronic and Energetic Landscapes of Perovskite Solar Cells: High Local Charge Carrier Mobility, Reduced Recombination, and Extremely Shallow Traps”. In: *Journal of the American Chemical Society* 136.39 (Sept. 2014), pp. 13818–13825. DOI: [10.1021/ja506936f](https://doi.org/10.1021/ja506936f).
- [113] Zongqi Li et al. “Cost analysis of perovskite tandem photovoltaics”. In: *Joule* 2.8 (2018), pp. 1559–1572.
- [114] Michael Gostein, Bill Marion, and Bill Stueve. “Spectral Effects in Albedo and Rearside Irradiance Measurement for Bifacial Performance Estimation”. In: *2020 47th IEEE Photovoltaic Specialists Conference (PVSC)*. IEEE, June 2020. DOI: [10.1109/pvsc45281.2020.9300518](https://doi.org/10.1109/pvsc45281.2020.9300518).
- [115] Thomas C. R. Russell et al. “The Influence of Spectral Albedo on Bifacial Solar Cells: A Theoretical and Experimental Study”. In: *IEEE Journal of Photo-*

- tovoltaics* 7.6 (Nov. 2017), pp. 1611–1618. DOI: [10.1109/jphotov.2017.2756068](https://doi.org/10.1109/jphotov.2017.2756068).
- [116] Y. Park et al. “Work function of indium tin oxide transparent conductor measured by photoelectron spectroscopy”. In: *Applied Physics Letters* 68.19 (May 1996), pp. 2699–2701. DOI: [10.1063/1.116313](https://doi.org/10.1063/1.116313).
- [117] Teng Zhang et al. “Analysis of a device model for organic pseudo-bilayer solar cells”. In: *Journal of Applied Physics* 112.8 (Oct. 2012), p. 084511. DOI: [10.1063/1.4759165](https://doi.org/10.1063/1.4759165).
- [118] L. J. A. Koster et al. “Device model for the operation of polymer/fullerene bulk heterojunction solar cells”. In: *Physical Review B* 72.8 (Aug. 2005), p. 085205. DOI: [10.1103/physrevb.72.085205](https://doi.org/10.1103/physrevb.72.085205).
- [119] Zhihong Wu et al. “n-Type Water/Alcohol-Soluble Naphthalene Diimide-Based Conjugated Polymers for High-Performance Polymer Solar Cells”. In: *Journal of the American Chemical Society* 138.6 (Feb. 2016), pp. 2004–2013. DOI: [10.1021/jacs.5b12664](https://doi.org/10.1021/jacs.5b12664).
- [120] Lijun Chen et al. “Solution-Processed MoO<sub>x</sub> Hole-Transport Layer with F4-TCNQ Modification for Efficient and Stable Inverted Perovskite Solar Cells”. In: *ACS Applied Energy Materials* 2.8 (July 2019), pp. 5862–5870. DOI: [10.1021/acsaem.9b01004](https://doi.org/10.1021/acsaem.9b01004).
- [121] Yuanwei Jiang et al. “Post-annealing Effect on Optical and Electronic Properties of Thermally Evaporated MoO<sub>x</sub> Thin Films as Hole-Selective Contacts for p-Si Solar Cells”. In: *Nanoscale Research Letters* 16.1 (May 2021). DOI: [10.1186/s11671-021-03544-9](https://doi.org/10.1186/s11671-021-03544-9).
- [122] Ming Zhang et al. “Single-layered organic photovoltaics with double cascading charge transport pathways: 18% efficiencies”. In: *Nature Communications* 12.1 (Jan. 2021). DOI: [10.1038/s41467-020-20580-8](https://doi.org/10.1038/s41467-020-20580-8).

- [123] Dan Li et al. “Amino-functionalized conjugated polymer electron transport layers enhance the UV-photostability of planar heterojunction perovskite solar cells”. In: *Chemical Science* 8.6 (2017), pp. 4587–4594. DOI: [10.1039/c7sc00077d](https://doi.org/10.1039/c7sc00077d).
- [124] Nurlan Tokmoldin et al. “Extraordinarily long diffusion length in PM6:Y6 organic solar cells”. In: *Journal of Materials Chemistry A* 8.16 (2020), pp. 7854–7860. DOI: [10.1039/d0ta03016c](https://doi.org/10.1039/d0ta03016c).
- [125] Christian Stelling et al. “Plasmonic nanomeshes: their ambivalent role as transparent electrodes in organic solar cells”. In: *Scientific Reports* 7.1 (Feb. 2017). DOI: [10.1038/srep42530](https://doi.org/10.1038/srep42530).
- [126] Ram Narayan Chauhan et al. “Silicon induced stability and mobility of indium zinc oxide based bilayer thin film transistors”. In: *Applied Physics Letters* 109.20 (Nov. 2016). DOI: [10.1063/1.4968001](https://doi.org/10.1063/1.4968001).
- [127] Na Li et al. “Extraction of Contact Resistance and DC Modeling in Metal Oxide TFTs”. In: *IEEE Journal of the Electron Devices Society* 7 (2019), pp. 127–133. DOI: [10.1109/jeds.2018.2885136](https://doi.org/10.1109/jeds.2018.2885136).
- [128] Zhiming Chen et al. “Counterion-tunable n-type conjugated polyelectrolytes for the interface engineering of efficient polymer solar cells”. In: *Journal of Materials Chemistry A* 5.36 (2017), pp. 19447–19455. DOI: [10.1039/c7ta05246d](https://doi.org/10.1039/c7ta05246d).
- [129] Zachary C Holman et al. “Infrared light management in high-efficiency silicon heterojunction and rear-passivated solar cells”. In: *Journal of Applied Physics* 113.1 (2013), p. 013107.
- [130] Robin Kerremans et al. “The Optical Constants of Solution-Processed Semiconductors—New Challenges with Perovskites and Non-Fullerene Acceptors”. In: *Advanced Optical Materials* 8.16 (May 2020), p. 2000319. DOI: [10.1002/adom.202000319](https://doi.org/10.1002/adom.202000319).
- [131] Hiroyuki Fujiwara and Robert W. Collins, eds. *Spectroscopic Ellipsometry for Photovoltaics*. Springer International Publishing, 2018. DOI: [10.1007/978-3-319-95138-6](https://doi.org/10.1007/978-3-319-95138-6).

- [132] Tobias A. F. Koenig et al. “Electrically Tunable Plasmonic Behavior of Nanocube–Polymer Nanomaterials Induced by a Redox-Active Electrochromic Polymer”. In: *ACS Nano* 8.6 (June 2014), pp. 6182–6192. DOI: [10.1021/nn501601e](https://doi.org/10.1021/nn501601e).
- [133] Olivier Carton et al. “Optical Characterization of Porous Sputtered Silver Thin Films”. In: *Journal of Spectroscopy* 2013 (2013), pp. 1–6. DOI: [10.1155/2013/307824](https://doi.org/10.1155/2013/307824).
- [134] Laura M. Herz. “Charge-Carrier Mobilities in Metal Halide Perovskites: Fundamental Mechanisms and Limits”. In: *ACS Energy Letters* 2.7 (June 2017), pp. 1539–1548. DOI: [10.1021/acsenergylett.7b00276](https://doi.org/10.1021/acsenergylett.7b00276).
- [135] Ji-Ting Shieh et al. “The effect of carrier mobility in organic solar cells”. In: *Journal of Applied Physics* 107.8 (Apr. 2010), p. 084503. DOI: [10.1063/1.3327210](https://doi.org/10.1063/1.3327210).
- [136] A. Baumann et al. “A New Approach for Probing the Mobility and Lifetime of Photogenerated Charge Carriers in Organic Solar Cells Under Real Operating Conditions”. In: *Advanced Materials* 24.32 (July 2012), pp. 4381–4386. DOI: [10.1002/adma.201200874](https://doi.org/10.1002/adma.201200874).
- [137] Sven Ruehle. “The detailed balance limit of perovskite/silicon and perovskite/CdTe tandem solar cells”. In: *physica status solidi (a)* 214.5 (Feb. 2017), p. 1600955. DOI: [10.1002/pssa.201600955](https://doi.org/10.1002/pssa.201600955).
- [138] Minjin Kim et al. “Conformal quantum dot–SnO<sub>2</sub> layers as electron transporters for efficient perovskite solar cells”. In: *Science* 375.6578 (Jan. 2022), pp. 302–306. DOI: [10.1126/science.abh1885](https://doi.org/10.1126/science.abh1885).
- [139] Pei-Yang Gu et al. “Pushing up the efficiency of planar perovskite solar cells to 18.2% with organic small molecules as the electron transport layer”. In: *Journal of Materials Chemistry A* 5.16 (2017), pp. 7339–7344. DOI: [10.1039/c7ta01764b](https://doi.org/10.1039/c7ta01764b).

- [140] Wei Liu et al. “Low-Bandgap Non-fullerene Acceptors Enabling High-Performance Organic Solar Cells”. In: *ACS Energy Letters* 6.2 (Jan. 2021), pp. 598–608. DOI: [10.1021/acsenergylett.0c02384](https://doi.org/10.1021/acsenergylett.0c02384).
- [141] Junjiang Wu et al. “Towards a bright future: The versatile applications of organic solar cells”. In: *Materials Reports: Energy* 1.4 (Nov. 2021), p. 100062. DOI: [10.1016/j.matre.2021.100062](https://doi.org/10.1016/j.matre.2021.100062).
- [142] Bo Chen et al. “Bifacial all-perovskite tandem solar cells”. In: *Science Advances* 8.47 (Nov. 2022). DOI: [10.1126/sciadv.add0377](https://doi.org/10.1126/sciadv.add0377).
- [143] Michele De Bastiani et al. “Efficient bifacial monolithic perovskite/silicon tandem solar cells via bandgap engineering”. In: *Nature Energy* 6.2 (Jan. 2021), pp. 167–175. DOI: [10.1038/s41560-020-00756-8](https://doi.org/10.1038/s41560-020-00756-8).
- [144] Chan Ul Kim et al. “Optimization of device design for low cost and high efficiency planar monolithic perovskite/silicon tandem solar cells”. In: *Nano Energy* 60 (June 2019), pp. 213–221. DOI: [10.1016/j.nanoen.2019.03.056](https://doi.org/10.1016/j.nanoen.2019.03.056).
- [145] Hongjiang Li et al. “Revealing the output power potential of bifacial monolithic all-perovskite tandem solar cells”. In: *eLight* 2.1 (Oct. 2022). DOI: [10.1186/s43593-022-00028-w](https://doi.org/10.1186/s43593-022-00028-w).
- [146] Emanuele Centurioni. “Generalized matrix method for calculation of internal light energy flux in mixed coherent and incoherent multilayers”. In: *Applied Optics* 44.35 (Dec. 2005), p. 7532. DOI: [10.1364/ao.44.007532](https://doi.org/10.1364/ao.44.007532).
- [147] Michele De Bastiani et al. “Recombination junctions for efficient monolithic perovskite-based tandem solar cells: physical principles, properties, processing and prospects”. In: *Materials Horizons* 7.11 (2020), pp. 2791–2809. DOI: [10.1039/d0mh00990c](https://doi.org/10.1039/d0mh00990c).
- [148] Dewei Zhao et al. “Efficient two-terminal all-perovskite tandem solar cells enabled by high-quality low-bandgap absorber layers”. In: 3.12 (Nov. 2018), pp. 1093–1100. DOI: [10.1038/s41560-018-0278-x](https://doi.org/10.1038/s41560-018-0278-x).

- [149] Ke Xiao et al. “All-perovskite tandem solar cells with 24.2% certified efficiency and area over 1 cm<sup>2</sup> using surface-anchoring zwitterionic antioxidant”. In: *Nature Energy* 5.11 (2020), pp. 870–880.
- [150] Salman Manzoor et al. “Optical modeling of wide-bandgap perovskite and perovskite/silicon tandem solar cells using complex refractive indices for arbitrary-bandgap perovskite absorbers”. In: *Optics Express* 26.21 (Oct. 2018), p. 27441. DOI: [10.1364/oe.26.027441](https://doi.org/10.1364/oe.26.027441).
- [151] Pankaj Yadav et al. “Exploring the performance limiting parameters of perovskite solar cell through experimental analysis and device simulation”. In: *Solar Energy* 122 (Dec. 2015), pp. 773–782. DOI: [10.1016/j.solener.2015.09.046](https://doi.org/10.1016/j.solener.2015.09.046).
- [152] Lioz Etgar et al. “Mesoscopic CH<sub>3</sub>NH<sub>3</sub>PbI<sub>3</sub>/TiO<sub>2</sub> Heterojunction Solar Cells”. In: *Journal of the American Chemical Society* 134.42 (Oct. 2012), pp. 17396–17399. DOI: [10.1021/ja307789s](https://doi.org/10.1021/ja307789s).
- [153] Seungchan Ryu et al. “Voltage output of efficient perovskite solar cells with high open-circuit voltage and fill factor”. In: *Energy Environ. Sci.* 7.8 (2014), pp. 2614–2618. DOI: [10.1039/c4ee00762j](https://doi.org/10.1039/c4ee00762j).
- [154] Chengxi Zhang et al. “Recent progress of minimal voltage losses for high-performance perovskite photovoltaics”. In: *Nano Energy* 81 (Mar. 2021), p. 105634. DOI: [10.1016/j.nanoen.2020.105634](https://doi.org/10.1016/j.nanoen.2020.105634).
- [155] Shuxia Tao et al. “Absolute energy level positions in tin- and lead-based halide perovskites”. In: *Nature Communications* 10.1 (June 2019). DOI: [10.1038/s41467-019-10468-7](https://doi.org/10.1038/s41467-019-10468-7).
- [156] Ranbir Singh et al. “The effects of crystal structure on the photovoltaic performance of perovskite solar cells under ambient indoor illumination”. In: *Solar Energy* 220 (May 2021), pp. 43–50. DOI: [10.1016/j.solener.2021.01.052](https://doi.org/10.1016/j.solener.2021.01.052).

- [157] Guiying Xu et al. “Integrating Ultrathin Bulk-Heterojunction Organic Semiconductor Intermediary for High-Performance Low-Bandgap Perovskite Solar Cells with Low Energy Loss”. In: *Advanced Functional Materials* 28.42 (Aug. 2018), p. 1804427. DOI: [10.1002/adfm.201804427](https://doi.org/10.1002/adfm.201804427).
- [158] Kyoungwon Choi et al. “Thermally stable, planar hybrid perovskite solar cells with high efficiency”. In: *Energy & Environmental Science* 11.11 (2018), pp. 3238–3247. DOI: [10.1039/c8ee02242a](https://doi.org/10.1039/c8ee02242a).
- [159] E Raoult et al. “Optical Characterizations and Modelling of Semitransparent Perovskite Solar Cells for Tandem Applications”. In: *36th Eur. Photovolt. Sol. Energy Conf. Exhib.* 2019, pp. 757–763.
- [160] Chang-Wen Chen et al. “Optical properties of organometal halide perovskite thin films and general device structure design rules for perovskite single and tandem solar cells”. In: *Journal of Materials Chemistry A* 3.17 (2015), pp. 9152–9159. DOI: [10.1039/c4ta05237d](https://doi.org/10.1039/c4ta05237d).
- [161] Peter G. Gordon et al. “Work function of doped zinc oxide films deposited by ALD”. In: *Journal of Materials Research* 35.7 (Nov. 2019), pp. 756–761. DOI: [10.1557/jmr.2019.334](https://doi.org/10.1557/jmr.2019.334).
- [162] Hyo-Joong Kim et al. “Work function and interface control of amorphous IZO electrodes by MoO<sub>3</sub> layer grading for organic solar cells”. In: *Solar Energy Materials and Solar Cells* 141 (Oct. 2015), pp. 194–202. DOI: [10.1016/j.solmat.2015.05.036](https://doi.org/10.1016/j.solmat.2015.05.036).
- [163] Kevin M. McPeak et al. “Plasmonic Films Can Easily Be Better: Rules and Recipes”. In: *ACS Photonics* 2.3 (Feb. 2015), pp. 326–333. DOI: [10.1021/ph5004237](https://doi.org/10.1021/ph5004237).
- [164] “The work functions of copper, silver and aluminium”. In: *Proceedings of the Royal Society of London. Series A. Mathematical and Physical Sciences* 210.1100 (Dec. 1951), pp. 70–84. DOI: [10.1098/rspa.1951.0231](https://doi.org/10.1098/rspa.1951.0231).

- [165] Zhanglin Guo et al. “The high open-circuit voltage of perovskite solar cells: a review”. In: *Energy & Environmental Science* 15.8 (2022), pp. 3171–3222. DOI: [10.1039/d2ee00663d](https://doi.org/10.1039/d2ee00663d).
- [166] Hu Quee Tan et al. “Optimizing bifacial all-perovskite tandem solar cell: How to balance light absorption and recombination”. In: *Solar Energy* 231 (Jan. 2022), pp. 1092–1106. DOI: [10.1016/j.solener.2021.12.040](https://doi.org/10.1016/j.solener.2021.12.040).
- [167] Yuan Gao et al. “Performance optimization of monolithic all-perovskite tandem solar cells under standard and real-world solar spectra”. In: *Joule* 6.8 (Aug. 2022), pp. 1944–1963. DOI: [10.1016/j.joule.2022.06.027](https://doi.org/10.1016/j.joule.2022.06.027).
- [168] James E. Bishop et al. “Spray-cast multilayer perovskite solar cells with an active-area of 1.5 cm<sup>2</sup>”. In: *Scientific Reports* 7.1 (Aug. 2017). DOI: [10.1038/s41598-017-08642-2](https://doi.org/10.1038/s41598-017-08642-2).
- [169] Dong Hoe Kim et al. “Outlook and Challenges of Perovskite Solar Cells toward Terawatt-Scale Photovoltaic Module Technology”. In: *Joule* 2.8 (Aug. 2018), pp. 1437–1451. DOI: [10.1016/j.joule.2018.05.011](https://doi.org/10.1016/j.joule.2018.05.011).
- [170] Kristin L. Sainani. “Dealing With Non-normal Data”. In: *PM&R* 4.12 (Dec. 2012), pp. 1001–1005. DOI: [10.1016/j.pmrj.2012.10.013](https://doi.org/10.1016/j.pmrj.2012.10.013).
- [171] Xinhua Zhuang et al. “Gaussian mixture density modeling, decomposition, and applications”. In: *IEEE Transactions on Image Processing* 5.9 (1996), pp. 1293–1302. DOI: [10.1109/83.535841](https://doi.org/10.1109/83.535841).